University of Pennsylvania
ScholarlyCommons

Publicly Accessible Penn Dissertations

2018

Spatio-Temporal Dynamics Of Phytoplankton Biomass From Ocean Color Remote Sensing And Cmip5 Model Suites

Priya Sharma
University of Pennsylvania, priyash@sas.upenn.edu

Follow this and additional works at: https://repository.upenn.edu/edissertations

Part of the Climate Commons, Ecology and Evolutionary Biology Commons, and the Environmental Indicators and Impact Assessment Commons

Recommended Citation
Sharma, Priya, "Spatio-Temporal Dynamics Of Phytoplankton Biomass From Ocean Color Remote Sensing And Cmip5 Model Suites" (2018). *Publicly Accessible Penn Dissertations*. 3307.
https://repository.upenn.edu/edissertations/3307

This paper is posted at ScholarlyCommons. https://repository.upenn.edu/edissertations/3307
For more information, please contact repository@pobox.upenn.edu.

Spatio-Temporal Dynamics Of Phytoplankton Biomass From Ocean Color Remote Sensing And Cmip5 Model Suites

Abstract
Phytoplankton are the base of the marine food web, and, importantly, drive the biological carbon pump, the combination of photosynthesis, organic carbon sinking and subsurface decomposition of organic matter which effectively sequesters carbon away from the atmosphere. Our knowledge of phytoplankton activity is currently advancing fast through developments of multiple ocean-color remote sensing algorithms and via developments in ecological modules incorporated in climate models. While climate models are projecting relatively clear trends in ocean ecology over the next century, distinguishing between interannual variability and ocean biology trends from satellite observations is difficult. Short record length, satellite data continuity issues and strong interannual variability all impact quantified trends. Additionally, commonly observed chlorophyll-a is not strictly indicative of underlying phytoplankton biomass because of phytoplankton adaptation. This thesis investigates the trends, interannual variability and seasonality in new size-partitioned phytoplankton biomass products, with a focus on the Sea-Viewing Wide Field-of-View Sensor (SeaWiFS) mission period (1997-2010). In Chapter 2 we found phytoplankton biomass increases in the warm ocean regions over this period, opposing common expectations of decreases in warming oceans. Biomass increases are due to increased physical mixing of the watercolumn and are partially attributed to the large scale El Nino Southern Oscillation (ENSO) phenomenon. Recent studies have highlighted the emergence of different types of ENSO, with a shift towards more Central Pacific ENSO events. Chapter 3 uses statistical techniques (agglomerative hierarchical clustering (AHC), empirical orthogonal functional analysis (EOF)) on phytoplankton biomass to characterize ENSO "flavors" in the tropical Pacific. For the first time, we empirically derive biological indices for different ENSO types and show high correlations with existing climate indices. In Chapter 4 we examine in depth seasonal in phytoplankton ecology between the North Eastern Pacific subpolar region and contrast it with North Atlantic subpolar ecology. We discuss drivers of biological changes (iron, nutrients, light, mixing). We reveal large differences between biological variables across ocean-color algorithms, as well as across the latest generation Earth System model suite (Carbon Model Intercomparison Project, CMIP5). Chapter 5 summarizes our findings and future work suggestions. Future work should link surface phytoplankton ecology to ocean-atmosphere carbon fluxes and ocean carbon pump efficiency.

Degree Type
Dissertation

Degree Name
Doctor of Philosophy (PhD)

Graduate Group
Earth & Environmental Science

First Advisor
Irina Marinov

This dissertation is available at ScholarlyCommons: https://repository.upenn.edu/edissertations/3307

Keywords
ENSO, Long-term Trend, Phytoplankton Biomass, Phytoplankton Functional Types, Seasonality, Spatio-temporal

Subject Categories
Climate | Ecology and Evolutionary Biology | Environmental Indicators and Impact Assessment | Environmental Sciences

This dissertation is available at ScholarlyCommons: https://repository.upenn.edu/edissertations/3307

SPATIO-TEMPORAL DYNAMICS OF PHYTOPLANKTON BIOMASS FROM OCEAN COLOR REMOTE SENSING AND CMIP5 MODEL SUITES

Priya Sharma

A DISSERTATION

in

Earth and Environmental Science

Presented to the Faculties of the University of Pennsylvania

in

Partial Fulfillment of the Requirements for the

Degree of Doctor of Philosophy

2019

Supervisor of Dissertation

_____

Irina Marinov

Assistant Professor, Earth and Environmental Science

Graduate Group Chairperson

_____

Douglas J. Jerolmack,

Professor, Earth and Environmental Science

Dissertation Committee

David Goldsby, Associate Professor, Earth and Environmental Science

Jane Dmochowski, Senior Lecturer, Earth and Environmental Science

Awnesh Singh (External), Senior Lecturer, The University of the South Pacific

Tihomir S. Kostadinov (External), Assistant Professor, California State University

SPATIO-TEMPORAL DYNAMICS OF PHYTOPLANKTON BIOMASS FROM OCEAN COLOR REMOTE SENSING AND CMIP5 MODEL SUITES

COPYRIGHT

2019

Priya Sharma

This work is licensed under the
Creative Commons Attribution-
NonCommercial-ShareAlike 3.0
License

To view a copy of this license, visit

https://creativecommons.org/licenses/by-nc-sa/3.0/us/

Dedication page

To Mr. Ajay Kumar Sharma and Mrs. Sashi Kiran

(my parents)

and

Ms. Anisha Khatoon

(my best friend)

ACKNOWLEDGMENT

“An idea that is developed and dwell into realization is more imperative than an idea that lives only as an idea”

- Buddha

Thus, I would like to thank all those people who have and has somehow contributed towards making it possible and helped in the accomplishment of my idea into a thesis. With great pleasure, I would like to thank my Principle Advisor Irina Marinov, who has been a constant support in structuring up and guiding towards the completion of this thesis. Thank you for believing in me and being a mentor.

Sincere gratitude to my co-advisors; Awnesh Singh and Tihomir Kostadinov, who provided support in numerous ways: scientific advice, technical and challenging me with science questions. Thank you Tihomir Kostadinov for providing the data and data-related advises. "Vinaka Vakalevu" (Thank you in Fijian) Awnesh, for providing all resources at the University of the South Pacific. Thank you to Anna Cabre for the unlimited technical advice and guidance, despite situated on a different continent (Spain).

I would like to acknowledge the Graduate committee members for their robust scientific feedback on my research, and for providing a platform to develop my scientific career. Thank you to Faculty, and administrative staffs of Earth and Environmental Science department in providing resources, information’s, especially Joan, Arlene and Audrey. My deepest gratitude goes to the Graduate students for the heartfelt and infinite support throughout my PhD journey, for sharing their positive energy and warm hugs. I would also like to acknowledge all the undergraduates of the climate group for helping me to accomplish my scientific goals.

I would like to extend my warm-hearted appreciation to my family and friends for their continuous love, support and belief in me. An overwhelming appreciation to my parents, Mr Ajay Sharma and Ms Shashi Kiran, my siblings, and in-laws their boundless love and support. A special thanks to my best friend, Anisha, for reminding me that I am lucky to have so many loving people to encourage me and not forgetting my niece and nephews who provided me with warmth, much love and some cheerful days. I would like to thank everyone who has contributed both proficiently and individually towards the completion of this research.

University of Pennsylvania Benjamin Franklin Fellowship provided funding support towards my education. President Gutmann Leadership Award and GAPSA Travel Award were provided for travels for the conferences. Ocean Carbon and Biogeochemistry (OCB) support (WHOI), Intergovernmental Oceanographic Commission (IOC, Government of Flanders in the Kingdom of Belgium), and University Corporation for Atmospheric Research (UCAR) travel grants supported the cost of summer school, training and workshop.

ABSTRACT

SPATIO-TEMPORAL DYNAMICS OF PHYTOPLANKTON BIOMASS FROM OCEAN COLOR REMOTE SENSING AND CMIP5 MODEL SUITES

Priya Sharma

Irina Marinov

Phytoplankton are the base of the marine food web, and, importantly, drive the biological carbon pump, the combination of photosynthesis, organic carbon sinking and subsurface decomposition of organic matter which effectively sequesters carbon away from the atmosphere. Our knowledge of phytoplankton activity is currently advancing fast through developments of multiple ocean-color remote sensing algorithms and via developments in ecological modules incorporated in climate models. While climate models are projecting relatively clear trends in ocean ecology over the next century, distinguishing between interannual variability and ocean biology trends from satellite observations is difficult. Short record length, satellite data continuity issues and strong interannual variability all impact quantified trends. Additionally, commonly observed chlorophyll-a is not strictly indicative of underlying phytoplankton biomass because of phytoplankton adaptation. This thesis investigates the trends, interannual variability and seasonality in new size-partitioned phytoplankton biomass products, with a focus on the Sea-Viewing Wide Field-of-View Sensor (SeaWiFS) mission period (1997-2010). In Chapter 2 we found phytoplankton biomass increases in the warm ocean regions over this period, opposing common expectations of decreases in warming oceans. Biomass increases are due to increased physical mixing of the watercolumn and are partially attributed to the large scale El Nino Southern Oscillation (ENSO) phenomenon. Recent studies have highlighted the emergence of different types of ENSO, with a shift towards more Central Pacific ENSO events. Chapter 3 uses statistical techniques (agglomerative hierarchical clustering (AHC), empirical orthogonal functional analysis (EOF)) on phytoplankton biomass to characterize ENSO “flavors” in the tropical Pacific. For the first time, we empirically derive biological indices for different ENSO types, and show high correlations with existing climate indices. In Chapter 4 we examine in depth seasonal in phytoplankton ecology between the North Eastern Pacific subpolar region and contrast it with North Atlantic subpolar ecology. We discuss drivers of biological changes (iron, nutrients, light, mixing). We reveal large differences between biological variables across ocean-color algorithms, as well as across the latest generation Earth System model suite (Carbon Model Intercomparison Project, CMIP5). Chapter 5 summarizes our findings and future work suggestions. Future work should link surface phytoplankton ecology to ocean-atmosphere carbon fluxes and ocean carbon pump efficiency.

TABLE OF CONTENTS

ACKNOWLEDGMENT IV

ABSTRACT V

TABLE OF CONTENTS VI

LIST OF TABLES IX

LIST OF ILLUSTRATIONS X

CHAPTER 1: INTRODUCTION 1

1.1 Role of Phytoplankton and the biological pump 1

1.2 Phytoplankton size structure and physiological characteristics 1

1.3 Effects of climate warming 3

1.4 Phytoplankton variables and their measurements 3

1.5 Broad goals and research questions 7

CHAPTER 2: INCREASING BIOMASS IN THE WARM OCEANS: UNEXPECTED NEW INSIGHTS FROM SEAWIFS 11

2.1 Introduction 12

2.2 Data and Methods 12

2.3 Global Trends in Biomass and Chl-a 13

2.4 ENSO impacts on phytoplankton Biomass and PFTs in the Tropical Pacific 13

2.5 Variability/trends in carbon biomass in the Subtropical Gyres 14

2.6 Decoupling between biomass and Chl-a in subtropical gyres 16

2.7 Trends in gyre sizes 18

2.8 Summary and conclusions 18

2.9 Acknowledgments 19

CHAPTER 3: CONTRASTING ENSO "FLAVORS" WITH SATELLITE DERIVED OCEAN PHYTOPLANKTON BIOMASS IN THE TROPICAL PACIFIC.....23

3.1 Introduction.....24

3.2 Data and Methodology.....25

3.2.2 Preprocessing and Statistical Techniques.....25

3.3 Chl-a and Biomass in the equatorial Pacific region.....26

3.4 ENSO signatures of biomass.....26

3.5 Possible Drivers Responsible for EPEN and CPEN-related Biomass Variations.....28

3.6. Summary.....30

3.7 Acknowledgements.....31

CHAPTER 4: OCEAN PHYTOPLANKTON BIOLOGY IN THE NORTH EAST PACIFIC IN MULTIPLE SATELLITE PRODUCTS AND CMIP5 CLIMATE MODELS.....35

4.1 Introduction.....36

4.2 Methods.....38

4.3 OSP Background: a quick review.....41

4.4 Global phytoplankton regimes.....42

4.5 Contrasting PAPA versus NABE.....43

4.6.0 Biological seasonality across CMIP5 models in the northern subpolar regimes.....46

4.7. Conclusions.....52

4.7 Acknowledgements.....53

CHAPTER 5: CONCLUSION.....63

5.1 Synopsis.....63

5.2 Gaps and limitations.....64

5.3 Future Plans.....66

APPENDIX A: SUPPORTING INFORMATION FOR INCREASING BIOMASS IN THE GLOBAL WARM OCEANS: UNEXPECTED NEW INSIGHTS FROM SEAWIFS.....69

A.1 Introduction.....69

A.2. Data and Methods 69

A.3 Active mixing length scales calculations 71

A.4 Trend Calculations. 71

A.5 Error analysis of phytoplankton biomass and PFTs linear trends 73

APPENDIX B: SUPPORTING INFORMATION FOR CONTRASTING ENSO TYPES WITH SATELLITE DERIVED OCEAN PHYTOPLANKTON BIOMASS IN THE TROPICAL PACIFIC.....91

B.1 Introduction 91

APPENDIX C: SUPPORTING INFORMATION FOR OCEAN PHYTOPLANKTON BIOLOGY IN THE NORTH EAST PACIFIC IN MULTIPLE SATELLITE PRODUCTS AND CMIP5 CLIMATE MODELS 96

C.1 Introduction 96

BIBLIOGRAPHY 107

INDEX 129

LIST OF TABLES

Table 4.1: Synopsis of PFT algorithms and the relevant variables used in the study

Table A1: Generalized Least Square (GLS) Trends of monthly anomalies of the Kostadinov et al. (2016) derived products and OCI Chlorophyll-a for 1997-2010 period with 1-sigma error.

Table A2. Table of linear correlation coefficients of the monthly anomalies of biological variables with the multivariate ENSO index (MEI)

Table A3: GLS trends and 1-sigma errors of monthly anomalies for biological variables in the subtropical gyres

Table A4: GLS trends and 1-sigma errors of monthly anomalies for physical variables in the subtropical gyres

Table B1: Synopsis of variables, original data resolution and source used in this study

Table C1: Summary of the 13 CMIP5 models and their ecological modules used in this study

Table C2: Seasonal indices (e.g. seasonal amplitude and strength) against variables across 13 CMIP5 models

Table C3: Temporal monthly correlation coefficients for the biological variables in the first column against the physical variables first row for the North Pacific Box.

Table C4: Temporal monthly correlation coefficients for the biological variables in the first column against the physical variables first row for the North Atlantic Box

LIST OF ILLUSTRATIONS

Figure 1.1: The three main phytoplankton size groups: microphytoplankton [20-50 μm], nanophytoplankton [2-20 μm] and picophytoplankton [0.5-2 μm]

Figure 1.2: Relationship between average phytoplankton size and light, nutrients and biomass.

Figure 1.3: Adapted from Mouw et al. (2017): Schematic of satellite product inputs utilised in each PFT algorithm.

Figure 2.1: GLS trends for deseasonalised monthly anomalies of backscattering derived PFTs, biomass and physical variables at 68% confidence level

Figure 2.2: Time series of deseasonalised anomalies of tropical Pacific phytoplankton biomass, micro-fraction, Chl-a, gyre size and the MEI index and biomass composite

Figure 2.3: Climatology for active mixing length (L_{MIX}) depth and percentage change/trends for the variables in all the months throughout 1997-2010 in the North Pacific (NPAC) gyre

Figure 3.1: Maps of average and standard deviation for the ocean surface Chlorophyll-a (Chl-a) and surface phytoplankton biomass computed over the September 1997 to December 2007 period.

Figure 3.2: Spatial patterns of the surface phytoplankton biomass anomaly during 5 different ENSO events via clustering and their corresponding composites.

Figure 3.3: Longitude-time distribution of the anomaly of physical and biological variables.

Figure 4.1: Temporal correlation of monthly decimal logarithm of phytoplankton biomass from various algorithm with physical indices (e.g. sea surface temperature)

Figure 4.2: Comparative analysis of two subpolar boxes in the North Pacific (45-50ºN, 140-150ºW, includes OSP, in red) and North Atlantic (45-50ºN, 25-35ºW, in blue, close to NABE) for the biological variables

Figure 4.3: Same as Figure 4.2 except for the physical variables

Figure 4.4: Climatologies of the ecological and physical variables in the subpolar box at North Pacific (45-50ºN, 140-150ºW, includes OSP) across CMIP5 earth system models

Figure 4.5: Climatologies of the ecological and physical variables in the subpolar box at North Atlantic (45-50ºN, 25-35ºW, close to NABE) across CMIP5 earth system models

Figure 4.6: Strength of normalized seasonality of ecological and physical variables across CMIP5 models for North Pacific against North Atlantic.

Figure 4.7: Ecological and physical mechanisms in the subpolar box at North Pacific (45-50ºN, 140-150ºW, includes OSP, denoted by colored circles) and North Atlantic (45-50ºN, 25-35ºW, close to NABE, denoted by colored stars using the CMIP5 suites.

Figure 5.1: Climatology of SST, total surface pCO2 and the two pCO2 components driven by temperature and biology at (top) OSP in the NP box, (bottom) in the NA box.

Figure 5.2: Temporal correlations between monthly pCO2, pCO2 with temperature effect and pCO2 without temperature effect (biology) with Chl-a, B05 biomass and TK16 biomass

Figure A1: Spatial distribution of the 5 main biomes in the study

Figure A2: 1997-2010 global average maps of log decimal phytoplankton biomass and percentage PFTs.

Figure A3: Non-ENSO trends for deseasonalised monthly anomalies of backscattering derived PFTs, biomass and physical variables at 68% confidence level

Figure A4: ENSO trends for deseasonalised monthly anomalies of backscattering derived PFTs, biomass and physical variables at 68% confidence level

Figure A5: GLS trends for deseasonalised monthly anomalies of variables for Northern Hemisphere and Southern Hemisphere winter months over the 1997-2010 period

Figure A6. Temporal correlations between deseasonalized monthly anomalies of the variables over the 1997–2010 period at the 95% confidence level

Figure A7: The climatological classification of the phytoplankton active mixing length scale (L_{MIX}) as Case 1 (L_{MIX}=MLD), Case 2 (L_{MIX}=L_{EK}), or Case 3 (L_{MIX}=L_{OZ}).

Figure A8: Climatology for active mixing length scale (L_{MIX}) depth measurements and percentage change/trends for the variables in all the months throughout 1997-2010 in the NATL

Figure A9: Same as Figure A8 except for South Pacific Gyre (SPAC)

Figure A10: Same as Figure A8 except for South Atlantic Gyre (SATL)

Figure A11: Same as Figure A8 except for Indian Gyre (IOCE)

Figure A12: Percentage change/Trends in all the months through 1997-2010 in the 5 subtropical gyres for the three cases in active mixing length scale.

Figure A13: GLS trend slope values for the total phytoplankton biomass (% y^{-1}), and PFT fractions for the subtropical gyres via Monte Carlo Simulations.

Figure B1: Spatial structures for first three EOF modes of phytoplankton biomass and their corresponding time functions with N_{CT} and N_{WP} climate indices.

Figure B2: Spatial structures for combined-regression EOF modes and their corresponding time functions for the phytoplankton biomass anomalies with N_{CT} and N_{WP} climate indices

Figure B3: Time series of the phytoplankton biomass El Niño Index, the Chl-a El Niño Index, and (b) the biomass ENSO Index and the Chl-a ENSO Index.

Figure C1: Temporal correlation of monthly percent microphytoplankton from various algorithm with physical indices (e.g. sea surface temperature)

Figure C2: Active mixing length scale (L_{MIX}) climatology derived as in Brody et al (2014) for 1 x1 degree grid.

Figure C3: Global map of the percentage occurrence for each case used to construct the (L_{MIX}) active mixing length scale, (a) Case 1: MLD, (b) Case 2: L_{EK} and (c) Case 3: L_{OZ} during the SeaWiFS period (1997-2010).

Figure C4: Climatologies of the ratio of zooplankton and phytoplankton in the subpolar box at North Pacific (45-50ºN, 140-150ºW, includes OSP) across CMIP5 models.

Figure C5: (Adapted from Cabre et al. 2016): Temporal correlation of monthly decimal logarithm of phytoplankton biomass with physical indices for 1997-2010 period in TK16 observed fields and in the CMIP5 multimodel mean.

CHAPTER 1: Introduction

1.1 Role of Phytoplankton and the biological pump

Phytoplankton are microscopic organisms omnipresent in surface ocean. They can be approximately separated into 3 phytoplankton groups: picoplankton [size from 0.5-2μm] such as cyanobacteria and eukaryotes; nanoplankton [2-20 μm] such as coccolithophores and dinofallegates; and microplankton [20-50 μm] such as diatoms (Figure 1.1). Phytoplankton contain chlorophyll-a (Chl-a) pigment that harvests light for photosynthesis. The photosynthetic activity of marine phytoplankton is the base of the marine food web and supports trophic efficiency. Trophic efficiency is the transfer of energy from one trophic level of food web to the next. These primary producers contribute half of the global primary production and are important determinants of global fisheries yield (Friedland et al., 2012). Photosynthesis by phytoplankton is also the primary phase of the ocean biological pump that takes inorganic carbon (CO_2) from the atmosphere and stores it in the deep ocean as organic carbon, effectively sequesters carbon from the atmosphere for centuries to millennia (Eppley & Peterson, 1979).

Phytoplankton convert the inorganic carbon to organic carbon via photosynthesis. Once the carbon is fixed in both hard or soft tissue, phytoplankton either stay in the euphotic zone to be recycled back into nutrients and CO_2 by zooplankton (top-down) and bacteria, or aggregates as organic matter. These organic matters then sink to the subsurface ocean, where the respiration or remineralization of organic matter gets converted back to nutrients and CO_2. The above process continuously depletes nutrients and CO_2 from the ocean surface and transfers them to the subsurface ocean (Thomsen et al., 2017). The carbon and nutrient rich subsurface water are either exchanged vertically with the surface water (particularly in regions of wind-driven upwelling such as subpolar gyres, equatorial oceans or eastern ocean boundaries (Yoo & Park, 2009)) or is slowly laterally transported across the ocean basins via thermohaline circulation (controlled by the temperature and salinity) at very long-time scales (Wunsch, 2002). Ocean circulation and mixing therefore affects the distribution of nutrients in the ocean interior and the supply of nutrients to the surface layers.

1.2 Phytoplankton size structure and physiological characteristics

Phytoplankton cell size is a fundamental master trait that affects most ecological processes for phytoplankton (Maranon, 2015), as well as sinking rates and thus the biological pump and indirectly climate (Litchman & Klausmeier, 2008; Litchman et al., 2015). Size classifications tend to closely correspond to the various phytoplankton functional types (PFTs) with phytoplankton of similar size having similar biogeochemical and ecological roles in the ecosystem (Le Quéré et al., 2005). Phytoplankton require light, nutrients (bottom-up) and suitable temperatures to thrive, and different species and phytoplankton size groups have different physiological needs. Nutrient concentrations and the nutrient stoichiometry in water (e.g. the ratio of 2 different nutrients such as phosphate (PO_4) to nitrate (NO_3)) is a strong indicator of phytoplankton abundance and size structure (Weber and Deutsch, 2010). Studies confirm that nutrient uptake is size dependent (Figure 1.2a) (Chen & Liu, 2010). As the cell size increases, the diffusion boundary cell membrane thickens, reducing the

nutrient diffusion into the cell. The change in thickness implies that the nutrient concentration threshold below which cells cannot sustain a given growth rate increases rapidly with cell size. Small phytoplankton due their thinner cellular wall membrane and larger surface area to volume ratio, effectively uptake nutrients. (Boyd et al., 2013).

Additionally, diatoms have large vacuoles present to store the nutrients, which allow them to increase the effective surface to cytoplasm ratio, maintain higher nutrient uptake rates for longer, and exploit nutrient pulses more effectively than other taxa of the same group (Maranon et al., 2014; Maranon, 2015). As an extra complication, taxa with small or no vacuoles have a growth rate that decreases with increasing size, because of increasing intracellular distances for the transport of nutrients. Because of their smaller size, small phytoplankton are more prone to be grazed than large phytoplankton. Large phytoplankton can outcompete or escape their predators, and therefore are expected to dominate during the high nutrient bloom season. Due to their large cell size, large phytoplankton are typically thought to have a higher sinking rate and be a major contribution of both primary production and of the carbon export to the deep ocean. The relationship between cell size and their contribution to the total phytoplankton biomass is shown in Figure 1.2b. Some estimate that siliceous diatoms contributes 20-25% of primary production (Nelson et al., 1995) whereas coccolithophores (an intermediate size or nano-plankton group) contribute 10% of carbon export to the deep ocean (Jin et al., 2006).

Phytoplankton have ability to adapt to different environment light levels. At low light levels, phytoplankton require more pigments (Chl-a) for photosynthesis. At high light environment, they require fewer pigments (Figure 1.2d). Therefore, phytoplankton adapting to different environmental light levels is known as photoacclimation or photoadaptation, denoted by the ratio of Chl-a relative to carbon (Chl:C) (Geider et al., 1996). In addition, light absorption decreases with larger cell size due to Chl-a pigment, which increases causing self-shading (packaging effect) (Finkel, 2001, Finkel et al., 2004). Previous studies have shown a linear relationship between light and phytoplankton growth and the photoacclimation parameter (Geider et al., 1996). Increase in light elevates the phytoplankton growth rate and lowers the requirement for Chl-a pigment by phytoplankton for photosynthesis, reflected by the decline in Chl:C ratio (Figure 1.2c&d, Geider et al., 1996). Apart from surface light (represented by the photosynthetically active radiation, PAR) in the ocean, the light penetration in the water column and shoaling (or shallowing) of mixed layer depth, trapping plankton in the highly-lit surface layer can also determine the changes in the photosynthetic pigment or photoacclimation parameter. The light penetration in the water column is denoted by the diffuse attenuation coefficient for downwelling irradiance at 490 nm (Kd_{490}). For example, a decrease in Chl-a pigment and photoacclimation parameter (Chl:C) can be driven by increase in surface light (PAR) and/or increase in light penetration in the water column (that is decrease in Kd_{490}) and/or shoaling of mixed layer depth (Westberry et al., 2016, Behrenfeld et al., 2016). Additionally, some small phytoplankton also need specifically high temperatures (e.g. diazotrophs). Considering the environmental factors such as nutrients and light and the size structures of phytoplankton, generally the large phytoplankton such as diatoms will bloom in nutrient rich conditions (e.g. subpolar gyres), whereas small phytoplankton are favored in low nutrient regimes e.g. subtropical gyres (Boyd et al., 2013)

1.3 Effects of climate warming

The warming trend recorded in the global surface ocean since the mid-20th century (Levitus et al., 2000, Levitus et al., 2009) is projected to continue into the 21st century (Solomon et al., 2007; IPCC 2013) and is bound to impact phytoplankton size groups, growth and organic carbon remineralization both directly (for example by the physiological effect of temperature on growth) and indirectly by influencing other key environmental factors, e.g. nutrient and light availability for photosynthesis (Boyd et al., 2014). The changes in phytoplankton size structure, in turn can affect biological carbon pump, the amount of carbon stored in the ocean and ultimately atmospheric carbon dioxide (CO_2). For example, if small phytoplankton will become more widespread at the expense of large phytoplankton (Doney, 2006) – under the assumption of small phytoplankton having a lower export production – then the net export of organic matter to the deep ocean will decrease, a positive feedback on partial pressure of atmospheric CO_2 (pCO_2). Shifts in phytoplankton group size for the global/regional ocean on seasonal to interannual time scales have been detected in in-situ data (Corno et al., 2007; Montes-Hugo et al., 2009; Lomas et al., 2010; Hinder et al., 2012; Agirbas et al., 2015), remote sensing products (Polovina & Woodworth, 2012; Racault et al., 2014; Freeman & Lovenduski, 2015) and global modeling studies (Boyd & Doney, 2002; Bopp et al., 2005; Polovina et al., 2011; Laufkötter et al., 2013; Marinov et al., 2013)

Additionally, shifts in phytoplankton functional group composition due to variations in the environmental factors (e.g. temperature, light) can drive changes in the biogeochemical cycles, since water stoichiometry can change depending on plankton composition. For example, siliceous diatoms have low nitrate: phosphorus (N:P) ratios characteristic of the red superfamily (Arrigo, 2004; Sarthou et al., 2005) and these diatoms bloom in high nutrient waters with similar stoichiometry. Small phytoplankton have low Carbon: Nitrate (C:N) ratios compared to larger phytoplankton, which reflects more storage of nitrogen in their cells and reduced carbon-rich macromolecules, contributing to an increased total biomass of nitrogen-containing molecules. Therefore, changes due to global warming can alter the phytoplankton species composition, and as a result affect the ratio of the N:P and C:N in the ocean. The nutrient ratios covary between different regions of the ocean and is maintained by the ocean circulation. The changes in N:P and C:N ratio due to environmental changes can alter the carbon export to deep ocean (Weber & Deutsch, 2010).

1.4 Phytoplankton variables and their measurements

The concentration of pigment Chl-a in seawater is an indicator of phytoplankton abundance and of the level of biological activity and is often used to assess spatial and temporal distribution patterns of biological productivity in the ocean. Traditionally, satellite-based Chl-a has been used to assess the spatial and temporal distribution of phytoplankton abundance and ocean biological productivity (Behrenfeld et al., 2002). However, as described in section 1.2, changes in light and nutrients can result in changes in cellular Chl-a (Rodríguez et al., 2006) not always associated with phytoplankton biomass changes (Laws & Bannister, 1980; Paasche, 1998; Behrenfeld et al., 2002; Behrenfeld et al., 2005; Behrenfeld et al., 2016). Phytoplankton photoacclimate by adjusting their photosynthetic pigment (Chl-a). Therefore, Chl-a is not the best indicator for phytoplankton community structure and abundance; so, we need independent estimates for biomass.

1.4.1 *In situ* measurements

In situ measurements of Chl-a and biomass are obtained using the fluorometric method to a filtered water sample. Chl-a is extracted in acetone from the samples. Then the principle of fluorescence is applied, where Chl-a fluoresce in the red wavelengths when they are excited by blue wavelengths of light. The measured relative strength of Chl-a and fluorescence is then used to calculate the Chl-a concentration (Berman & Eppley, 1974). Biomass concentrations can be traditionally determined microscopically from the average cell volumes measured for each individual species comprising the population. Another method is using the ATP (adenosine tri-phosphate) concentrations as a measure of biological carbon. ATP is a ubiquitous component of the living cells making up the plankton and one is maintained at a reasonably constant concentration in respect to total cell carbon in healthy organism (Berman & Eppley, 1974). Modern methods of determining biomass concentration is using a flow-cytometric sorting and elemental analysis of carbon (Graff et al., 2012). Flow cytometry is used to isolate phytoplankton from the total particle field. Phytoplankton samples are then analyzed for total carbon content. However, sample collection from field sites are expensive, therefore the global coverage of in situ measurements are poor, hence remote sensing is a useful tool to asses global ocean phytoplankton.

1.4.2 Remote sensing and algorithms

Phytoplankton cells affect the optical properties of the water column via absorption and backscattering (Stramski & Kiefer, 1991; Mobley et al., 2002), which allows for the detection of their characteristics via passive optical ocean color remote sensing, such as the particle size distribution. The particle size distribution (PSD) is a fundamental property linking ocean color remote sensing and ecosystem properties. Bio-optical algorithms have recently been applied to detect phytoplankton biomass (C) separately from Chl-a and retrieve the carbon-based phytoplankton size groups (Behrenfeld et al., 2005; Kostadinov et al., 2009; Roy et al., 2013). There are four types of optical algorithms used to derive phytoplankton biomass and PFTs: radiance-based, abundance-based, absorption-based and backscattering-based algorithms (Figure 1.4).

Radiance-based algorithms are based on theoretical relationships between second-order anomalies of reflectance spectra/radiance and specific phytoplankton groups (Alvain et al., 2005; 2008) .They classify PFTs based on the shape and/or magnitude or the satellite-observed spectral remote sensing reflectance (Rrs(λ)) or normalized spectral water leaving radiance (nLw(λ)). Abundance-based algorithms are based on the general observation that in the global open ocean a change in Chl-a concentration is associated with a change in phytoplankton composition or size structure. Experimentally it has been observed that large phytoplankton have greater Chl-a concentration compared to the small phytoplankton's due to their cell size and absorption efficiency of light. Experimentally derived Chl-a thresholds are imposed to recognize the shift in phytoplankton size by monitoring the ocean Chl-a concentration (Yentsch & Phinney, 1989; Chisholm, 1992; Uitz et al., 2006; Brewin et al., 2010; Hirata et al., 2011).

The absorption-based algorithms use the spectral magnitude or shape of phytoplankton absorption signal. The magnitude of phytoplankton absorption is related to the pigment composition and total pigment concentration. Due to the pigment packaging, the size information is contained within the absorption spectrum. The magnitude of phytoplankton absorption is dominated by the Chl-a

concentration at the peak wavelength of 443nm (Ciotti & Bricaud, 2006; Bracher et al., 2009; Mouw & Yoder, 2010; Roy et al., 2013; Mouw et al., 2017). The backscattering-based products are derived from the spectral total backscattering coefficient using the spectral remote sensing reflectance (Rrs(λ)). The backscattering coefficient/slope decreases according to a power law function with increasing wavelength. The spectral slope of particle backscattering coefficient is determined from the total backscattering. The spectral slope of particle backscattering coefficient is then used to retrieve the PSD and reference abundance of particles from a look-up-table that is constructed using Mie scattering theory. The biovolumes are then converted to carbon concentrations using existing allometric relationships (Menden-Deuer & Lessard, 2000) and assuming that living cells make up 1/3 of all the particles, as described in Kostadinov et al. (2009, 2016). Backscattering-based algorithm retrieves information on all particles rather than just phytoplankton (Kostadinov et al., 2009, 2010, 2016). This dissertation primarily uses biomass and PFT products derived from SeaWiFS reflectance from Kostadinov et al., (2016) due to its sophistication and the first and only product that calculates the biomass for PFTs.

One of the main goals of continued global ocean color observations is detecting long-term changes in ocean ecosystems. Several studies have analyzed trends in remotely sensed variables in recent decades, with a primary focus on Chl-a products, for example, Gregg et al. (2003), Gregg (2005), Behrenfeld et al. (2006), Polovina et al. (2008), Martinez et al. (2009), Siegel et al. (2013). No obvious global trend was reported using a single satellite mission, but some regional trends have been reported (see Chapter 2). Nonetheless, there are several limitations to our abilities to detect a long-term trend in the ocean ecosystem using satellite ocean color data:

i) the short length of satellite records relative to the time scales over which significant changes in the ecosystem happen, even with anthropogenic influences;

ii) existence of temporal and spatial gaps in satellite records (e.g. SeaWiFS available from 1997 to 2010) due to clouds or sensor malfunctions;

iii) existence of calibration issues of different ocean color sensors and their assimilation i.e. challenges in merging of multiple satellite records.

iv) presence of natural climate variability on multi-annual to decadal timescales.

Observed variations in community structure and biogeochemical processes of the tropics, North Pacific, and the North Atlantic have been linked to the ENSO (El Niño Southern Oscillation), PDO (Pacific Decadal oscillation), NPGO (North Pacific Gyre Oscillation) and/or NAO (North Atlantic Oscillation) (Chavez et al., 1999; Bates, 2001; Karl et al., 2001; Di Lorenzo et al., 2008, 2010; Messié & Chavez, 2012; Sydeman et al., 2013). The recent discovery of various flavors of ENSO events complicates our understanding of the response of ocean biology further (Capotondi et al., 2014; Capotondi & Sardeshmukh, 2017). Recent studies have reported the various types ("flavors") of ENSO events and contrasted and constructed indices for the new ENSO types, as we will address in detail in Chapter 3.

Very few studies have looked at the influence of autocorrelation in the data set and the presence of gaps (Saulquin et al., 2013; Beaulieu et al., 2013). Beaulieu et al. (2013) took both into account and used the Weatherhead et al. (1998) methodology to predict the number of years required to distinguish a trend from noise in the Chl-a satellite data. The short duration of most modern observations requires this kind of power analysis of trends or similarly, a trend emergence analysis,

which has been performed for other modeled oceanic variables – e.g. ocean carbon sink (McKinley et al., 2016) and acidification (Carter et al., 2016). These power analyses studies generally conclude that approximately 30-40 years of observation are required to detect climate-driven trends (Henson et al., 2010), emphasizing the importance long-term satellite observations of the Earth system for ocean biology. Because of limited long-term observational time series for ocean biology, climate models are a critical tool for quantifying the contribution of internal variability to future trends, for assessing whether observed trends are outside natural variability, and understanding the long-term changes in ocean biogeochemical and ecological process. The Kostadinov et al. (2016) product is only available for the SeaWiFS period (1997-2010), therefore most of the investigation in this dissertation is limited to 13 years only.

1.4.3 Modelling Efforts

Earth systems climate models (ESMs) are ocean-atmosphere coupled models that closes the carbon cycle. The concept of climate models was proposed through Coupled Model Intercomparison Project (CMIP), that was established as a standard experimental protocol for studying the output of coupled atmosphere-ocean general circulation models (AOGCMs). CMIP5 is the fifth phase of the experimental designed to further advance the knowledge of the climate variability and climate change (Taylor et al., 2011). The experiment has model suite simulations and model ensemble members. In the climate earth system model suite, single model has simulations with different carbon emission scenarios (preindustrial control and representative concentration pathways' - RCPs) and are very different from each other not fully representing the real world. The model simulations in the suite have different physical, biological and ecological components that are embedded together. RCPs are atmospheric greenhouse gas concentration projections (Taylor et al., 2011). The four RCPs, RCP2.6, RCP4.5, RCP6, and RCP8.5, are named after a possible range of radiative forcing values in the year 2100 relative to pre-industrial values (+2.6, +4.5, +6.0, and +8.5 Wm^{-2}, respectively).

Numerous models simulate the existing processes in the marine ecosystem that range from simple ones that have one or two concentrations of the components, to highly complex ones with multiple phytoplankton sizes and nutrients (Heinle and Slawig, 2013). For example, NPZD model that is one of the medium complex models frequently used in climate research due to its realistic representation of marine ecosystem. NPZD models simulate the interactions of the four variables nutrients (N), phytoplankton (P), zooplankton (Z) and detritus (D). The mathematical formulation of the internal fluxes varies in kind and complexity. For example, the growth of phytoplankton can be modelled to be limited by nutrients only, to be limited additionally by light or even by more factors (Heinle & Slawig, 2013). Further terms varying in their formulation and known to be highly relevant for the model outcome are the closing terms of phytoplankton and zooplankton. Often, they are modelled by linear functions. Models have been used to study the emergence of trend in physical ocean/atmosphere drivers of ocean biology in 21st century model simulations (Henson et al., 2010; Diffenbaugh & Scherer, 2011; Hawkins & Sutton, 2012; Mahlstein et al., 2012; Mora et al., 2013; Lyu et al., 2014; Henson et al., 2017). Separately, some recent studies have compared models and observations to depict the decadal variability, historical trends and future response of Chl-al concentration, primary production (PP; Henson et al., 2009), Chl-a, phytoplankton biomass (Cabré et al., 2016; Friedrichs et al., 2007), oxygen (Cabré et al., 2015). To diagnose the long-term climate impacts on the spatio-temporal ocean ecology processes, it is vital to pursue an investigative study

on the spatio-temporal signals of phytoplankton group sizes, biomass, and Chl-a with the past and current available data and tools.

1.5 Broad goals and research questions

The broad goal of the thesis is to study the spatio-temporal dynamics of the novel phytoplankton biomass using ocean color remote sensing and CMIP5 climate model suites. Chapter 2 evaluates the trends and interannual variability in ocean Chl-a, PFTs, total phytoplankton biomass using Kostadinov et al. (2009, 2016) latest SeaWiFS satellite dataset of phytoplankton biomass and PFTs for 1997-2010. The research questions we address here are:

- What are the trends and interannual variability in ocean Chl-a, PFTs, total biomass and photoacclimation parameter (Chl:C) over this time period?
- What are the oceanic physical drivers (mixed layer depth (MLD), sea surface temperature (SST), photosynthetically active radiation (PAR), and Wind speed behind the Chl-a, PFTs, total biomass and Chl:C variability?

Chapter 3 characterizes the types (or “flavors”) of ENSO with satellite derived ocean phytoplankton biomass, and Chl-a in the Tropical Pacific for the 1997-2010 period. Specifically,

- Can the EP and CP “flavors” of ENSO be clearly separated using satellite derived ocean phytoplankton biomass?
- What are the physical drivers behind the biological changes observed for each ENSO type?

Chapter 4 employs a comparative analysis and review of phytoplankton biomass and PFTs from various algorithms and CMIP5 model suites in northern subpolar regions, with a specific focus on two sites of high interest to the oceanographic community at the moment: the North East subpolar Pacific around Ocean Station PAPA (OSP, 45-50°N, 140-150°W) and the North Atlantic subpolar regions close to the NABE site (45-50°N, 25-35°W).

- How does the seasonal cycle in biomass and PFTs differ across the multiple satellite algorithms and CMIP5 models at the two sites of interest?
- What are the drivers of the seasonal changes in biological indices in the observed data and CMIP5 models? Are there consistent mechanistic differences between the functioning of the marine ecosystem at the two subpolar sites of interest?

Finally, Chapter 5 summarizes the thesis results, discusses gaps in the current knowledge of ocean ecology and proposes potential future questions that can be addressed jointly by satellite algorithms and Earth System Models.

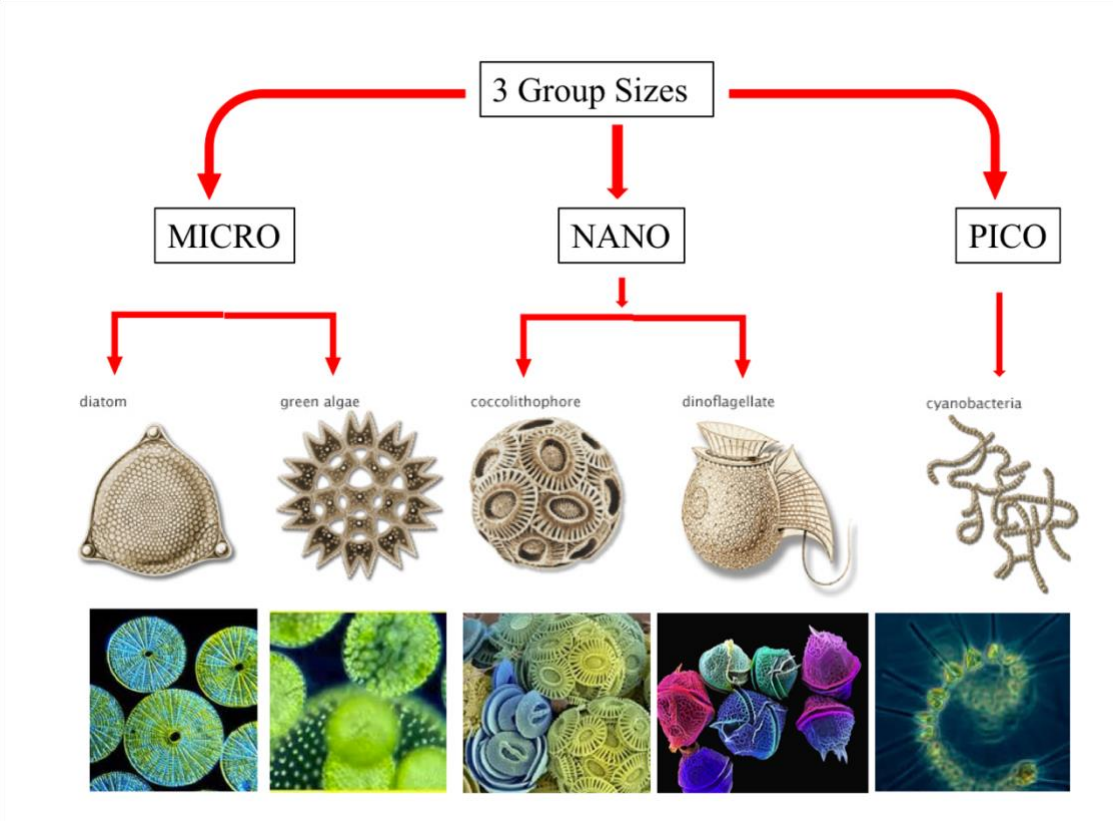

Figure 1.1: The three main phytoplankton size groups: microphytoplankton [20-50 μm], nanophytoplankton [2-20 μm] and picophytoplankton [0.5-2 μm]

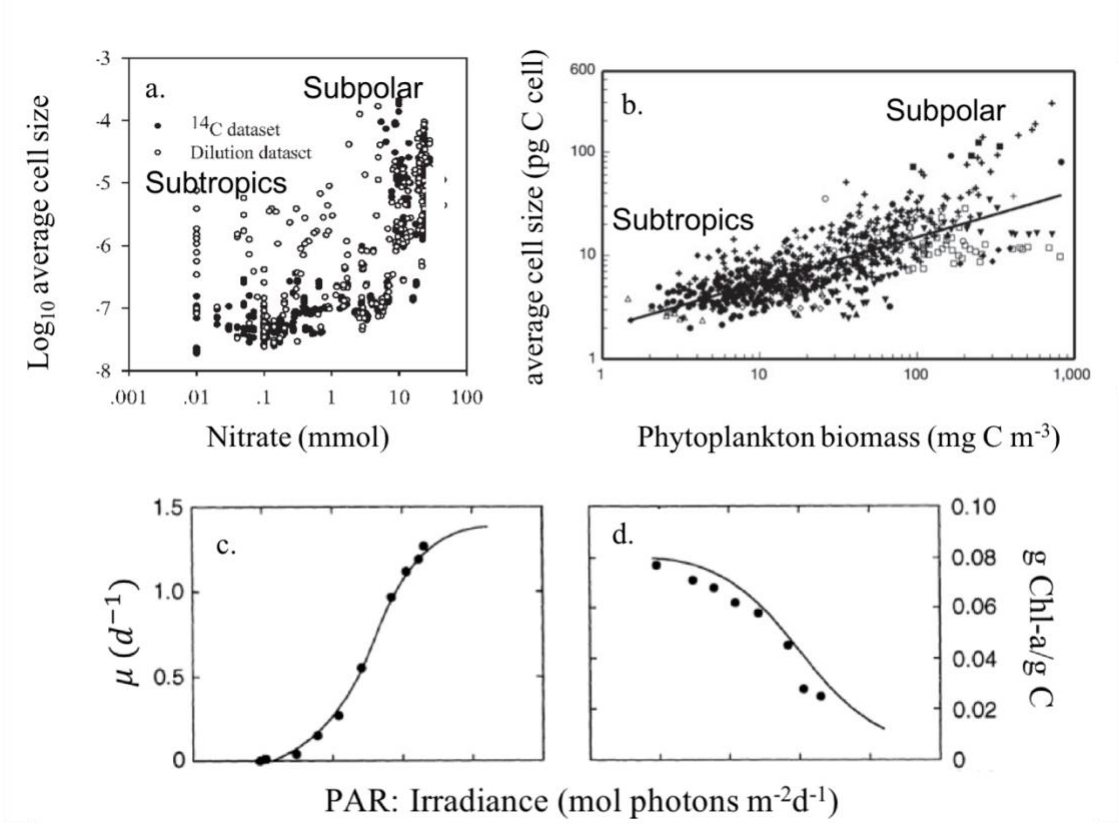

Figure 1.2: Relationship between average phytoplankton size and light, nutrients and biomass. (a) illustrates the logarithmic relationship between logarithmic average cell size and nutrients. The open and closed circles show the two methods of data collection from various locations of global ocean: polar (Arctic and Antarctic) to subtropical and tropical regions, mostly in the open ocean, but also included some coastal sites adapted from Chen and Liu (2010) (b) a linear relationship between average cell size and phytoplankton biomass from various locations shown by the various shapes. Data in b are from the Norwegian Sea (white uptriangles), the North Atlantic (white downtriangles), the Iceland Basin (black uptriangles), Irminger Sea (white circles), Long Island Sound (black squares), North Sea black diamonds), Benguela Upwelling (black downtriangles), Oregon upwelling (crosses), Indian Ocean (white diamonds), mesocosms in the Bergen fjord (white squares), and meridional transects in the Atlantic Ocean (black circles). The image in b is from Irigoien et al. (2004). The relationship between light and growth and photoacclimation is shown by c & d from Geider et al. (1996).

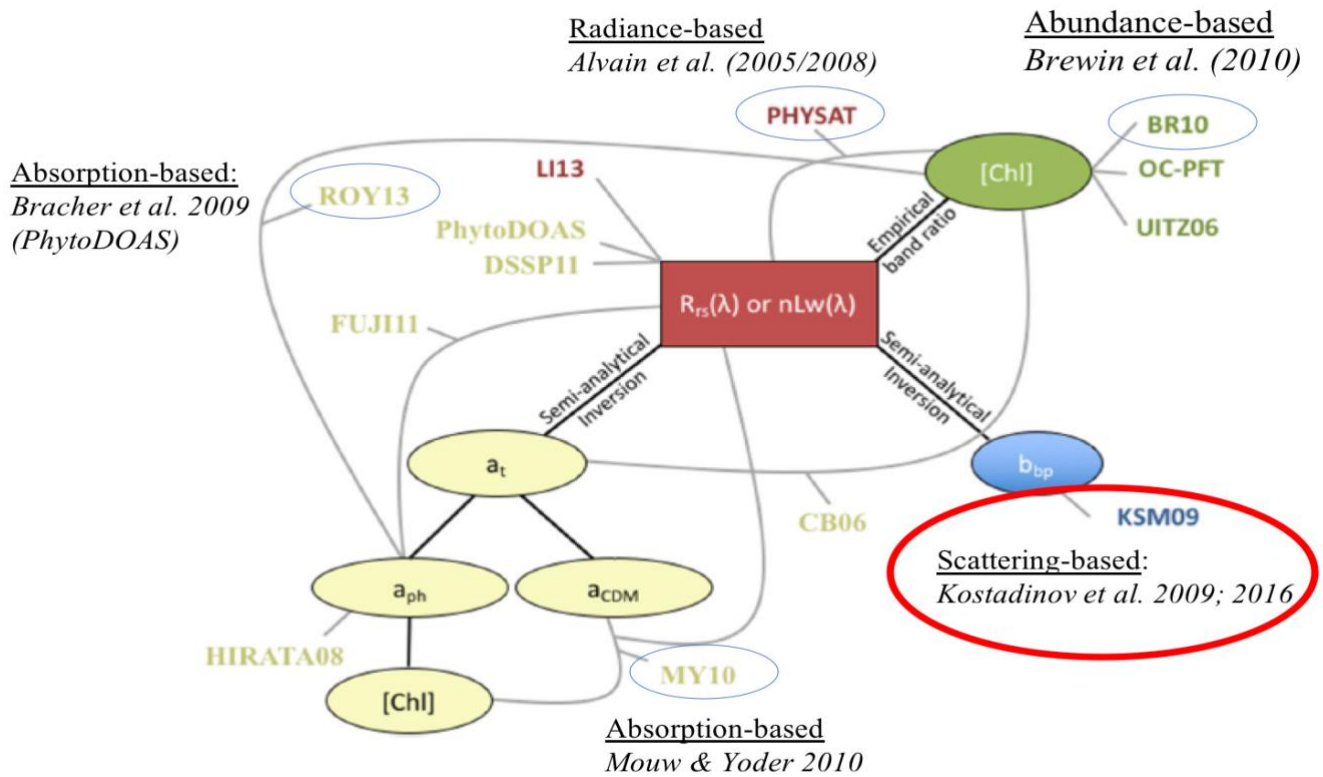

Figure 1.3: (Adapted from Mouw et al. (2017)) Schematic of satellite product inputs utilised in each PFT algorithm. The red box indicates the Rrs(λ) measured by a satellite radiometer. Closed Ovals are derived satellite products and their connection to Rrs(λ) is indicated as black lines. Gray lines indicate the connection of satellite input products used in the various PFT algorithms. The color of the algorithm abbreviation text indicates the algorithm type: abundance (green), radiance (red), absorption (yellow) and scattering (blue). Open oval in red shows the PFT algorithm used throughout the dissertation and the open oval in blue shows the PFT algorithms used in chapter 4.

CHAPTER 2: Increasing biomass in the warm oceans: Unexpected new insights from SeaWiFS

Submitted for publications as:

Sharma, P., Marinov, Cabre, A., Kostadinov T.S. and Singh A., (*GRL: Accepted)* Biomass of phytoplankton is not decreasing in low latitude oceans: new insights from SeaWiFS

Abstract:

Marine phytoplankton biomass and community structure are expected to change under global warming, with potentially significant impacts on ocean carbon, nutrient cycling, and marine food webs. Previous studies have indicated decreases of primary production and Chlorophyll-a concentrations and oligotrophic gyre expansions from satellite ocean-color measurements, purportedly due to global warming. We review this topic via a reanalysis of a novel backscattering-based phytoplankton functional type (PFT) and phytoplankton biomass time-series over the 1997-2010 period. Unlike previous work, we find that globally the biomass and the percent of large (small) phytoplankton increase (decrease). The oligotrophic gyres contract or expand depending on the Chlorophyll-a threshold definition employed. In the subtropical gyres, Chlorophyll-a trends are likely due to physiological changes, while the increasing biomass trends are due to winds and relevant mixing length scale increases.

2.1 Introduction

Oxygenic photosynthesis by phytoplankton contributes to nearly half of the biosphere's net primary production (NPP) (Field et al., 1998). The density contrast between the surface layer and underlying cooler nutrient-rich waters below the permanent pycnocline is expected to increase with a warmer ocean surface (Capotondi et al., 2012). This enhanced stratification will likely reduce nutrient supply to the surface and decrease ocean biological productivity differentially across biomes (Behrenfeld et al., 2006). It also will affect the biological pump, which effectively sequesters carbon away from the atmosphere for centuries to millennia (Eppley & Peterson, 1979). It is then crucial to understand any changes in phytoplankton biomass and size structure, as pico-phytoplankton typically outcompete micro-phytoplankton in nutrient-poor environments (e.g. Weber & Deutsch, 2010).

Traditionally, satellite-based Chlorophyll-a (Chl-a) has been used to assess the spatial distribution and temporal evolution of phytoplankton abundance and productivity (Behrenfeld et al., 2002; Boyce et al., 2010). No significant global temporal trends in Chl-a were found using single ocean color satellite missions that span ~10 years (Gregg et al., 2003; Gregg, 2005; Polovina et al., 2008; Henson et al., 2010; Vantrepotte & Mélin, 2011; Siegel et al., 2013; Beaulieu et al., 2013; Gregg & Rousseaux, 2014). Gregg et al. (2017) recently used a new satellite merged 18-year time series and found no significant trend in global annual median Chl-a from 1998 to 2015. Wernand et al., (2013) reconstructed Chl-a changes from Forel-Ule scale records for the century long 1889-2000 period and found compensating Chl-a trends in different ocean regions.

Little work has been done on looking for trends in satellite-derived phytoplankton biomass (Behrenfeld et al., 2006) and community size structure (Kostadinov et al., 2010). Here we add to the subject by studying trends and interannual variability in the novel backscattering-based PFT-partitioned phytoplankton biomass (Kostadinov et al., 2009, 2010, 2016), and comparing to Chl-a over the 1997-2010 SeaWiFS period. Our objective is to explore the underlying physical mechanisms responsible for observed biological trends across the warm regions (region with average SST>15ºC that includes tropical and subtropical biomes).

2.2 Data and Methods

We study the biological long-term trends and interannual variability in the warm oceans (region with average SST > 15ºC that includes tropical and subtropical biomes, Figure S1). We use a 9km backscattering-based particle size distribution (PSD) phytoplankton biomass in mg m^{-3}, PFT biomass fractions expressed in percent [picophytoplankton (0.5–2 µm diameter), nanophytoplankton (2–20 µm) and microphytoplankton (20–50 µm), hereafter micro%, nano% and pico% as in Kostadinov et al. (2016), and 9km Chl-a (OCI (R2014)) for the SeaWiFS period 1997-2010. We derive a photoacclimation parameter (hereafter Chl/C_{B16}) based on Behrenfeld et al. (2016) (Section A.1). We derive the active mixing length scale (L_{MIX}) for phytoplankton (Brody & Lozier, 2014, 2015), and the mixed layer depth (de Boyer Montégut et al., 2004). Other variables used are sea surface temperature (SST), 10m windspeed (Berrisford et al., 2011), air-sea heat-flux (positive into the ocean), photosynthetically active radiation (PAR), diffuse attenuation coefficient for downwelling irradiance at 490 nm (Kd_{490}) and particulate inorganic carbon (PIC). Section A.1-A.2 provides details on data sources and definitions. High-resolution variables are down-sampled to a 1° grid using a averaging kernel. If >50% of the pixels being averaged are invalid data, the

pixel is assigned a missing data value (as in Kostadinov et al., 2017). All monthly time resolution datasets are used. All anomalies are relative to the 1998-2010 mean seasonal cycle, unless stated otherwise. We use generalized least square (GLS) regression to calculate temporal trends in variables (as in Beaulieu et al., 2013) and present the uncertainty at the 68% confidence level (~0.3 p-value) unless stated otherwise. A Monte-Carlo based error analysis (Figure A13, Section A.4) confirms that trends are meaningful or significant at the 68% confidence interval. Note that significant here means that the 68% confidence interval (unless stated otherwise) of the slope of the GLS regression of the monthly anomalies on time in years does not cross the zero line. Section A.3 further separates the ENSO and non-ENSO trend components, confirming the significance of our results and confidence analysis.

2.3 Global Trends in Biomass and Chl-a

The 1997-2010 trends in total phytoplankton biomass are found to be significantly positive over most of the global ocean (Figure 2.1a, Table A1). Weak but significant negative trends (-0.5 to -1 $\%y^{-1}$) are only found along the equatorial and subtropical east Atlantic and off the west coast of Africa. Similar significant positive trends are observed for the micro% and nano% (Figure 2.1d-e). In contrast, the pico% (Figure 2.1f) shows negative trends globally.

The spatial trends in Chl-a (Figure 2.1b) are comparable to those in Siegel et al. (2013, their Figure 4b). In cold regions (approximately north of 40ºN and south of 40ºS, Figure A1), Chl-a increase patterns are identical to those found in the biomass. In warm regions, however, there are prominent significant negative Chl-a trends along the west coast of North Africa, the Indian and Pacific subtropical gyres, contrary to the positive trends in biomass. Similar declines in low-latitude Chl-a have been observed in previous SeaWiFS-based studies over different periods (Gregg, 2005; Henson et al., 2010; Vantrepotte & Mélin, 2011; Siegel et al., 2013; Gregg & Rousseaux, 2014). In warm regions, competing positive and negative trends in Chl-a cancel out (Figure 2.1b); hence the significant positive global trend is dominated by basin wide increases in Chl-a within the cold regions (Table A.1). In contrast to Chl-a, significant positive trends are found for biomass in the warm region and the cold regions.

How much of the biological trends in Figure 2.1 are ENSO driven? In most of the subtropics and subpolar regions, the positive Non-ENSO trend in biomass dominates over the negative ENSO biomass trend, showing an overall global significant positive trend (See Section A.3, Figures A3-A4). In the tropical Pacific tongue, the strong positive trends in biomass and Chl-a are due to the added effects of the strong positive ENSO trend and a weak positive Non-ENSO trend. The warm and cold SH regions individually explain 44% and 46% of the global biomass increase in Figure 1 (Table A1, Section A.3). We focus here on understanding the warm region trends. The tropical Pacific tongue and the subtropical gyres explain 33% and 21% of the warm biomass trends, respectively.

2.4 ENSO impacts on phytoplankton Biomass and PFTs in the Tropical Pacific

El Niño Southern Oscillation (ENSO) is the strongest global climate natural fluctuation on interannual time-scales, with a warm (El Niño) and a cold (La Niña) phase. Sustained El Niño phase generates long-lasting positive SST anomalies across the equatorial Pacific basin associated with

weaker-than-average trade winds, an eastward expansion of the warm pool leading to increased water stratification in the east, a flattening of the thermocline/nutricline (Chavez et al., 1998; Stone et al., 1999; Strutton & Chavez, 2000; Turk et al., 2001; Christian et al., 2001; Radenac et al., 2001), and decrease in phytoplankton growth along most of the tropical Pacific cold tongue except in the western region where phytoplankton increases (Radenac et al., 2012).

We find that most interannual variability in phytoplankton biomass and Chl-a is associated with ENSO in the tropical Pacific tongue, as indicated by significant negative correlations between the multivariate ENSO index (MEI) and the analyzed variables (Figure 2.2a; Table A2). During La Niña (negative MEI), strong westward trade winds shoal the eastern Pacific nutricline and increase both vertical nutrient supply to the surface and westward lateral nutrient inputs from the eastern equatorial Pacific, increasing biomass, Chl-a, micro% and nano%, and decreasing pico% (Figure 2.2b). The opposite happens during El Niño.

During our study period, a decreasing trend in MEI followed by an increasing trend (with a time split at 2002) was found to be significant at 95% confidence interval and more meaningful than a simple single linear trend (Figure 2.2a). The preferred time split was found by performing two separate linear regressions on MEI from 1999 to the split time and from the split time to the end (2010) for every possible split time (as in Beaulieu et al., 2012)**.** Biomass and Chl-a first decrease during 1999-2002, when the MEI timeseries is increasing (hereafter, 'El Niño' like state) and then increases when the MEI is decreasing (hereafter, 'La Niña' like state) during 2002-2010. The trend over the full SeaWiFS period is dominated by the transition from the large 1997-98 El Niño event to the increasingly negative MEI period of 2002-2010, and corresponds to an increase in tropical Pacific biomass and Chl-a (compare Figure 2b with Figure 2.1a,b,d).

2.5 Variability/trends in carbon biomass in the Subtropical Gyres

Global warming is expected to further stratify the subtropical gyres (Polovina et al., 2011). With decreased nutrient supply to the surface oligotrophic ocean, the phytoplankton biomass will likely decrease (Behrenfeld et al., 2006; Boyce et al., 2010) and shift from large to small-sized species (Boyd & Doney, 2002; Bopp et al., 2005; Corno et al., 2007). We show here results contrary to this hypothesis. The 1997-2010 period is dominated by declines in the pico% and increases in the micro%, nano% and biomass in the subtropical gyres, significant everywhere except for the North Atlantic Gyre (NATL, Table A.3). Most of the error bars do not cross the horizontal and vertical zero line in Figure S13, which indicates that most of the PFTs and biomass are significant at 68% confidence interval. We note that biomass and micro%/nano% is not significantly correlated with MEI in the subtropical gyres (Table A3). What could then drive the observed biomass increases?

Following up on recent efforts (Brody & Lozier, 2014, 2015), we derive a phytoplankton active mixing length scale (L_{MIX}, details in Section A.2) that accounts for mixing due to a large negative heat-flux (out of the ocean) generating deep convective mixing to the base of the seasonal pycnocline (L_{MIX} =MLD, Case 1), mixing proportional to wind energy denotes by Ekman length scale (L_{MIX}=L_{EK}, Case 2), and reduced turbulent mixing when large positive heat-flux (into the ocean) counteracts wind mixing (L_{MIX} =L_{OZ}, Case 3, Figure A.5). The contribution of the various Cases to L_{MIX} (meaning the percentage of pixels with one or the other case) is shown in Figure A12.

We find positive interannual correlations between L_{MIX} and biomass anomalies (Figure A6d) in the subtropical gyres, consistent with a deepening of the active mixing-length scale increasing vertical nutrient supply. Interannually, biomass is more tightly positively coupled to winds and L_{EK} in the subtropics than to MLD (Figures A6b-e). Heatflux into the ocean and biomass are negatively correlated (Figure A6c) across all gyres, indicating that as ocean heat uptake is weakening the biomass is increasing. The temporal correlation between monthly biomass and physical variables is weaker when seasonality is removed (not shown) compared to when the seasonality is included (Figure A6), as expected from other recent work (e.g. Dave & Lozier, 2010; Cabre et al. 2016).

We find that L_{MIX} increases in all the gyres where biomass increases significantly (except in NATL) throughout our study period (Table A1). We further analyze the monthly trends in biomass and physical drivers across all gyres. In the North Pacific gyre (NPAC), L_{MIX} /MLD/L_{EK} all peak in Jan/Feb when heat is lost from the ocean and the water column mixes deeply, bringing more nutrients to the surface and setting up the large April biomass bloom (Figure 2.3a). A secondary biomass bloom is in July/August. In this gyre, both biomass and L_{MIX} increase every month of the year over the 1997-2010 period. The highest increase in Biomass is in late winter/early spring (February-March) and is explained by increased February ocean heat loss, decreased March ocean heat uptake and wind-driven L_{MIX} (Figure 2.3c-g, Figure A5). Note that one sigma error bars do not cross zero line indicating that the trends are significant at 68% confidence interval for the winter months.

NATL gyre Biomass peaks in July/August; a secondary biomass peak in January/February/March corresponds to strong winds and ocean heat loss driving maxima in MLD/L_{EK} /L_{MIX} (Figure A8). Over the period studied, we find the largest increase in biomass in Feb/March, corresponding to intensified heat flux loss and L_{MIX} (February/March), and increased MLD (January/February, Figure A8c-g). The largest drop occurs during April, corresponding to enhanced stratification, a shift to more (less) frequent Case 3 (Case 2) mixing and hence L_{MIX} decrease. Overall, monthly trends cancel each other, resulting in a weak negative but insignificant biomass trend.

The South Pacific gyre (SPAC) biomass (Figure A9a) shows one major peak in winter (June/July/August). Biomass increases significantly over 1997-2010 in all months. We propose that a combination of ocean heatflux loss (significant trends 8 monthsy^{-1}), increased winds (and L_{EK}, June-December), MLD (July-November) and L_{MIX} (August-January) contribute to the biomass growth in this domain (Figure A9c-g). The largest increase in the major seasonal peak of biomass (JJA*)* corresponds to stronger winds, reduced ocean heatflux uptake (in June/August) and an increase in August L_{MIX} (likely driven by a shift from Case 3 to Case 1).

In the South Atlantic gyre (SATL) we see a single biomass peak in wintertime (June/July/August), when heat flux is at its most negative, and L_{MIX}/MLD/L_{EK} all peak together. An increase in annually averaged biomass is driven by increases in 5 months of the year (Figure A10c). Most increase in biomass is in May-June-July and can only be partially explained by a significant decrease in heatflux in May-June, a significant increase in MLD in June-July and a significant increase in L_{MIX} in May and July (Figure A10c-g).

The major peak in Indian (IOCE) gyre biomass is in June/July/Aug, corresponding to the period of maximum heatflux loss and both deepest MLD and strongest winds. The increase in biomass in the IOCE is largest in May/June/July when L_{MIX} is given by a combination of MLD and L_{EK} (Figure

A11c-g). We partially ascribe the early winter increase in biomass to a significant increase in MLD and L_{MIX} in April/May/June, combined with wind increases (May-August).

In addition to the discussed bottom-up effects (increased nutrient supply), it is possible for increases in L_{MIX} to increase phytoplankton biomass via top-down effects. If deeper L_{MIX} dilutes zooplankton more than phytoplankton (Boss & Behrenfeld (2010), this gives phytoplankton a boost as grazing pressure is reduced. Additionally, observed SST increases directly contribute to the increase in phytoplankton growth but also intensify zooplankton growth and grazing pressure. In the absence of global zooplankton data time series, it is challenging to clarify the potential contribution from a top-down mechanism.

In summary, we can partially ascribe the 1997-2010 increase in subtropical gyre biomass and a community shift towards more micro/nano% (less pico%) to an increased nutrient renewal during winter, as MLD and/or L_{MIX} increase by enhanced wind-mixing and wintertime ocean heat loss (deeper convective mixing to the base of the permanent pycnocline). The contribution of Cases 1-3 to the average L_{MIX} seasonal cycle and the changes in these Cases are detailed in Figure A.12. The year-averaged contribution of Case 1 and 2 L_{MIX} into each subtropical gyre L_{MIX}, increase for all the gyres, while Case 3 L_{MIX} decreases for most of the gyres (Table S4), as L_{MIX} increases during winter but remains approximately constant throughout the rest of the year. However, these changes are not significant, which suggests that the different mixing contributions remain approximately constant throughout our 1997-2010. Wintertime trends in L_{MIX} and biomass seem better coupled in some gyres (e.g. NPAC) but more decoupled in others (e.g. SATL).

It is known that increased carbondioxide (CO_2) in surface water decreases the pH (increased ocean acidification) and causes calcareous organisms to dissolve (Doney et al., 2009; Mackey et al, 2015). However, some studies report that an elevated CO_2 favors photosynthesis in coccolithophores (which belong to the nano-phytoplankton group), thus increasing or restoring their calcification after an adaptation period (Iglesias-Rodriguez et al., 2008; Schluter et al., 2014; Krumhardt et al., 2016). Some recent studies have noticed coccolithophore abundance increase in response to surface partial pressure of carbondioxide ($spCO_2$) increase (Krumhardt et al., 2016; Rivero-Calle et al., 2015). Rivero-Calle et al. (2015) claim that North Atlantic coccolithophore abundance increased from 2% to 20% from 1965 to 2010. In our study, we find increases in $spCO_2$ and nano% trends for all gyres (Table A3). Satellite-derived PIC (coccolithophores proxy) trends are positive only in the SATL and NATL gyres (Table A3). We posit that increasing trends in $spCO_2$ contributed to increased coccolithophore presence in the NATL and SATL gyres, consistent with increases in PIC and nano%.

2.6 Decoupling between biomass and Chl-a in subtropical gyres

A major finding is the strong decoupling between Chl-a and biomass trends (Figure 2.1a & e) in the subtropical gyres. Overall, we find increases in biomass in all the gyres over the 1997-2010 period and decreases in Chl-a in three of the gyres (NPAC, NATL, IOCE). Why are biomass and Chl decoupled? First, ocean color can only sample the few upper meters of the water column, above the Deep Chlorophyll Maximum (DCM) conditions (Volpe et al., 2012). Thus, part of the phytoplankton vertical distribution is undetected by satellites that explain the extremely oligotrophic character that gyres display when sampled via remote sensing (Volpe et al., 2007). Second, the photoacclimation process, known to be dominant in the subtropics (e.g., Siegel et al. 2013;

Barbieux et al., 2018), introduces variability in Chl-a uncoupled from the biomass.

Although the large-scale, climatological distribution of Chl-a largely reflects patterns in nutrient supply and thereby differences in phytoplankton abundances (Figure S2a-b), changes in light and nutrients can result in changes in pigment composition (Chl-a) (Rodríguez et al., 2006) not necessarily associated with biomass changes (Laws & Bannister, 1980; Paasche, 1998; Behrenfeld et al., 2002; Behrenfeld et al., 2005; Behrenfeld et al., 2016;). Phytoplankton photoacclimate by adjusting their photosynthetic pigment (Chl-a), such that a decrease in Chl/C_{B16} and Chl-a may be due to: (1) increase in surface light availability (PAR), (2) increase in light penetration in the water-column (decrease in K_d(490)), or (3) shoaling of MLD, trapping plankton in the highly-lit surface layer (Westberry et al., 2016). Throughout the analyzed SeaWiFS period, trends in Chl/C_{B16} are consistent in sign with trends in Chl-a in all the subtropical gyres. These trends are negative in the NPAC, NATL and IOCE (insignificant in IOCE) and positive in the SPAC and SATL (Table A.3). We further analyze the monthly trends to explain Chl-a and Chl/C_{B16} trends.

The Chl-a peaks (lowest) in winter, December-February (September-October) for NPAC, when the MLD is deeper (shallow), PAR is lowest (highest) and light-penetration is weakest, Kd490 maxima (strongest, Kd_{490} minimum). Over the period we find that the significant MLD shoaling, and Kd_{490} decrease in the NPAC gyre drives Chl-a decrease from April to December (Figure A.3h-l). The changes in biomass and Chl-a are coupled in late winter and spring but decoupled during the summer months. In NATL, Chl-a also peaks in winter months and is lowest from April-June. A significant decrease in Kd_{490} in the NATL gyre drive Chl-a to decrease (especially April-June, Figure A6h-l). The biomass and Chl-a changes are decoupled over the period in NATL gyre. In both NPAC and NATL, Chl/C_{B16} decreases as cells acclimate to the increased exposure to light (Table A3) during summer months.

For the gyres in the Southern Hemispheres, the Chl-a is maximum during the winter months (June-to-August), when the MLD is deeper, PAR is lowest and Kd_{490} at maxima. The combination of year-average MLD shoaling, Kd_{490} decrease, and PAR increase that is observed in the IOCE could be driving the small decrease in Chl/C_{B16}. A significant MLD shoaling and Kd_{490} decrease, drive Chl-a and Chl/C_{B16} decrease from January-April and increase in Kd_{490} from May-August control the increase in Chl/C_{B16} (Figure A11h-l). Both biomass and Chl-a are changes are coupled and driven by MLD deepening throughout the period.

In contrast, year-average MLD deepening and Kd_{490} increase cause a small Chl/C_{B16} increase in the SPAC and SATL. The significant MLD deepening and Kd_{490} increase in SPAC are mostly observed during July-Nov, that is consistent with Chl-a increase. The significant MLD deepening, and Kd_{490} increase in SATL for July-August explains the increase in Chl/C_{B16} and Chl-a. We also note that the Biomass and Chl-a are coupled in both the gyres, commonly driven by the deepening of MLD (Figure A10-11h-l).

We also found that Chl-a and Chl/C_{B16} show a strong positive interannual correlation in the subtropical gyres whilst biomass and Chl/C_{B16} are weakly correlated. In agreement with recent work (Siegel et al., 2013; Behrenfeld et al., 2016; Westberry et al., 2016), we conclude that acclimation strongly impacts Chl/C_{B16} ratios and hypothesize that the above acclimation trends, rather than biomass trends, explain the 1997-2010 subtropical gyre Chl-a trends.

We also note that the magnitude of the trends in Chl-a has changed slightly from the standard (STD) algorithm (R2010) processing to the Ocean Color Index (OCI) algorithm processing (R2014); the globally averaged trends in Chl-a became less negative/more positive (and more like our biomass) for the OCI. Signorini et al. (2015) analyzed trends in Chl-a for both the STD and OCI algorithms for all subtropical gyres and also reported similar trends as our Chl-a trends amongst the different sensors and algorithms, with small differences in the magnitude.

2.7 Trends in gyre sizes

Previous studies have claimed an increase in gyre size over recent decades corresponding to an expansion of the low Chl-a core (Martinez et al., 2009). Polovina et al. (2008) concluded that the Pacific and Atlantic subtropical gyres are expanding at average annual rates from 0.8% to 4.3% throughout the 1998-2006 SeaWiFS period, and ascribed this to climate-driven increases in SST and vertical stratification. Irwin and Oliver (2009) reported expansion of the hyper-oligotrophic subtropical gyres during the 1998–2007 period.

We find that the trends in gyre sizes depend on the considered Chl-a threshold over the period 1997-2010 (Table A3). When using low thresholds, e.g., Chl-a<0.07 mg/m^3, as in previous studies (McClain et al., 2004; Polovina et al., 2008; Signorini & McClain, 2012; Signorini et al., 2015), we find insignificant positive trends in three of the gyres, and significant negative trends in the SPAC and SATL gyres. When discussing the gyre size using higher thresholds (e.g., Chl-a<0.11 mgm^{-3}), the effect of ENSO becomes important. A negative MEI is associated with a broader Tropical Pacific tongue and smaller Pacific, Indian and SATL gyres (Table A2). During the SeaWiFS period, we find decreases in the oligotrophic gyre sizes associated with the transition towards a La Niña state (see Section 2.4 and Figure 2.2a) that causes the tropical biomes to expand and the subtropical gyres to shrink (Figure 2.2b, compare solid and dashed lines).

2.8 Summary and conclusions

This paper examines the trends and interannual variability of new estimates of biomass and PFT fractions in comparison to changes in Chl-a over the 1997-2010 period. We find a global increase in biomass, micro% and nano%. This increase differs from previous findings and is somewhat surprising given previously reported decreases in Chl-a (previously used as a proxy of biomass) in the warm regions.

In the subtropical gyres, some previous literature claimed that increased stratification has already resulted in decreased phytoplankton abundance and primary production (Figure 3 of Behrenfeld et al., 2006; Figure 1 of Martinez et al. 2009) and an expansion of the low Chl-a oligotrophic biome (Polovina et al., 2008; Irwin & Oliver, 2009). We find instead that over 1997-2010, biomass increases in all subtropical gyres while Chl-a decreases in the NPAC, NATL and IOCE gyres. We can partially ascribe the biomass increases to negative heat-flux trends and stronger winds during winter deepening the L_{MIX}. Acidification-affected coccolithophore might also change biomass, particularly in the SATL. In contrast, we suggest that subtropical Chl-a decreases are photoacclimation driven. Therefore, Chl-a is not the best indicator for phytoplankton community structure and abundance.

In the tropical Pacific, we ascribe instead the observed increase in biomass over the 1997-2010 period to a trend towards a more La Niña-like state. Figure 2.2 confirms that the 1999-2004 Chl-a and NPP decrease reported for the warm ocean by Behrenfeld et al. (2006) is not a climate change signal as reported but a reflection of ENSO-driven variability in the tropical Pacific tongue. We also find that the oligotrophic gyres contract or expand depending on the Chl-a threshold employed, and the 1997-2010 contraction of Chl-a<0.11 subtropical biomes is due to a slight trend towards more "La-Nina" conditions.

One caveat for this study is the relatively weak local interannual correlations between our various physical metrics and biomass (Figure A6), despite strong correlations on seasonal timescales (Cabre et al. 2016). This discrepancy has been recently discussed in other recent studies (e.g. Lozier et al., 2011; Dave & Lozier, 2013), suggesting that other factors not addressed here may play a role in the observed interannual correlations and trends, e.g., advection of nutrients from the subpolar to the subtropical gyres, or mesoscale eddy dynamics (Palter et al., 2005; Ayers & Lozier, 2010; Dufois et al., 2016; Lehahn et al., 2017) and changes in the grazing pressure (Boss & Behrenfeld, 2010).

We cannot, at present, assign the biomass trends to climate-driven change, because of the short duration of ocean color satellite measurements. A reliable detection of trends would require a 20-30 year timeseries in the tropics and a 40 year timeseries elsewhere (Henson et al., 2010). Further merging of color products between various missions is critical for future clean separation of natural variability and climate-driven signals in ocean biology, with important ecological and biogeochemical impacts, as well as implications for fishery industries.

2.9 Acknowledgments

This work was supported by NASA grant #NNX13AC92G to Marinov and Kostadinov. A. Cabre is grateful for the ''Beatriu de Pinos'' fellowship and the program Marie Curie Actions COFUND of the 7th Framework Program for Research and Technological Development of the European Union. We acknowledge research advice and conversations with Dr. L. Smith (Marine Ecosystem Dynamics Research Group, JAMSTEC, Japan) and Dr. S. Brody (McKinsey & Company). We thank Penn students Danica Fine and David Shields for support in early stages of this work and Robin Zhang for the final stages of the work. Our phytoplankton biomass and PFT data are available at https://doi.pangaea.de/10.1594/PANGAEA.859005.

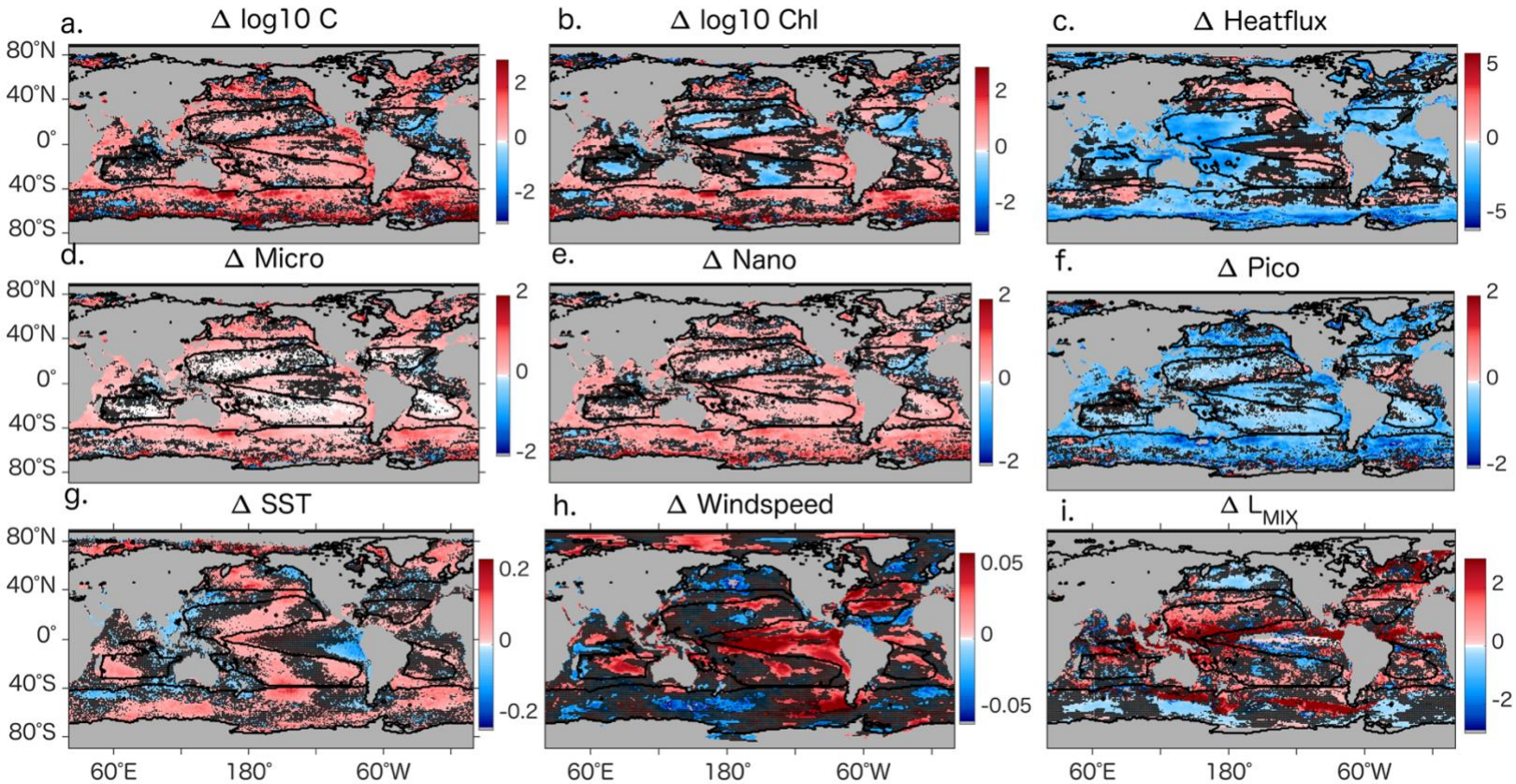

Figure 2.1. GLS trends for deseasonalised monthly anomalies of SeaWiFS-derived (a) phytoplankton biomass concentration, (b) Chl-a concentration, (d) fraction micro-phytoplankton, (e) fraction nano-phytoplankton, and (f) fraction pico-phytoplankton, all in $\%y^{-1}$. Linear trends in (c) heatflux ($Wm^{-2}\ y^{-1}$), (g) SST ($^{o}Cy^{-1}$), (h) windspeed ($ms^{-1}\ y^{-1}$) and (i) L_{MIX} (my^{-1}). All trends are for the 1997-2010 period. Pixels with statistically insignificant trends at the 68% confidence interval ($p<0.3$) are hatched. Biomes are (Figure A1) delimited by black contours.

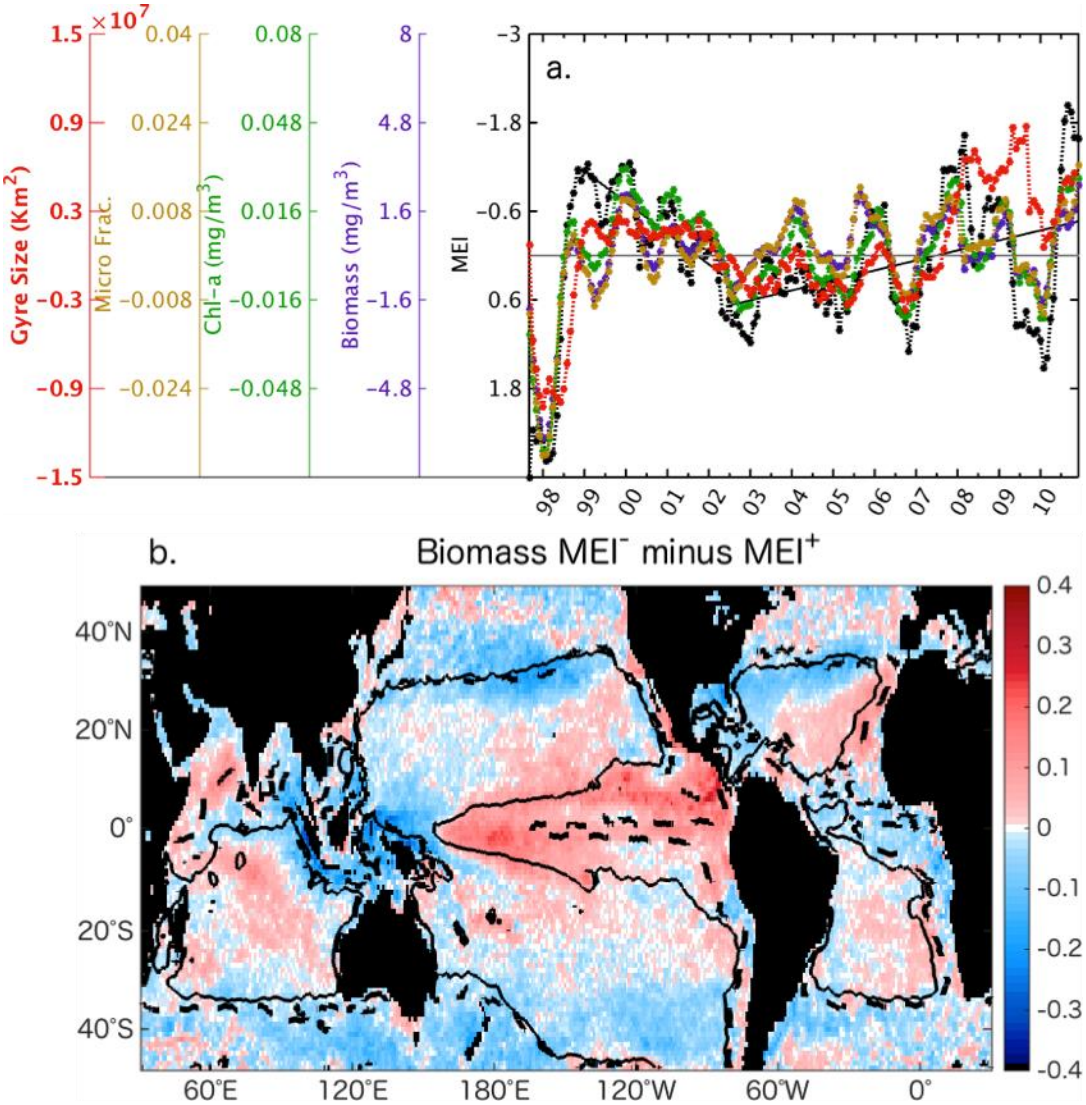

Figure 2.2. (a) Time series of deseasonalised anomalies of tropical Pacific tongue biomass, micro-fraction, Chl-a, gyre size and the MEI index. Note that the y-axis of MEI timeseries is reversed (black). (b) Difference in biomass anomalies during large negative (>-1, red – during cold phase) and positive phases (<+1, blue, during warm Phase) of the MEI. The black solid and dashed lines is the Chl-a contour at 0.11 mgm^{-3} during large positive MEI and negative MEI, respectively

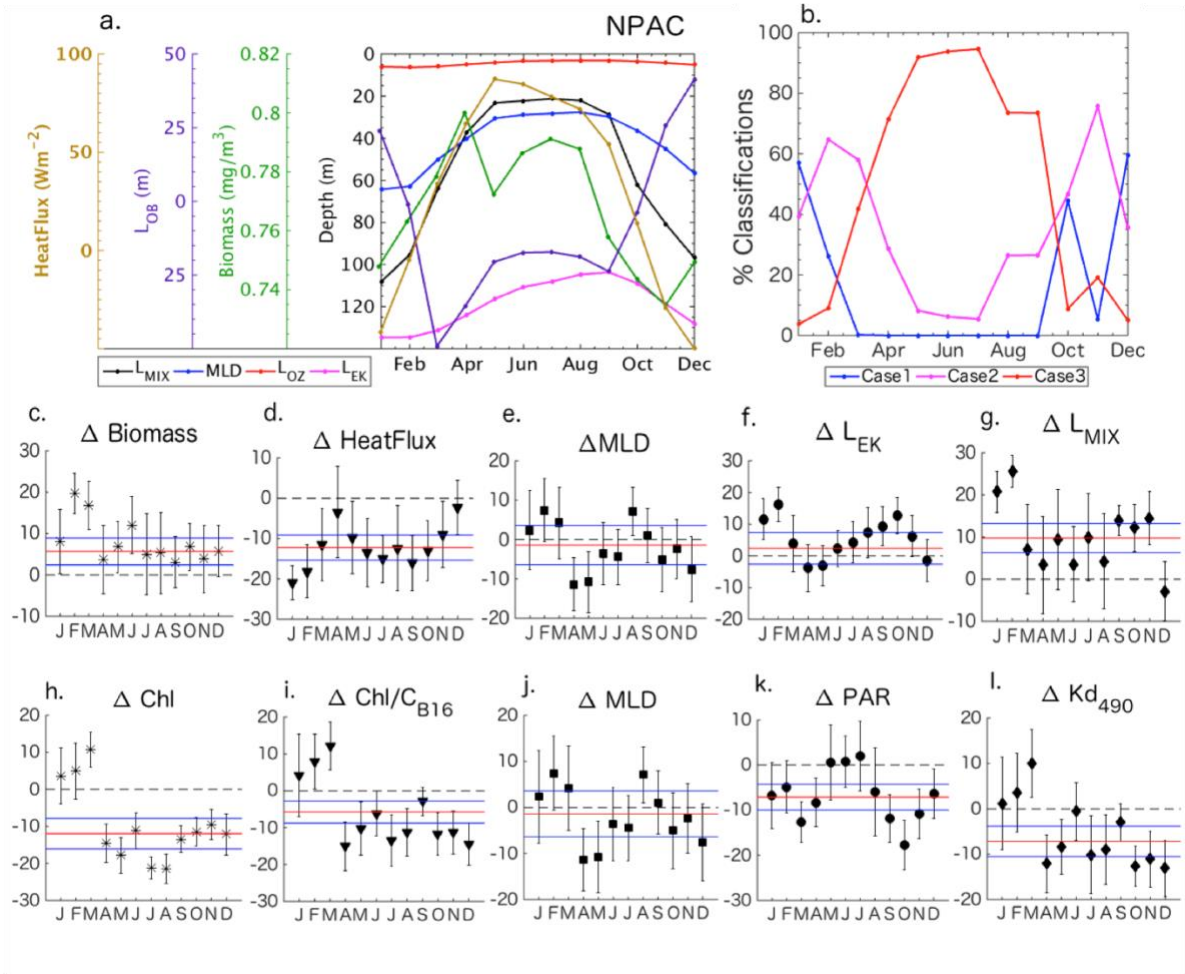

Figure 2.3. (a) 1997-2010 averaged monthly climatology for L_{MIX} depth measurements for the NPAC with mixing depth measurements derived for all the cases 1 (MLD), 2 (L_{EK}), and 3 (L_{OZ}) from surface atmospheric forcing's. Log_{10} phytoplankton biomass and surface heatflux averaged monthly values are in green and gold. (b) 1997-2010 averaged monthly climatology for percentage of pixels in the gyre that are classified as Case 1, 2, or 3 mixing. (c) Percentage change/trends in all the months throughout 1997-2010 in the NPAC for the biome-averaged (c) Biomass, (d) Heatflux, (e) MLD, (f) L_{EK}, and (g) L_{MIX}, (h) Chl-a, (i) Chl/C_{B16}, (j) MLD, (k) PAR, (l) Kd_{490}. The red line is the total percentage change of biomass over the 1997-2010 period and the blue line is the +/- one-sigma error (or 68% confidence interval, $p<0.3$) associated with the total percentage change of biomass.

CHAPTER 3: Contrasting ENSO "flavors" with satellite derived ocean phytoplankton biomass in the Tropical Pacific

Submitted for publication as:

Sharma, P., Singh, A., Marinov, I., and Kostadinov, T.S., (Submitted to GRL-under revision) Contrasting ENSO flavors with satellite derived ocean phytoplankton biomass in the Tropical Pacific

Abstract:

Observed variations in the tropical phytoplankton community structure and biogeochemical processes have been linked to the El Niño Southern Oscillation (ENSO), a driver of large-scale natural climate variability on interannual time-scales. Satellite bio-optical algorithms have allowed us to derive complex biological parameters from the surface ocean via remote sensing, providing a scientific platform to investigate biological relationships with climate indices. Studies have focused in-depth on contrasting flavors of the ENSO with various physical parameters with only a few recent studies focusing on satellite-observed Chlorophyll-a (Chl-a), with however none focusing on phytoplankton biomass itself. Here we review the "flavors" of ENSO and its effect on backscattering-based biomass using different statistical techniques, over the 1997-2007 period. We also contrast the responses of phytoplankton biomass with those of Chl-a and their physical drivers in various "flavors" of ENSO. Signatures of various ENSO "flavors" are observed in the physical and biological fields.

3.1 Introduction

Phytoplankton are microscopic cellular organisms omnipresent in the surface ocean. The photosynthetic activity of phytoplankton is the first level of the marine food chain and supports trophic efficiency. Moreover, phytoplankton affect the optical properties in water column via light absorption and backscattering (Stramski & Kiefer, 1991; Mobley et al., 2002) which allows for their detection via passive ocean-color remote sensing. Remote sensing is a reliable tool (in addition to *in situ* data) for gathering observational data on spatio-temporal scales to characterize the structure and function of global marine ecosystems and to achieve predictive understanding. Phytoplankton adjusts its Chl-a composition to changes in environmental conditions such as light. Consequently, Chl-a may not be the best indicator for phytoplankton community structure and abundance. Therefore, we need independent estimates for phytoplankton biomass. Bio-optical algorithms have previously been applied to detect phytoplankton biomass separately from Chl-a (Behrenfeld et al., 2005; Kostadinov et al. 2009, 2010, 2016). Results from recent studies show that variations in ocean biogeochemical processes in the tropics are linked to the El Niño Southern Oscillation (ENSO) phenomenon (Gierach et al., 2012; Radenac et al., 2012).

ENSO phenomenon oscillates between a warm (El Niño) and a cold (La Niña) phase. Tropical-extratropical interactions, atmospheric pressure teleconnections, and ocean-atmosphere feedbacks stimulate anomalous variations in trade wind strength and sea surface temperature (SST). The evolution of ENSO events is well-documented over the past two decades (Wang & Weisberg, 2000). The scientific literature has been well established on the different “flavors” of El Niño and their characteristics (e.g. El Niño Modoki), that contrast that of the classic Eastern Pacific El Niño (EPEN). El Niño Modoki (Ashok et al., 2007) is one of the recent El Niño “flavors” that have been discovered with multiple nomenclatures, such as the “Warm-Pool El Niño” (Kug et al., 2009) “Central Pacific El Niño”, CPEN (Kao & Yu, 2009) or “Dateline El Niño” (Larkin & Harrison, 2005a,b).

The maximum SST anomalies confined in the central-eastern equatorial and dominantly in the central equatorial tropical Pacific region contrasts the EPEN and CPEN, respectively. Multiple studies have focused on distinguishing EPEN and CPEN using SST (Ashok et al., 2007), sea surface salinity (Ashok et al., 2007; Singh et al., 2011), precipitation (Feng & Li, 2011; Zhang et al., 2011), and subsurface temperature (Yu & Kim, 2010), however a couple of new studies discuss the impacts of EPEN and CPEN based on satellite-derived Chl-a (Turk et al., 2011; Radenac et al., 2012; Messié & Chavez, 2013) and primary production (PP) and phytoplankton growth (Racault et al., 2016; Racault et al., 2017). However, no study has characterized different flavors of El Niño using backscattering-based phytoplankton biomass.

In this manuscript, we use novel backscattering-based phytoplankton biomass data to diagnose further and contrast El Niño “flavors” and their characteristics over the 1997-2007 period. For the first time, we also define a biological index for EPEN and CPEN. Section 3.2 of the manuscript describes the datasets and statistics utilised in the paper. Section 3.3 is a comparison of the Chl-a, and phytoplankton biomass anomalies in the Pacific equatorial region. Section 3.4 contrasts the EPEN and CPEN signatures of biomass using different statistical techniques. In Section 3.5, we document the likely mechanisms responsible for observed ENSO-related biomass variations. The main findings are summarized in Section 3.6.

3.2 Data and Methodology

3.2.1 Data sets

The monthly 9 km horizontally gridded biomass product derived from a backscattering-based algorithm (Kostadinov et al., 2009, 2010, 2016) is used and is available from https://doi.pangaea.de/10.1594/PANGAEA.859005. The backscattering spectral slope and the magnitude are used as the inputs to the algorithm to retrieve the parameters of an assumed power law particle size distribution (PSD). Using the PSD, the volume concentrations for different plankton size classes are calculated. Then, the existing allometric relationships (Menden-Deuer & Lessard, 2000) are applied to convert the biovolumes to the total carbon concentrations. We also used 9km Chl-a (OCI: R2014) maps for the SeaWiFS period 1997-2010. The magnitudes of Chl-a have changed slightly from the standard (STD) algorithm (R2010) processing to the OCI algorithm processing. Chl-a and biomass are expressed in mg m^{-3}.

Physical variables used are 10m daily windspeed (Berrisford et al., 2011), OSCAR ocean currents (Bonjean & Lagerloef, 2002), TOA/TRITON isothermal depth ($Z_{20°C}$: depth of the 20°C) (Michael J. McPhaden et al., 1998), and HadISST1 sea surface temperature (SST). Table S1 provides details on data sources, and resolution. The Multivariate El Niño Index (MEI) was acquired from the National Center of Atmospherics Research (NCAR) climate data portal at https://climatedataguide.ucar.edu/. Time series of EPEN and CPEN indices (N_{CT} and N_{WP}, respectively) were constructed as in Ren and Jin (2011) using the HadISST1 dataset. The piecewise linear combination of the climate indices, Niño-3 and Niño-4 are used to construct the EPEN and CPEN indices with conditioned by the ENSO phase. All the spatial datasets were obtained for the tropical Pacific region [30°S-30°N, 120°E-70°W] over the 1997-2010 period. Table S1 provides a complete list of variables and their sources.

3.2.2 Preprocessing and Statistical Techniques

Seven monthly maps (in 2008 and 2009) had less than 60% of the data available for biomass and Chl-a over the 1997-2010 period, therefore we only analyze data for the 1997-2007 period that had 100% temporal coverage. For Chl-a, the possibility was to adapt the Radenac et al. (2012) method and temporally replace the monthly maps with Aqua-MODIS ocean color maps. However, there are no other satellite data available for biomass using specifically Kostadinov et al. (2009, 2010) algorithms to replace the missing maps in our biomass data. Daily datasets were converted to monthly resolution. The 9km resolution Chl-a and biomass products were re-gridded on a 1° grid using an averaging kernel (Kostadinov et al., 2017). Nearest neighbor linear extrapolation was applied to fill in the data gaps due to sparse clouds.

To obtain the interannual signal, all datasets were first detrended over their respective periods to remove any long-term variability. Anomalies were calculated with respect to 1998-2007 period as some datasets were available only from September-1997 by removing the mean monthly climatology. The anomalies were then filtered using 13-month Hanning-filter to remove any remaining high-frequency signals. Filtering was performed on all the variables except Chl-a, as empirical orthogonal function (EOF) analysis on filtered and unfiltered Chl-a anomalies show similar ENSO patterns and loadings for the first three modes. Using unfiltered Chl-a anomalies allowed for

an additional 5 months of data at the beginning and end of the Chl-a timeseries. The Chl-a EOF patterns are consistent with Radenac et al. (2012) except for the magnitudes, which can be explained by the improved algorithms used to derive Chl-a. Biomass and Chl-a anomalies are log-normally distributed, as biological indices can span up to 3 orders of magnitude (Racault et al., 2016).

3.3 Chl-a and Biomass in the equatorial Pacific region

The 10-year mean phytoplankton biomass (Figure 3.1b) shows relatively low concentrations in the oligotrophic subtropical gyres ([Chl-a] <0.11 mgm^{-3} (natural-log value of -0.96 mgm^{-3}; see Figure 3.1a), and comparatively high levels in the Central and South America ocean margins and the equatorial upwelling systems. The high biomass in these areas is due to the cold nutrient-rich water upwelled at the equatorial and coastal ocean surface waters supporting phytoplankton growth. Despite the nutrient concentration being high in the upwelling systems, the phytoplankton biomass is less than the time-averaged biomass concentration for the equatorial region (<1.2 mg m^{-3}, natural-log value) due to the iron-limited and grazer levels maintaining the growth-loss imbalance (Lundry et al., 2003). We observe robust biomass features near Papua New Guinea (PNG) and Solomon Islands coastal areas. Messié and Radenac (2006) suggest that elevated biomass concentrations are possibly due to the oceanic islands that deflect the deep ocean currents, flow, and wind circulation that allows horizontal advection and intermittent upwelling. The mean biomass pattern is similar to the mean Chl-a structure in Figure 3.1a and in Radenac et al. (2012; see their Figure 1): maxima in the tropical-tongue region and minima in the northern and southern subtropical gyres.

The interannual biomass variability (Figure 3.1d) mimics the Chl-a variability (Figure 3.1c; see Radenac et al., 2012 their Figure 1b) with maximum variability encompassed from the American coasts along curving trajectories towards 170°E at the equator. High variability is seen off the Californian coast and in the South American upwelling systems, and around PNG and Solomon Islands. The interannual variability pattern for Chl-a is relatively higher and pronounced at the southern edge of the tropical tongue then biomass variability (Figure 3.1b). This variability is possibly due to the contraction and expansion of the tropical tongue/subtropical gyres during ENSO events.

3.4 ENSO signatures of biomass

3.4.1 EOF analysis

An EOF analysis of logarithmic phytoplankton biomass anomalies (Figure B.1a) shows that the first EOF mode explains 29.3% of the variance. The spatial structure exhibits negative loadings extending from the coast of California, along the ITCZ region towards the equator to 180°E. This feature is somewhat mirrored at the equator with the negative loadings outspreading from the coast of South American along curving trajectories towards the equator to about 170°E. Positive loadings are found north of PNG and surrounding New Caledonia. Its principal component (PC) is positively correlated with the EPEN index (R = 0.71) suggesting that the negative loadings on EOF1 show a

decrease of biomass during EPEN events. Our result is consistent with Messie and Chavez (2012) who performed an EOF analysis on Chl-a as a proxy for biomass.

The second and third EOF modes (Figure B1c&e) explain 17.8% and 13.0% of the variance, respectively. Although both these EOF modes explain a total of 30.8% of the variance of biomass anomalies, a North test (North et al., 1982) verifies that the second and third EOF modes cannot be distinguished in a statistically significant way indicating that the signals are not well separated and cannot be physically explained. These limitations using the EOF procedure were also encountered by Singh et al. (2011) for sea surface salinity anomalies. Consequently, to effectively extract the dominant modes of variability, a combined regression-EOF (CR-EOF) analysis was performed on the biomass anomalies.

In performing the CR-EOF analysis, the CPEN index was first regressed onto the biomass anomalies. An EOF analysis was then carried out on the residuals of the regression values (residual is the variable minus the reconstructed variable that is derived from regression coefficients) to obtain the EP signature of ENSO (Singh et al., 2011). This method was applied to SST anomalies by Kao and Yu (2009) to separate EP and CP ENSO events. The first EOF explains 28.26% of the total variance in biomass anomalies (Figure B2a&b). The corresponding PC time series is positively correlated with N_{CT} (R = 0.81). The spatial pattern is similar to the EOF1 on the biomass anomalies in Figure S1a giving us confidence in the method applied to characterize El Niño flavors.

Using EPEN index as the regressor, the first EOF has a spatial structure of a large negative biomass pattern encompassed between 155°E-170°W, 5°S-5°N and explains 23.90% of the variance (Figure B2c&d). Positive biomass loadings are observed at the eastern outer edges of the tropical tongue and in the far northwestern Pacific. The corresponding PC is positively correlated with N_{WP} (R = 0.79) indicating a decrease (increase) in biomass in the western-central (eastern) Pacific during CPEN events. The spatial feature is consistent with the second mode of EOF analysis of Chl-a in Messie and Chavez (2013).

3.4.2 AHC Analysis

The dominant patterns for both EPEN and CPEN events were obtained using the CR-EOF analysis. However, to better discriminate between El Niño flavors, due to possible limitations in using the EOF procedure (see Singh et al. 2011), we choose to use the agglomerative hierarchical clustering (AHC) technique to resolve El Niño “flavors” better.

Five clusters were identified using the AHC technique out of 124 monthly maps during 1997-2007 for the biomass anomalies. These five clusters represent Intermediate CPEN, CPEN, La Niña (LN), equatorial recovery, and EPEN conditions explaining 28.8%, 15.32%, 20.72%, 19.8% and 15.32% of the variability, respectively (Figure 3.2a-e). The extracted time series with cluster maps are shown in Figure 3.2f. Our cluster patterns for the biomass are similar to the 5 clusters identified by Radenac et al. (2012) but for Chl-a over the 1997-2010 period. We chose to keep the terminologies of the clusters similar as Radenac et al. (2012) for a consistent comparison.

Spatial patterns of Clusters 1 and 2 exhibit the intermediate CPEN and CPEN signals, respectively (Figure 3.2a&b). In cluster 1, the minimum biomass (less than -0.08 mgm^{-3}) is located between 150-160°E at the equator with curving trajectories of negative biomass anomalies extending towards the eastern Pacific along about 10°N-15°S. As the intermediate CPEN develops into CPEN (see Figure 3.2f), the negative core in the western Pacific grows and occupies a more extensive

region [150°E-170°W, 5°N-5°S]. The two curving trajectories of negative biomass anomalies are replaced with positive anomalies in the eastern Pacific. The timing of biomass cluster 2 from AHC analysis are consistent with the previously documented CPEN events in 2002-03 and 2004-05 (Ashok et al., 2007; Kao & Yu, 2009; Yeh et al., 2009; Kug et al., 2009; McPhaden et al., 2011; Singh et al., 2011; Kim & Yu, 2012; Radenac et al., 2012), however noting that the 2004-05 event is classified as an intermediate CPEN due to the magnitude of the biomass anomalies. The CPEN pattern from AHC is comparable to the spatial pattern obtained from the CR-EOF analysis (see Figure B2b).

Cluster 3 captures the spatial feature of LN, and the timing coincides with events in 1999-2000, and 2000-01 (Figure 3.2c). The maximum biomass concentration is 10°N off the equator near the Central American coast, extending to the central Pacific Ocean between 0-5°N. The southern curving trajectory seen during cluster 1 and remain in cluster 3 albeit with dominantly positive biomass anomalies. Negative biomass anomalies are observed in the far western Pacific above PNG. During LN, the Eastern Pacific equatorial high biomass/Chl-a tongue is at its maximum extent due to the steepening of the basin-wide gradient of thermocline and nutricline across the region resulting in more upwelled nitrate and iron concentrations in the euphotic layer, preconditioning the waters for phytoplankton growth (Christian et al., 2001b). Cluster 4 shows equatorial recovery with a spatial structure similar to that during LN (cluster 3) but with significantly reduced anomalies in the eastern Pacific.

Cluster 5 represents the EPEN event in 1997-1998 and 2006-07 (Figure 3.2e). Cluster 5 spatial feature resembles the spatial feature in Figure B.2a. A few studies characterized the 2006-07 event as a CPEN event (Radenac et al. 2012, their Table 1). Representative examples of DJF (December to the following January) composites of biomass anomalies (Figure 3.2g-k) give confidence that the clusters are not artifacts from the AHC analysis, rather they depict accurate instances biomass distribution. The subtle differences between the clusters and composites remind us of the uniqueness of each event.

3.5 Possible Drivers Responsible for EPEN and CPEN-related Biomass Variations

3.5.1 Biomass in the equatorial region

Figure 3.3 illustrates the time-longitude distributions of the SST, zonal wind, thermocline (represented by the Z_{20^oC}), Chl-a and biomass anomalies averaged between 5°N–5°S. Maximum positive SST anomalies are observed during El Niño events in 1997-98 and 2002-03, 2004-05 and 2006-07 (Figure 3.3a). During EPEN, anomalous westerly winds (Figure 3.3b) drive the strong anomalous eastward currents (not shown) advecting the nutrient poor (Figure 3.3d&e) warm pool waters eastward. As a result, tropical Pacific encounters long and persistent positive SST anomalies that enhances the vertical stratification and deepens the thermocline in the eastern tropics (Figure 3.3c) that weakens the upwelling. Overall, a flattened thermocline results over the basin (Chavez et al., 1998; Stone et al., 1999; Strutton & Chavez, 2000; Turk et al., 2001; Christian et al., 2001a; Radenac et al., 2001).

The nitracline and equatorial undercurrent (EUC) deepening and weakened upwelling of cold nutrient rich waters due to aforementioned process (nitrate-depleted surface layer; see Figure 3 schematics in Messié & Chavez, 2012) causes the decline in the phytoplankton growth in most of the tropical tongue region (Radenac et al., 2012; Messié & Chavez, 2012 and references therein). The primary driver of the anomalous biological changes is due to variations in the nutricline depth (depth where the nutrient concentration declines rapidly), decreasing nitrate content in the eastern Pacific during El Niño events and vice-versa for LN events (Messié & Chavez, 2012). Deepening of the nutricline/thermocline or phytoplankton mixing length scales dilutes the phytoplankton in the surface ocean (Brody & Lozier, 2014) and thus allowing less sunlight to penetrate to the deeper water for photosynthesis. The lack of light in the deep water column limits the photosynthesis and phytoplankton growth, that is reflected in our biomass distribution (Figure 3.3e) during EPEN event. Messié and Chavez (2012) and Park et al. (2011) report similar changes but in Chl-a and also suggest that the light and nutrients drive the changes in the equatorial Pacific.

Studies have shown deeper ferricilne (depth at which iron concentration changes rapidly) than nutricline (Gordon et al., 1997) in the iron-limited equatorial Pacific (Martin et al., 1994). The ferricilne and nutricline is coupled during El Niño when the ferricilne and EUC deepens (Barber et al., 1996; Wilson & Adamec, 2001; Johnson et al., 2002), thus reducing the vertical transfer of nutrient and iron concentration in the region (Chavez et al., 1999; Wang et al., 2005). Low supply of nitrate and iron suppresses the phytoplankton growth. Consequently, we observe Chl-a and biomass decrease during the 1997-98 EPEN (Figure 3.3d&e, respectively), in agreement with previous work showing decreased Chl-a and PP during the same period (Christian et al., 2001a; Messié & Radenac, 2006; Behrenfeld et al., 2006; Radenac et al., 2012). A decrease in PP, ranging between 0.056-0.9 PgC/yr has been reported in previous studies during the 1997-98 EPEN event using different PP algorithms (Carr et al., 2006; Messié & Chavez, 2012; Racault et al., 2017).

Consistent with Kug et al. (2009) and Radenac et al., (2012), we report 1998-99, 1999-2000, and 2000-01 as LN years. Figure 3.3b shows an enhancement of the easterlies during LN events, driving strong westward currents (not shown) and pushing the warm-pool further west. In the central-eastern equatorial Pacific, the surface water is colder than normal (Figure 3.3a). The thermocline/nitracline tilt across the equatorial Pacific becomes steeper [deeper (shallower) in the west (east)]. The intensified upwelling in the eastern Pacific is nutrient abundant, which preconditions the surface waters for phytoplankton growth and elevates the Chl-a and biomass concentrations (Figure 3.3d&e). The prolonged 1998-2001 LN event had exceptionally strong SST anomalies, and was reported as an event that triggered significant phytoplankton blooms along the equatorial Pacific (Martin et al., 1994; Chavez et al., 1999; Murtugudde et al., 1999; Ryan et al., 2002; 2006; Messié & Radenac, 2006).

CPEN impacted the 2002-2005 period. The anomalous westerly winds are constricted to the western-central region extending the warm-pool to the central Pacific region only. The magnitude of the eastward extension of the warm-pool and the anomalous SST during EPEN is stronger than that of CPEN (Figure 3.3a). Radenac et al. (2012) suggested that zonal wind does not affect the eastern equatorial upwelling since its impact is confined within the central Pacific region. Therefore, nutrients are in excess in the eastern equatorial region, and the vertical movement of the thermocline will possibly not impact the biological activity. Instead, Radenac et al. (2012) proposed that the iron supply reduction due to EUC deepening terminates the phytoplankton growth, in agreement with Messie and Chavez (2012). In contrast, Messié and Chavez (2013) using the second mode of the EOF analysis, which has similar spatial features as CPEN show that the Chl-a decrease in western-central region is due to an increase in barrier layer ("the layer between the

mixed layer and the top of the thermocline" (Vialard & Delecluse , 1998)) thickness and occurrence. The location and variations in barrier layer characteristics are governed by multiple mechanisms such as strengthened subtropical convergence due to intensified zonal winds, strong halocline between the warm-pool and cold tongue front and high rates of precipitation (Messié and Chavez (2013).

Furthermore, our characterization and response of biomass and physical parameters to CPEN and EPEN events over the 1997-2010 period are consistent with previous studies in the Equatorial Pacific (Turk et al., 2011; Radenac et al., 2012; Gierach et al., 2012; Racault et al., 2017). Notably, the composites reveal that the southern and northern edges of the negative biomass and Chl-a anomalies closely match the meridional extent of the anomalous eastward current. We observe that Chl-a and biomass are in sync with CP and EP ENSO between 10°N-10°S, except beyond these latitudes. In the subtropics, Chl-a and biomass are decoupled mostly owing to photoacclimation (the ability of the phytoplankton to adjust to light levels, Siegel et al., 2013). In summary, majority of the studies observed that decreases in tropical biological activity are governed by the disturbance in wind circulation that affects the vertical and horizontal transfer efficiency of nutrient content to the surface ocean (Ashok & Yamagata, 2009; Radenac et al., 2012; Gierach et al., 2012; Messié & Chavez, 2012, 2013; Racault et al., 2017).

3.5.2 Defining ENSO Metrics with Biomass

The distinctly different ENSO patterns observed using biomass anomalies allows us to define metrics to capture the different ENSO phases. We identify three most variable regions: the first region (R1) is delimited between 2.5°N-2.5°S, 147°E-170°W; the second region (R2) is between 4.5-12.5°N and 85-112°W and; the third region (R3) is between 13.5-20.5°S and 75-87°W. We empirically define the normalized biomass and Chl-a El Niño index (Figure B3a&b), using an empirical relationship as defined by the following equation:

$$\text{Biomass El Niño index} = [PhytoA]_{R1} - 0.3^{*}[PhytoA]_{R2} - 0.3^{*}[PhytoA]_{R3} \qquad \text{Eq 3.1}$$

PhytoA is the normalized area-weighted average biomass anomalies (or Chl-a anomalies) in the defined region boxes. The biomass and Chl-a El Niño index can distinguish between EPEN and CPEN events and has the high correlation of 0.71 and 0.92, respectively, with the Trans-Niño Index (TNI-defined as "the normalized difference between the normalized SST anomalies averaged in the Niño1+2 and Niño4 regions" (Trenberth & Stepaniak, 2001)).

Becasue the biomass and Chl-a signatures are different during the El Niño and LN episodes, we define a biomass ENSO index using normalized sum between the normalized area-weighted average biomass anomalies in the first two regions (R1+R2). The biomass ENSO index allows separating the warm and cold phase of ENSO (Figure B3a&b). Biomass and Chl-a ENSO indices are highly correlated with Southern Oscillation Index (SOI) of 0.77 and 0.81, respectively. The cluster timeseries fairly correspond with the Biomass El Niño Index and Biomass ENSO Index (Figure B3) that can be used to identify CPEN, EPEN and LN events.

3.6. Summary

The objective of this research was to contrast EPEN and CPEN events in the tropical Pacific using satellite backscattering-derived phytoplankton biomass for the 1997-2007 period for the first time.

Considering that the data from single SeaWiFs mission has several maps missing in year 2008, and the Kostadinov et al. (2010) product is not available for an extended period, we restricted our analysis from year 1997-2007. Using EOF, CR-EOF and AHC on biomass, we showed that EPEN events in biomass are evident in 1997-98 and 2006-07, intermediate CPEN and CPEN events between 2002-2005, and LN events in 1999-2001. We report similar drivers for biomass and Chl-a, as indicated by Radenac et al. (2012) for Chl-a only. During the CPEN events, changes in the vertical supply of iron concentrations due to EUC vertical displacement (Radenac et al., 2012) and the strength of subtropical gyres (Messié & Chavez, 2013) drawdowns the biological activity in the iron-limited region. During EPEN, anomalous westerly winds drive strong anomalous eastward currents. The nutrient-deprived western warm waters extend to 130°W reducing the upwelling and deepening the nitracline and EUC. Reduced surface nutrients reduce the biological activity, lowering the biomass and Chl-a concentrations. Each EPEN and CPEN event will impact the phytoplankton abundance differently, affecting the fish abundance and thus fisheries industries (Racault et al., 2017).

This study focused on using satellite derived ocean-color products to understand the variability of biomass on ENSO timescales. Possible mechanisms to explain biomass distribution have been highlighted. What remains to be investigated is how the frequency of different ENSO flavors and their amplitude affect the long-term biomass trend. It should be noted however that a clean separation is required to distinguish the natural forcing from anthropogenic forcing (Henson et al., 2010). Another interesting question to be addressed is how the different ENSO flavors affect the phytoplankton biomass in the sub-polar regions.

3.7 Acknowledgements

Kostadinov et al. (2009, 2010, 2016) products are available at https://doi.pangaea.de/10.1594/PANGAEA.859005.

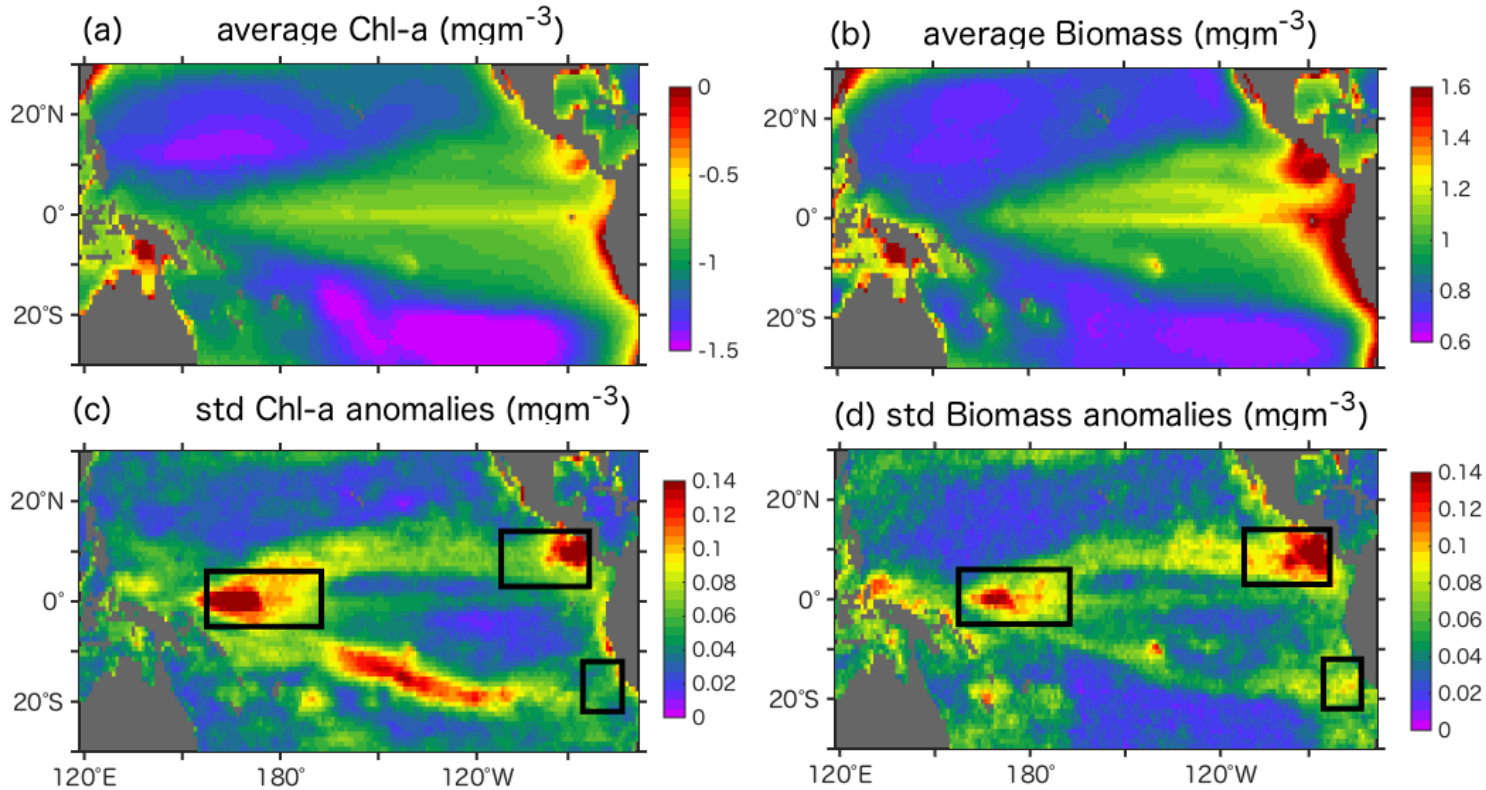

Figure 3.1: Mean and standard deviation maps for the Chlorophyll-a (a&c) and phytoplankton biomass (b&d) for the September-1997 to December-2007 period. The three regions R1, R2 and R3 in black are regions with maximum variability chosen using Figure 3.1d.

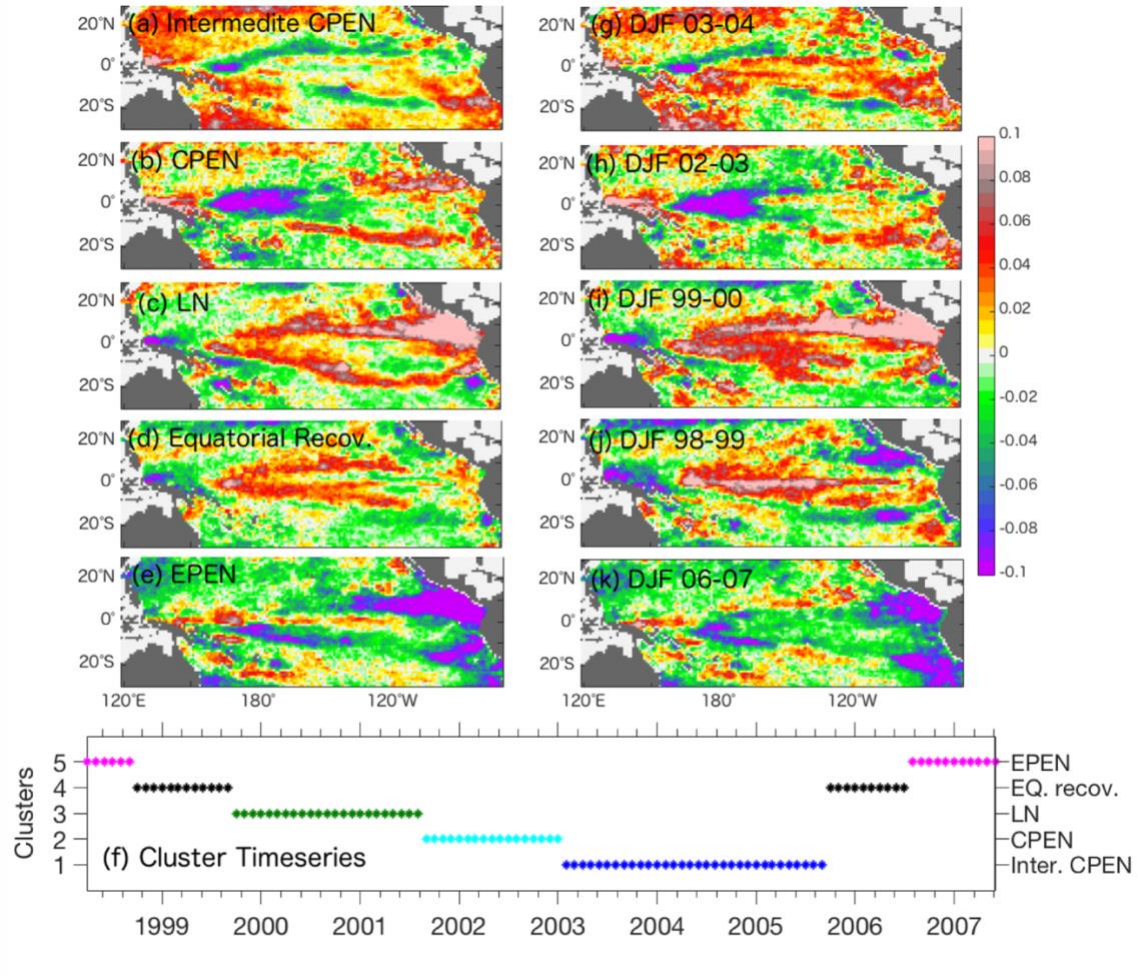

Figure 3.2. Phytoplankton Biomass spatial maps for the (a) EPEN, (b) equatorial recovery conditions, (c) LN, (d) Intermediate CPEN, (e) CPEN events, and the (f) Custer time series from AHC analysis. Three monthly DJF composites of biomass anomalies for the years: (g) 2003-2004 Intermediate CPEN, (h) 2002– 2003 CPEN, (i) 1999-2000 LN, (j) 1998–1999 equatorial recovery and, (k) 2006-2007 EPEN event.

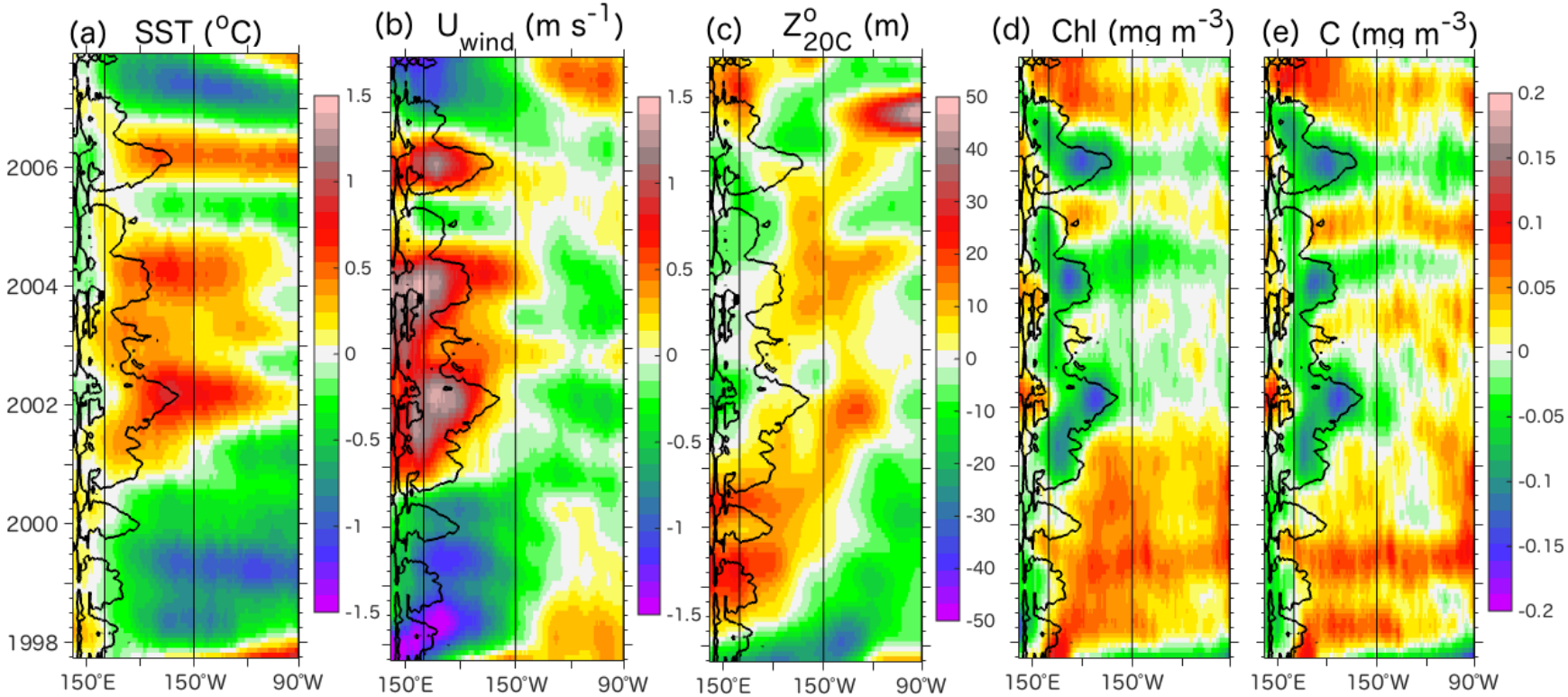

Figure 3.3: Time-longitude map for the (a) SST, (b) Zonal Windspeed (positive eastwards) (c) isothermal depth (positive deepens) (d) Chl-a and, (e) biomass anomalies averaged between 5ºS-5ºN. Note: We chose to show the surface chlorophyll-a thresholds lower than 0.1mg/m^3 as in Radenac et al. (2012) for comparison (in black contour lines). Vertical solid lines indicate the Niño3 (150ºW, 90ºW) and Niño4 (160ºE, 150ºW) boxes.

CHAPTER 4: Ocean phytoplankton biology in the North East Pacific in multiple satellite products and CMIP5 climate models

To be submitted:

Sharma, P., Singh, A., Marinov, I., and Kostadinov, T.S., (JGR) Ocean phytoplankton biology in the North East Pacific in multiple satellite products and CMIP5 climate models

Abstract:

The study investigates the seasonal dynamics of phytoplankton ecology in a North East Pacific subpolar box (NP) that includes the Ocean Station PAPA (OSP), a region of large interest for the oceanographic community because it is one of the largest regions with high-nutrient low chlorophyll-a (HNLC). Here, a seasonal variation between the subpolar North Pacific OSP box with an equivalent subpolar regime chosen for the North Atlantic (NA) is intercompared using ocean surface chlorophyll-a and various satellite-based biomass products and explore bottom-up physical drivers of ocean biology: sea surface temperature (SST), mixed layer depth (MLD), turbulent mixing indices related to wind stirring and buoyancy forcing. Additionally, we analyze output from multiple latest generation (CMIP5) Earth System Models (ESMs) with explicit marine ecological modules and compare it with satellite-based products for biomass and phytoplankton functional types (PFTs) in our areas of interest. The pattern of seasonal cycle is qualitatively consistent in the NA box across the various PFTs and biomass. However, the seasonal cycles across both satellite-based algorithms and across CMIP5 models show vast differences (both qualitative and quantitative) at NP with varying month of bloom suggestive of different biological-physical interactions and PFT succession. For example, the NP seasonality in some satellite algorithms seems to suggest strong phytoplankton light-limitation, while in others it suggests nutrient limitation of growth. Many of the models suggest that the grazer population keeps a tighter check on phytoplankton growth at NP compared to the NA. Most models show deeper mixed layer depths and higher nutrient concentrations at NP compared to satellite datasets. Iron limitation, long known as a determinant of phytoplankton growth at NP, is under-represented in the CMIP5 models at NP.

4.1 Introduction

Phytoplankton (ranging from 1 μm to over 100 μm diameter) are typically classified into different phytoplankton functional types (PFTs) based on their ecological and biogeochemical functions, and different PFTs occupy different spatial and temporal niches of the ocean. One such classification is based on cell size, as rates of metabolic processes (e.g. nutrient uptake, light-limited photosynthesis, maximal photosynthesis) and key traits including minimum subsistence quotas, maximum nutrient storage capacity, susceptibility to grazing (Hansen et al., 1994; Armstrong, 2003), and sinking rate are all known or hypothesized to correlate with cell size. It has been shown for example that smaller cells (e.g., picophytoplankton) compete better under chronic nutrient limitation (Edwards et al., 2012), whereas larger cells (e.g. microphytoplankton or diatoms) have a competitive advantage under plentiful or fluctuating nutrient supply (Litchman et al., 2009). Seasonal, interannual and longer-term environmental (e.g. nutrients, light, temperature) changes affect phytoplankton productivity, loss and biomass. In turn, the health and competitiveness of different PFTs under changing environmental conditions might feedback on the functioning of the biological pump (Litchman et al., 2015; Litchman & Klausmeier, 2008; Maranon, 2015) and ultimately climate. For example, as the ocean stratifies with future climate warming, a reduced surface nutrient supply is expected to increase the relative abundance of small phytoplankton versus larger phytoplankton (diatoms) in oligotrophic gyres (Bopp et al., 2001; Doney, 2006, Marinov et al., 2013; Cabré et al., 2015). Given that larger diatoms are traditionally thought to export more carbon to the deep ocean compared to the small plankton, the shift from diatoms to small phytoplankton could result in less biological carbon sequestration in the deep ocean, and hence a potential positive feedback with increasing atmospheric pCO_2.

Numerous studies have investigated the phytoplankton distributions, their community size structure and their biogeochemical processes in the subpolar regimes, especially in the North Pacific (Harrison, 2002; Ayers & Lozier, 2010; Mackinson et al., 2015) and North Atlantic regions (Dandonneau et al., 2004; Barton et al., 2013; Brody & Lozier, 2014; Barton et al., 2016) using *in situ* measurements, satellite and modelling data. The ecology at OSP has been contrasted in the past with the North Atlantic subpolar region ecology using models (Cabré et al., 2016, Mahadevan et al., 2012; Cole et al., 2015) and satellite algorithms (Zhang et al., 2017). In the subpolar regimes, it is commonly thought that small phytoplankton are top-down controlled by microzooplankton grazing (Landry et al., 1993), whereas large phytoplankton exhibit bottom up control by macronutrients or iron (Fe). Much literature has already been devoted to OSP (Harrison et al., 1999, Harrison, 2002). OSP is an offshore station along the Line P transect in the subarctic northeast Pacific (NEP) Ocean at 50ºN and 145ºW, has one of the longest-running programs for oceanic data collection, with observations commencing in 1956. OSP and the nearby Line P hydrographic stations are sampled by ship three times a year in February, June and August/September by the Department of Fisheries and Ocean Canadian Institute of Ocean Sciences. OSP is a high nutrient-low chlorophyll (HNLC; Martin & Fitzwater, 1988): the upwelling of cold, nutrient-rich water from deep in the ocean provides a consistent supply of macro-nutrients, but the low chlorophyll-a (Chl-a) content suggests that productivity is not as high as would be predicted given the nitrate availability as it is not completely depleted throughout the year. Phytoplankton photosynthesis at OSP is controlled by both Fe and light limitation at different times of the year. Phytoplankton here are the base of the food chain for a variety of heterotrophs (Brodeur et al., 2002), and ultimately for commercially important Pacific salmon (Aydin et al., 2005).

In satellite oceanography, Chl-a has been the historical proxy of algal biomass concentration (Siegel et al., 2013). However, by the well-known process of photoacclimation, phytoplankton regulate their intracellular Chl-a concentration, and Chl/C ratio, in relation to environmental factors such as light and nutrients. Therefore, Chl-a is not a good proxy for phytoplankton biomass (Kruskopf and Flynn, 2005, Alvarez-Fernandez and Riegman, 2014). To circumvent the issue of using Chl-a as a proxy of biomass, newer methods have focused on developing alternative algal biomass concentration based on backscattering coefficients (Behrenfeld et al., 2005; Kostadinov et al., 2009, 2010, 2016; Antoine et al., 2011, Loisel et al., 2011; Graff et al., 2012), absorption-based (e.g., Ciotti & Bricaud, 2006; Bracher et al., 2009; Mouw & Yoder, 2010; Bricaud et al., 2012; Roy et al., 2011, 2013), abundance-based (e.g., Devred et al., 2006; Uitz et al., 2006; Brewin et al., 2010; Hirata et al., 2011), reflectance-based (Alvain et al., 2005, 2008, 2012), described in detail in chapter 1. While significant differences exist among these algorithms, to first order all agree that large cells dominate in high-chlorophyll waters and small cells dominate in oligotrophic waters, also in agreement with in situ findings (e.g. Dandonneau et al. 2004, DuRand et al. 2001, Steinberg et al. 2001).

The North East subpolar Pacific around OSP is currently a region of high interest to the oceanographic community, with the so-called EXPORTS campaign – jointly sponsored by NASA and NSF and involving at least 14 different oceanographic groups at present– currently under way in the area (http://oceanexports.org). To provide a background for current community work, here we perform a comparative analysis and review of phytoplankton biomass and PFTs from various algorithms and CMIP5 model suites in the northern subpolar regions, with a specific focus on two sites: a box chosen around the OSP area (45-50°N, 140-150°W, hereby referred to as “NP” and a North Atlantic subpolar box close to the previously-monitored NABE site (45-50°N, 25-35°W, hereby referred to as the “NA”). Specific questions we address are:

- How does the seasonal cycle in biomass and PFTs differ across the multiple satellite algorithms and CMIP5 models at the two subpolar sites?

- What are the drivers of the seasonal changes in biological indices in the observed data and CMIP5 models? Are there consistent mechanistic differences between the functioning of the marine ecosystem in the Pacific and Atlantic subpolar regions?

- We review the previously observed interannual variability in the NE Pacific and discuss whether current PFT satellite color products can detect such variability.

Below we start with a detailed description of methodology (Section 4.2). We next present a quick overview of the biological literature at OSP (Section 4.3) and investigate the drivers of subpolar phytoplankton biology in a global context (Section 4.4). Section 4.5 is a comparative analysis of a grouping of satellite-based biomass and PFT products at our 2 sites of interest. Section 4.6 presents a CMIP5 model inter-comparison. We conclude the paper with a discussion and summary.

4.2 Methods

4.2.1 Input satellite datasets

A list of biomass/PFT products used in the study and their respective algorithms are described in Table 4.1. We use PFT/biomass variables that were either from the backscattering-based, absorption-based, radiance-based or abundance-based algorithms that were easily accessible online. We chose the algorithms/variables in Table 4.1 because they had at least one or more PFTs variables and also these datasets were easily accessible.

Table 4.1: Synopsis of PFT algorithms and the relevant variables used in the study. We note that the PhytoDOAS product has large temporal data gaps in our region of interest.

Algorithm publication(s)/Location	**Acronym used in text**	**Variables/Units**	**Temporal/Spatial resolution**
ABSORPTION-BASED ALGORITHMS			
Bracher et al. (2009), Bracher et al. (2017) *downloaded from:* https://doi.pangaea.de/10.1594/PANGAEA.870486	PhytoDOAS	Chl-a in Diatoms, (mg/m^3) %$micro_{CHL}$	Aug-2002-Dec 2012 Monthly 0.5 degree
Mouw and Yoder (2010) *downloaded from:* https://doi.pangaea.de/10.1594/PANGAEA.860474	MY10	Size fraction of large phytoplankton Hereafter %micro	Jan 1998 – Dec 2010 9km - monthly
ABUNDANCE-BASED ALGORITHM			
Brewin et al. (2010), Brewin et al. (2011) *downloaded from:* http://catalogue.ceda.ac.uk/uuid/7201151d40683a4420da90c30640d4fa	BR10	percent of Micro – chl-a, nano – chl-a and pico – chl-a Hereafter %$micro_{CHL}$, %$nano_{CHL}$, %$pico_{CHL}$	10yr (1997-2007) climatology 9km
RADIANCE-BASED ALGORITHM			
Alvain et al. (2005), Alvain et al. (2008) *downloaded from:*	PHYSAT	Frequency of detection of diatoms (% of days)	1997-2010 Sept 97 – Dec 10 9km (Only in certain regions of the world: North Atlantic;

http://www.seanoe.org/data/00326/43749/		Hereafter %micro$_{freq}$	Equatorial & Tropical South Pacific; Southern Ocean)
BACKSCATTERING-BASED ALGORITHMS			
Behrenfeld et al. (2005)	B05	Total Biomass (mg/m^3)	9km
Kostadinov et al. (2009), Kostadinov et al. (2010), Kostadinov et al. (2016) Downloaded from https://doi.pangaea.de/10.1594/PANGAEA.870486	TK16	Total Biomass (mg/m^3), Micro Frac, Nano Frac, Pico Frac Hereafter %micro, %nano, %pico	9km
Stramski et al. (2008)	S08	Total Biomass (mg/m^3)	9km

Additionally, the global monthly 9 km composites of SeaWiFS Chl-a concentration (derived from the Ocean Color Index (OCI) algorithm), photosynthetically available radiation (PAR), and diffuse attenuation coefficient for downwelling irradiance at 490 nm (Kd_{490}) from SeaWiFS (2014 reprocessing), were obtained from NASA's Ocean Color Web (http://oceancolor.gsfc.nasa.gov) for the years 1997-2010. Chl-a, PAR and Kd_{490} are expressed in mgm^{-3}, Einstein m^{-2} day^{-1} and m^{-1}, respectively. All monthly gridded data from the above table was down-sampled to a 1° resolution using two-dimensional convolution with an averaging kernel (as in Kostadinov et al., 2017). If >50% of the pixels being averaged were invalid data, the pixel in the down-sampled image was assigned a missing data value. We calculate a photoacclimation parameter, which approximates Chl/C, following Eq. S10 in Behrenfeld et al. (2016) using the above, PAR and Kd_{490} parameters and MLD described under section 2.2:

$$\mathrm{Chl}/\mathrm{C}_{B\prime 16} = Chl{:}C = \frac{1+e^{-0.15\,PAR}}{1+e^{-3I_{ML}}}, \text{ where } I_{ML} = PAR \times e^{-0.5Kd_{490}\times MLD} \qquad \text{[Eq. 4.1]}$$

Note that the photoacclimation parameter $\mathrm{Chl}/C_{B\prime 16}$ model above is independent of any observed Chl-a input and biomass. A complete derivation with equations is in Appendix A.3 and Behrenfeld et al. (2016).

4.2.2 Other input variables

5-day gridded density profiles on a global 0.5° grid were used from the Simple Ocean Data Assimilation (SODA) model (soda.tamu.edu, (Carton et al., 2000, Carton & Giese, 2008) to calculate active mixing length scale (L_{MIX}, see details in Brody et al (2014)). Prior to any calculations, the 5-day data were converted to monthly averages. A merged MLD product was obtained from http://www.science.oregonstate.edu/ocean.productivity/mld.html. The merged MLD product is a

temporal combination of numerical derivation of MLD from Simple Ocean Data Assimilation (SODA) model (soda.tamu.edu; Carton et al., 2000; Carton & Giese, 2008) from 1998-2004, the Fleet Numerical Metrology and Oceanography Center model (Clancy & Sadler, 1992) from 2004-2005 and Hybrid Coordinate Ocean Model (Bleck, 2002) from 2005-2010, hereafter "W'16 MLD" or "MLD". The obtained MLD was defined as the depth at which the potential density exceeded a surface reference value (generally 10 m) by 0.125 kgm^{-3} (Westberry et al., 2016).

The global monthly 4km Advanced Very High Resolution Radiometer (AVHRR) satellite-derived sea surface temperature (SST) imagery was obtained from the NASA Physical Oceanography Distributed Active Archive Center (PO.DAAC, http://podaac.jpl.nasa.gov/AVHRR-Pathfinder) for 1997-2009. We further used 13-year (1997-2009) monthly 1° gridded time series of surface ocean heat flux (Wm^{-2}) obtained from Objectively Analyzed air-sea Fluxes (OAFlux) project via http://oaflux.whoi.edu/data.html. The time series for SST and surface ocean heat flux was only available until 2009. We chose to use AVHRR and OAFLUX, because it was one of the most cited products. Daily 10 m wind data on a 1° horizontal grid from the ERA–Interim Reanalysis (http://www.ecmwf.int/, (Berrisford et al., 2011) was converted to monthly data. Global monthly surface partial pressure of carbon dioxide ($spCO_2$) on a 1° grid was obtained from the Carbon Dioxide Information Analysis Center (CDIAC, http://cdiac.ornl.gov/) (Takahashi et al., 2009). Derivation of the active mixing length scale follows developments by Brody and Lozier (2014, 2015). Calculations on active mixing length scale L_{MIX} is explained in detail in Appendix A.4, which is a depth at which the phytoplankton are primarily mixed.

4.2.3 CMIP5 Models

We used parameters from a group of Earth System simulations from the recent Coupled Model Intercomparison Project CMIP5 (Taylor et al. 2012) that incorporate ocean ecosystem representation with at least two phytoplankton groups. CMIP5 model output was downloaded from *http://pcmdi9.llnl.gov/esgf-web-fe/*. We chose 13 models based on the availability of the variable phytoplankton (phyto or biomass), diatoms, integrated primary production (Int(PP)), MLD, PAR, Chl-a, nitrate (NO_3), iron (Fe), zooplankton and C/Chl-a. The models used are CESM1-BGC, GFDL-ESM2G, GFDL-ESM2M, GISS-E2-H-CC, GISS-E2-R-CC, HadGEM2-ES, MPI-ESM-MR, MPI-ESM-LR, NorESM1-ME, CanESM2, IPSL-CM5A-MR, IPSL-CM5A-LR, MRI-ESM1. We note that only a subset of these models has multiple phytoplankton groups, these are: CESM1-BGC, GFDL-ESM2G, GFDL-ESM2M, GISS-E2-H-CC, GISS-E2- R-CC, HadGEM2-ES, and IPSL-CM5A-MR. HadGEM2-ES, MRI-ESM1 and MPI-ESM-MR are the models with fixed C/Chl ratios. Model output is used for the SeaWiFS time span (1998 to 2010). Years 1998 to 2005 are based on the historical CMIP5 scenario forced by observed atmospheric changes (both anthropogenic and natural). Years 2006 to 2010 are based on the RCP8.5 emission scenario (Riahi et al. 2011). Table C1 provides details and references for the models. All model output was resampled to a 1° grid. We note as a caveat that a direct comparison between the observed (Figure 4.3c) and modeled light (IPAR in Figure 4.4,4.5) is unrealistic as 'IPAR' from models is the net downward shortwave flux at sea the surface whereas the SeaWiFS product is the photosynthetically active radiation (PAR) at the ocean surface, that is energy flux from the Sun in the 400-700nm range.

4.3 OSP Background: a quick review.

Fe stress at OSP has been confirmed by numerous biophysical and biochemical markers (Roche et al., 1996, Wong et al., 1999). In-situ Fe addition experiments showed that pennate diatoms grow up and drawdown nitrate and silicate (Martin & Fitzwater, 1988; Boyd et al., 1998). The importance of Fe in the NEP Subarctic was partly established by three mesoscale Fe fertilization experiments: the Subarctic Iron Enrichment for Ecosystem Dynamics Study (SEEDS) in 2001, Subarctic Ecosystem Response to Iron Enrichment Study (SERIES) in 2002, and SEEDS II in 2006. Takeda and Tsuda (2005) (SEEDS) saw an increase of 2-5 times in nanoplankton but a 45-fold increase in diatoms. Marchetti et al. (2006) saw an increase in all size classes followed by a diatom bloom over 8 days, whereas Uematsu et al. (2009) observed no diatom bloom with picophytoplankton dominating the biomass and productivity increase. Because the phytoplankton communities were very similar before fertilization for all three experiments – dominated by small phytoplankton (prymnesiophytes and cholorophytes), the diversity of responses to Fe fertilization suggests an important role for grazing dynamics (for further discussion, see Kearney et al. (2013)). Iron-light co-limitation during winter at OSP was suggested by Boyd et al. (1996) and demonstrated by Maldonado et al. (1999).

Additionally, Wong et al. (2002) note that diatoms around OSP have unusually high silicate (Si) requirements, which can also act as limiting nutrient in the rare cases of excess iron (Fe). Smaller phytoplankton types thrive relative to the larger species under conditions of nutrient limitation, and therefore make up the bulk of phytoplankton biomass at OSP and other offshore stations along Line P (Mackinson et al., 2015). There is low seasonal variability of primary production at OSP (Harrison, 2002). Plant et al. (2016) investigated the mechanisms that initiate bloom conditions at OSP with net community production (NCP) measurements from 2008-2013. OSP waters have a permanent and sharp salinity gradient, which produces a density gradient that limits the mixing of the water column to depths of 120m. The mixed layer varies between 40m in the summer to 90-120m in winter (Timothy et al., 2013). The deepest mixing occurs in February to March and entrains nitrate, salt and Fe back into the surface layer. As surface waters warm and freshen (starting around April), and wind speeds decrease, the MLD shoals to a minimum that can reach even 20m by August. The phytoplankton seasonal cycle exhibits two peaks: at the end of May (Spring bloom) and at the beginning of August (Plant et al., 2016) with a local minimum between these two peaks corresponding to the annual peak in zooplankton and therefore grazing. The shallow mixing depths increase the concentration of zooplankton, which supports grazing on phytoplankton species (Plant et al., 2016).

Episodic Chl-a events have been previously noted at OSP (Parslow, 1981), due to natural climatic variabilities such as ENSO, PDO and NPGO affecting the nutrient (Di Lorenzo et al., 2008; Messié & Chavez, 2013) and iron inputs or episodic iron input following a volcanic fertilization events (Kearney et al., 2015). The boundary between the coastal, nitrate limited area and the Fe limited offshore area can shift more offshore due to El Niño and onshore due to La Niña events. Lower winter nitrate supply during El Niño is estimated to have reduced new production by 40% and possible shifted large phytoplankton to a smaller phytoplankton size (and a longer food chain) with possible effects on higher trophic levels (Whitney et al., 1998).

4.4 Global phytoplankton regimes

To understand the global drivers of variability in phytoplankton, we show monthly temporal correlations of logarithmic decimal phytoplankton biomass and physical indices in Figure 4.1 for the three carbon-based algorithms (TK16, B05 and S08) and in Figure C1 for percent Micro phytoplankton (TK16 %micro, MY10 %micro, PhytoDOAS %micro$_{CHL}$ and PHYSAT %micro$_{freq}$).

SST and TK16 Biomass are inversely correlated in the tropics and mid latitudes, as has been shown before when using Chl-a instead of biomass (Irwin & Oliver, 2009; Martinez et al., 2009). The relationship is positive when correlating biomass (or Chl-a) with MLD (not shown) or with wind (Figure 4.1). Kahru et al. (2010) saw a strong correlation wind-Chl, but Chiswell et al. (2013) found a much weaker correlation, which suggest that the driver of Chl-a is complex. In general, SST, wind, and MLD indicate the level of mixing, such that more mixing (colder, increased wind speed, or deeper MLD) exposes phytoplankton to deep cold nutrient waters favorable for growth at low and mid latitudes. In agreement, wind and SST hold an inverse relationship (e.g. Seager & Murtugudde, 1997; Kahru et al., 2010). North of 40ºN and south of 40ºS (light-limited regime), the correlation is opposite to the one found at low latitudes, which indicates that the phytoplankton growth can be triggered if MLD or wind decrease. These relationships were also reported when using Chl-a (Wilson & Adamec, 2001; Henson et al., 2009; Cabré et al., 2016), TK16 Biomass (Cabré et al., 2016) and phytoplankton timeseries (Barton et al., 2015) with SST and MLD. These opposite correlations seen in light-limited regions can be explained if strong mixing tend to increase the depth of vertical mixing sufficiently to remove phytoplankton from the euphotic zone and therefore reduce their average light levels required for photosynthesis.

The active mixing length scale (L_{MIX}) was introduced by Brody et al. (2014) as a proxy for the nutrient supply to the surface water via mixing. L_{MIX} switches between convective mixing - usually represented by MLD (as in Dutkiewicz et al., (2001)), wind mixing (L_{EK}) and stratification or changes in surface heat fluxes (e.g. Taylor and Ferrari (2011)). For the Northern subpolar region where our OSP and NABE box are located, the ocean gradually gains heat during February and March (Figure C2), such that the area covered by case 1 (L_{MIX} = MLD) gradually shrinks and slowly transitions to case 2 ($L_{MIX} = L_{EK}$) as the wind intensifies counteracting the convective mixing in April through September (Figure C2). L_{MIX} for North Atlantic subpolar is given by the MLD (Case 1) in December, January, February, and partially in March. In contrast, North Pacific subpolar, L_{MIX} is given by L_{EK} in January through May. The difference between North Atlantic and North Pacific, in spite of being in similar wind regimes, is due to the convective mixing counteracting the wind-driven mixing in the North Atlantic. Evidence being that the MLD is much deeper in the North Atlantic compared to the Subpolar North Pacific (at least in the Eastern region). In the subpolar region, the L_{MIX} is driven by wind or L_{EK} (Case 2) at least 70-80% of a complete annual cycle (Figure C2).

The seasonal correlation of TK16 biomass with L_{MIX} is similar to the winds, significant and positively correlated in subtropics and subtropical front and negatively correlated in the subpolar regions (Figure 4.1b&c). In the subtropics the enhancement of vertical mixing via L_{MIX} boosts the phytoplankton growth during winter (January-March), whereas in the subpolar regions vertical mixing negatively affects the phytoplankton growth during winter and it is the increase in light during spring that allows the phytoplankton to bloom. We also investigate the Heatlfux-biomass relationship independent of that from L_{MIX} (as case 1). Heatflux-TK16 Biomass correlation patterns are similar to SST-Biomass in subpolar. The positive relationship between Heatflux- TK16 Biomass

(Figure 4.1d) suggests that the ocean heat gain in the subpolar is associated with increase in biomass, which is consistent with “convection shutdown theory” proposed by Ferrari et al. (2015). The theory suggests that as the water column gains heat after the winter cooling, the stratification develops in the water column. The reduction of the mixing of surface water with deep water, traps the winter nutrients in the surface ocean triggering the phytoplankton bloom in subpolar regions. The negative Heatflux- TK16 Biomass relationship in low latitudes suggests that as the ocean gains heat (positive into ocean), the water column stratification develops, restricting the mixing of already shallow MLDs, that reduced the nutrient supply for photosynthesis despite high levels of light being available. Positive seasonal correlation between TK16 Biomass and PAR in the subpolar regions coincide with the light during spring. Light is readily available in the subtropics all year around for the phytoplankton, therefore opposite sign for the correlations exist between light and Biomass (Figure 4.1e). Cabre et al (2016) show similar results using the TK16 biomass and PAR.

Local grazing activity that may differ at various locations and affect the biomass and Chl-a independent of the locations and their correlation with the physical indices (Follows & Dutkiewicz, 2002). For example, due to the difference in the environmental conditions, phytoplankton production and species composition, the copepods in the North Pacific lay their eggs just after winter hibernation before the copepods in the North Atlantic that lay their eggs after spring. Such difference allows the grazing to be stronger in the North Pacific during the spring bloom (as the larvae is ready to feed on bloom) than in North Atlantic (Cole et al., 2015). During the SEEDS and SERIES experiment, Tsuda et al. (2007) observed that the grazing rate of copepods were 35% of primary production at OSP.

The strength of correlation of S08 biomass-physical and TK16 biomass-physical indices are similar except in the inner subtropical gyres where the TK16 biomass show stronger relationship with SST, L_{MIX} and Heatflux (compare Figure 4.1a-e and k-o). The biomass-physical relationships in the B05 biomass are much weaker than in TK16 & S08 biomass in the tropics and subtropics albeit the signs are similar. North of 40ºN and below south of 40ºS, B05 exhibits stronger correlations with all the physical variables. The fact that correlations are strong at low and mid-latitudes for TK16 and S08 and strong in high-latitudes for B05 suggests that TK16 and S08 might be biased towards nutrient-limited characteristics of subtropical regimes whereas B05 is biased towards light-limited estimates of subpolar regimes. TK16 %micro and MY10 %micro relationship with physical indices is stronger than the relationship of physical indices with PhytoDOAS $\%micro_{CHL}$ and PHYSAT $\%micro_{freq}$ (Figure C1). However, the correlation significance is greater in MY10 with physical indices for the subpolar regions than that of the TK16 %micro, indicative that MY10 has similar light-limited biases as B05. TK16 %pico show similar correlation patterns as to TK16 %micro with opposite signs.

4.5 Contrasting PAPA versus NABE

4.5.1 Seasonal cycles in multiple biomass products

Figure 4.2 shows the seasonal cycle of phytoplankton biomass, PFT and Chl-a for different datasets (Table 4.1) in the NP and NA regions. Despite being in similar climate regimes (with similar light and wind patterns), OSP and NABE are thought to represent different ecological regimes. Buesseler and Boyd (2009) argue that the (light and nitrate limited) North Atlantic has a very

efficient export of organic matter to 100m and weak attenuation of the particulate organic matter flux below 100m, whereas the (light and iron limited) North Pacific has low export ratios and strong attenuation within the upper 100m, perhaps because small phytoplankton dominate. At OSP, previous work has shown that bottom-up control related to Fe limitation is most important for large phytoplankton (Muggli & Harrison, 1996; Harrison, 2006; Marchetti et al., 2006), whereas microzooplankton grazing exerts a strong top-down control on pico- and nanoplankton. Iron-light co-limitation of primary production results in high nitrogen and silicate even during the summer (Whitney et al., 1998, Harrison et al., 2004). In the NP, the mixed layer varies seasonally between 40m in summer and 90-120m in winter, thereby allowing winter replenishment of nitrate and silicate to the mixed layer. Westberry et al. (2016) pointed out major differences between Chl-a and biomass cycles in the NP and NA subpolar boxes, as indicated by the Chl-a product and B05 biomass product (reproduced in Figure 4.2f&m). They observe that the NP and NA boxes exhibit similar magnitude biomass cycles, although the seasonal cycle of Chl-a is much larger in the NA and almost absent in the NP. They argue that hence Chl-a is not a good indicator for biomass, and that the differences in the Chl-a and biomass cycles for the NP reflect instead strong iron-dependent photoacclimation.

Figure 4.2 shows that in the NA, a major peak occurs in spring when light-limited phytoplankton can bloom as light increases and winter nitrate levels are still high. During summer a nitrate limited, low Chl-a and biomass regime develops (Sverdrup, 1953), and a secondary, weaker bloom in the fall as nutrients start to grow again. The seasonal pattern for the NA box (blue line) is qualitatively consistent across satellite products, with blooms in %micro, %nano, total biomass and Chl-a in April to June across all products. TK16 and Chl-a have more pronounced secondary fall peaks than the B05 product and the fall peak is associated with peaks in both %micro and %nano.

In contrast, at NP, various products are both qualitatively and quantitatively inconsistent with each other. The average month in which maximum biomass occurs varies among different products, from August-September in the B05 product, October-November in the S08 product, to November-December in the TK16 products. The S08 or TK16 products (Figure 4.2) show with far less seasonal biomass variation in the NP box when compared to B05 (as in Westberry et al. (2016)). The results imply a very different story from Westberry et al. (2016), more in line with the “classical” understanding of the NP ecology (Evans & Parslow, 1985): zooplankton keeps large phytoplankton from blooming in the spring and summer in the NP, whereas photoacclimation is less important there than suggested by Westberry et al. (2016). Kostadinov et al. (2017) extending work of Hirata et al. (2012), made a global and regional intercomparison of the various biomass products and found that the variables from various algorithms agree globally to some extent, whilst vast differences exist in the regional picture, such as in subtropics (North Atlantic Drift Region and Subtropical Gyre West).

The authors caution that TK16 PFTs (Figure 4.2b,g,k) can be more trusted than the total TK16 biomass (Figure 4.2a). The TK16 biomass is calculated from the number of particles assuming that most particle backscatters are mostly living cells or organic detritus and spherical in shape. On the other hand, the TK16 PFTs are a function of particle size distribution (PSD) slope that is independent of TK16 biomass, but they are not independent of each other (Kostadinov et al. 2016). Both BR10 and TK16 products show %nano dominating over %micro and %pico at NP, with two seasonal peaks in %nano (Figure 4.2b,c,h&l): an initial one in the spring and a second one either in October (BR10) or December (TK16). MY10 %micro and PHYSAT $\%micro_{freq}$ show one long

seasonal peak from May through September, with a larger diatom peak in PHYSAT %micro$_{freq}$ (Figure 4.2d&e).

4.5.2. Physical Drivers of Seasonality at PAPA and NABE

A comprehensive investigation on physical drivers of seasonality in TK16 product has been documented in the global and subpolar regions by Cabré et al. (2016), but on a wider geographic scale. At the NA box (Figure 4.3, blue), we observe that as the MLD and/or L_{MIX} decreases (Figure 4.3a,b,&g), perhaps due to the combination of decrease in wind speed (Figure 4.3b) and/or heat gain by the ocean (positive, Figure 4.3d) and/or increase in light availability (Figure 4.3g), the biomass, %PFTs, and Chl-a increases across all the products during spring. As the phytoplankton growth increases during the spring, the surrounding nutrient in the waters decrease that is observed in Figure 4.3f, where the nutrient concentration declines in the NA box. The shoaling of the vertical mixing parameters (MLD and L_{MIX}), traps the nutrients from the winter mixing that allows bloom. However, the fall bloom can be explained by the opposite mechanism, where the increase in MLD and/or L_{MIX} due to the combination of increase in wind speed (Figure 4.3b) and/or heat loss by the ocean breaking the summer stratification and allows mixing of surface waters with deep nutrient rich waters. We observe a small peak in nutrient from September to December (Figure 4.3f in blue), that is reflected by the increase in phytoplankton growth (Figure 4.1i-j,m).

In contrast, as described earlier the NP box has a different seasonal cycle. TK16 biomass, %micro and %nano (Figure 4.2a-b,g), S08 biomass (Figure 4.2j), BR10 %micro$_{CHL}$ and %nano$_{CHL}$ (Figure 4.2c&h), MY10 %micro$_{CHL}$ (Figure 4.2e) and Chl-a (Figure 4.2m), slightly capture the fall bloom. A very small fall bloom in MY10 %micro$_{CHL}$ and Chl-a are observed. The drivers of fall bloom in the NP are consistent with those ones in the NA. However, unlike NA, biomass at NP during spring/summer is decreasing across all the products except in B05 biomass, PHYSAT, and MY10, indicating that the other mechanisms play a role. The winter mixing at NA is deeper than at NP allowing more nutrients to get exposed to surface ocean in NA than NP. Therefore, as the MLD, and L_{MIX} are shoaling during the spring in NP (Figure 4.3a-c&e), one can postulate that perhaps not enough nutrients are being trapped in the water column to boost the phytoplankton growth compared to NA. But this cannot be true because the nutrients are available in abundance at NP, as previously reported (Martin & Fitzwater, 1988; Martin et al. 1989). As previous studies have shown, it is possible that Fe limitation, or grazers such as zooplankton could be keeping the phytoplankton biomass in check following the spring bloom (Sommer, 1996; Cole et al., 2015).

Overall to explicitly separate the physical mechanisms controlling the biology at NP, we conduct a correlation of physical indices against all the biomass and PFTs over 1997-2010 period. The correlation of physical indices against B05 biomass, PHYSAT, and MY10 (Table C3) over 1997-2010 period suggest light limitation at NP. Stronger winds, and deeper L_{MIX} dilutes the surface phytoplankton and thus cause light-limitation decreasing the B05 biomass, PHYSAT, and MY10 percent micro. The correlations for S08 biomass and Chl-a are insignificant with physical indices at NP indicating weak and/or no relationship exists. However, TK16 %micro and %nano suggest nutrient rather than light limitation during spring. Strengthened winds and ocean heat loss deepens the L_{MIX}, replenishing the surface waters with more nutrients. Increased nutrients are favorable to larger phytoplankton, that outcompetes the small phytoplankton increasing the total biomass. We

notice that TK16 %pico seems to act like the B05, PHYSAT, and MY10. We further explore the above mechanisms at NA and NP using the models.

4.6.0 Biological seasonality across CMIP5 models in the northern subpolar regimes.

We next analyze in detail the annual cycle of biological indicators and physical/biogeochemical stressors across CMIP5 models for the NP (Figure 4.4) and the NA box (Figure 4.5). To summarize our findings across the 2 subpolar regimes, we also perform scatterplots of most important properties across models in Figure 4.6 and 4.7.

4.6.1 Seasonal cycle in CMIP5 models at NP:

In our observations at NP, MLD peaks at around 70m during winter and shallows to 20m during the summer months (Figure 4.3); most models reproduce reasonably well the summer and winter seasonality and magnitude except for NorESM1 and CESM1 which deepen excessively during winter (~200-400m). The NO_3 cycle generally follows the MLD annual cycle at NP and is high during winter and low during summer. The observed winter and summer NO_3 (Figure 4.2) levels are 9-12 mmol m^{-3} and 4-6 mmol m^{-3}, respectively. All the models underestimate the winter NO_3 levels (<9 mmolm^{-3}), except MPI-ESM-MR, NorESM1-ME and HadGEM2-ES that are similar to the observed NO_3 levels. MPI-ESM-MR, and NorESM1-ME overestimated (>6 mmol m^{-3}) the NO_3 levels in summer, while the remaining models underestimate them by an order of magnitude. Observed surface Fe levels typically stay between 0.05 and 0.1 nM in late spring and winter (Harrison, 2002) at OSP. All models in the NP box show Fe concentration between 0.2nM and 2nM, for winter and summer respectively, except GISS-E2-H-CC that shows a constant Fe concentration of 1.5nM throughout the year. In general, the Fe concentration is overestimated for NP box in CMIP5 models.

At NP, phytoplankton biomass and Chl-a are fundamentally different across various observed databases and CMIP5 models. Most CMIP5 models show Chl-a and phytoplankton peak during May and in a few models a secondary small peak in November (rather than September), with values below 60mg/m^3 (5mmol/m^3) in accordance with observations. However, MPI-ESM-MR, HadGEM2-ES, and NorESM1-ME show phytoplankton values up to 4 times larger (Figure 4.4a), that is presumably due to largest NO_3 levels that fuels the phytoplankton growth (Figure 4.4d). Models at NP show high diatom fraction during winter (HadGEM2-ES, CESM1-BGC) or spring months (GISS, GFDL models) when MLD is deeper and nutrients are abundant, and lowest during the summer months when MLD is shallowest and the system is more stratified. The HadGEM2-ES model has the largest fraction of diatoms at NP, accounting for 50- 80% of the biomass and peak in Feb-March and in Sept-Oct when the Fe and NO_3 levels are at their maximum. The CESM1 model has the second highest diatom fraction, accounting for 30-50% of the total biomass (Figure 4.4e). Despite its very deep MLD in winter and spring and considerable amount of winter/spring surface nitrate, CESM1 model has the second lowest surface Fe among all models (and the third lowest surface Fe/NO_3 ratio, and it has a modest seasonal cycle of phytoplankton biomass and Chl-a relative to its nitrate (Figure 4.6a). In the GFDL model diatom fraction is overall <10% of the phytoplankton

population (Figure 4.4e) during spring. In the highly-stratified and nitrate limited summer waters, the smaller plankton account for the majority of the biomass, as indicated by the drop in NO_3 relative to Fe in the summer months (Figure 4.4g&h). Cabre et al. (2016) show that models tend to have unrealistic dominance of small phytoplankton in HNLC waters during blooming months also. IPSL diatom fraction model accounts for approximately 20% of the phytoplankton population, which is greater than GFDL. The difference could be owing to greater NO_3 concentration in IPSL than GFDL at NP.

4.6.2 Phytoplankton at NA

In NA, the observed MLD (W'16 MLD) peaks at around 100-150m during winter and shallows to 20m during the summer months (Figure 4.3); most models reasonably represent the summer seasonality and magnitude compared to the observed MLD (Figure 4.5i). Almost all models show deeper MLD during winter (up to 200 or 400m), except HadGEM2-ES, CanESM2, MRI-ESM1 and IPSL-CM5A-MR which are consistent with the observed MLD. The NO_3 levels are lower at NA box, ~3-5 $mmolm^{-3}$ during winter and less than 1 $mmolm^{-3}$ during summer. The winter NO_3 concentrations in most of the models are close to observed winter NO_3 values, except IPSL-CM5A-MR, GFDL-ESM2G and NorESM1-ME overestimates the NO_3 concentration (Figure 4.5g). The observed Fe concentration is between 0.71-1.56nM at NA (Laës et al., 2003). CESM1-BGC**,** GFDL-ESM2G, GFDL-ESM2M show reasonable Fe concentrations at NA, whereas most of the models underestimate the Fe concentration values throughout the annual cycle, except GISS-E2-H-CC and GISS-E2-H-CC overestimates the Fe concentration values. HadGEM2-ES and MPI-ESM-MR show a constant value of 1.5nM throughout the annual cycle (Figure 4.5h).

The classical 2 bloom feature (a strong light-nutrient co-limited spring bloom and a weaker fall bloom corresponding to an increased MLD and resupply of nitrate) is visible for some of the models in both phytoplankton biomass and Chl-a. The peaks in model biomass, Chl-a, and percent diatoms occur in May-June and correspond (in most models) to MLD decreasing, in agreement with a hypothesized Sverdrup-like light limitation of biology. In other words, the peaks in percent diatom, and biomass occur after the peaks in MLD. The NO_3 decreases during the peak in MLD and diatoms suggesting the nutrient depletion in the system due to phytoplankton growth. CanESM-2 is the only model that show one winter peak in phytoplankton biomass possibly due to shallow MLD throughout the annual cycle and a slight deeper winter MLD. The GFDL model does not show a fall bloom in the phytoplankton biomass but obvious fall peak in diatom/phyto (diatom relative to phytoplankton biomass) and Chl-a. GFDL model diatom accounts for <15% of total phytoplankton biomass, and greater percentage by small phytoplankton.

4.6.3 Comparison of NP and NA seasonal cycle and their mechanisms

To summarize model behavior, we perform scatterplots of the most important properties across models and plot the NP boxes against the NA boxes (Figure 4.6). Important additional properties at the two sites across models are shown in Figure 4.7 and Table C2. Our expectation, based on fundamental understanding of OSP dynamics (Section 4.3), observations of Chl-a (Figure 4.2m) and multiple biomass products (Figure 4.2), is that the seasonal cycles of phytoplankton biomass

and Chl-a should be smaller in the NP box compared to the NA box. We verify if the same exists across all the CMIP5 models.

We calculate the normalized amplitude of the seasonal cycle for a variable as the difference between the maximum and minimum values, normalized to the average variable value. The normalized parameters allow us to look at the relative seasonal changes in variables, rather than absolute change, normalizing to uncertainties across models. We find that phytoplankton biomass, Chl-a and PP vary by up to 5 times during the seasonal cycle (Figure 4.6h-j) in the models. On average, models with a larger phytoplankton biomass seasonal cycle tend to have a stronger Chl-a, PP and zooplankton seasonal variability (Figure 4.7). Based on a comparison of the seasonal cycle of Chl-a, biomass and PP at the NA and NP sites we can broadly separate the models in two categories: Group 1 (CESM1, 2GFDL, 2GISS, 2IPSL, MRI models), and Group 2 (HadGEM2, NorESM, CanESM2 and 2MPI models).

GROUP 1 models (CESM1, the two GFDL, two GISS, two IPSL, MRI) are characterized by

normalized Chl-a, biomass and PP seasonal cycles which are weaker in the NP than in the NA box (Figure 4.6 & Table C2). Reflecting the weaker phytoplankton blooms in the NP, these models also have weaker normalized zooplankton seasonal cycles in the NP. We hypothesize that weaker seasonal cycles in phytoplankton is partly due to (Hypothesis 1) weaker Fe supply and biological uptake at NP and partly due to (Hypothesis 2) tighter zooplankton grazing at NP relative to NA.

Hypothesis 1: weaker Fe supply. A weaker Fe supply at NP (relative to NA) would limit growth (particularly of larger phytoplankton) and would result in less Fe uptake at NP relative to NA during the growing season. This mechanism is reflected by the weaker normalized Fe seasonal cycle at NP compared to NA in most Group 1 models. The weaker Fe seasonal cycle we observe might in turn be explained by (a) a weaker MLD seasonal intensity at NP (~1-2) relative to NA (~2-3) which would decrease the vertical supply of Fe as observed in our data or (b) due to a smaller fraction of wind-driven Fe reaching the NA relative to NA.

Hypothesis 2: tighter zooplankton grazing. As shown in Figure 4.6l, C4, Table C2 and Figure 4.7f, the ratio of Zoo/Phyto (zooplankton biomass relative to phytoplankton biomass) is higher at the NP compared to the NA box during all months of the year in these models (with the exception of GFDL-ESM2M, where the relationship switches in the summer). This switch suggests a grazer population that keeps a tighter check on phytoplankton growth at OSP compared to the NA throughout the year. Note that grazing is tighter happens despite the overall average zooplankton biomass is lower at NP. The 2 GFDL models stand out especially in the NA box, with unusually large peak PP and zooplankton biomass relative to their peak phytoplankton biomass, indicative of a relatively strong zooplankton control in this model (Figure 4.7f, also see large zoo/phyto ratios in Table C2). We find that Group 1 models (except for GISS models) have a smaller diatom fraction at NP than at NA. This observation agrees with both Hypotheses above. Both a weaker normalized seasonal nutrient supply, in particular Fe, or a tighter control of grazers (particularly of larger phytoplankton) would contribute to a smaller diatom fraction at NP relative to NA.

GROUP 2 models (HadGEM2, NorESM, CanESM2 and two MPI models) are characterized by normalized Chl-a, biomass and PP seasonal cycles which are stronger in the NP than in the NA box (Table C2, Figure 6.6). Additionally, the HadGEM2, MPI and NorESM models are characterized by unusually large blooms at NP, with average and maximum values in PP and biomass about 2-

4 times larger at NP compared to NA. The above observation is rather counterintuitive and opposes the classical Chl-a observations and our classical understanding of NP and NA dynamics (Section 6.4.5, also Figure 4.2). We hypothesize that the unusual phytoplankton behavior in these models is due to a combination of (unrealistic Mechanism 1) higher nutrient uptake at NP and (unrealistic Mechanism 2) less efficient zooplankton grazing at NP relative to NA.

Unrealistic Mechanism 1: We note that unlike Group 1 of models, the seasonal MLD cycles at NA and NP are close to each other in Group 2 models (Figure 4.6e &Table C2). The HadGEM2, NorESM and 2 MPI models have larger average NO_3 at NP compared to NA. Assuming NO_3 limitation at NA, this would result in larger phytoplankton blooms at NP compared to NA. Additionally, Group 2 models which include Fe as a model tracer the stronger normalized Fe seasonal cycle at NP compared to NA (HadGEM2, 2 MPI models and NorESM1, Table C2), again reflecting the higher nutrient uptake (less nutrient limitation) at NP.

Unrealistic Mechanism 2: can be applicable to the HadGEM2 and MPI models only, as the NorESM model does not providing the grazing information as one their model variable output, whereas the CanESM model has under-represented zooplankton grazing at our locations of interest (e.g. Figure C4). Corresponding to stronger phytoplankton blooms, the HadGEM2 and MPI models have larger average zooplankton at NP compared to NA (Figure 4.7f), as well as larger seasonal variability in Zooplankton [max(Zoo) – min(zoo)] at NP compared to NA. However, as shown in Figure 4.6 & C4, the ratio of Zoo/Phyto is weaker at NP compared to NA box during most months of the year, reflecting a weaker zooplankton control on phytoplankton in the NP compared to the NA.

In conclusion, based on our current understanding of phytoplankton dynamics and observational assessments (Section 4.3-4.5), we propose that the Group 1 models are more realistic in their assessment of phytoplankton seasonal dynamics at NA and NP. We discuss the potential reasons in Section 4.6.5.

4.6.4 Seasonality of Chl-a relative to phytoplankton biomass

Cells photoacclimate to the increase in light supply during summer, reducing their Chl-a production relative to biomass; this decrease is reflected in the C/Chl model calculated as in Behrenfeld (2015) (see Methods and Figure 4.2n). Incident radiation shows a maximum around June across models, where the peak values vary by up to 30% across models at both sites (Figure 4.4&4.5). All other models allowing a varying C/Chl ratio, indeed show that the phytoplankton C/Chl ratio increases during summer months at both locations (Fig 4.4c,4.5c), as expected from photoacclimation arguments (Westberry et al., 2016). Interestingly, the peak C/Chl is larger in the NP box compared to NA for all models except for IPSL-CM5A-MR, despite similar light levels at the two sites. This finding agrees with the observation of Westberry et al. (2016) (their Figure 4.4) who argued that the NP and NA difference in C/Chl is not due to different acclimation (light) effects at these 2 sites, but to the relatively stronger Fe limitation at NP, which would limit Chl-a and increase C/Chl at NP relative to NA. We observe that latter is true for our more realistic models (Group 1 models*),* as shown by a ratio of normalized Fe concentration higher in NA than NP (Table C2). We notice that C/Chl is larger in models relative to the expected $\mathrm{Chl}/C_{B'16}$ (Figure 4.2n); the reasons for which will be explored in future work.

4.6.5 Grazing, Iron and light in the CMIP5 models

We propose that differential modeling of grazing and iron limitation creates the large inter-model changes observed across models in Section 4.6, particularly in the HNLC regions.

Grazing: Various modeling groups make different choices with respect to representing the phytoplankton and zooplankton groups. However, most groups include the basic Nutrient Phytoplankton Zooplankton Detritus (NPZD) biogeochemical model. A single spectrum of zooplankton in the model represents the highest trophic level grazing on a single phytoplankton class (Robson, 2014). Zooplankton is typically included in the models as a "top closure term" which means that the mortality rate in the zooplankton compartment is treated as both a natural and predatory mortality rate (Edwards & Yool, 2000). For example, the GFDL model does not have any zooplankton groups, only a specific grazing rate of each PFT, while the IPSL model has 2 zooplankton size groups. Grazing is the dominant loss term for phytoplankton in the real ocean (Banse, 1994). However, as summarized in Table C1, there are systematic and large differences in grazing parameterizations across biogeochemical modules embedded in ESMs that – we propose – can explain most of the observed differences observed between the Group 1 and Group 2 models in Section 4.6.

We note that models in Group 2 have one phytoplankton type (NorESM, CanESM2 and two MPI models), with the single exception of the HadGEM2 model. Among models with only one type of phytoplankton, MPI-ESM and NorESM1-ME use a Holling type II shape to parameterize grazing, which assumes a hyperbolic predator intake rate with increasing prey concentration following a Michaelis–Menten curve. Models CanESM2, and MRI-ESM1 (with simple NPZD biogeochemical modules) use a Holling type III shape, which assumes a sigmoid predator intake rate, with accelerating predator intake at very low prey concentrations and saturation at high prey concentrations. Additionally, all of these models include phytoplankton loss and aggregation terms as a linear or quadratic function of phytoplankton concentration. The more sophisticated HadGEM2 model applies a Holling type II curve to parameterize grazing, with additional switches on predation rates depending on abundances of small and large phytoplankton.

Group 1 models (CESM1, the two GFDL, two GISS, two IPSL) have at least two phytoplankton types; the one exception is model MRI with 1-phytoplankton type. The GISS-E2 models apply the Ivlev formulation to parameterize grazing (similar to Holling type II) with a grazing rate independent of phytoplankton type, while the other Group 1 models have a grazing that depends on phytoplankton types. Specifically, IPSL-CM5A models include two types of zooplankton and apply a Holling type II grazing scheme with grazer preference, again in order to ensure that grazers can keep up with small phytoplankton but not with diatoms. CESM1 applies a Holling type III grazing formulation also with different predator intake rates for small and large phytoplankton, again decoupling phytoplankton biomass from PP and breaking the relationship expected for bottom-up control alone. Finally, in the GFDL-ESM2 models, zooplankton are not modeled as a separate group; grazing losses are instead modeled as a function of phytoplankton to the power of 2 for small phytoplankton and 4/3 for large phytoplankton, in order to ensure that zooplankton are able to easily and effectively graze on small phytoplankton than on diatoms, as observed in situ (Dunne et al., 2005). Since the GFDL models have a very large fraction of small phytoplankton at both NP and NA, the grazers thrive resulting in a strong role for zooplankton as reflected by a very large Zoo relative to Phytoplankton biomass (see Figure 4.6l, 4.7f and Zoo/Phyto ratios in Table C2), as

well as a decoupling between PP and phytoplankton biomass, with a relatively low phytoplankton biomass relative to PP in this model (see Figure 4.6e).

Concluding, we note that in the most complex models (IPSL, CESM1, GFDL), the fraction of small phytoplankton is always larger at NP compared to NA, presumably due to lesser nutrient supply at NP. Because of their size-dependent grazing parameterization, grazers can keep down the phytoplankton population at NP most efficiently, resulting in a lower seasonal uptake of nutrients and lower normalized Chl-a and biomass seasonality in these models at NP compared to NA. We propose that the resulting Group 1 model biological patterns match better the seasonal cycles across satellite-based products than the group 2 models. Our observations agree with previous work (Hashioka et al., 2013), that different grazing parameterizations create large differences in the relative contributions of bottom-up versus top-down factors in the control of phytoplankton blooms across models. Studies also suggest that the lack of model-data assessment of zooplankton and the knowledge gap between the zooplankton modelers and observationalists is one of the reasons why zooplankton are poorly simulated in biogeochemical models (Everett et al., 2017).

Iron: Recent global compilations of dissolved iron (Tagliabue et al., 2012) and GEOTRACES project transects (Mawji et al., 2015) revealed that there are many features of dissolved Fe (dFe) distribution that are either missing or heavily biased in the current generation of models (Tagliabue et al., 2016). The existence of significant model biases indicates problems in the current parameterizations of Fe cycling and the quantification of Fe sources and sinks. We are far from having a clear picture of global ocean Fe. Fe is particularly challenging to detect and model because of its extremely low (nanomolar) concentrations and complex dynamics which includes transformation of Fe between dissolved and particulate pools via scavenging, desorption, and remineralization mediated by the presence of organic ligands (produced in turn by bacteria). The global dFe budget and distribution are sensitive to the strength and concentration of the subsurface ligand. Including prognostic ligands in models clearly improves the subsurface dFe distribution in ocean biogeochemistry models (Tagliabue et al., 2016), e.g. ligand presence helps maintain the subsurface Fe maxima (Pham & Ito, 2018).

Sources of Fe are another large unknown in our modeling and understanding of Fe cycling generally in models and specifically at OSP. Fe can be brought to the oceans by atmospheric dust, but also from sedimentary, hydrothermal, volcanic, sea ice- and iceberg-derived sources, all of which vary hugely geographically. Sedimentary and hydrothermal vent Fe sources were found to be the important sources of the subsurface dFe maxima in the thermocline of low-dust regions in the Pacific Ocean and also travel via water pathways for long distances (Nishioka & Obata, 2017 and references therein). Given the potential role of the subsurface dFe as a source for Fe-limited upwelling regions (Tagliabue et al., 2014), these external sources can have far-reaching effects on the marine ecosystems and the biological carbon pumps. In HNLC waters, differences in Fe supply can strongly affect the amplitude of the seasonal variation in biology. For example, Nishioka and Obata (2017) point to more Fe in intermediate waters in the Western Pacific Subpolar Gyre compared to the Eastern subpolar (Alaskan) gyre due to more intense sedimentary sources in the Western Pacific; this difference in Fe explains the lower surface macronutrient consumption and lower amplitude of seasonal variation in biogeochemical parameters in the Eastern compared to the Western subpolar gyre.

Finally, the amount and type of irradiance that penetrates through the water column is also an important issue when studying phytoplankton productivity and community structure. Kvale et al. (2017) show for example that global PP is sensitive to the light attenuation parameter, and that this sensitivity will increase with transient forcing in the future, while Gnandesikan et al. (2009) highlight ocean water clarity impact on warm ocean circulation and the Walker atmospheric circulation. And yet, ocean models routinely offer rather crude parameterizations of light attenuation and neglect the spectral quality of light. One direction for recent model development is the incorporation of spectral light, explicit radiative transfer, and representation of optical constituents in some global ocean models (e.g. Dutkiewicz et al., 2015; Kim et al., 2015; Gregg and Rousseaux, 2016). More sophisticated light penetration models in future climate model generations might improve the light limitation of biology and biology-ocean physics feedbacks.

4.7. Conclusions

Our paper provides a comprehensive analysis of the drivers of biological seasonality in the northern subpolar North Atlantic and North Pacific regions, in a global context and when comparing these in detail. Estimates from satellite-based color products and from CMIP5 models are compared. The observed NP box is a high-nutrient, iron-limited region which contrasts in both Chl-a and phytoplankton biomass seasonality with the more studied macronutrient-limited subpolar NA. Our main findings are summarized below:

- The large-scale seasonal patterns derived from correlations of physical tracers with biomass products are consistent to a first order to those found across CMIP5 models (Cabre et al., 2016). As expected, the northern subpolar regions are characterized by positive biomass-SST (or %Micro-SST) correlations, and negative correlations between biomass and L_{MIX}/windspeed across most biomass products, indicative of predominant light limitation of biology on the seasonal time scale. At least in the TK16, S08, PHYSAT, MY10 products these correlations seem to be stronger in the NA compared to the NP. The MY10 and TK16 products show strong differences in the subpolar region indicative that the MY10 is biased towards light-limitation estimates similar to B05.

- The satellite products are overall consistent in predicting the seasonal cycle at NA but widely different in their predictions of biomass and PFT seasonality at NP, particularly at HNLC sites such as OSP. The seasonal cycle in biomass differs strongly across the satellite algorithms (by 1-2 fold) in the NP, while the intermodel variability across CMIP5 models is even larger (up to an order of magnitude across models) consistent with our previous observations in Cabré et al. (2016)

- Differences across CMIP5 models are very large. The seasonal cycle in biomass differs up to an order of magnitude across CMIP5 models at the two subpolar sites (NP and NA boxes). It is therefore hard to find consistent mechanistic differences between the functioning of the marine ecosystem in the Pacific and Atlantic subpolar regions across CMIP5 models. We ascribe the differences to tighter grazing control of phytoplankton and less iron supply in the NP.

There are multiple technical challenges associated with this project. For many modelers, the PFT products derived from satellite algorithms are considered as ‘observations’ (not algorithm products

per se) and used as a reference for validating model outputs (Quéré et al., 2005; Stock et al, 2014; Cabré et al., 2016). First and foremost, satellite algorithms have a unique set of challenges and biases, as data retrieval from these algorithms is based on a set of theoretical assumptions. Data retrieval from these algorithms is based on either empirical or theoretical assumptions. Traditional satellite products of Chl-a and primary production have large error margins associated with them that are not spatially homogeneous (Szeto et al., 2011), for example the satellite Chl-a algorithm has a factor of 2 range error (Campbell et al., 2002). While Chl-a is certainly a useful variable, it is carbon biomass in the living phytoplankton that is the variable of most direct relevance to carbon cycle and biogeochemical studies; it is also the unit of PFT accounting in climate models.

However, biomass-based PFT products are so-far less studied and verified *in situ* compared to the Chl-a product and the now "classical" B05 biomass. We refer readers to the comparison of the most recent biomass PFT products, highlighting methodological differences between algorithms (Kostadinov et al., 2017; Mouw et al., 2017). One challenge in comparing phytoplankton biomass products is what actually constitutes 'biomass'. Observations have shown that components other than phytoplankton carbon (zooplankton, total particulate carbon, dissolved organic matter) play a role in light attenuation, affecting the satellite-inferred biomass fields; this problem is dealt with in different ways by different research groups. Detrital matter (Bricaud et al., 2010) is rather weakly constrained. Colored dissolved organic matter (CDOM) and its contribution to light absorption are observed to vary in different regions of the ocean (Jerlov, 1953; Nelson & Siegel, 2013). Recent work has suggested a potentially important role for CDOM in setting phytoplankton community structure via alteration of the visible light spectrum, particularly in the highly productive regions (Dutkiewicz et al., 2015).

Secondly, we acknowledge differences between our MLD product and other products from the literature (Westberry et al 2016). Large differences across MLD products, even using the same MLD definition, are a constant challenge in oceanography. Future improvements on our work will take into account a combination of sources for MLD and the implication of such uncertainty for our understanding of ocean biology. Our results highlight the need for further development work in modeling of zooplankton dynamics, iron cycling and light uptake in HNLC regions, in order to bring both future generation of global climate models into closer agreement with each other and with observations. At the same time, the large spread across satellite products in HNLC areas makes it abundantly clear that in-situ data collection in the subpolar regions – as proposed by the ongoing NASA EXPORTS campaign – is much needed, to validate both satellite algorithms and models.

4.7 Acknowledgements

Kostadinov et al (2009; 2010; 2016) products are available at https://doi.pangaea.de/10.1594/PANGAEA.859005.

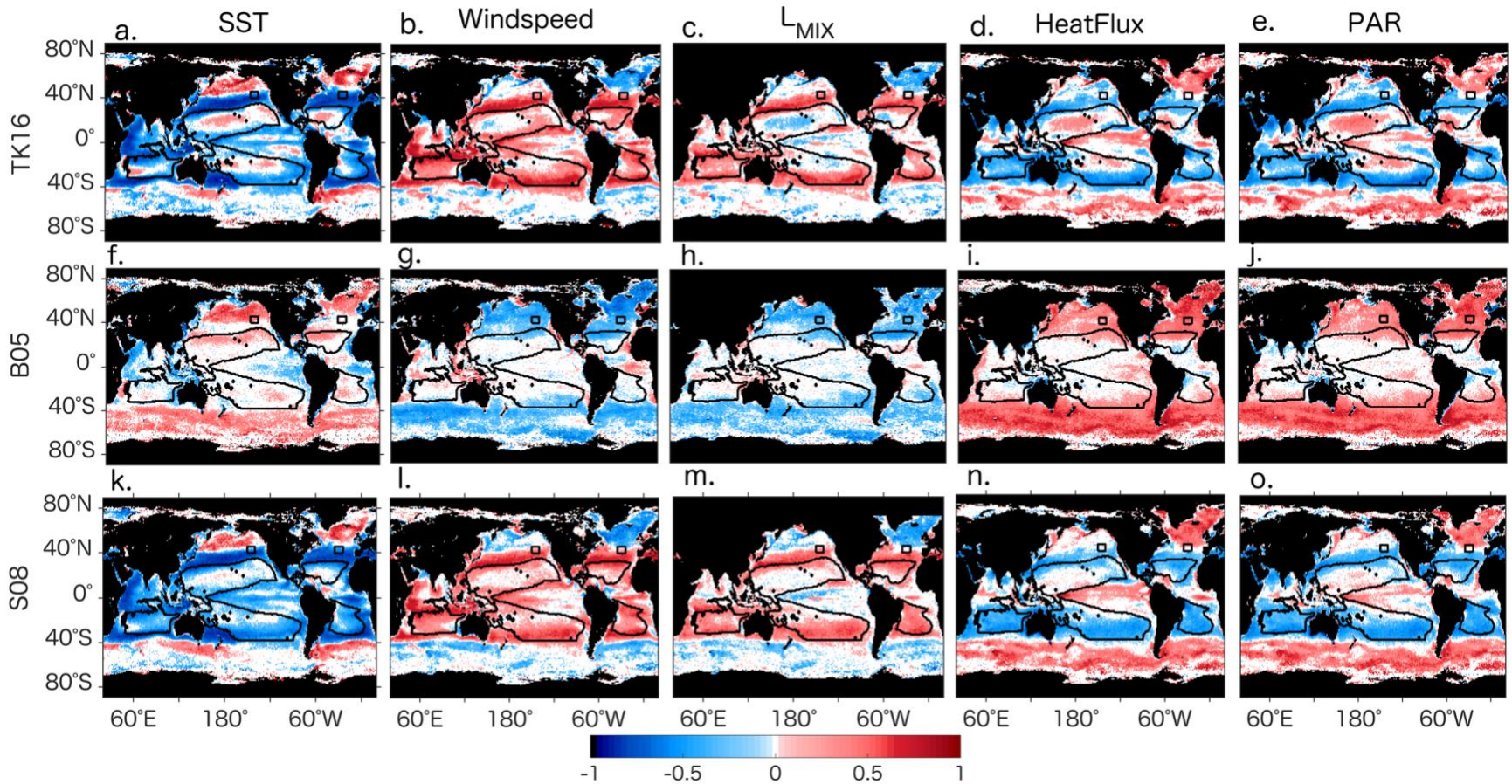
a. SST
b. Windspeed
c. L_{MIX}
d. HeatFlux
e. PAR
f.
g.
h.
i.
j.
k.
l.
m.
n.
o.
TK16
B05
S08
80°N
40°N
0°
40°S
80°S
60°E
180°
60°W
-1
-0.5
0
0.5
1

Figure 4.1: Temporal correlation of monthly (Top Panel, a-e) decimal logarithm of phytoplankton biomass (TK16) from Kostadionv et al. (2009, 2010, 2016) with sea surface temperature (SST), wind speed, active mixing length scale (L_{MIX}), Heatflux (positive into ocean) and photosynthetically active radiation (PAR) during the SeaWiFS period (1997–2010). Center Panel (f-j) is the temporal correlation between the decimal logarithm of phytoplankton biomass (B05) from Behrenfeld et al. (2005) and above physical variables. Bottom Panel (k-o) is the temporal correlation between the decimal logarithm of phytoplankton biomass (S08) from Stramski et al. (2008) and above physical variables. The correlation in the red and blue areas are statistically significant at the 95% level ($P<0.05$). Non-significant correlations are shown in white. Long-term trend is removed from the full time series by detrending the data. The two black boxes are North Pacific (45-50ºN, 140-150ºW, includes OSP, in red) and North Atlantic (45-50ºN, 25-35ºW, in blue, close to NABE). The black contour lines are the 5 subtropical gyres (see Figure A1)

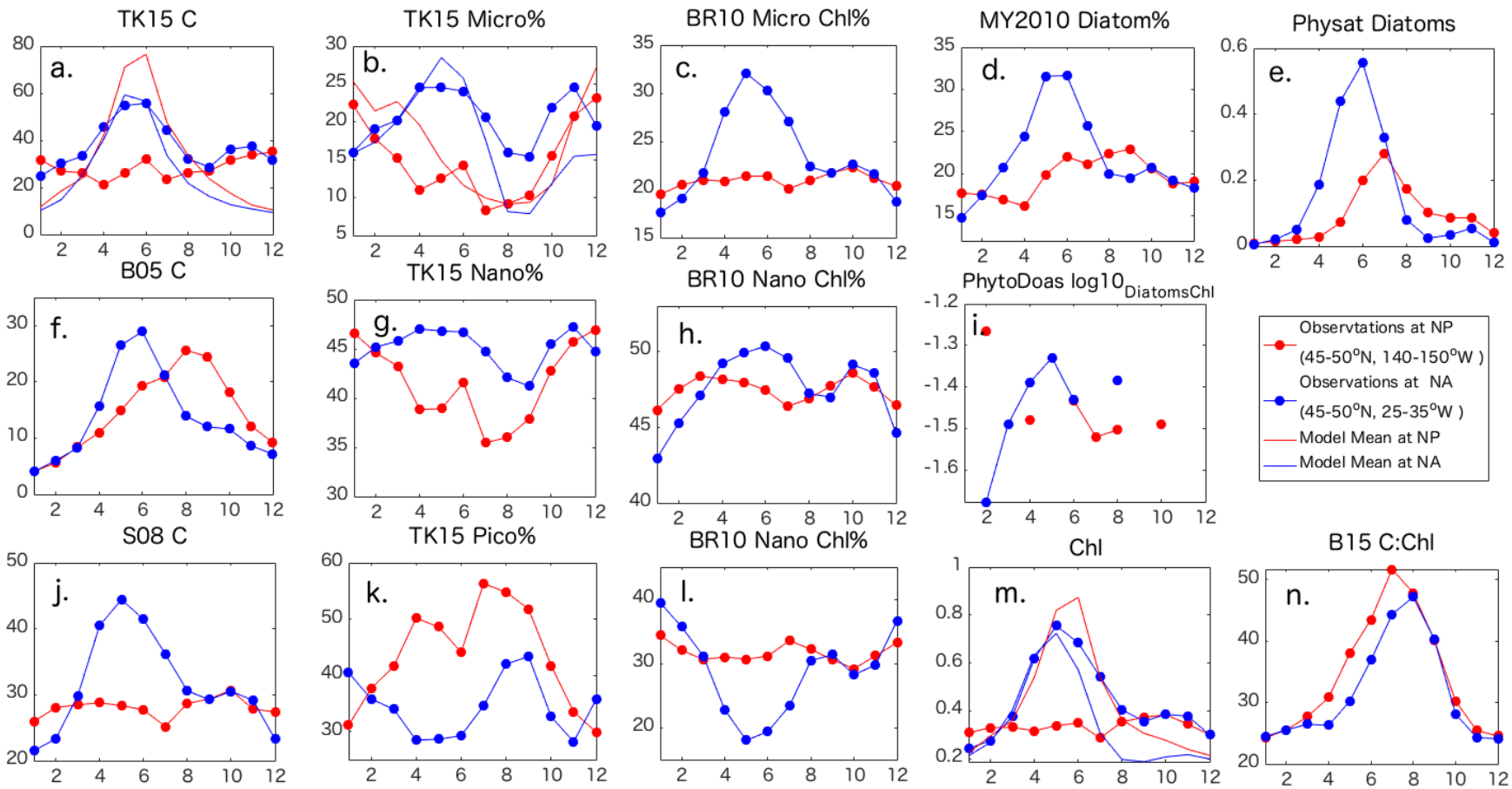
TK15 C
a.
TK15 Micro%
b.
BR10 Micro Chl%
c.
MY2010 Diatom%
d.
Physat Diatoms
e.
B05 C
f.
TK15 Nano%
g.
BR10 Nano Chl%
h.
PhytoDoas log10DiatomsChl
i.
Observtations at NP
(45-50°N, 140-150°W)
Observations at NA
(45-50°N, 25-35°W)
Model Mean at NP
Model Mean at NA
S08 C
j.
TK15 Pico%
k.
BR10 Nano Chl%
l.
Chl
m.
B15 C:Chl
n.

Figure 4.2: Comparative analysis of two subpolar boxes in the North Pacific (45-50ºN, 140-150ºW, includes OSP, in red) and North Atlantic (45-50ºN, 25-35ºW, in blue, close to NABE). SeaWIFS-based data analysis includes climatologies of (a, f, j) 3 phytoplankton biomass products from space (Behrenfeld et al. (2005), B05, Stramski et al. (2008), S08, Kostandinov et al. (2016) denoted as TK16). (b) percent Micro, (g) percent Nano and (k) percent pico phytoplankton from Kostadinov et al. (2016), (c) percent of Chl-a in Micro, (h) Nano and (i) Pico from Brewin et al (2010, 2011), (e) Frequency of detection of diatoms from Alvain et al (2005, 2008), (i) Chl-a in diatoms from Bracher et al (2009, 2017), (d) Size fraction of large phytoplankton from Mouw and Yoder et al. (2010b), (m) SeaWifS Chl-a and (n) Behrenfeld et al. (2015) photoacclimation model ($C/Chl_{B'16}$). The plain red and blue lines are in subplots a,b and m are the CMIP5 multi-model mean of phytoplankton biomass, percent microphytoplankton and Chl-a.

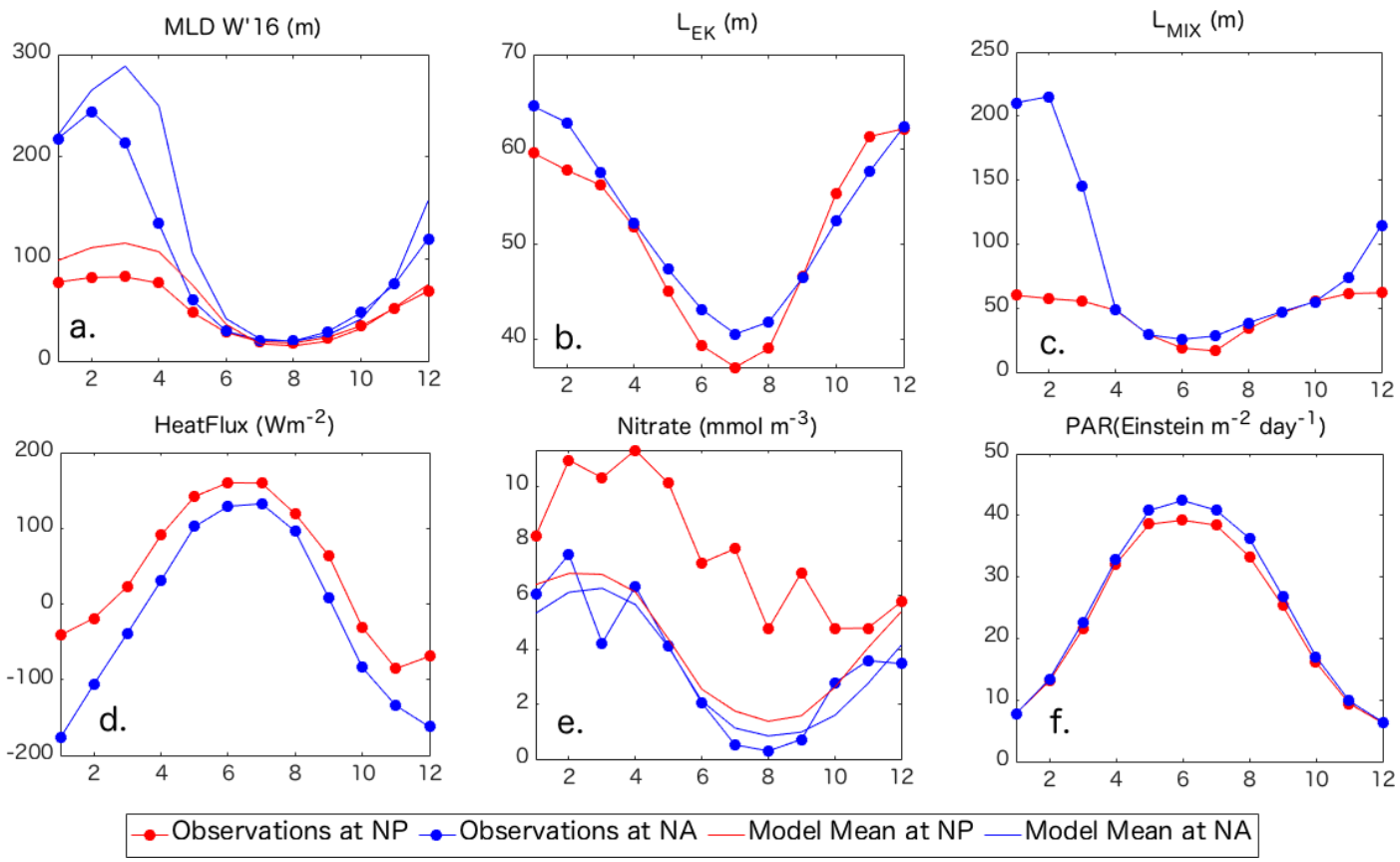

Figure 4.3 Comparative analysis of two subpolar boxes in the North Pacific (45-50ºN, 140-150ºW, includes OSP, in red) and North Atlantic (45-50ºN, 25-35ºW, in blue, close to NABE) for the physical variables. The variables include climatologies of (a) mixed layer depth from Westberry et al (2016) (MLD W'16), (b) Ekman length scale L_{EK}, (c) active mixing length scale (L_{MIX}), (d) Heat Flux, (e) nitrate, and (f) Photosynthetically active radiation (PAR). The plain red and blue lines are in subplots a and e are the CMIP5 multi-model mean of MLD and Nitrate.

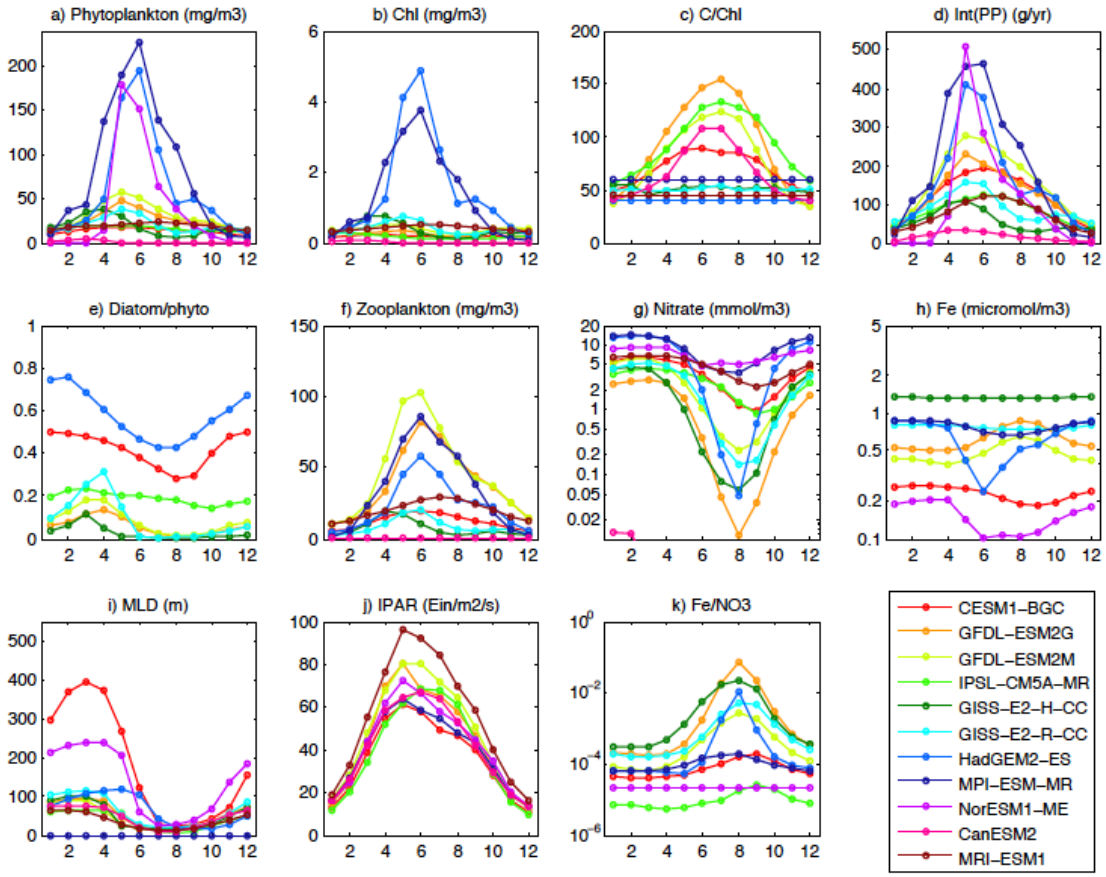

Figure 4.4: Climatologies of the ecological and physical variables in the subpolar box at North Pacific (45-50ºN, 140-150ºW, includes OSP). The variables includes climatologies of (a) Phytoplankton biomass (C), (b) Chl-a, (c) photoacclimation parameter (C:Chl-a ratio), (d) Intergrated Primary Production [Int(PP)], (e) Diatom/Phytoplankton biomass ratio, (f) Zooplankton, (g) Nitrate, (h) Iron (Fe), (i) mixed layer depth (MLD), (j) net downward shortwave flux (IPAR) and (k) Iron/Nitrate (Fe/NO_3) ratio. Note: 1micromol/L = 1millimol/m3 and 1nM = micromole/m3

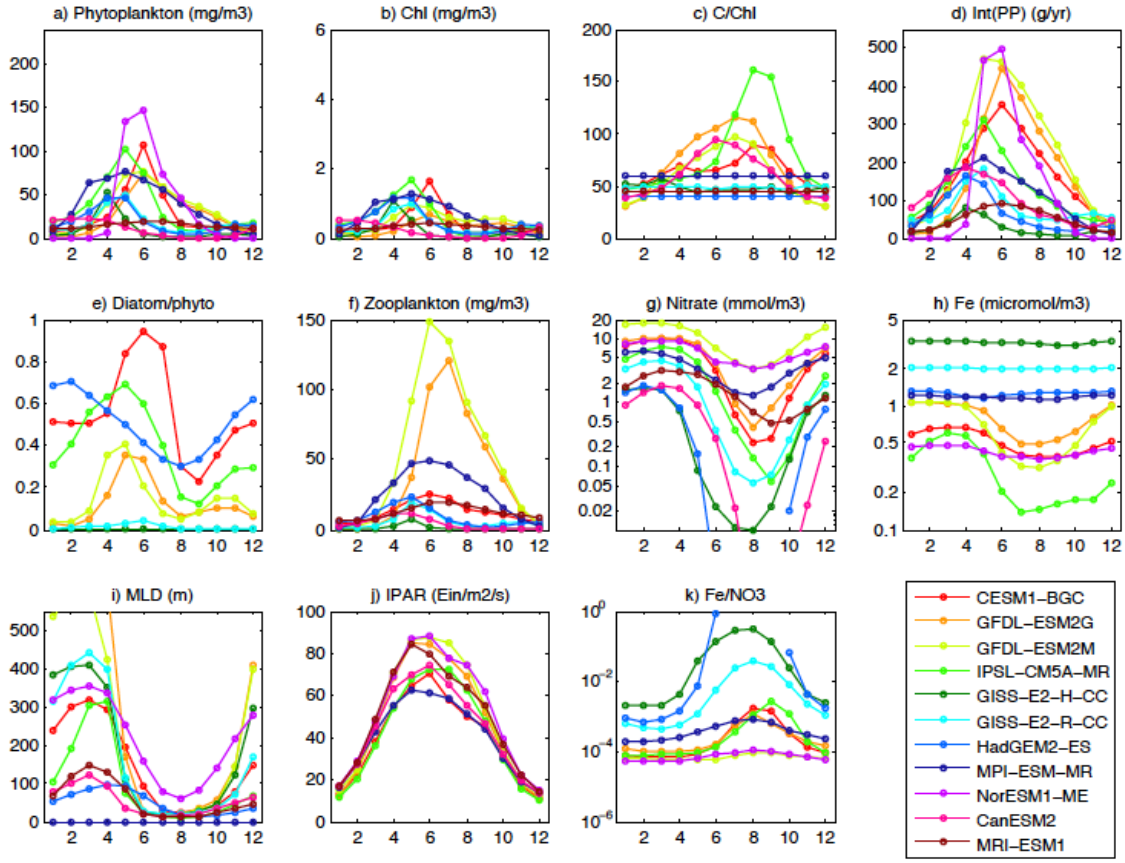

Figure 4.5: Climatologies of the ecological and physical variables in the subpolar box at North Atlantic (45-50ºN, 25-35ºW, close to NABE). The variables includes climatologies of (a) Phytoplankton biomass (C), (b) Chl-a, (c) photoacclimation parameter (C:Chl-a ratio), (d) Intergrated Primary Production [Int(PP)], (e) Diatom/Phytoplankton biomass ratio, (f) Zooplankton, (g) Nitrate, (h) Iron (Fe), (i) mixed layer depth (MLD), (j) net downward shortwave flux (IPAR) and (k) Iron/Nitrate (Fe/NO_3) ratio.

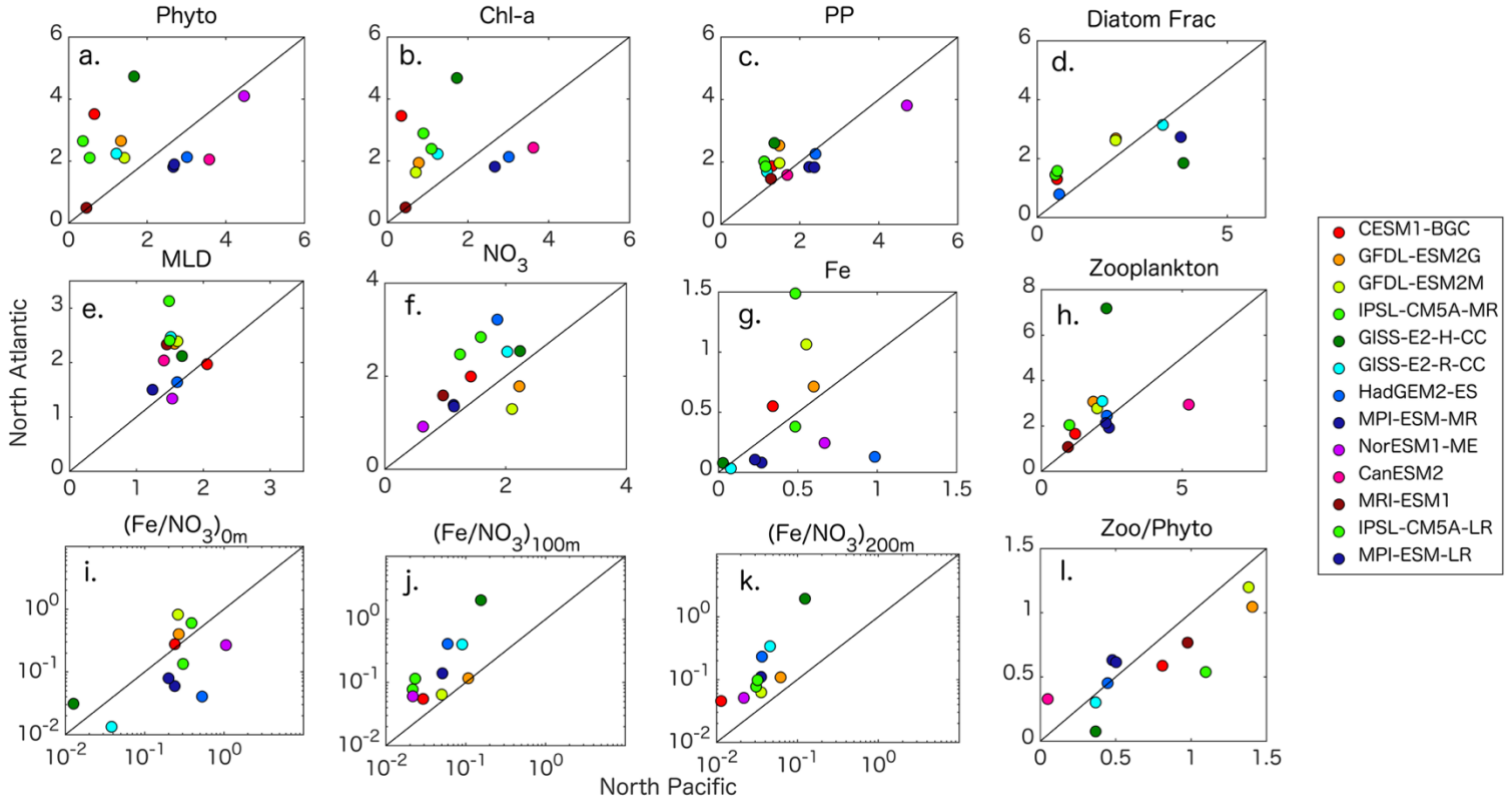

Figure 4.6: Strength of normalized seasonality of ecological and physical variables across CMIP5 models for North Pacific against North Atlantic. Normalized seasonality is the difference between maximum and minimum concentrations over the average cycle. The units for biomass (phyto), primary production (pp), nitrate, iron (fe), zooplankton (zoo), chlorophyll-a (Chl-a), and mixed layer depth (MLD) are mmol/m^{3,} g/yr, mmol/m^{3,} micromole/m^3, mmol/m^{3,} mg/m^3, Einstein/m^2/day, and m, respectively.

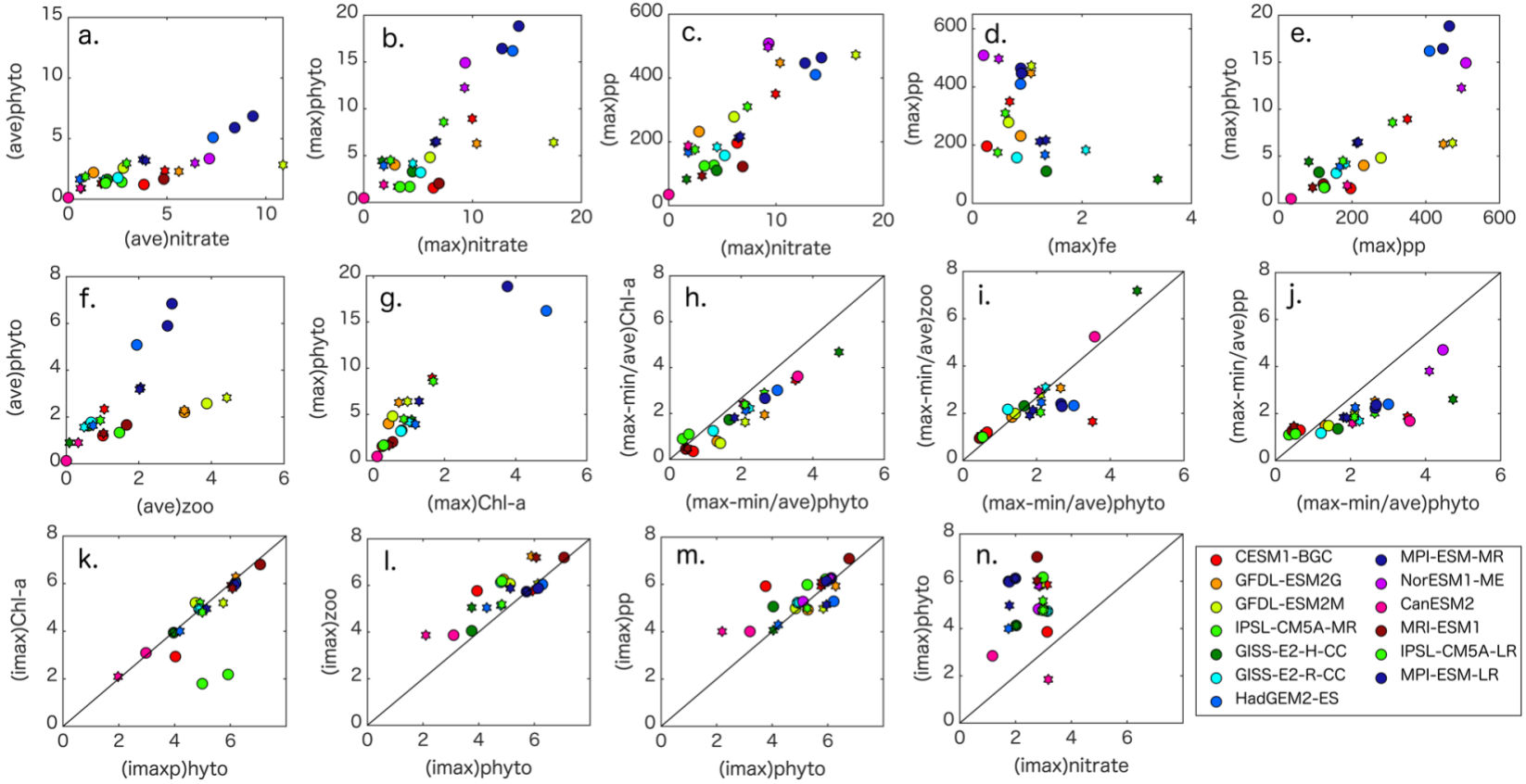

Figure 4.7: Ecological and physical mechanisms in the subpolar box at North Pacific (45-50ºN, 140-150ºW, includes OSP, denoted by colored circles) and North Atlantic (45-50ºN, 25-35ºW, close to NABE, denoted by colored stars using the CMIP5 suites. The abbreviations, 'ave' stands for average, 'max' stands for maximum and 'imax' stands for month of maximum in the variables. The units for biomass (phyto), primary production (pp), nitrate, iron (fe), zooplankton (zoo), chlorophyll-a (Chl-a) are mmol/m^{3,} g/yr, mmol/m^{3,} micromole/m^3, mmol/m^{3,} and mg/m^3, respectively.

CHAPTER 5: Conclusion

Manifested changes due to both natural climate variability and human-induced global warming are not limited to the earth's surface and atmosphere, but also appear strongly in the global ocean system, in ocean physics, biogeochemistry and ecology. Some of the changes and variability observed so far are in the global ocean primary production and in the transport of carbon from the surface to the deep ocean (i.e., the oceanic carbon pump) driven by the ocean phytoplankton in the top layers of the ocean. The warming trend is projected to continue into the 21st century (Solomon et al., 2007; IPCC 2013) and is bound to impact phytoplankton size group structure, growth and organic carbon remineralization (breakdown). Phytoplankton cell size plays a fundamental role in ocean ecology. Therefore, it is critical to understand the link between ocean physics and biogeochemistry and plankton biology and productivity at the ocean surface.

Because of the reduced costs and their global coverage (compared to in-situ measurements), the study of marine ecology and biogeochemical processes via remote sensing and climate models is rapidly evolving. We contribute to the existing literature by investigating the trends, interannual variability and seasonality for critical global ocean biological parameters (e.g., Chl-a, biomass, phytoplankton functional groups) using remote sensing datasets and CMIP5 model outputs over the recent past (1997-2010). In doing so, we seek to investigate the fundamental physical and biogeochemical mechanisms that drive variability in ocean phytoplankton biology both globally and for specific areas of interest (subtropical gyres in Chapter 2, tropical Pacific in Chapter 3, northern hemispheric subpolar biomes in Chapter 4).

5.1 Synopsis

This dissertation mainly examines the novel backscattering-based phytoplankton biomass, PFTs and ocean surface Chl-a over 1997-2010 period. We explored the possibility of existing 13-year trends of phytoplankton biomass and PFTs. One of the major and unexpected findings in chapter 2 was increase in the global phytoplankton biomass, percent micro phytoplankton and percent nanophytoplankton. Approximately 44% of the positive trend in biomass is due to the warm region which is comprised of tropics and subtropics. The global increase in biomass is unexpected given previously reported decreases in Chl-a (previously used as a proxy of biomass) in the warm regions. In chapter 2 we focus on the trends in warm regions, importantly the tropical tongue and subtropical gyres. Previous literature claims that due to ocean surface warming that triggers density contrast (stratification) between the deep and surface ocean water column are the main reasons for the decline in Chl-a and primary production in subtropical gyres (Behrenfeld et al., 2006; Martinez et al 2009) and an expansion of the low Chl-a oligotrophic biome (Polovina et al., 2008; Irwin & Oliver, 2009). Contrary to the previous theory, we report an increase in biomass for all the 5 subtropical gyres over the 1997-2010 period. We do report a decrease in Chl-a in at least three (NPAC, NATL and IOCE) of the subtropical gyres but owing to the enhanced stratification in the water column but the rather physiological response (photoacclimation) of phytoplankton to the light. Biomass increase in subtropical gyres can be ascribed partially to negative heat-flux trends and

stronger winds during winter deepening the active mixing length scale. Therefore, we suggest that Chl-a is not the best indicator for phytoplankton community structure and abundance; instead biomass is a true representation of phytoplankton community structure. The biomass increase in tropical Pacific was mostly driven by the trends in Multivariate ENSO index and not a climate change signal as previously reported by Behrenfeld et al. (2006).

The Tropical Pacific upwelling region is predominantly driven by ENSO, the dominating ocean-atmosphere coupled oscillation on our planet on interannual timescales. The Scientific community has suggested that "No two El Niño events are quite alike" (Wyrtki, 1975) based on their characteristics. ENSO complexity and diversity complicates the ocean biology further in the tropical and global ocean. In Chapter 3 we characterized the uniqueness and differences in different types of ENSO using phytoplankton biomass over 1997-2007. We observe clearly the Central Pacific (CP or Modoki) ENSO, a newly characterized ENSO type fundamentally different from the classical Eastern Pacific ENSO, using various robust statistical techniques. We report physical drivers for biomass and Chl-a similar to those indicated by Radenac et al. (2012) for Chl-a only. During CP El Nino events, changes in the vertical supply of iron concentrations due to the vertical displacement of the Eastern Equatorial Undercurrent (EUC) (Radenac et al., 2012), and the strengthening of the subtropical gyres cause a decline in biomass and Chl-a concentrations. During EP El Nino events, anomalously weak westerly winds drive strong anomalous eastward currents. The nutrient-deprived (less well mixed, deeper nitracline) western warm waters then extend further to 130°W, reducing upwelling and deepening the nitracline and EUC in the central and Eastern Pacific. Reduced surface nutrients reduce the biological activity, lowering the biomass and Chl-a concentrations in central and eastern Pacific. Our empirically-derived biomass index for ENSO flavors is found to be highly correlated with existing climate indices, strongly suggesting that the index can be used to separate the ENSO flavors.

In Chapter 4, seasonality comparison in the biology across various novel satellite-based products and CMIP5 models revealed that North East Pacific subpolar box (NP) around Ocean Station PAPA (OSP) is very different than the equivalent subpolar regime chosen for the North Atlantic (NA). The satellite products are overall consistent in predicting the seasonal cycle at NA but widely different in their predictions of biomass and PFT seasonality at the HNLC region around OSP. We analyze the detailed variability in Chl-a and biomass in 3 current satellite products. The link between large-scale climate modes (PDO and NPGO), vertical mixing of nutrients and phytoplankton ecology is analyzed in the context of previously observed interannual variability at OSP for the 1997-2010 period. CMIP5 Climate models show a large spread in seasonal cycles of nutrients, Chl-a, Biomass and Productivity at both NA and NP. This spread is larger than in the satellite models. The seasonal cycles of phytoplankton biomass, Chl-a and productivity are smaller across the most realistic model set (Group 1) in the NP box compared to the NA box, in agreement with our current understanding of phytoplankton dynamics and most satellite products analyzed in Chapter 4. We ascribe this assessment to tighter grazing control of phytoplankton and less iron supply in the NP.

5.2 Gaps and limitations

Major limitations and gaps for satellite algorithm data were detailed in Chapter 1. One hindrance for the data analyst or high-end climate modeler is the consistent upgrade of a satellite products,

as algorithm developers (e.g. NASA) continue improving their algorithms for accuracy and best results. Developers constantly improve algorithms that commonly change the magnitude of the geophysical variables depending on the mission/objective of the algorithm for specific water bodies (e.g. the OCI R-2014 SeaWiFS algorithm was an upgraded product to improve the Chl-a measurements in clear water). An important caveat we need to acknowledge is that most of the analysis in this dissertation was performed on a coarse resolution data both spatially (monthly 1x1 degree grid) and temporally (monthly data) rather than high resolution data (daily 9km datasets). Some critical biological fluctuations occur at mesoscale/microscale dynamics and range from hours to weeks only, e.g. biology driven by mesoscale eddies. We have not addressed the emerging theory of phytoplankton biology at these smaller temporal and spatial scales in satellite or climate models.

Indeed, data records need to be lengthy and homogeneous to adequately understand the state of the climate trends, natural climate variability and develop statistically robust results. It is equally essential for data to be accurate and/or with, at least, information about its expected accuracy. Reliable detection of trends would require a 20-30 year time series in the tropics and a 40-year time series elsewhere (Henson et al., 2010) and even more than 100 years to measure the ENSO variability accurately (Stevenson et al., 2010). We believe that, although the length of the data is short, the robust statistical analysis of these observational time series allows us to propose new assumptions and mechanisms and allows us to provide robust validation of data against the model results. It is clear that longer time-series are necessary to adequately separate the long-term climate trends from (natural or forced) climate variability. Some statistical work has suggested that reliable detection of climate-driven trends would require a 20-30 year time series in the tropics and a 40-year time series elsewhere (Henson et al., 2010) and more than 100 years to measure the ENSO variability accurately (Stevenson et al., 2010). This timescale would suggest that, while we did find statistically significant trends in ocean biology over the 13-year period of SeaWiFs (1997-2010), these might indeed not be due to climate warming but to some multiannual climate variability. Although the length of the data is short, the robust statistical analysis of these observational time series in this dissertation allows us to propose new assumptions and mechanisms and allows us to provide robust comparison of multiple datasets and against the model results.

In Chapter 5 we discussed possible biological reasons for the large uncertainties in plankton ecology we observe across the latest generation climate models for the subpolar regimes. Biases, gaps and limitations in both satellite datasets and climate models are, however, non-trivial to resolve with in-situ data since in-situ data does not have global spatial and temporal coverage. Limited field measurements or short length of data, and inconsistency of satellite-based datasets often affects the ability of modeling groups to improve biological model parametrizations in the context of complex climate models and decreases model skill. Models are highly susceptible to the parametrization of ecological parameters that have complex functions in the ecosystem e.g. zooplankton grazing (e.g. Hashioka et al. 2013; Everett et al., 2017). This results in vastly different representations of bottom-up (nutrient, temperature/light-driven) versus top-down (grazer) impacts on ocean phytoplankton biomass and productivity across models, as discussed in Chapter 5.

5.3 Future Plans

This dissertation focused on data available from 1997-2010, investigating on extended dataset beyond 2010 would allow us to decipher long-term changes in the phytoplankton biomass and PFTs. What more remains to be investigated is the effect of mesoscale/microscale processes such as horizontal advection, and phytoplankton cellular dynamics on biology, the frequency of different ENSO flavors and their amplitude and their effects on the long-term biomass trend across various product and the difference of the biomass/PFT patterns during the unique ENSO across the multiple products.

It would be interesting to continue the work on the subtropical and tropical oceans (Chapters 2 and 3) by analyzing the ENSO signature in surface biology (as we did for satellite-data) across the historical period up to present in CMIP5 models. Important questions include: (i) What is the biological response to CP El Nino compared to the regular El Nino across CMIP5 models? (ii) Is the calculated ENSO signature (and flavors of ENSO) in surface biology and its implications for ocean productivity be the same across models, satellite-based datasets and in-situ observations? One way that phytoplankton impact the global carbon cycle is via their direct impact on air-sea CO_2 fluxes. Air-sea CO_2fluxes depend on the difference in CO_2 in air and surface seawater. In turn, the CO_2 partial pressure in seawater (spCO_2) is mainly a function of temperature, total CO_2 concentration or dissolved inorganic carbon, alkalinity and salinity of the water. The effects of temperature and total CO_2 on CO_2 are the most important ones in surface water. The total CO_2 in surface waters decreases via phytoplankton photosynthesis and increases via organic matter remineralization.

Following techniques from Takahashi et al. (1993, 2002) and McKinley et al. (2006) we are attempted to separate the observed CO_2 fluxes over the 1997-2010 period into biological and temperature-driven components and understand how much surface ocean CO_2 and resulting air-sea CO_2 fluxes are affected by ocean biology. The results show that at Ocean Station PAPA in the North East Pacific, there is an almost perfect compensation between the biological and temperature-driven seasonal cycles of CO_2 (Figure 5.1). During spring and summer blooms, phytoplankton act to reduce strongly CO_2 via photosynthetic uptake, while warmer temperatures affect the solubility of gases, increasing CO_2. The opposite patterns are observed during wintertime when the system is dominated by respiration/remineralization. The current work in this direction is inspired by the recent paper of Fay et al. (2017), who focused on the observed correlations between CO_2 and satellite-based Chl-a. With the new products presented in Chapter 4, we can expand their work to multiple biomass products and CO_2-biomass carbon correlations. As expected, the preliminary results show that CO_2 and its seasonal cycle depend mostly on temperature in the low latitudes but depend strongly on biology (as reflected by the phytoplankton biomass) in the high latitude, including subpolar regimes (Figure 5.).

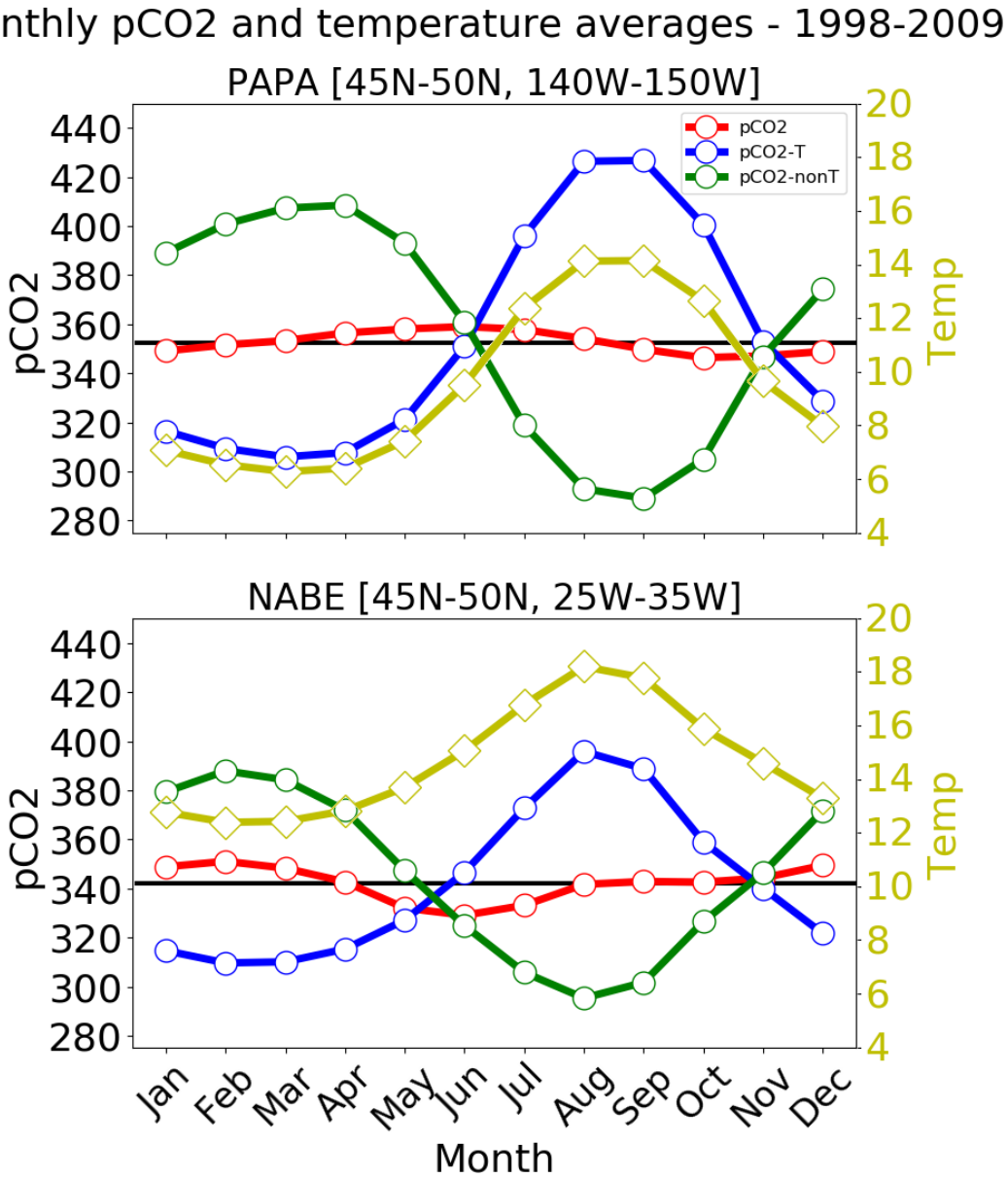

Figure 5.1 Ocean temperature, total surface pCO_2 and the two pCO_2 components driven by temperature and biology at (top) OSP in the NP box, (bottom) in the NA box. Note an almost perfect compensation between the biological and temperature-driven seasonal cycles of pCO_2. Separation of pCO_2 based on McKinley et al. (2006). pCO_2 data is based on CDIAC dataset

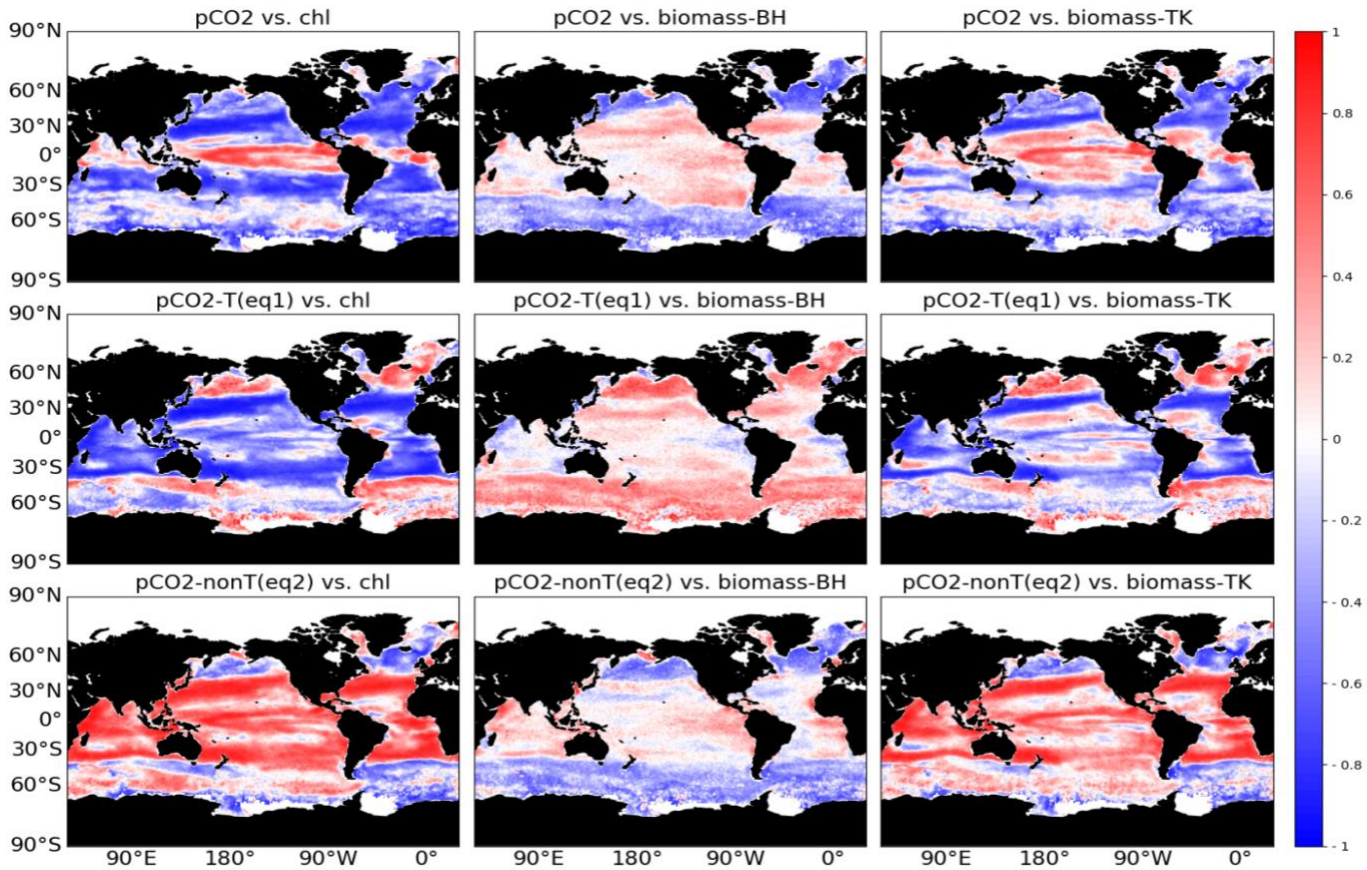

Figure 5.2: Temporal correlations between monthly pCO2, pCO2 with temperature effect and pCO2 without temperature effect (biology) with Chl-a (first column), B05 biomass (second column), and TK16 biomass (last column).

APPENDIX A: Supporting Information for Increasing biomass in the global warm oceans: Unexpected new insights from SeaWiFS

Submitted for publication as:

Sharma, P., Marinov, Cabre, A., Kostadinov T.S. and Singh A., (*GRL: Accepted*) Biomass of phytoplankton is not decreasing in low latitude oceans: new insights
from SeaWiFS

A.1 Introduction

We provide the information on the data and methods used in this paper (A.2), calculation of the active mixing length scales, L_{MIX} (A.3) trends calculation (A.4) and error analysis of linear trends on biomass and PFTs (A.5).

We present also (1) spatial distribution of the biomes (Figure A1), (2) one figure (Figure A2) to show the mean distribution of the biological variables, (3) spatial maps of Non-ENSO trend and ENSO trend (Figure A3 and Figure A4) to support Figure 2.1 (3) spatial trend maps for the winter months for the variables (Figure A5), and 3 more additional Figures (Figure A7, A8, A9, A10, A11 and A12) to support section 2.5 and section 2.6 in Chapter 2, (4) an additional figure (Figure A13) to support the error analysis results shown in Table A.3 & A.4, (5) a Table (Table A.1) to support Section 2.3, (6) an additional table (Table A2) to summarize the Figure 2.2 and (7) the trends table (Table A3 & A4) for the gyres to support section 2.5 and 2.6.

A.2. Data and Methods

We use the total and size-partitioned biomass (mg/m^3) and PFTs [pico-phytoplankton (0.5–2 µm in equivalent spherical diameter), nano-phytoplankton (2–20 µm) and micro-phytoplankton (20–50 µm)] product derived from a backscattering-based particle size distribution (PSD) algorithm (Kostadinov et al., 2009, 2010, 2016) for the period 1997-2010. The PSD algorithm uses the magnitude and spectral slope of the backscattering coefficient to retrieve the parameters of an assumed power-law PSD. Using the PSD parameters, the volume concentrations for three different size classes are calculated. The biovolumes are then converted to carbon concentrations using existing allometric relationships (Menden-Deuer & Lessard, 2000). We express PFT fractions in percentage. The Kostadinov et al. (2016) phytoplankton products are available at https://doi.pangaea.de/10.1594/PANGAEA.859005.

The global monthly 9 km composites of SeaWiFS Chl-a concentration (derived from the Ocean Color Index (OCI) algorithm), photosynthetically available radiation (PAR), diffuse attenuation coefficient for downwelling irradiance at 490 nm (Kd_{490}), and particulate inorganic carbon (PIC) from SeaWiFS (2014 reprocessing), were obtained from NASA's Ocean Color Web (http://oceancolor.gsfc.nasa.gov) for the years 1997-2010. Chl-a and PIC are expressed in mgm^{-3}; PAR and Kd_{490} in Einstein m^{-2} day^{-1} and m^{-1}, respectively. The 9 km gridded data was down-

sampled to a 1° resolution using with an averaging kernel. If >50% of the pixels being averaged were invalid data, the pixel in the down-sampled image was assigned a missing data value.

5-day gridded temperature, salinity and density profiles on a global 0.5° grid were used from the Simple Ocean Data Assimilation (SODA) model (soda.tamu.edu, (Carton, et al., 2000; Carton & Giese, 2008) to calculate mixed-layer depth (MLD), using a critical potential density threshold of 0.03 kg m^{-3} relative to 10 meters (de Boyer Montégut et al, 2004). Prior to any calculations, the 5-day data were converted to monthly averages.

We calculated the photoacclimation parameter, which approximates Chl/C, following Eq. S10 in Behrenfeld et al. (2016) using the above MLD, PAR and K_d parameters:

$$\mathrm{Chl}/\mathrm{C}_{B\prime 16} = Chl{:}C = \frac{1+e^{-0.15\,PAR}}{1+e^{-3I_{ML}}}, \text{ where } I_{ML} = PAR \times e^{-0.5\,Kd \times MLD} \qquad \text{[Eq. A1]}$$

We also estimated Chl/C using the SeaWiFS Chl-a and Kostadinov et al. (2016) biomass. However, we chose to use the photoacclimation parameter estimated using Behrenfeld et al. (2016) model because $\mathrm{Chl}/C_{B\prime 16}$ was independent of any observed Chl-a input and biomass. $\mathrm{Chl}/C_{B\prime 16}$ showed robust trends over this period (Table A1) which have the same sign in each gyre with those of Chl; this supports our hypothesis that photoacclimation, rather than biomass, explains the trend in SeaWiFS Chl-a.

The global monthly 4km Advanced Very High Resolution Radiometer (AVHRR) satellite-derived sea surface temperature (SST) imagery was obtained from the NASA Physical Oceanography Distributed Active Archive Center (PO.DAAC, http://podaac.jpl.nasa.gov/AVHRR-Pathfinder) for 1997-2009. We further used 13-year (1997-2009) monthly 1° gridded time series of surface ocean heat flux (Wm^{-2}) obtained from Objectively Analyzed air-sea Fluxes (OAFlux) project via http://oaflux.whoi.edu/data.html. The time series for SST and surface ocean heat flux was only available until 2009. We chose to use AVHRR and OAFLUX, since it was one of the most cited products. Daily 10 m wind data on a 1° horizontal grid from the ERA–Interim Reanalysis (http://www.ecmwf.int/, (Berrisford et al., 2011) was converted to monthly data. The active mixing length depth (L_{MIX}), which estimates the depth to which phytoplankton is mixed, was derived using the surface heat flux, wind speed and seawater density as in Brody and Lozier (2014, 2015), see Text S2. Global monthly surface partial pressure of carbon dioxide ($spCO_2$) on a 1° grid was obtained from the Carbon Dioxide Information Analysis Center (CDIAC, http://cdiac.ornl.gov/) (Takahashi et al., 2009). The Multivariate El Niño Southern Oscillation Index (MEI) was acquired from the climate data guide portal provided by National Center for Atmospheric Research (NCAR) at https://climatedataguide.ucar.edu/. The monthly MEI (Wolter & Timlin, 1993) is defined as the first seasonally varying principal component of six atmosphere–ocean variable fields in the tropical Pacific basin (i.e. sea level pressure, zonal and meridional wind speed, sea surface and air temperatures, and total cloudiness).

We define our warm region where the 1997-2009 averaged SST > 15ºC (that includes tropical and subtropical biomes). The tropical Pacific and the five subtropical gyres are defined monthly using criteria adapted from Cabré et al. (2016), based on monthly Chl-a concentration level, phytoplankton size composition, and geographic constraints (biomes shown in Figure S1). The tropical Pacific tongue comprises the Pacific region where the average Chl-a is greater than 0.11 mgm^{-3}. The subtropical gyres are pico-phytoplankton dominated regions with Chl-a lower than 0.11 mgm^{-3}, where biomass seasonal reproducibility is less than 30% (Cabré et al., 2016) with latitude

[0^0<Latitude<30^0] and ocean basin restrictions. We chose to focus mainly on the warm regions because our preliminary studies show very weak interannual correlations between physical variables and biological variables in cold regions in comparison to warm regions.

The anomalies we present are always relative to the 1998-2010 mean seasonal cycle. Since biomass, Chl-a, and PIC are log-normally distributed and the magnitude of biological indices can span up to 3 orders of magnitude (Racault et al., 2016), their trends are calculated in log space. Note that we have removed the seasonal cycle from all the data when calculating trends and correlations (Figure 2.1, Figure 2.2). All correlations between biomass and physical indices are much stronger when the seasonal cycle is not removed.

A.3 Active mixing length scales calculations

Derivation of the mixing length scale follows developments by Brody and Lozier (2014, 2015). Active mixing length scale, $L_{MIX,}$ was defined for three cases. When the heat flux is large and negative (Case 1), the mechanism that drives surface mixing is convective mixing, which is generated by surface ocean cooling. Hence, the L_{MIX} in Case 1 is represented by the seasonal thermocline (MLD). During a small negative or positive heat flux under moderate or large winds (Case 2), the wind generated mixing is greater than the convective mixing. The L_{MIX} in Case 2 is represented by the Ekman length scale (L_{EK}), which is directly related to wind speed. When heat flux into the ocean is large and positive (Case 3), stratification counteracts the wind generated mixing. In this case, L_{MIX} is estimated by the Ozmidov length scale $L_{OZ} = (2\pi)\epsilon^{\frac{1}{2}} N^{\frac{-3}{2}}$, where ϵ is the turbulent kinetic energy dissipation and N^2 is the buoyancy frequency. L_{OZ} estimates the vertical scale of turbulent overturning in a stratified fluid. The buoyancy frequency parameter (N^2) is calculated using the Gibbs Sea Water (GSW) toolbox from the Thermodynamic Equation of Seawater – 2010 (TEOS10) software, where density is from SODA model. The switch between the three mixing length scales (depths) or cases is characterized by the relative strength of local buoyancy (determined by Obukhov length L_{OB}), which is directly proportional to wind forcing and inversely proportional to the heat flux (see Brody & Lozier, (2014, 2015)), such that if $|L_{OB}|$ is small wind mixing only affects the upper part of the ocean (Case 1 and Case 3) and if $|L_{OB}|$ is large wind forcing dominates (Case 2). For the 5 subtropical gyres, the percentage of pixels in a given subtropical gyre that are classified as Case1, Case2, and Case 3 for each month during 1997-2010 period are calculated and shown in Figure 3 (for IOCE), Figure A6-A7.

A.4 Trend Calculations.

We performed generalized least square (GLS) and ordinary least square (OLS) regression on all the variables. OLS tends to underestimate the variance because it ignores the auto-correlation between successive observations, and therefore inflates the test statistics on the regression coefficients (e.g. Wunsch, 1999; Beaulieu et al., 2013). We find that GLS errors approximately double the OLS ones. To account for 1-sigma intrinsic error in the estimation of trends in the PFTs and lognormal biomass, a Monte Carlo simulation was performed across biomes (A.5). The trend uncertainty when including algorithm uncertainty in our estimates of biomass and PFTs fractions is very similar to the trend uncertainty obtained when ignoring the algorithm uncertainty (Figure A13). Therefore, we conclude that we can safely ignore the 1-sigma intrinsic error bars in our data as the uncertainty due to assuming a linear regression model dominates the uncertainty in the data itself.

Many of the individual pixel trends were not very insignificant at 95% confidence interval, while statistically meaningful trends were found at 68% confidence interval (p-value < 0.3).

We separated the overall trend due to the ENSO and Non-ENSO by preforming multivariate analysis on biomass:

$$Var_{x,y}(t) = \alpha_{x,t}.t + \beta_{x,y}.MEI(t) + \xi_{x,y} \qquad \text{[Eq. A2]}$$

We regress the biomass anomalies with MEI and time. Then we compute the trends on the terms constructed above using the gradients (α, β, ξ), where $\alpha_{x,t}.t$ is the Non-ENSO term, $\beta_{x,y}.MEI(t)$ is the ENSO term, and $\xi_{x,y}$ is the residuals. We perform the GLS trend on the Non-ENSO term and ENSO term. We find that the trends in ENSO term is strongly positive in the tropics for the biomass and weakly negative in the subtropics. On the other hand, the trends in Non-ENSO term show weak positive trends in the tropical tongue, and positive trends in subtropics at 68% confidence interval.

We calculate the percentage contribution of the trends in the tropical and subtropical regions that explains the biomass trends of the warm region as follows:

$$\text{Percentage Contribution of trends by Tropical Tongue} = \frac{Area_{\frac{TROPICAL\ TONGUE}{WARM}} \times Trend_{TROPICAL\ TONGUE}}{\text{Trend}_{\text{WARM}}} \times 100 \qquad \text{[Eq. A3]}$$

where $Area_{\frac{WARM}{GLOBAL}}$ is the fractional area of the warm region, etc. Using Eq. A4 the percentage Contribution of trends by subtropics was calculated. We also calculate the percentage contribution of the trends in the warm and cold regions that explains the global biomass trends using:

$$\text{Trend}_{\text{GLOBAL}} \sim Area_{\frac{WARM}{GLOBAL}} \times Trend_{WARM} + Area_{\frac{COLD\ NH}{GLOBAL}} \times Trend_{COLD\ NH} + Area_{\frac{COLD\ SH}{GLOBAL}} \times Trend_{COLD\ SH}$$

$$\text{Percentage Contribution of trends by warm region} = \frac{Area_{\frac{WARM}{GLOBAL}} \times Trend_{WARM}}{\text{Trend}_{\text{GLOBAL}}} \times 100$$

[Eq. A4]

$$\text{Percentage Contribution of trends by cold region} = \frac{Area_{\frac{COLD\ SH}{GLOBAL}} \times Trend_{GLOBAL}}{\text{Trend}_{\text{GLOBAL}}} \times 100$$

Using numbers from Table A1, we can show that the warm and cold SH regions individually explain 44% and 46% of the global biomass increase, respectively. Note all the observations within the biomes were used to calculate the trends.

A.5 Error analysis of phytoplankton biomass and PFTs linear trends

Long-term linear trends in the anomalies (seasonal cycle removed) are estimated by fitting a generalized least square (GLS) regression model to PFTs fractions, and to the decimal logarithms of biomass and Chl-a (as a function of time). First, the GLS trend (and its standard deviation) is estimated when data are assumed to have no error bars. In this case, the trend standard deviation is a direct indication of the model fitness (standard deviation decreases as the model, in this case a line, reproduces better the observed data). However, the Kostadinov et al. (2016) products (biomass, PFT fractions) were provided with per-pixel uncertainty estimates (given as the standard deviation, 1σ) propagated from uncertainty estimates for the PSD parameters. To account for this error in the estimation of GLS trends in the PFTs and log-normal biomass, a Monte Carlo simulation was performed across biomes, as follows. For the biomass and PFTs time series, a realization that mimics a real observation (for each month and grid point) is obtained by adding a random number generated from a Gaussian distribution with mean zero and sigma equal to the intrinsic error value Kostadinov et al. (2016). Negative (or zero) biomass values were replaced with a very small number (e.g., $1e^{-12}$) before taking the logarithm of phytoplankton biomass. We then proceeded to analyze each realization as a real observation. First, we took the logarithm for the biomass time series, then subtracted the log seasonal cycle, and finally calculated the area-weighted average of all the anomalies in each biome, where a GLS regression was fitted for the simulated time-series to obtain the slope (trend). The procedure was repeated 10000 times and the standard deviation in the slopes accounted for the error in the realizations. Figure A13 illustrates the results when including (or excluding) 1-sigma intrinsic error bars in the calculation of trends. We show that the uncertainty in trends that we obtain when including 1-sigma intrinsic errors is very similar to the uncertainty obtained ignoring the intrinsic errors, for different PFTs and in different biomes. Because the error due to assuming a linear model is larger than the intrinsic error of the measurement (Figure A.13), we conclude that we can safely ignore the intrinsic errors. We performed the same steps as above for Monte Carlo simulations on ordinary least square (OLS) regression.

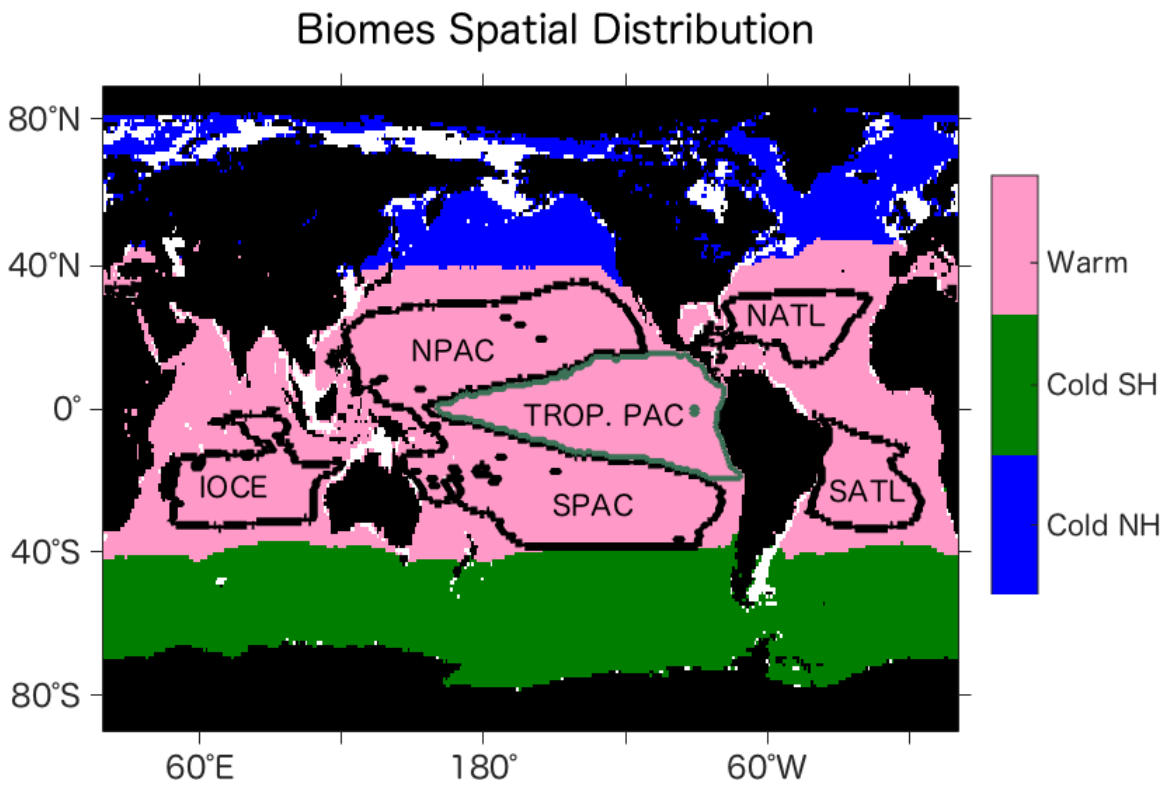

Figure A1: Spatial distribution of the biomes as defined in Text S1. Boundaries of the five geographical regions considered in the present analysis. The tropical Pacific cold tongue is shown in green contour line. The five subtropical oligotrophic gyres (North Pacific gyre (NPAC), South Pacific gyre (SPAC), Indian Ocean gyre (IOCE), North Atlantic gyre (NATL) and South Atlantic gyre (SATL) are delineated with black lines; boundaries are after Cabre et al. (2016). The global ocean is split into three sub-regions, namely Warm Ocean (pink, >15ºC average SST over 1997-2009), Northern Hemisphere Cold Ocean (blue) and Southern Hemisphere Cold Ocean (green). The data along the coastal ocean is not included in our analysis.

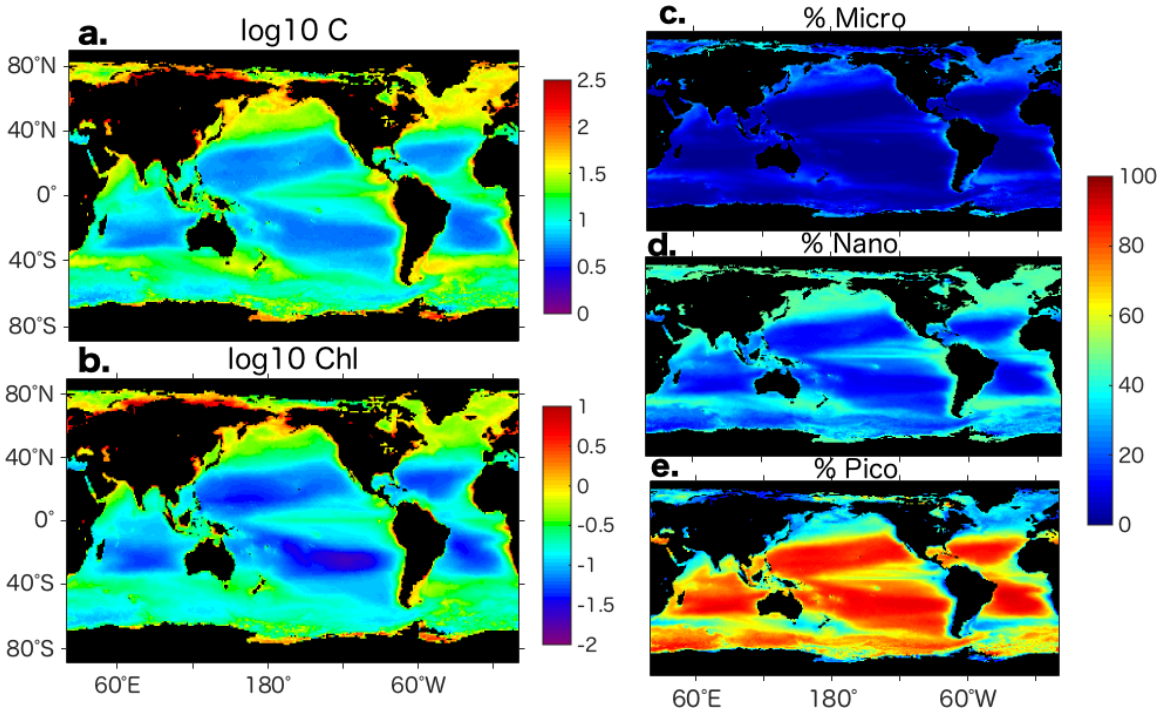

Figure A2: Global maps of (a) log decimal phytoplankton biomass (mgm^{-3}), (b) log decimal chlorophyll concentration (mgm^{-3}), (c) percentage micro-phytoplankton, (d) percentage nano-phytoplankton, (e) percentage pico-phytoplankton. Composites are based on the SeaWiFS period (September 1997–December 2010).

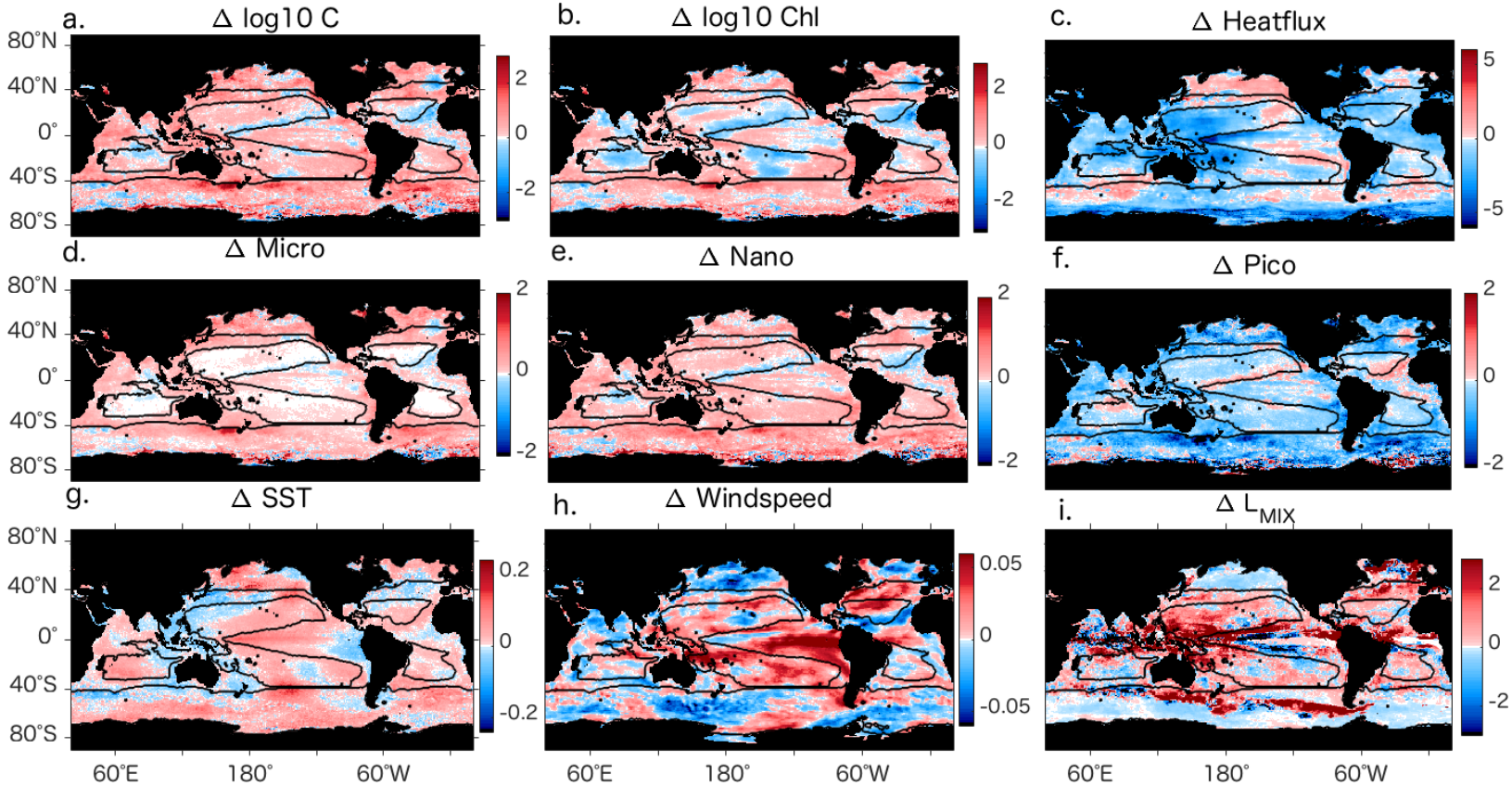

Figure A3: Non-ENSO trends for deseasonalised monthly anomalies of SeaWiFS-derived (a) phytoplankton biomass concentration, (b) Chl-a concentration, (d) fraction micro-phytoplankton, (e) fraction nano-phytoplankton, and (f) fraction pico-phytoplankton, all in $\%y^{-1}$. Linear trends in (c) heatflux ($Wm^{-2}\ y^{-1}$), (g) SST ($^{o}Cy^{-1}$), (h) windspeed ($ms^{-1}\ y^{-1}$) and (i) L_{MIX} (my^{-1}). All trends are for the 1997-2010 period and were calculated using GLS regression. Pixels with statistically insignificant trends at the 68% confidence level (p-value>0.3) are hatched. NB, in this figure all the pixels are significant at 68% confidence level. Biomes are (Figure A1) delimited by black contours.

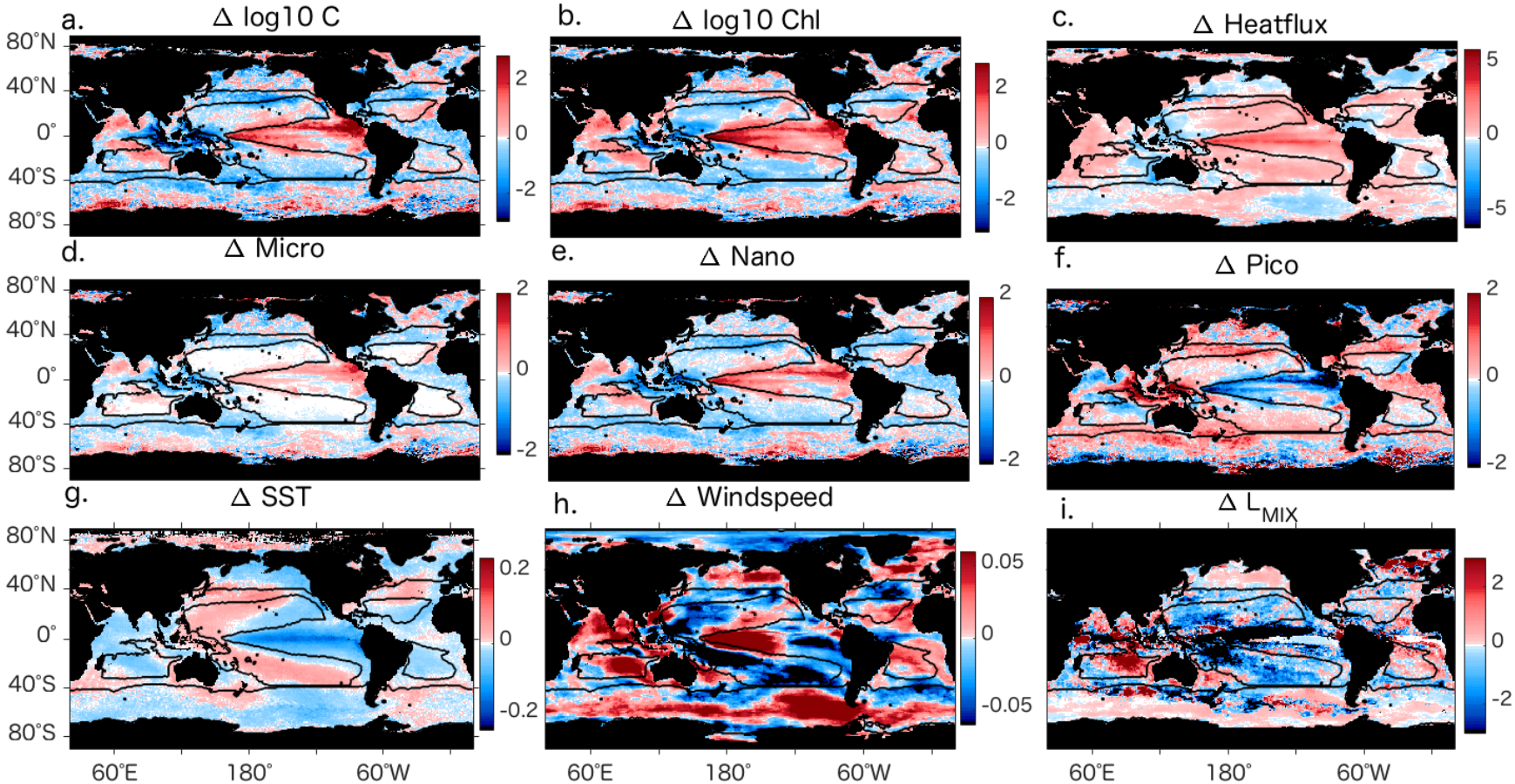

Figure A4: ENSO trends for deseasonalised monthly anomalies of SeaWiFS-derived (a) phytoplankton biomass concentration, (b) Chl-a concentration, (d) fraction micro-phytoplankton, (e) fraction nano-phytoplankton, and (f) fraction pico-phytoplankton, all in $\%y^{-1}$. Linear trends in (c) heatflux ($Wm^{-2}\ y^{-1}$), (g) SST ($^{o}Cy^{-1}$), (h) windspeed ($ms^{-1}\ y^{-1}$) and (i) L_{MIX} (my^{-1}). All trends are for the 1997-2010 period and were calculated using GLS regression. Pixels with statistically insignificant trends at the 68% confidence level (p-value>0.3) are hatched. NB, in this figure all the pixels are significant at 68% confidence level. Biomes are (Figure A1) delimited by black contours.

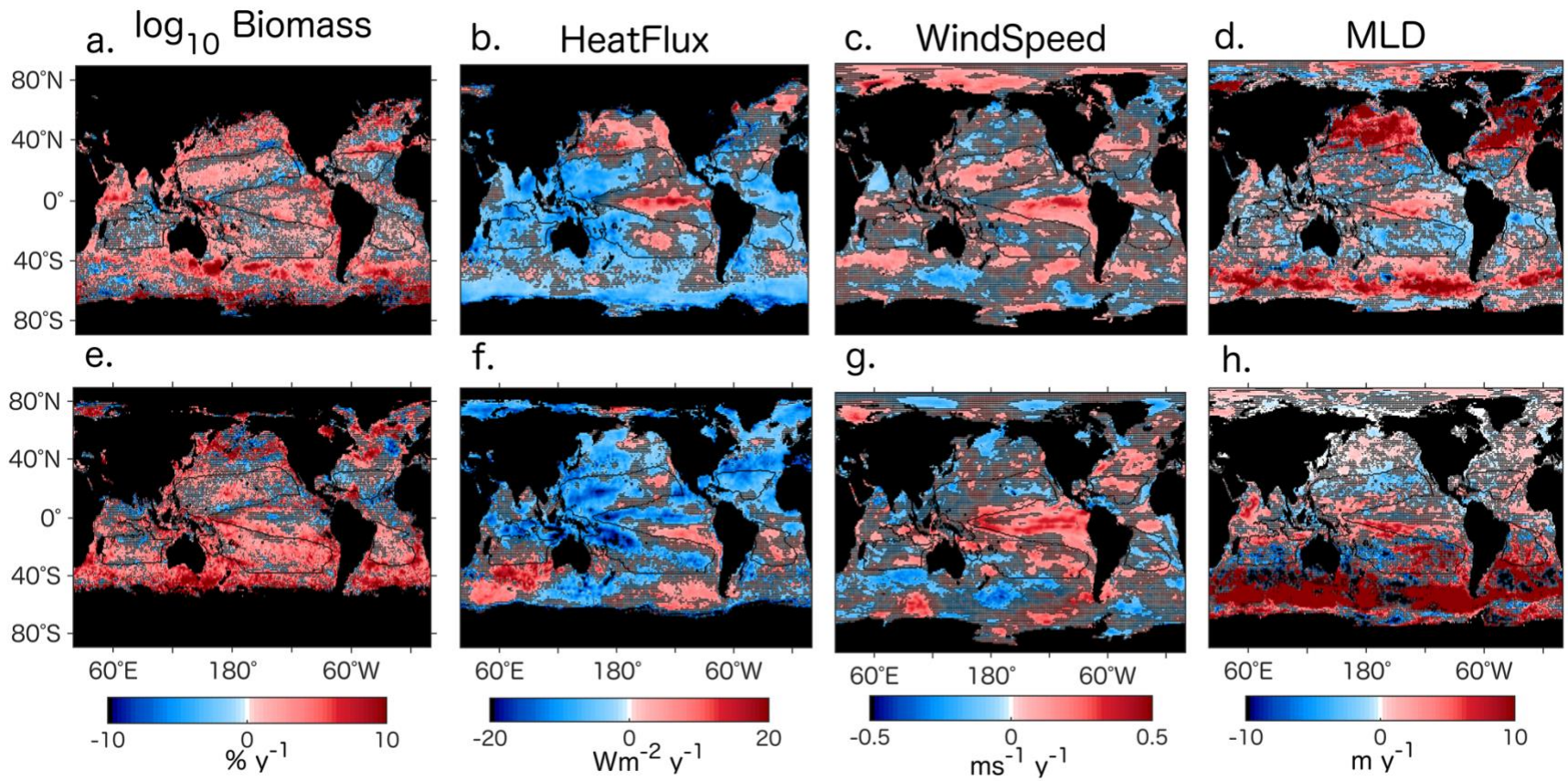

Figure A5: GLS trends for deseasonalised monthly anomalies of SeaWiFS-derived (a, e) phytoplankton biomass concentration, (b, f) heatflux, (c, g) windspeed, and (d, h) MLD for Northern Hemisphere winter months – JFMA (top panel, a-d) and Southern Hemisphere winter months (MJJA) for the 1997-2010 period (bottom panel, e-h). The pixels with no statistically significant trends at the 68% confidence level (p-value>0.3) are hatched. The subtropical gyres (Figure A1) are delimited by black contours.

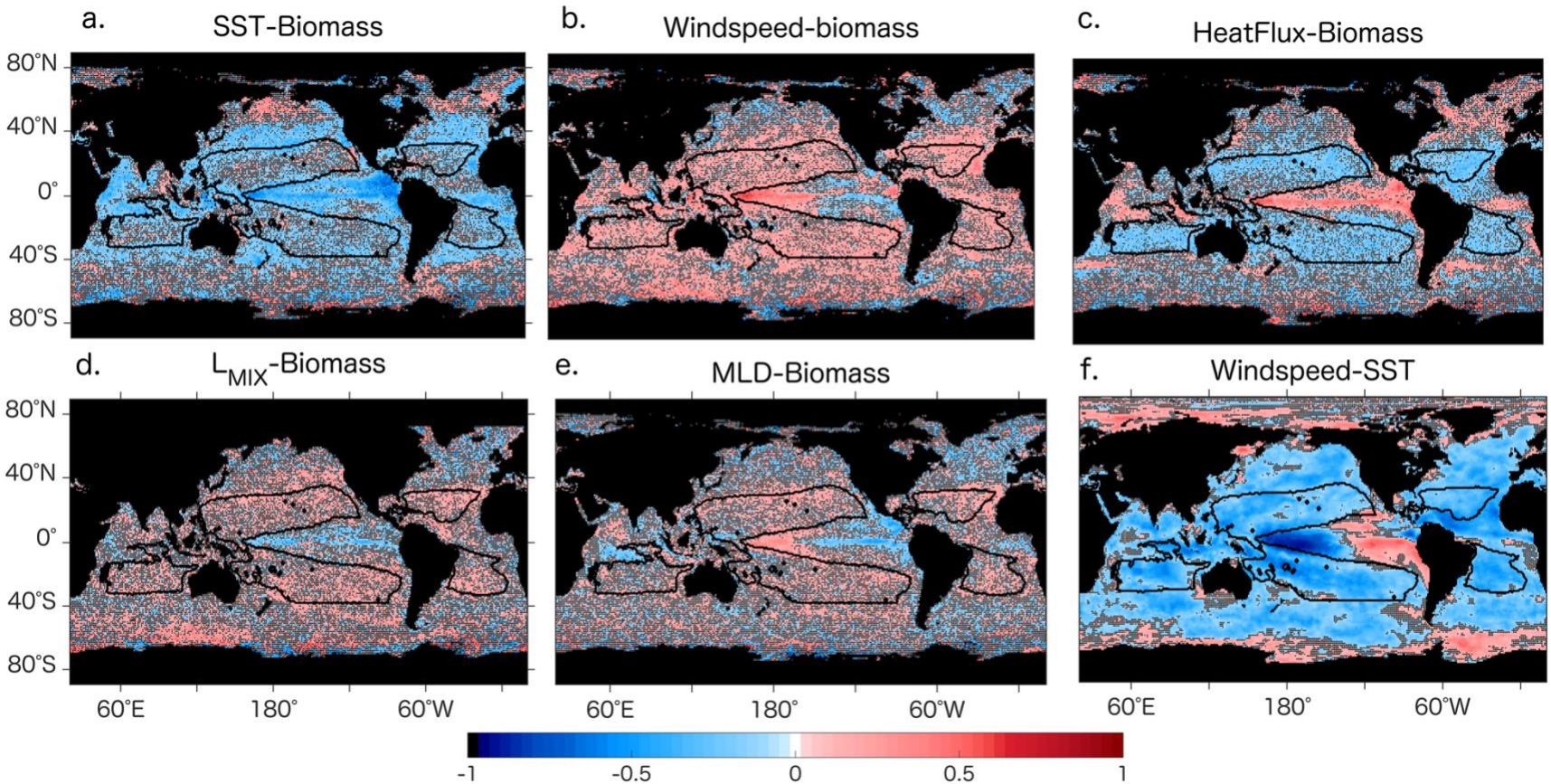

Figure A6. Temporal correlations between deseasonalized monthly anomalies of the (a) $\log_{10}$ of phytoplankton biomass and SST, (b) wind speed, (c) heatflux, (d) L_{MIX}, and (e) MLD for the 1997–2010 period. (f) Temporal correlation of deseasonalized wind speed and SST anomalies. Note: Long-term trend is removed. Blue-red colors represent correlations statistically significant at the 68% level ($p < 0.3$); non-significant correlations are hatched. The subtropical gyres (Figure A1) are delimited by black contours.

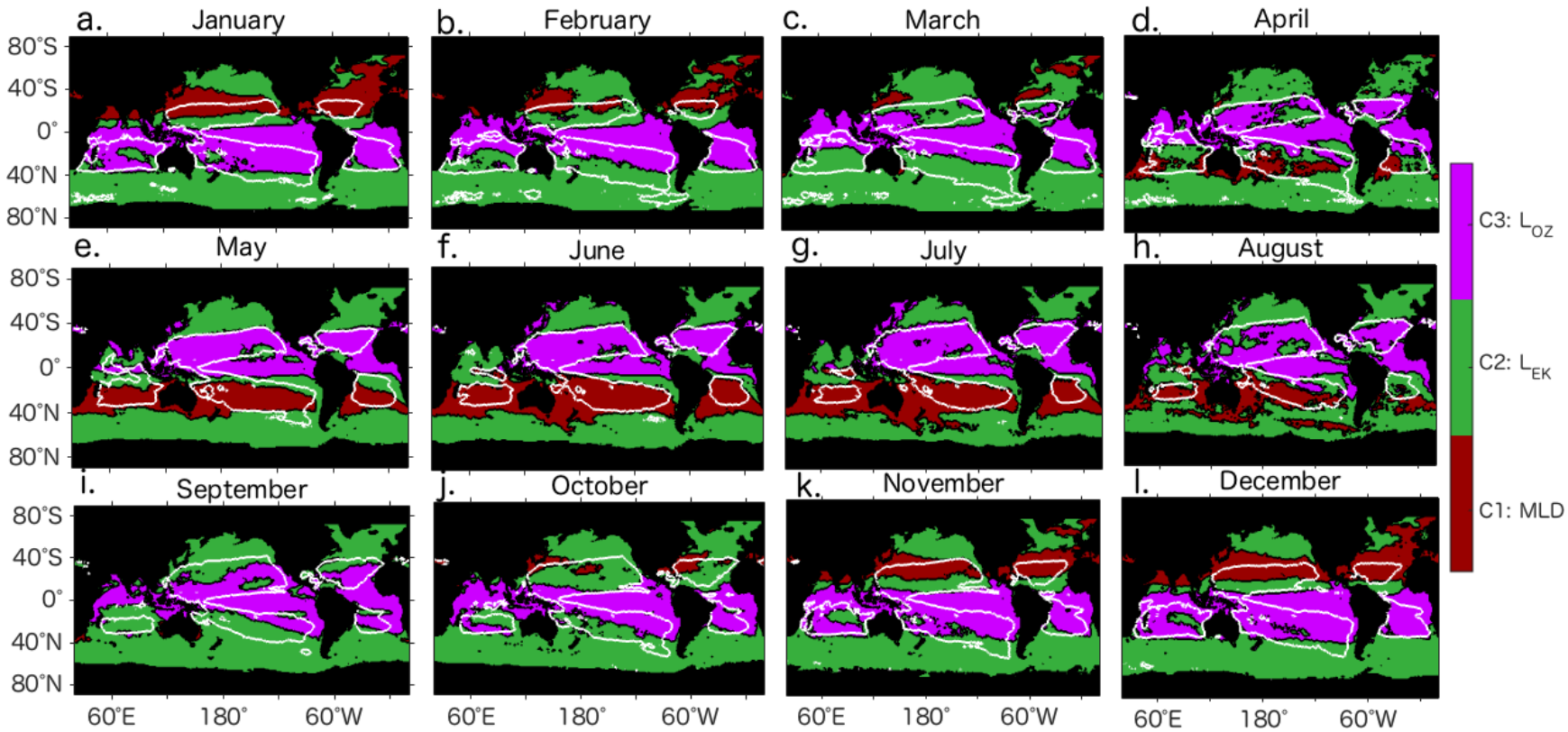

Figure A7: The classification of the phytoplankton active mixing length scale (LMIX) as Case 1 (red, L_{MIX}=MLD), Case 2 (green, L_{MIX}=L_{EK}), or Case 3 (purple, L_{MIX}=L_{OZ}) using the criteria from Brody et al (2014) for a 1x1 degree grid. For each pixel, the Case with the highest percentage occurrence (out of the 3 possible Cases) across all 1997-2010 January's was chosen to represent January, etc. The subtropical gyres (Figure S1) are delimited by white contours.

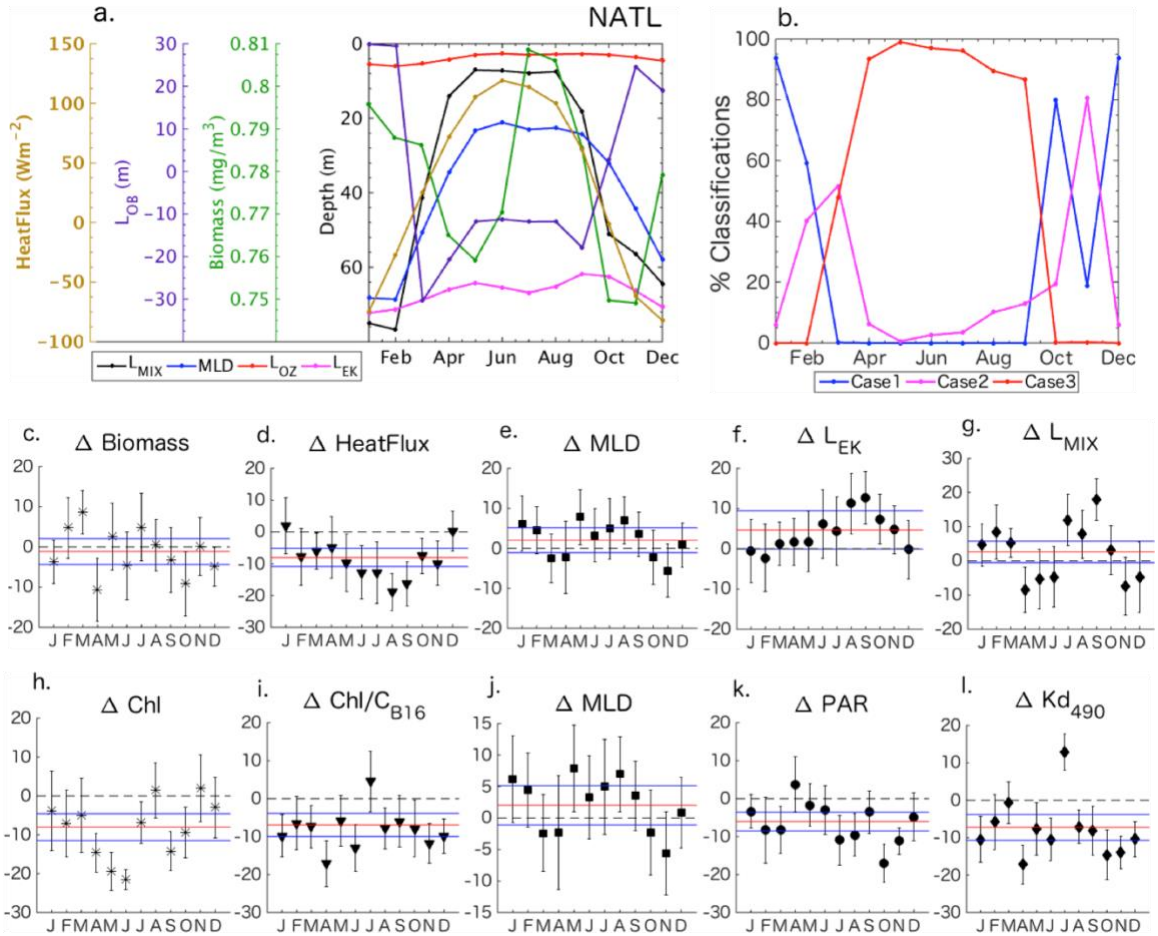

Figure A8: (a) 1997-2010 averaged monthly climatology for L_{MIX} depth measurements for the North Atlantic Gyre (NATL) with mixing depth measurements derived for all the cases 1 (MLD), 2 (L_{EK}), and 3 (L_{OZ}) from surface atmospheric forcing's. Log_{10} phytoplankton Biomass and surface heatflux averaged monthly values are in green and gold. (b) 1997-2010 averaged monthly climatology for percentage of pixels in the gyre that are classified as Case 1, 2, or 3 mixing. (c) Percentage change/Trends in all the months through 1997-2010 in the NATL for the biome-averaged (c) Biomass, (d) Heatflux, (e) MLD, (f) L_{EK}, and (g) L_{MIX}, (h) Chl-a, (i) Chl/C_{B16}, (j) MLD, (k) PAR, (l) Kd_{490}. The red line is the total percentage change of biomass over the 1997-2010 period and the blue line is the +/- one-sigma error associated with the total percentage change of biomass. The black dashed line is the zero line. Error bars crossing zero line indicates that the trends are insignificant at one sigma (or 68% confidence interval, p-value<0.3).

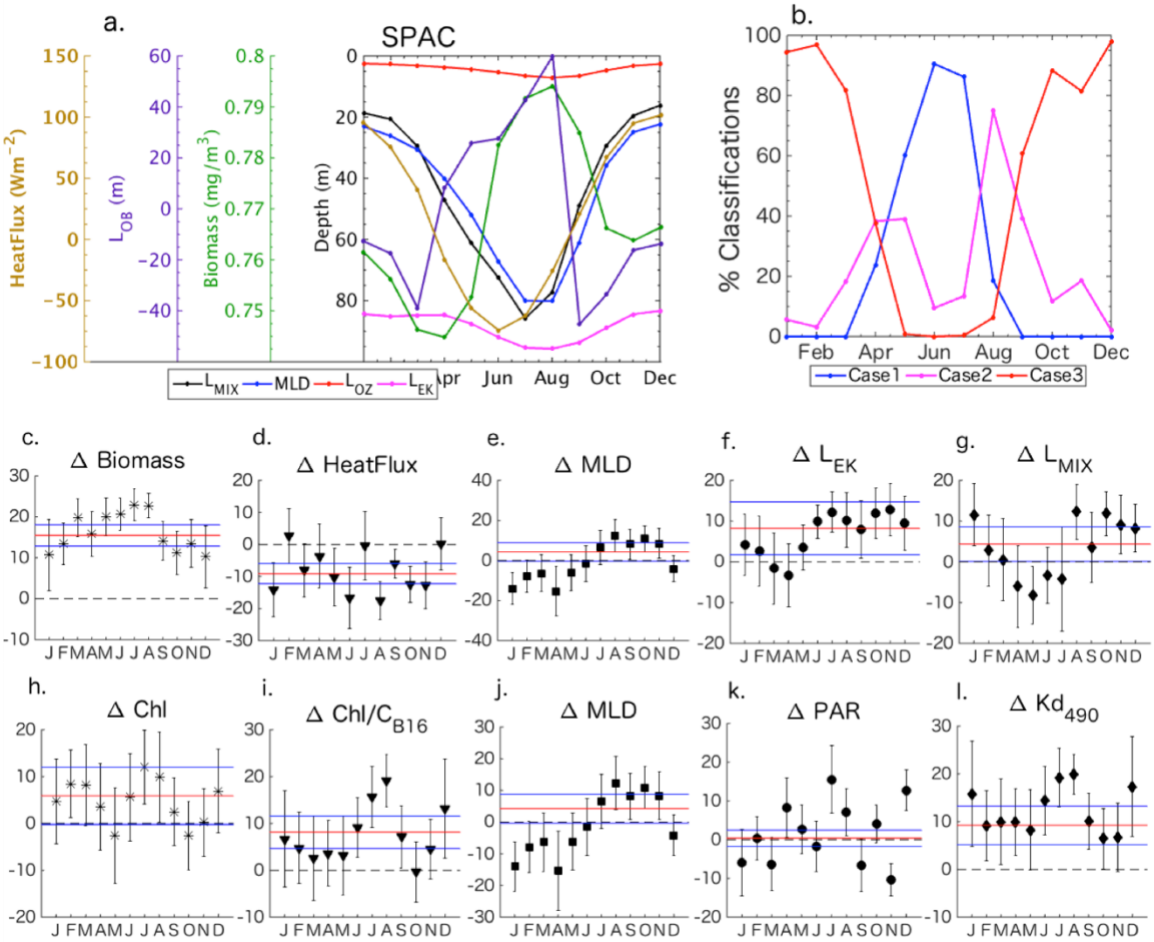

Figure A9: Same as Figure A8 except for South Pacific Gyre (SPAC)

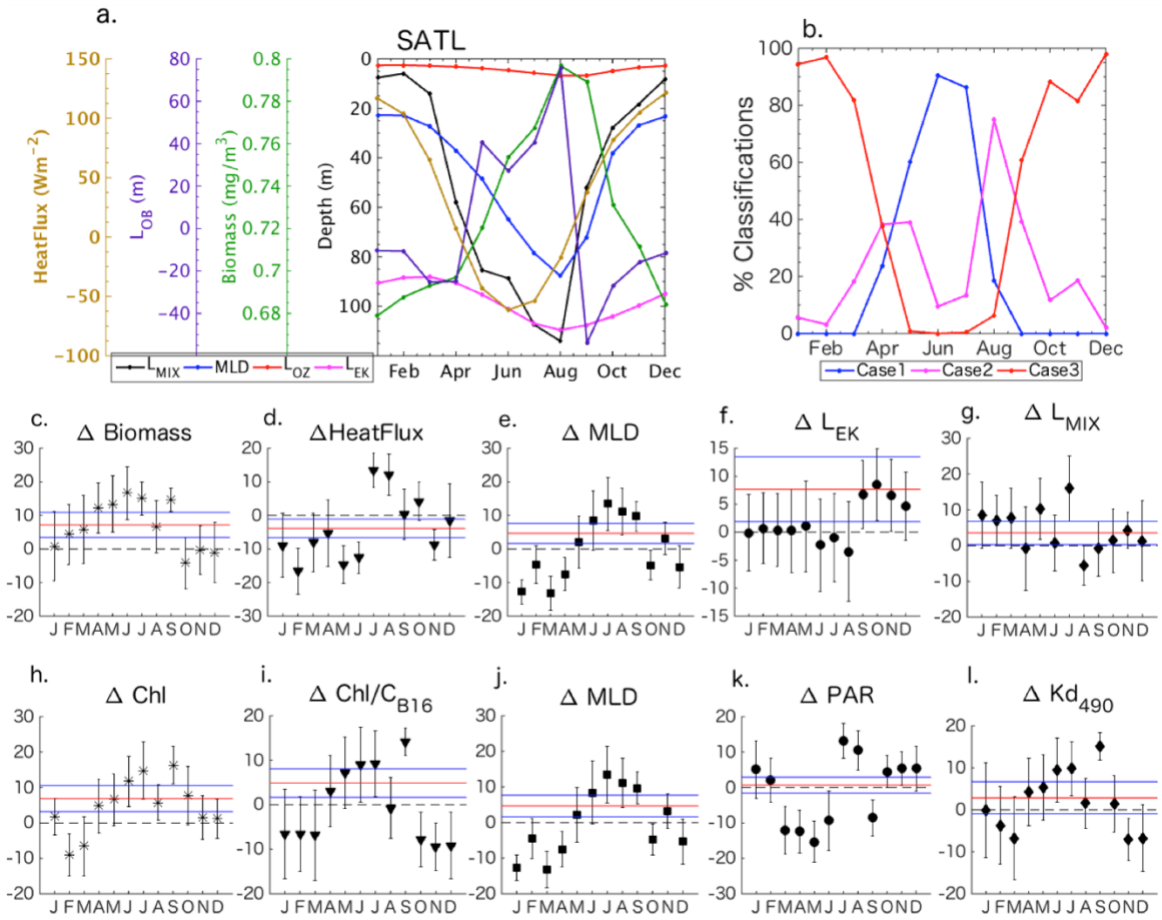

Figure A10: Same as Figure A8 except for South Atlantic Gyre (SATL)

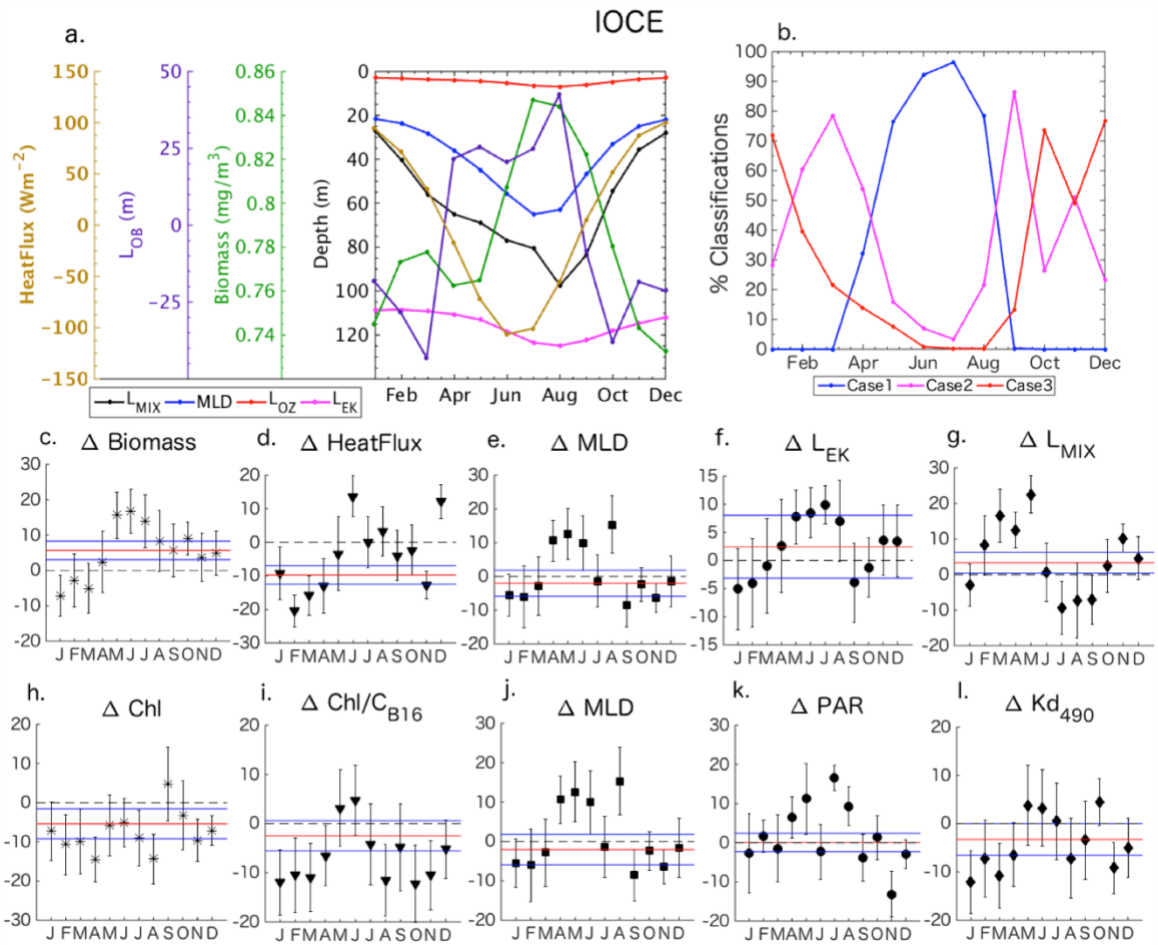

Figure A11: Same as Figure A8 except for Indian Gyre (IOCE)

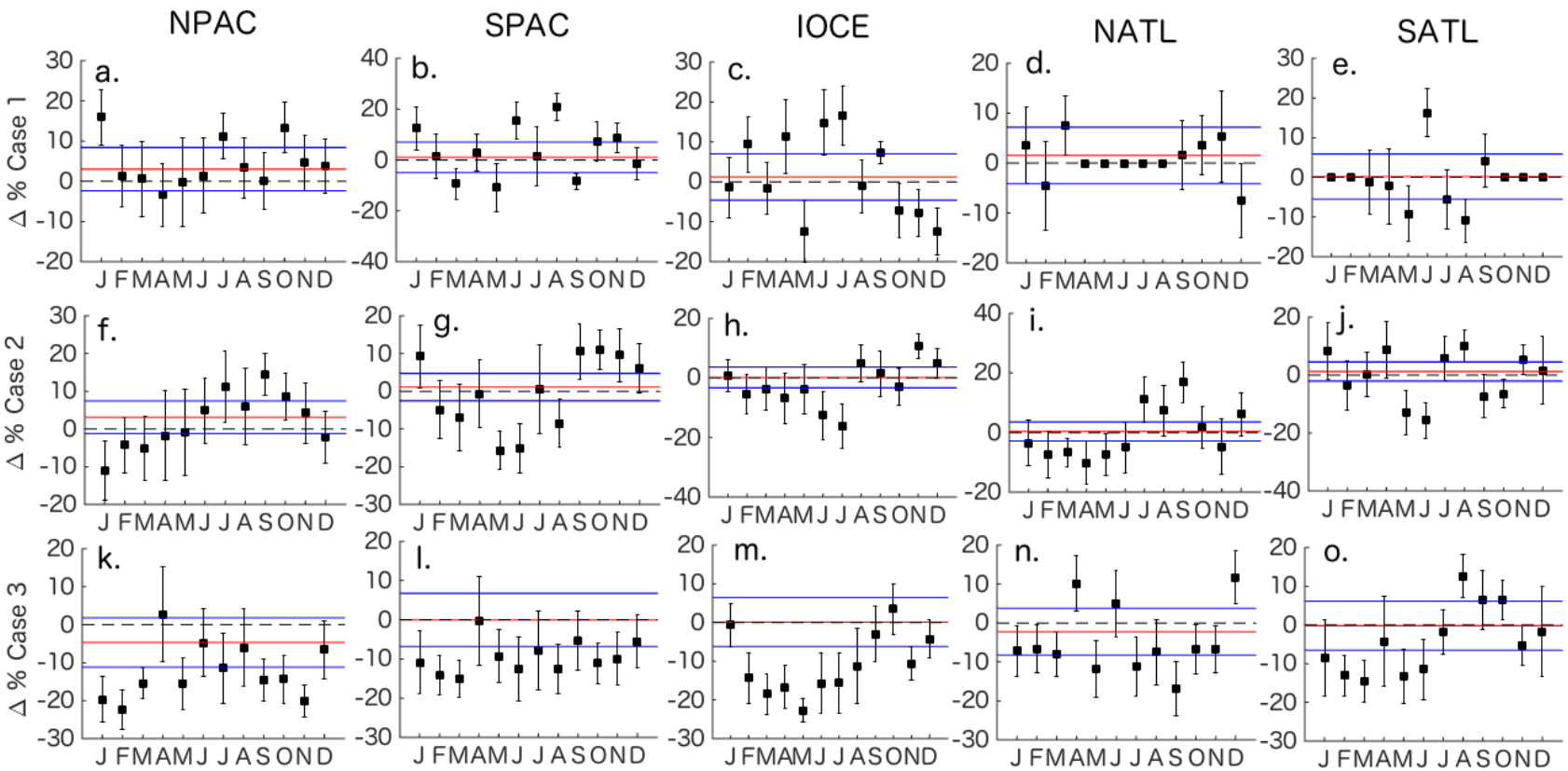

Figure A12: Percentage change/Trends in all the months through 1997-2010 in the 5 subtropical gyres for the three cases: (a-e) Case 1 (L_{MIX}=MLD), (h-j) Case 2 (L_{MIX}=L_{EK}), and (k-o) Case 1 (L_{MIX}=L_{OZ}). The red line is the total percentage change of case occurrences over the 1997-2010 period and the blue line is the +/- one-sigma error associated with the total percentage change of occurrence of the cases. The black dashed line is the zero line. Error bars crossing zero line indicates that the trends are insignificant at one sigma (or 68% confidence interval, p-value<0.3).

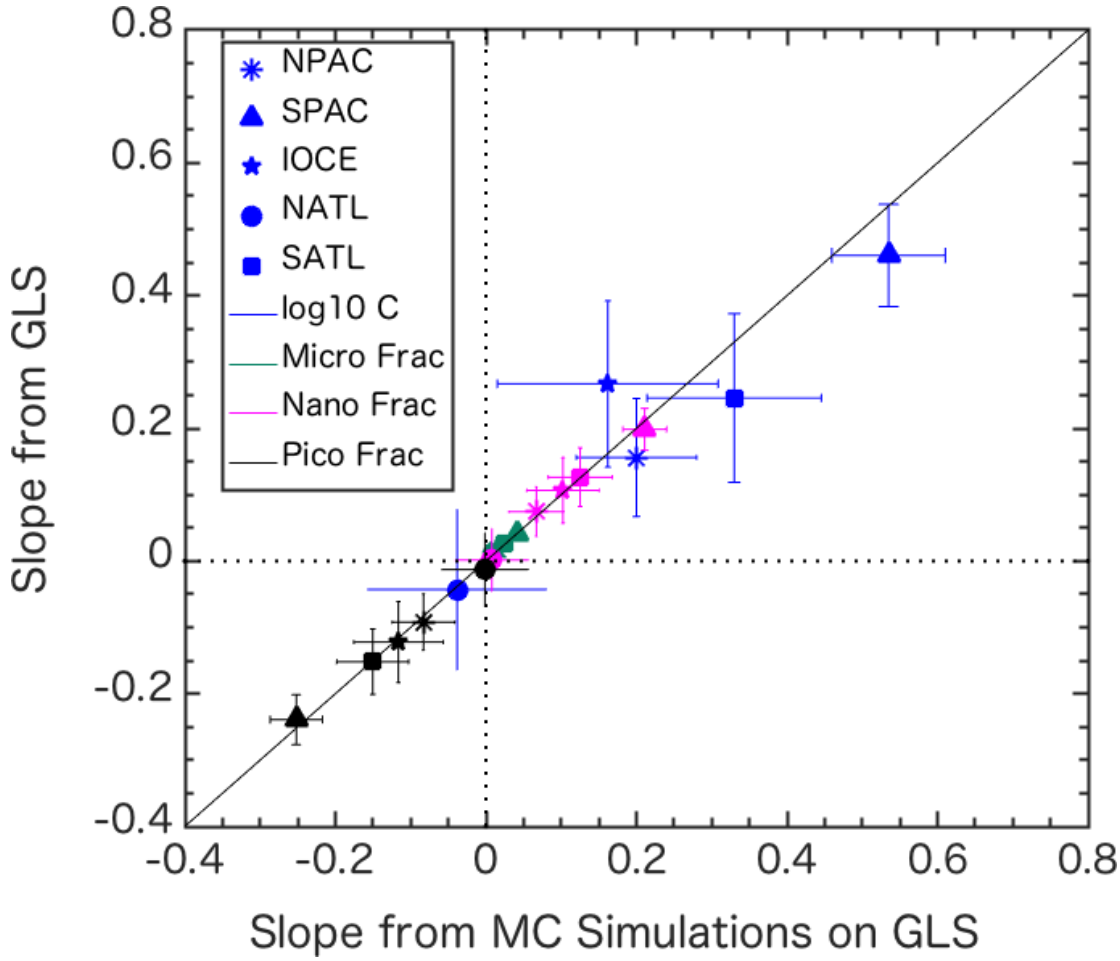

Figure A13: GLS trend slope values for the total phytoplankton biomass (% y^{-1}), and PFT fractions for the subtropical gyres [North Pacific (NPAC), South Pacific (SPAC), Indian Ocean (IOCE), North Atlantic (NATL) and South Atlantic (SATL)] where shapes represent the gyres and colors represent the variables (see the legend). Note that the trends in micro-phytoplankton Fraction (green) are also included in the figure except it is not visible as the trend values are very close to nano-phytoplankton fraction (behind the pink circle). The y-axis shows the slope obtained from the GLS regression with 1-sigma intrinsic errors (bars) generated using 'gls' model from MATLAB® for all the variables. The slopes on the x-axis were generated via Monte Carlo simulation (10000 times) on GLS, using the per-pixel uncertainty estimates (given as the standard deviation 1σ) propagated from uncertainty estimates for the parameters provided with the Kostadinov et al. (2016) products. See Text A3 for the detailed method on Monte Carlo simulation. The dashed horizonal and vertical line is the zero line. Error bars crossing the horizonal and vertical line is the zero line indicates that the trend is insignificant at one sigma or 68% confidence interval (p-value<0.3).

Variable Trends	Regions				
Ocean area (m^2)	**Global (3.6109e+14)**	**Warm (2.4345e+14)**	**Cold NH (4.0411e+13)**	**Cold SH (7.6846e+13)**	**Tropical Pacific (3.0748e+13)**
Log_{10} Biomass	0.41 ± 0.09 [a,b]	0.33 ± 0.1 [a,b]	0.69 ± 0.1 [a,b]	0.89 ± 0.1 [a,b]	0.59 ± 0.31 [a]
Log_{10} Chl-a	0.18 ± 0.03 [a,b]	0.1 ± 0.036 [a,b]	0.41 ± 0.07 [a,b]	0.58 ± 0.06 [a,b]	0.51 ± 0.38 [a]
Fraction Micro	0.12 ± 5e-03 [a,b]	0.09 ± 4.17 e-03 [a,b]	0.42 ± 0.03 [a,b]	0.32 ± 0.018 [a,b]	0.11 ± 0.06 [a]
Fraction Nano	0.18 ± 0.016 [a,b]	0.16 ± 0.01 [a,b]	0.17 ± 0.01 [a,b]	0.38 ± 0.02 [a,b]	0.26 ± 0.12 [a,b]
Fraction Pico	-0.31 ± 0.02 [a,b]	-0.24 ± 0.02 [a,b]	-0.58 ± 0.04 [a,b]	-0.70 ± 0.04[a,b]	-0.38 ± 0.18 [a,b]

Table A1: GLS Trends of monthly anomalies of the Kostadinov et al. (2016) derived products and OCI Chl-a for Sep 1997–Dec 2010 in $\%y^{-1}$ with 1-sigma error. Significant trends at the 68% (p-value<0.3) and 95% confidence level (p-value<0.05) are indicated by subscripted letters a and b. Acronyms are: NH – North Hemisphere; SH – South Hemisphere. Warm regions defined as areas where the 1997-2010 SST>15°C.

Correlation (Variable, MEI)	Tropical Pacific	NPAC	SPAC	IOCE	NATL	SATL
Log_{10} Biomass (mg/m^3)	**-0.71**	0.11	0.03	0.05	0.03	-0.02
Log_{10} Chl-a (mg/m^3)	**-0.88**	**0.4**	0.05	-0.06	-0.13	**-0.22**
Chl/$C_{B'16}$ (mg Chl/m^3)/(mg C/m^3)	**-0.65**	0.002	-0.06	-0.03	**-0.23**	**-0.3**
Fraction Micro	**-0.68**	0.07	-0.02	0.05	0.007	-0.08
Fraction Nano	**-0.71**	0.14	0.005	0.04	0.05	-0.04
Fraction Pico	**0.71**	-0.13	-0.0006	-0.04	-0.04	0.04
Biome Size (Chl>0.11/Chl<0.11)	**-0.54**	**0.43**	**0.24**	**0.25**	-0.08	**0.19**
Biome Size (Chl>0.07/Chl<0.07)	-0.16	-0.06	-0.1	**0.22**	0.01	**0.35**

Table A2. Table of linear correlation coefficients of the monthly anomalies of log_{10} biomass, log_{10} Chl-a, -micro-phytoplankton fraction, nano-phytoplankton fraction, and pico-phytoplankton fraction with the multivariate ENSO index (MEI) for the tropical Pacific and the 5 subtropical gyres. Period of analysis: Sep 1997–Dec 2010 (160 months). Significant correlations at the 95% confidence level indicated in bold. A positive MEI corresponds to the warm phase of ENSO (El Niño); a negative MEI corresponds to the cold phase of ENSO (La-Nina). A positive correlation coefficient means that the variable increases during El Niño events and/or decreases during La Niña events.

Variables	Subtropical Gyres				
	NPAC	**SPAC**	**IOCE**	**NATL**	**SATL**
Log_{10} Biomass (%y^{-1})	0.16 ± 0.09 [a]	0.46 ± 0.17 [a,b]	0.27 ± 0.13 [a,b]	0.04 ± 0.11	0.25 ± 0.13 [a]
Log_{10} Chl (%y^{-1})	'-0.21 ± 0.07 [a,b]	0.13 ± 0.14	-0.11 ± 0.08 [a]	-0.16 ± 0.07 [a,b]	0.15 ± 0.08 [a]
Chl/C_{B16} [(mg Chl m^{-3})/(mg C m^{-3})]y^{-1}	(-3.19 ± 1.66) e-05 [a]	(4.12 ± 1.76) e-05 [a,b]	(-1.81 ± 2.24) e-05	(-5.56 ± 0.20) e-05 [a,b]	(4.12 ± 1.76) e-05 [a,b]
Log_{10} PIC (% y^{-1})	-0.83 ± 0.96	-0.15 ± 1.12	-0.42 ± 1.43	4.32 ± 1.56 [a,b]	3.36 ± 1.44 [a,b]
Gyre Size (Chl-a<0.11 mgm^{-3}) (km^2 y^{-1})	-0.33 ± 0.16 [a,b]	-0.74 ± 0.06 [a,b]	-0.14 ± 0.1 [a]	-0.02 ± 0.03	-0.06 ± 0.025 [a,b]
Gyre Size (Chl-a<0.07 mgm^{-3}) (km^2 y^{-1})	0.018 ± 0.09	-0.26 ± 0.09 [a,b]	0.01 ± 0.05	0.012 ± 0.018	-0.08 ± 0.03 [a,b]
MLD SODA (m y^{-1})	-0.05 ±0.18	0.15 ± 0.15	-0.06 ± 0.11	0.07 ± 0.11	0.25 ± 0.16 [a]
PAR (Einstein m^{-2} day^{-1} y^{-1})	-0.05 ± 0.02 [a,b]	(2.45 ± 15.0) e-03	5.81e-04 ± 0.02	-0.05 ± 0.02 [a,b]	(4.62 ± 15) e-03
K_d(490) (nm y^{-1})	(-3.52 ± 1.64) e-05 [a,b]	(5.81 ± 2.54) e-05 [a,b]	(3.06 ± 3.07) e-05	(5.55 ± 2.65) e-05 [a,b]	(1.74 ± 2.34) e-05
Wind speed (m $s^{-1}y^{-1}$)	5.05 e-03 ± 5.0 e-03 [a]	0.02 ± 0.015 [a]	0.01 ± 0.01	0.01 ± 7.0e-03 [a]	0.01 ± 0.01
L_{MIX} (my^{-1})	1.08 ± 0.39 [a,b]	0.37 ± 0.36 [a]	0.38 ± 0.34 [a]	0.19 ± 0.23	0.29 ± 0.27 [a]
s*p*CO_2 (ppm y^{-1})	1.40 ± 0.10 [a,b]	1.33 ± 0.12 [a,b]	1.50 ± 0.095 [a,b]	1.25 ± 0.15 [a,b]	1.026 ± 0.16 [a,b]
Heat Flux (W$m^{-2}y^{-1}$)	-1.31 ± 0.34 [a,b]	-0.87 ± 0.03 [a,b]	-1.03 ± 0.3 [a,b]	-1.06 ± 0.38 [a,b]	-0.36 ± 0.26 [a]

Table A3: GLS trends and 1-sigma errors of monthly anomalies for either 1997-2010 (most variables), or 1997-2009 (HeafFlux) for the subtropical gyres. Significant trends at the 68% (p-value<0.3) and 95% (p-value<0.05) confidence level are indicated by subscripted letters a and b.

Variables	**Subtropical Gyres**				
	NPAC	**SPAC**	**IOCE**	**NATL**	**SATL**
Fraction Micro (%y^{-1})	0.02 ± 6.5e-03 [a,b]	0.04 ± 5.0e-3 [a,b]	0.03 ± 9.0e-3 [a,b]	0.01 ± 0.01	0.03 ± 5.0e-03 [a,b]
Fraction Nano (%y^{-1})	0.08 ± 0.038 [a,b]	0.21 ± 0.03 [a,b]	0.15 ± 0.06 [a,b]	1.63 e-03 ± 0.05	0.13 ± 0.05 [a,b]
Fraction Pico (%y^{-1})	-0.09 ± 0.04 [a,b]	-0.25 ± 0.04 [a,b]	-0.18 ± 0.07 [a,b]	-0.01 ± 0.05	-0.15 ± 0.05 [a,b]
SST (^{o}C y^{-1})	0.02 ± 7.5e-03 [a,b]	0.03 ± 0.017 [a]	0.02 ± 0.015 [a]	0.01 ± 0.01	0.02 ± 0.015 [a]
L_{OZ} (m y^{-1}**)**	-0.01 ± 0.015	0.012 ± 0.02	-8.57 e-03 ± 0.02	4.17e-04 ± 0.015	8.63e-03 ± 0.02
L_{EK} (m y^{-1}**)**	0.09 ± 0.19	0.33 ± 0.26 [a]	0.13 ± 0.3	0.12 ± 0.12	0.25 ± 0.19 [a]
Case 1 (%y^{-1})	0.68 ± 1.20	0.33 ± 1.90	0.44 ± 2.17	0.58 ± 2.18	0.06 ± 1.76
Case 2 (%y^{-1})	0.60 ± 0.83	0.18 ± 3.24	0.04 ± 0.9	0.08 ± 0.76	0.24 ± 0.67
Case 3 (%y^{-1})	-1.56 ± 2.16	-9.37 e-03 ± 2.04	0.04 ± 1.95	-0.96 ± 2.75	-0.07 ± 2.50

Table A4: GLS trends and 1-sigma errors of monthly anomalies for either 1997-2010 (most variables), or 1997-2009 (SST) for the subtropical gyres. Significant trends at the 68% (p-value<0.3) and 95% (p-value<0.05) confidence level are indicated by subscripted letters a and b.

APPENDIX B: Supporting Information for Contrasting ENSO types with satellite derived ocean phytoplankton biomass in the Tropical Pacific

Submitted for publication as:

Sharma, P., Singh, A., Marinov, I., and Kostadinov, T.S., (Submitted to GRL-under revision) Contrasting ENSO types with satellite derived ocean phytoplankton biomass in the Tropical Pacific

B.1 Introduction

We present (1) a summary of the variables used in this study (Table B1), (2) simple empirical orthogonal functional (EOF) modes of phytoplankton biomass and their corresponding principal component time series (Figure B1), (1) combined regression-(EOF) modes and their corresponding principal component time series (Figure B2) to separate the central and eastern Pacific El Niño events, and support the findings in the section 3.4.1 (3) the biomass and Chlorophyll-a index (Figure B3).

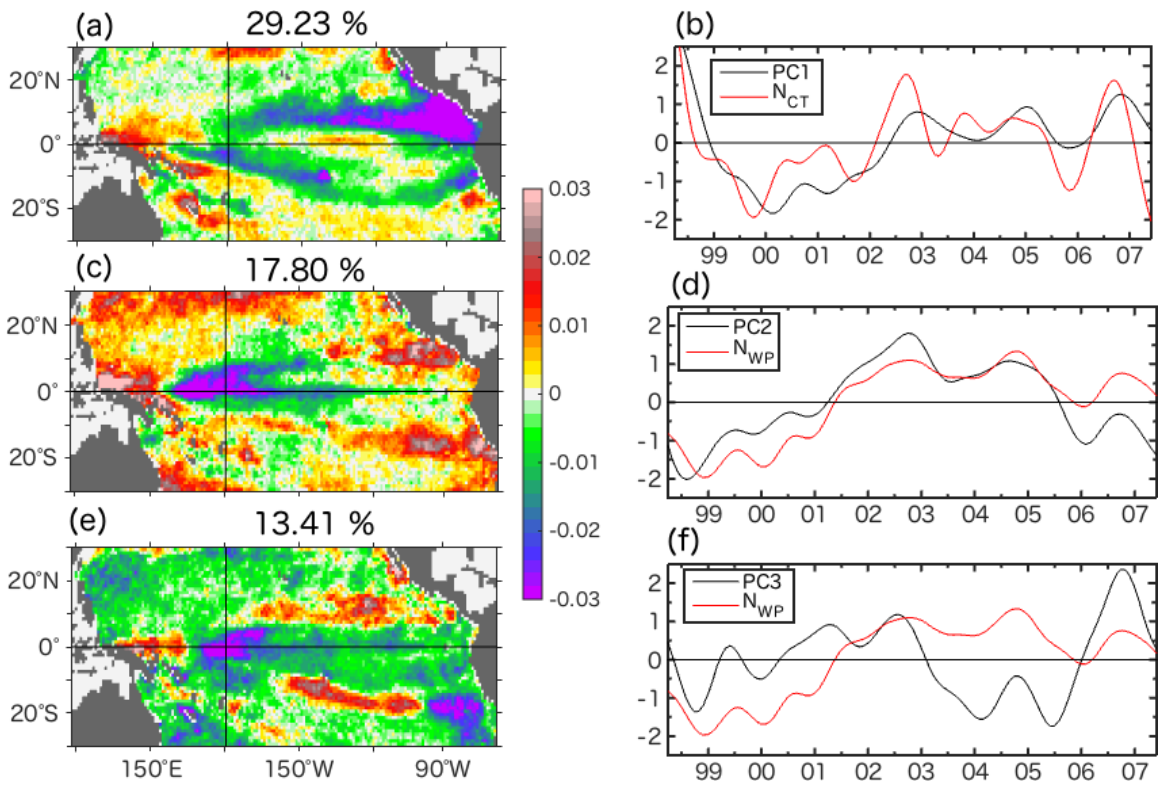

Figure B1: Spatial structures for (a) EOF mode 1, (c) EOF mode 2 and (e) EOF mode 3 and (b, d, and f) their corresponding principal component functions (in blue) for the phytoplankton biomass anomalies, respectively. The units are mg/m^3 and the time functions and indices are normalized. The red lines in the time functions are the 13-months Hanning filtered N_{CT} and N_{WP}

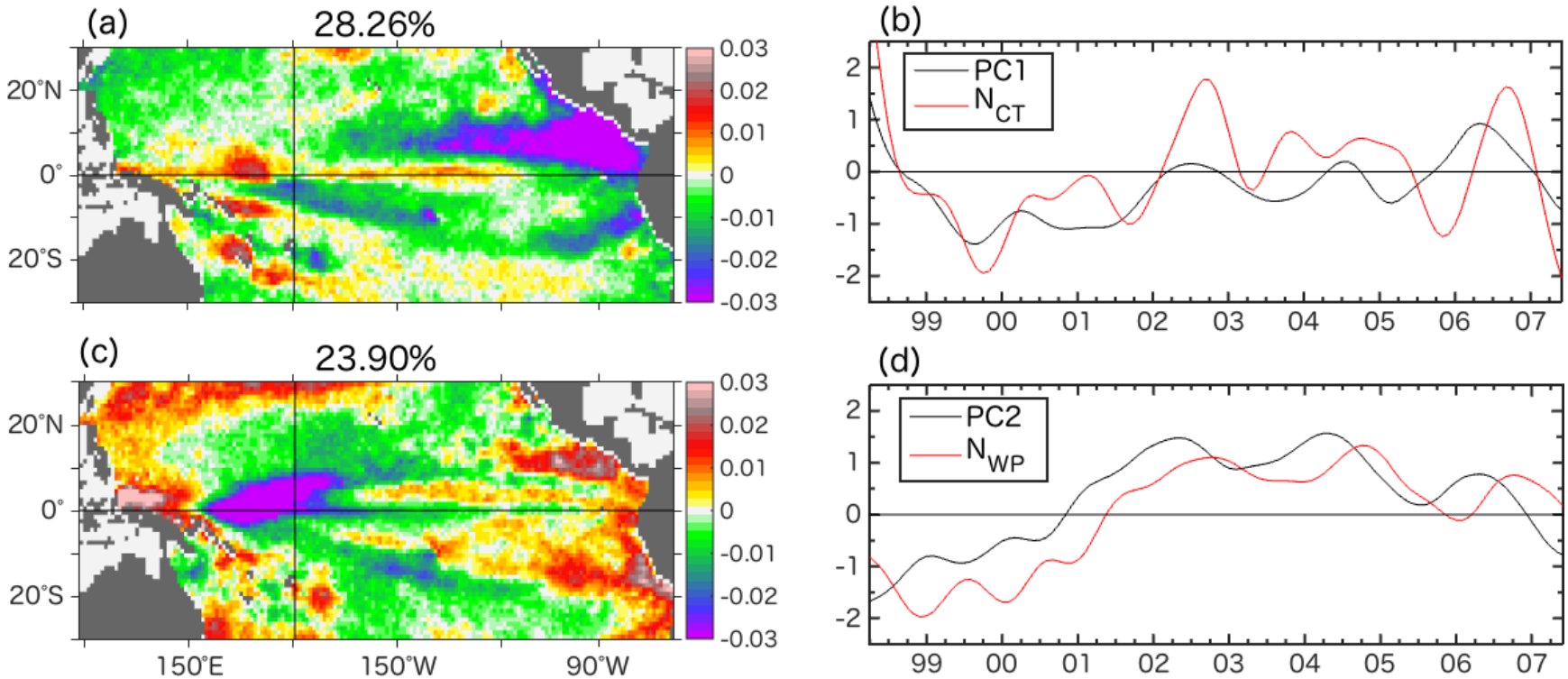

Figure B2: Spatial structures for combined-regression (a) EOF mode 1, (c) EOF mode 2 and their corresponding time functions ((b, d, in black) for the phytoplankton biomass anomalies, respectively. The units are mg/m^3 and the time functions and indices are normalized. The red lines in the time functions denote the 13-months Hanning filtered N_{CT} and N_{WP}

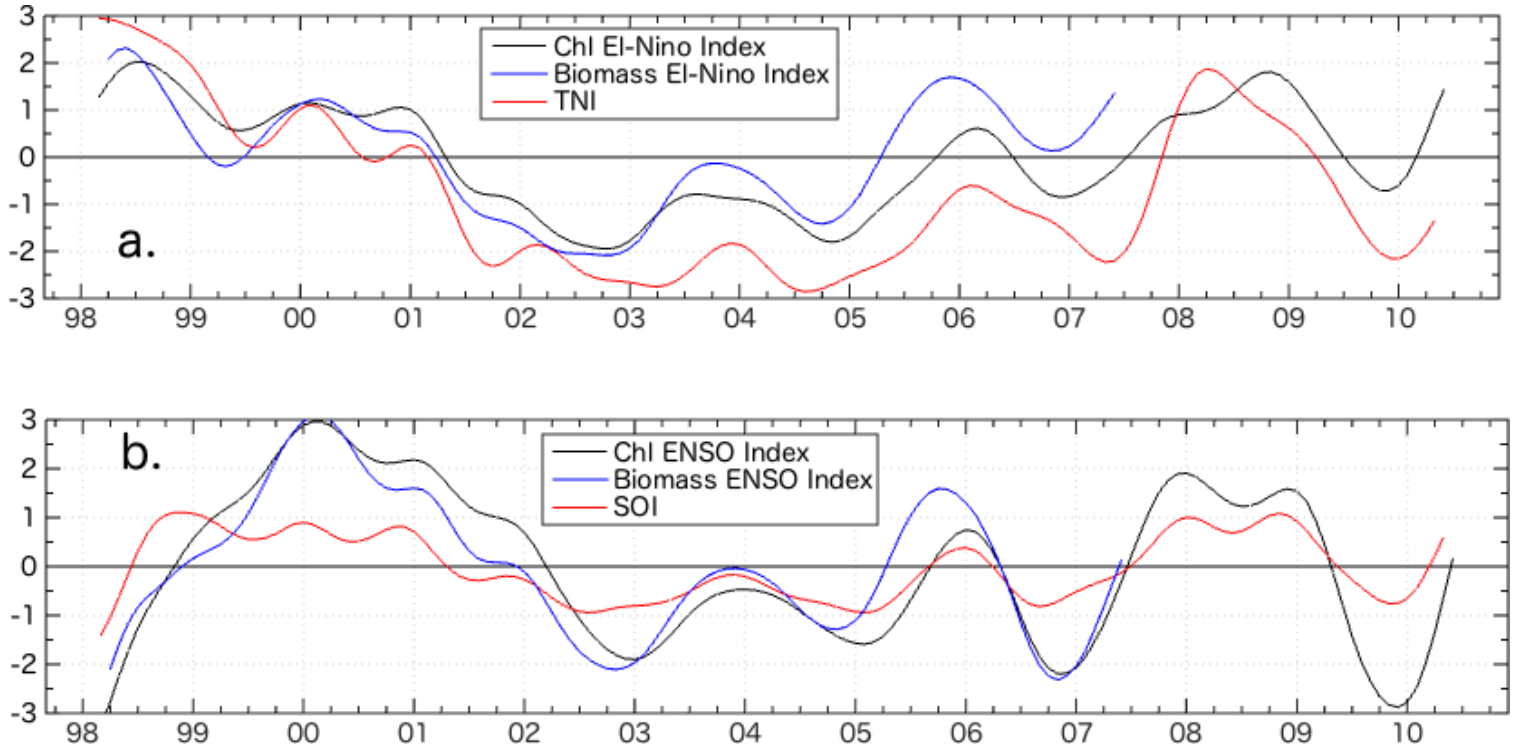

Figure B3: Time series of (a) the biomass El Niño Index, the Chlorophyll-a El Niño Index, and (b) the biomass and Chlorophyll-a ENSO Index with the 13-months Hanning filtered Southern Oscillation Index and Trans- Niño index superimposed in red. See section 5.2 for the definition of both indices. NB: For the Chlorophyll-a we adapted the Radenac et al (2012) method of replacing the missing maps with Aqua MODIS Chlorophyll-a maps, extending the timeseries to define a 1997-2010 CP and EP ENSO indices for biology.

Table B1: Synopsis of variables, original data resolution and source used in this study. NB: We only use data from September 1997- December 2010.All the datasets were downscaled to 1 degree at a monthly resolution.

Variables	**Spatial Resolution**	**Temporal Resolution**	**Source/ reference**
Chlorophyll-a, SeaWiFs Ocean Color Index OCI algorithm (R.2014) Units: mg/m^3	9km	Monthly September 1997-2010	http://oceancolor.gsfc.nasa.gov/ NASA Goddard Space Flight Center, Ocean Biology Processing Group; (2014)
Sea Surface Temperature (SST) Met Office Hadley Center Sea Ice and SST data set 1 (HadISST1). Units: ^oC	1°	Monthly September 1997-2010	https://www.metoffice.gov.uk/hadobs/hadisst/data/download.html Rayner et al. (2003)
Windspeed European Reanalysis (ERA–Interim) Units: m/s^2	1°	Daily 1990-2010	European Centre for Medium-Range Weather Forecasts (http://www.ecmwf.int/) Berrisford et al., 2011
Ocean currents Ocean Surface Current Analysis - Real time (OSCAR). Units: m/s^2	1/3 degree grid	5 day	https://podaac.jpl.nasa.gov/ws/search/granule/?datasetId=PODAAC-OSCAR-03D01&apidoc (Bonjean & Lagerloef, 2002)
$Z_{20°C}$ Units: m	Point data set	September 1997-2010	https://www.pmel.noaa.gov/tao/drupal/disdel/ (GTMBA Project Office of NOAA/PMEL)
Multivariate ENSO Index (MEI)		1850-2016	https://climatedataguide.ucar.edu/ National Center of Atmospherics Research (NCAR) climate data portal

APPENDIX C: Supporting Information for Ocean phytoplankton biology in the North East Pacific in multiple satellite products and CMIP5 climate models

To be submitted:

Sharma, P., Singh, A., Marinov, I., and Kostadinov, T.S., (JGR) Ocean phytoplankton biology in the North East Pacific in multiple satellite products and CMIP5 climate models

C.1 Introduction

We present 5 supporting Figures (Figures C1-C5): (1) Figure C1, temporal correlation of monthly percent micro phytoplankton from multiple satellite products with physics (Figure C1) to support section 4.4, (2) Active mixing length scale (L_{MIX}) climatology derived as in Brody et al (2014) (Figure C2 and C3) to support section 4.5, (3) the ratio of zooplankton biomass over phytoplankton biomass for CMIP5 models (Figure C4 and C5) to support section 4.4 and 4.5.

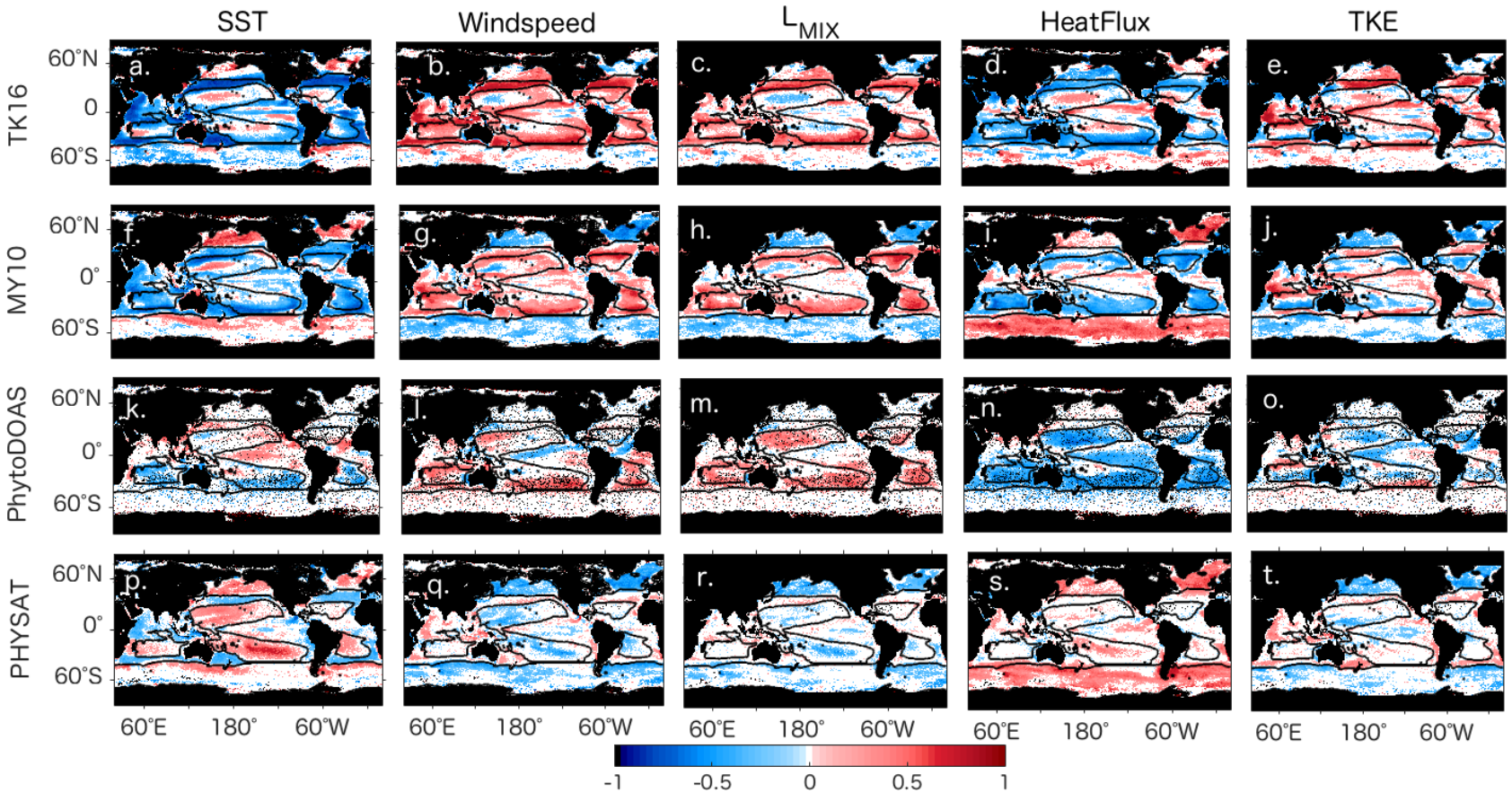

Figure C1. Temporal correlation of monthly (Top Panel, a-e) micro fraction (TK16) from Kostadinov et al. (2009; 2010; 2016) with sea surface temperature (SST), wind speed, active mixing length scale (L_{MIX}), Heatflux (positive into ocean) and Photosynthetically active radiation during the SeaWiFS period (1997–2010). Second Panel (f-j) is the temporal correlation between the decimal logarithm of micro fraction (MY2010) from Mouw and Yoder. (2010) and above physical variables. Third Panel (k-o) is the temporal correlation between the decimal logarithm of chlorophyll-a in

diatoms (PhytoDOAS) from Bracher et al. (2009; 2017) and above physical variables. Bottom Panel (p-t) is the temporal correlation between the frequency of detection of diatoms (PHYSAT) from Alvain et al. (2005; 2008) and above physical variables. The correlation in the red and blue areas are statistically significant at the 95% level ($P < 0.05$). Non-significant correlations are shown in white. Long-term trend is removed from the full time series by detrending the data. The subtropical gyres (Figure A1) are delimited by black contours

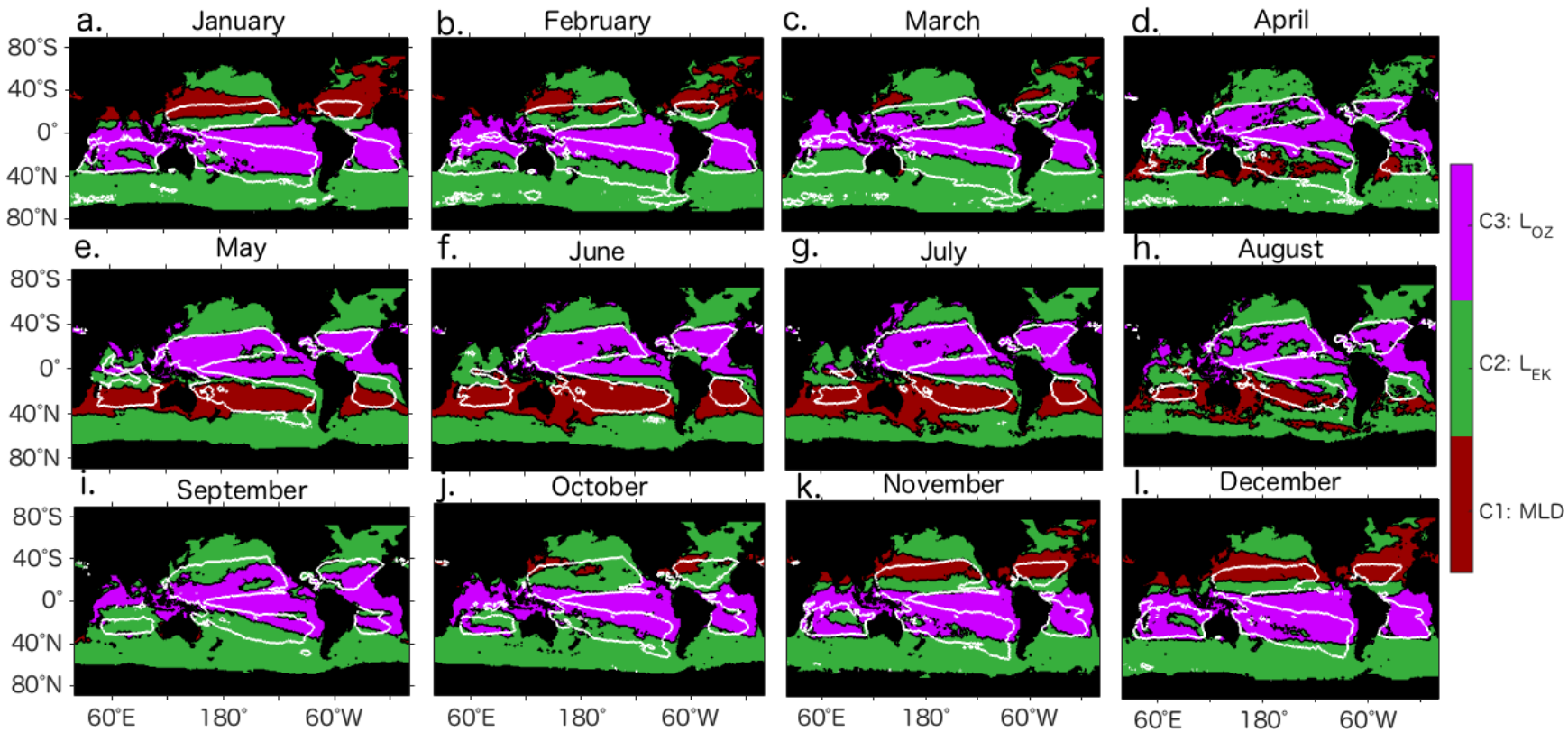

Figure C2. Active mixing length scale (L_{MIX}) climatology derived as in Brody et al (2014) and detailed in Methods for 1 x1 degree grid. Criterion for the climatology was constructed using the pixels that have highest percentage occurrence of the Case 1, or Case 2 or Case 3 in all January's during 1997-2010 periods. The subtropical gyres (Figure A1) are delimited by white contours

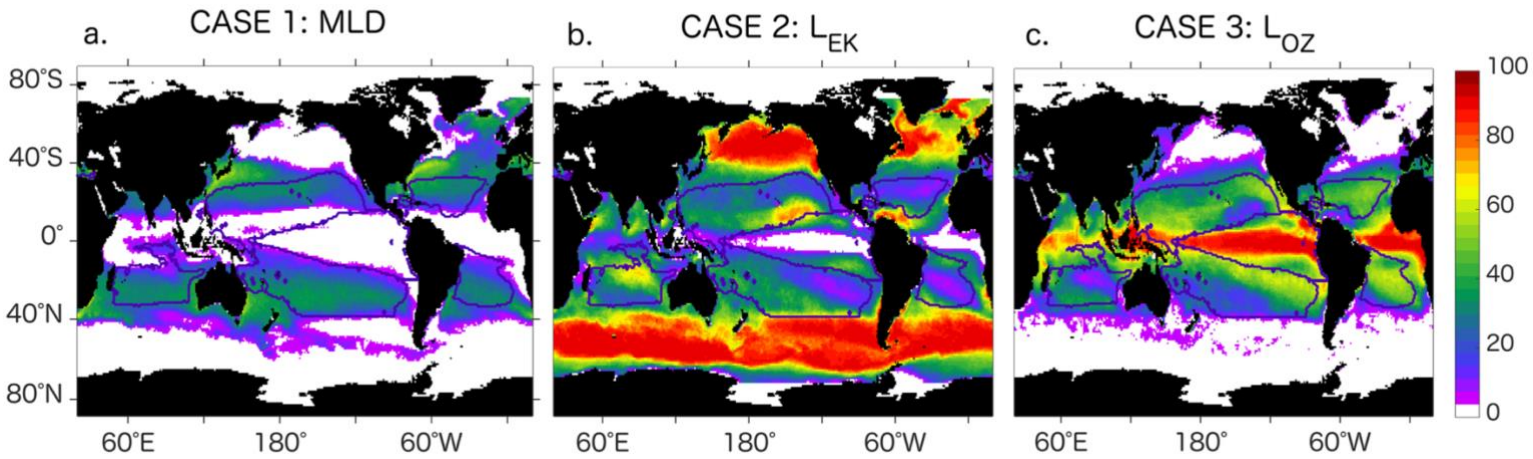

Figure C3. Global map of the percentage occurrence for each case used to construct the (L_{MIX}) active mixing length scale, (a) Case 1: MLD, (b) Case 2: L_{EK} and (c) Case 3: L_{OZ} during the SeaWiFS period (1997-2010). Cases are calculated as in Brody et al (2014, see Methods). The subtropical gyres (Figure A1) are delimited by black contours

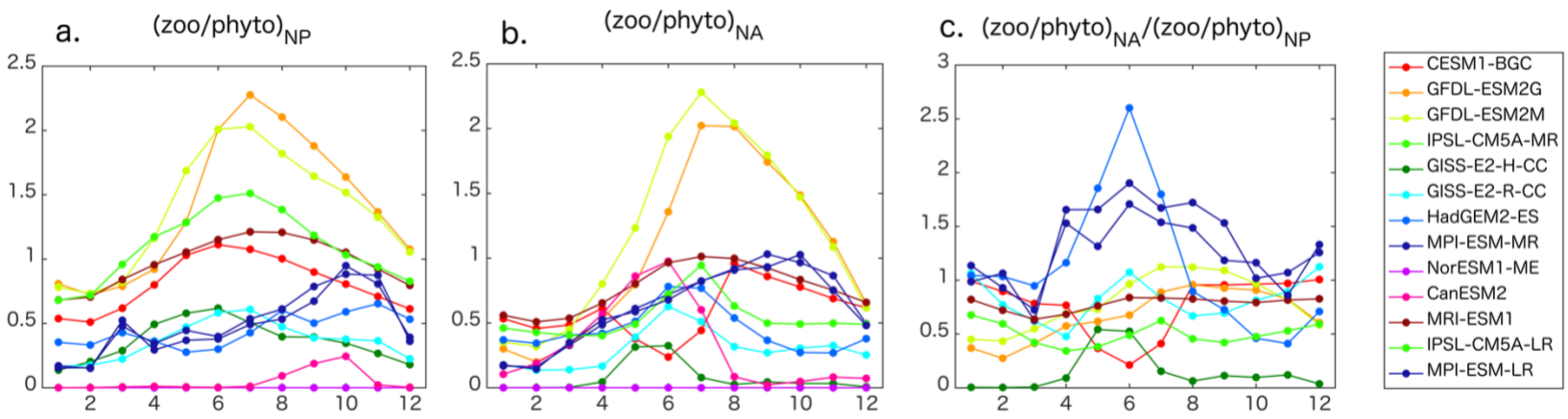

Figure C4: Climatologies of the ecological variables in the subpolar box at North Pacific (45-50ºN, 140-150ºW, includes OSP). The variables includes climatologies of (a) ratio of zooplankton biomass over phytoplankton biomass in North Pacific, $(zoo/phyto)_{NP}$ (b) ratio of zooplankton biomass over phytoplankton biomass in North Atlantic $(zoo/phyto)_{NA}$, and (c) ratio of ratio of zooplankton biomass over phytoplankton biomass in North Atlantic over ratio of zooplankton biomass over phytoplankton biomass in North Pacific $((zoo/phyto)_{NA}/(zoo/phyto)_{NP}$.

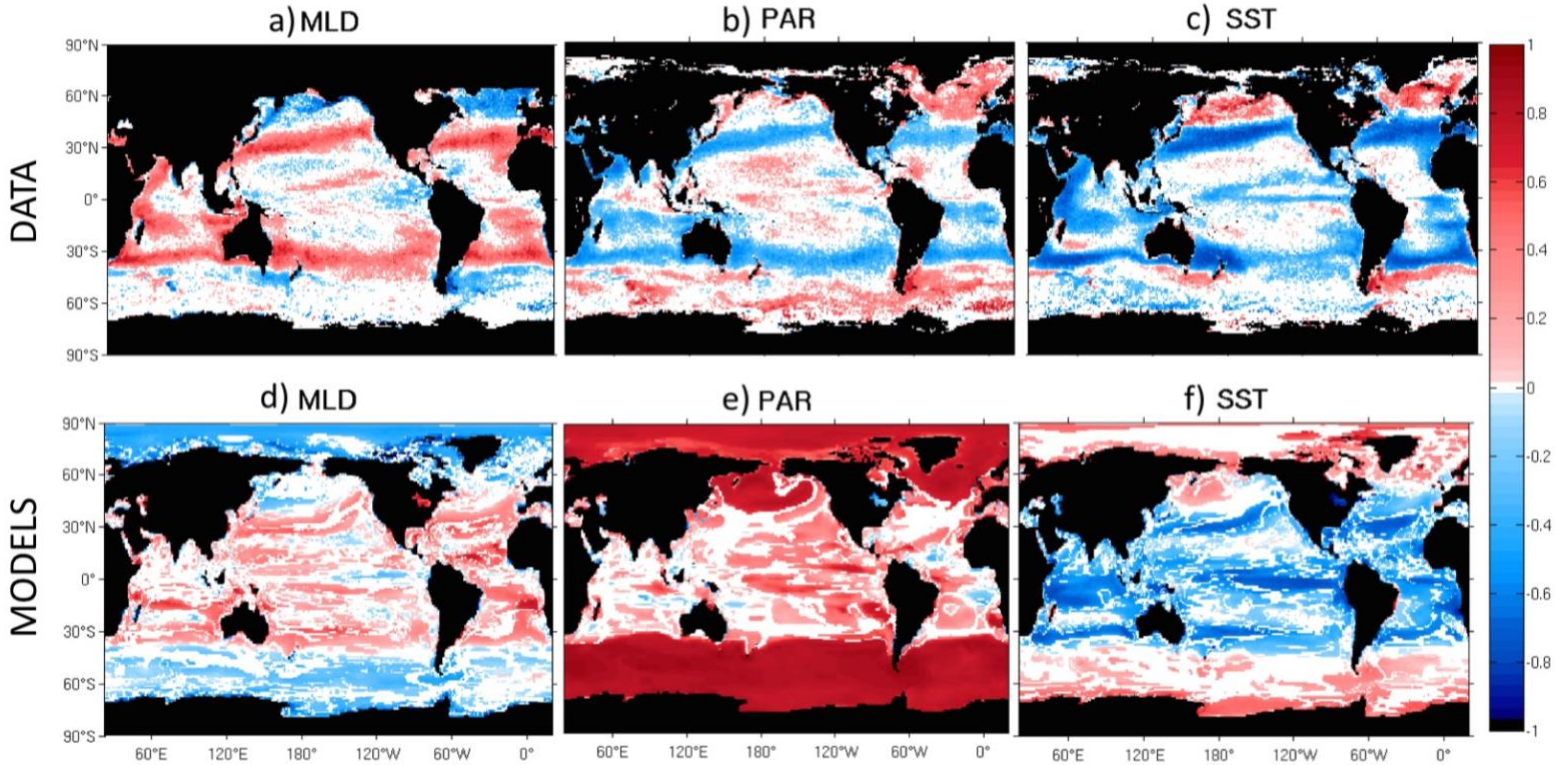

Figure C5 (Adapted from Cabre et al. 2016): Temporal correlation of monthly decimal logarithm of phytoplankton biomass with mixed layer depth (MLD), Photosynthetically active radiation (PAR), and sea surface temperature (SST) for 1997-2010 period in TK16 (I think this was TK10, put it as TK10 for now, or whatever Anna was using in the paper, we will change later) observed fields (a-c) and in the CMIP5 multimodel mean (d-f). The correlation for each model was calculated; then the weighted average of the model correlations was taken to obtain the multi-model mean correlation. The correlations in the red and blue areas are statistically significant at the 95% level ($P < 0.05$). Non-significant correlations are shown in white. Long-term trend is removed from the full time series by detrending the data.

Table C1: Summary of the CMIP5 models used in this study. We used 13 models. The eighth column presents the biogeochemical component of the earth system models and their references. Information on the following for each model is summarized in columns 2-6, respectively: spatial resolution in the atmosphere and ocean, explicitly modeled nutrients, ecology subroutine, references, and weight applied in the all-model averages. Variables list for seventh column: Phytoplankton biomass (phyto), Chlorophyll-a, Iron, Nitrate, diatoms, MLD, IPAR, zooplankton biomass, and integrated primary production (intpp). P, N Fe and Si stands for Phosphorus, Nitrogen, Iron and Silica.

Models	**Atm (levels, lon/lat)**	**Ocean (levels, lon/lat)**	**Nutrients**	**Phytoplankton Variables in models**	**Zooplankton In models**	**Variables analyzed (all 9 variables (~) from the model unless stated below)**	**Reference** **Ecological Module**	**Weight**
CanESM2	L35 2.8/2.8	L40 1.4/0.9	N (but also accounts for Fe limitation)	diatom, nanophyto, diazotroph	1 zooplankton	Diatom, Iron	CMOC-NPZD (Zahariev et al., 2008)	1
CESM1-BGC	L26 1.25/0.94	L60 1.125/0.27–0.53	(P), N, Fe, Si	large separated into diatoms and non- diatom, small cyanobacteria, diazotroph	1 class of zooplankton (with ability to capture ecological aspects of micro-and macro-)	~	MET (Moore et al., 2004, Moore et al., 2006)	1
GFDL-ESM2G	L24 2.5/2.0	L63 1/0.3-1	P, N, Fe, Si	Diatom Nanophyto diazotroph	No Zooplankton. Only specific grazing rate for each phytoplankton functional type	~	TOPAZ2 (Dunne et al., 2012)	1
GFDL-ESM2M	L24 2.5/2.0	L50 1/0.3–1	P, N, Fe, Si					1
GISS-E2-H-CC	L40 2.5/2	L26 1/1	N, Fe, Si	Diatoms, chlorophytes, cyanobacteria, coccolitophores	1 zooplankton	PAR	NOBM (Gregg, 2008)	1
GISS-E2-R-CC	L40 2.5/2	L32 1.25/1	N, Fe, Si					1

HadGEM2-ES	L38 1.25 /1.875	L40 1/0.3–1	N, Fe, Si	diatom, non-diatom	1 zooplankton	~	Diat-HadOCC (NPZD) (Palmer and Totterdell, 2001)	0.5
IPSL-CM5A-LR	L39 3.75/1.875	L31 2/0.5–2	P, N, Fe, Si	Diatoms, nanophyto	2 zooplankton (Micro and Meso)	~	PISCES (from HAMOCC5) (Aumont and Bopp, 2006, Séférian et al., 2013)	0.5
IPSL-CM5A-MR	L39 2.5/1.25	L31 2/0.5–2	P, N, Fe, Si					0.5
MPI-ESM-LR	L47 1.9	L40 0.4	P, N, Fe, Si	1(But separated into diatoms and calcifiers)	1 zooplankton	Diatom	HAMOCC5.2 (NPZD) (Ilyina et al., 2013)	0.5
MPI-ESM-MR	L23 1.125/1.121	L40 1.5	P, N, Fe, Si					0.5
MRI-ESM1	L23 1.125/1.121	L51 1/0.5	P, N	Diatom		Diatom, Iron	NPZD (Oschlies, 2001)	0.5
NorESM1-ME	L26 1.9/2.5	L53 1/1.25	P, N, Fe, Si	Phyto(But separated into diatoms and calcifiers)		Chlorophyll-a, Diatom, zooplankton	HAMOCC5.1 (NPZD) (Assmann et al., 2010)	1

Table C2: Seasonal indices (e.g. seasonal amplitude and strength) in/against variables across 13 CMIP5 models. The information in this table is represented at Figure 4.6 and Figure C4.

Models	**CESM 1-BGC**	**GFDL-ESM2 G**	**GFDL-ESM2 M**	**IPSL-CM5 A-MR**	**GISS -E2-H-CC**	**GISS -E2-R-CC**	**HadGEM 2-ES**	**MPI-ESM -MR**	**NorESM 1-ME**	**CanES M2**	**MRI-ESM 1**	**IPSL-CM5 A-LR**	**MPI-ESM -LR**
Variables	**Ratio of Seasonal Cycle Magnitude at the 2 locations. Seasonal Magnitude defined as Maximum minus Minimum (max-min)**												
Chl_{NA} / Chl_{NP}	20.56	2.66	2.78	9.20	1.57	1.62	0.23	0.33	**-**	5.05	0.86	4.08	**-**
$Phyto_{NA}$ / $Phyto_{NP}$	10.41	2.06	1.63	15.26	1.57	1.63	0.23	0.32	0.82	4.10	0.86	5.50	0.38
Zoo_{NA} / Zoo_{NP}	1.429	1.66	1.60	**-**	0.43	1.02	0.40	0.56	**-**	-	0.70	1.31	0.8
PP_{NA} / PP_{NP}	1.964	2.31	1.89	2.91	0.93	1.30	0.38	0.45	0.98	5.13	00.8	1.67	0.47
$Nitrate_{NA}$ / $Nitrate_{NP}$	1.784	3.51	2.39	2.16	0.37	0.87	0.13	0.48	1.30	-	0.56	0.81	0.54
MLD_{NA} / MLD_{NP}	0.792	8.13	7.65	5.27	4.58	4.43	0.78	**-**	1.37	1.68	2.59	2.72	1.27
Month of Maximum (imax) in the 2 regions of interest													
(imax)$phyto_{NA}$	6	6	6	5	4	5	4	5	6	2	6	5	6
(imax)$phyto_{NP}$	4	5	5	6	4	5	6	6	5	3	7	5	6
(imax)zoo_{NA}	6	7	6	0	5	5	5	6	-	4	7	5	6
(imax)zoo_{NP}	6	6	6	0	4	6	6	6	-	4	7	6	6
(imax)PP_{NA}	6	6	5	5	4	5	4	5	6	4	6	5	5
(imax)PP_{NP}	6	5	5	6	5	5	5	6	5	4	7	6	6

Ratio of annual averages and Ratio of maximum values													
zoo/phytoC_{NA}	0.449	1.42	1.56	-	0.09	0.31	0.45	0.63	-	0.37	0.79	0.505	0.63
zoo/phytoC_{NP}	0.840	1.48	1.50	-	0.38	0.39	0.38	0.43	-	0.005	1.00	1.10	0.47
(max)pp/(max)phyto C_{NA}	39.14	71.29	73.85	36.10	18.67	43.9	42.56	33.1	40.54	98.84	55.9	39.01	33.4
(max)pp/(max)phyto C_{NP}	126.11	57.76	57.88	75.52	33.63	49.1	25.32	24.6	34.08	76.326	60.3	74.78	27.2
Ratio of Seasonal Cycle Intensities at the 2 locations. Seasonal cycle intensity defined as (max-min)/ave at each location													
Fe_{NA}/ Fe_{NP}	1.61	1.19	1.92	3.06	2.7	0.43	0.13	0.30	0.36	-	-	0.78	0.46
Chl_{NA}/ Chl_{NP}	9.86	2.47	2.29	3.22	2.71	1.78	0.71	0.68	-	0.67	1.09	2.18	-
PP_{NA}/ PP_{NP}	1.44	1.70	1.32	1.83	1.92	1.44	0.94	0.82	0.80	0.94	1.14	1.63	0.77
Zoo_{NA} / Zoo_{NP}	1.37	1.66	1.39	-	3.10	1.43	1.05	0.80	-	0.56	1.14	2.05	0.92

Table C3: Temporal monthly correlation coefficients for the biological variables in the first column against the physical variables first row for the North Pacific Box.

Variables	SST	L_{MIX}	Heatflux	TKE	PAR	MLD	wind	L_{EK}
TK16 biomass	-0.007	0.22	-0.29	0.22	**-0.32**	0.14	0.23	0.23
B05 Biomass	**0.66**	**-0.68**	**0.59**	**-0.67**	**0.60**	**-0.73**	**-0.70**	**-0.69**
S08 Biomass	0.22	-0.11	0.046	-0.13	0.042	-0.18	-0.10	-0.10
SeaWiFS Chl-a	0.11	-0.02	-0.03	-0.062	-0.06	-0.01	0.01	0.01
TK16 Micro %	**-0.40**	**0.61**	**-0.61**	**0.61**	-0.67	**0.59**	**0.62**	**0.62**
TK16 Nano %	**-0.42**	**0.60**	**-0.58**	**0.59**	-0.61	**0.59**	**0.62**	**0.62**
TK16 Pico %	**0.42**	**-0.62**	**0.61**	**-0.61**	**0.65**	**-0.60**	**-0.63**	-0.63
Physat Diatom	**0.48**	**-0.57**	0.45	**-0.53**	**0.47**	**-0.54**	**-0.56**	**-0.56**
MY2010 Micro %	**0.52**	**-0.45**	0.30	**-0.47**	**0.29**	**-0.48**	**-0.46**	**-0.46**
PhytoDOAS Diatom Chl	-0.01	0.48	-0.59	0.46	-0.52	0.19	0.52	0.51
B15 Chl/C	**-0.53**	**0.92**	**-0.90**	**0.91**	**-0.91**	**0.87**	**0.92**	**0.93**

Table C4: Temporal monthly correlation coefficients for the biological variables in the first column against the physical variables first row for the North Atlantic Box

Variables	SST	L_{MIX}	Heatflux	TKE	PAR	MLD	Wind	L_{EK}
TK16 biomass	-0.045	**-0.47**	**0.58**	**-0.35**	**0.60**	**-0.46**	**-0.43**	**-0.44**
B05 Biomass	0.16	**-0.50**	**0.74**	**-0.57**	**0.78**	**-0.56**	**-0.62**	**-0.62**
S08 Biomass	0.097	**-0.56**	**0.69**	**-0.47**	**0.71**	**-0.57**	**-0.57**	**-0.57**
SeaWiFs Chl-a	0.047	**-0.50**	**0.67**	**-0.44**	**0.68**	**-0.52**	**-0.52**	**-0.53**
TK16 Micro %	-0.26	**-0.32**	0.26	-0.04	0.22	-0.19	-0.11	-0.11
TK16 Nano %	**-0.45**	-0.14	0.06	0.13	0.06	-0.01	0.08	0.08
TK16 Pico %	**0.33**	0.26	-0.18	-0.02	-0.17	0.13	0.04	0.04
Physat Diatom	0.02	**-0.41**	**0.68**	**-0.47**	**0.72**	**-0.47**	**-0.53**	**-0.53**
MY2010 Micro %	0.05	**-0.54**	**0.69**	**-0.47**	**0.69**	**-0.53**	**-0.58**	**-0.57**
PhytoDOAS Diatom Chl	-0.26	0.02	-0.53	0.51	-0.61	0.31	0.52	0.52
B15 Chl/C	**-0.71**	**0.57**	**-0.87**	**0.80**	**-0.87**	**0.69**	**0.88**	**0.87**

BIBLIOGRAPHY

Agirbas, Ertugrul et al. (2015). “Temporal changes in total and size-fractioned chlorophyll-a in surface waters of three provinces in the Atlantic Ocean (September to November) between 2003 and 2010”. In: Journal of Marine Systems 150, pp. 56–65. ISSN: 0924-7963. DOI: http://doi.org/10.1016/j.jmarsys.2015.05.008. URL: http://www.sciencedirect.com/science/article/pii/S0924796315001086.

Alvain, S., H. Loisel, and D. Dessailly (2012). “Theoretical analysis of ocean color radiances anomalies and implications for phytoplankton groups detection in case 1 waters”. In: Optics Express 20.2, pp. 1070–1083. DOI: 10.1364/OE.20.001070. URL: http://www.opticsexpress.org/abstract.cfm?URI=oe-20-2-1070.

Alvain, S. et al. (2005). “Remote sensing of phytoplankton groups in case 1 waters from global SeaWiFS imagery”. In: Deep Sea Research Part I: Oceanographic Research Papers 52.11, pp. 1989–2004. ISSN: 09670637. DOI: 10.1016/j.dsr.2005.06.015.

Alvain, S. et al. (2008). “Seasonal distribution and succession of dominant phytoplankton groups in the global ocean: A satellite view”. In: Global Biogeochemical Cycles 22.3. ISSN: 08866236. DOI: 10.1029/2007gb003154.

Alvarez-Fernandez, Santiago and Roel Riegman (2014). “Chlorophyll in North Sea coastal and offshore waters does not reflect long term trends of phytoplankton biomass”. In: Journal of Sea Research 91, pp. 35–44. ISSN: 1385-1101. DOI: https://doi.org/10.1016 / j. seares.2014.04.005. URL: http:/ /www.sciencedirect.com/science/article/pii/S138511011400077X.

Antoine, David et al. (2011). “Variability in optical particle backscattering in contrasting bio-optical oceanic regimes”. In: Limnology and Oceanography 56.3, pp. 955–973. ISSN: 0024-3590. DOI: 10.4319/lo.2011.56.3.0955. URL: https://doi.org/10. 4319/lo.2011.56.3.0955.

Arrigo, Kevin R. (2004). “Marine microorganisms and global nutrient cycles”. In: Nature 437, p. 349. DOI: 10.1038/nature04159. URL: http://dx.doi.org/10.1038/nature04159.

Ashok, Karumuri et al. (2007). “El Niño Modoki and its possible teleconnection”. In: Journal of Geophysical Research 112.C11. ISSN: 0148-0227. DOI: 10.1029/2006jc003798.

Assmann, K. M. et al. (2010). “An isopycnic ocean carbon cycle model”. In: Geosci. Model Dev. 3.1, pp. 143–167. ISSN: 1991-9603. DOI: 10.5194/gmd-3-143-2010. URL: https: //www.geoscimodel-dev.net/3/143/2010/.

Aydin, Kerim Y. et al. (2005). “Linking oceanic food webs to coastal production and growth rates of Pacific salmon (Oncorhynchus spp.), using models on three scales”. In: Deep Sea Research Part II: Topical Studies in Oceanography 52.5, pp. 757–780. ISSN: 0967-0645. DOI: https://doi.org/10.1016/j.dsr2.2004.12.017. URL: http://www.sciencedirect.com/science/article/pii/S0967064505000093.

Ayers, Jennifer M. and M. Susan Lozier (2010). “Physical controls on the seasonal migration of the North Pacific transition zone chlorophyll front”. In: Journal of Geophysical Research: Oceans 115.C5, n/a–n/a. ISSN: 2156-2202. DOI: 10.1029/2009JC005596. URL:http://dx.doi.org/10.1029/2009JC005596.

Barber, Richard T. et al. (1996). “Primary productivity and its regulation in the equatorial Pacific during and following the 1991–1992 El Niño”. In: Deep Sea Research Part II: Topical Studies in

Oceanography 43.4, pp. 933–969. ISSN: 0967-0645. DOI: https://doi.org/ 10.1016/0967 0645(96)00035-5. URL: http://www.sciencedirect.com/science/article/pii/0967064596000355.

Barbieux, Marie et al. (2017). “Assessing the Variability in the Relationship Between the Particulate Backscattering Coefficient and the Chlorophyll a Concentration From a Global Biogeochemical-Argo Database”. In: Journal of Geophysical Research: Oceans 123.2, pp. 1229–1250. ISSN: 2169-9275. DOI: 10.1002/2017JC013030. URL: https://doi.org/10.1002/2017JC013030.

Barton, A. D. et al. (2016). “Anthropogenic climate change drives shift and shuffle in North Atlantic phytoplankton communities”. In: Proc Natl Acad Sci U S A 113.11, pp. 2964–9. ISSN: 1091-6490 (Electronic) 0027-8424 (Linking). DOI: 10.1073/pnas.1519080113. URL: https://www.ncbi.nlm.nih.gov/pubmed/26903635.

Barton, Andrew D., M. Susan Lozier, and Richard G.Williams (2015). “Physical controls of variability in North Atlantic phytoplankton communities”. In: Limnology and Oceanography 60.1, pp. 181–197. ISSN: 00243590. DOI: 10.1002/lno.10011.

Barton, Andrew D. et al. (2013). “On the roles of cell size and trophic strategy in North Atlantic diatom and dinoflagellate communities”. In: Limnology and Oceanography 58.1, pp. 254–266. ISSN: 00243590. DOI: 10.4319/lo.2013.58.1.0254.

Bates, Nicholas R. (2001). “Interannual variability of oceanic CO2 and biogeochemical properties in the Western North Atlantic subtropical gyre”. In: Deep Sea Research Part II: Topical Studies in Oceanography 48.8, pp. 1507–1528. ISSN: 0967-0645. DOI: https://doi.org/10.1016/S0967-0645(00)00151-X. URL: http://www.sciencedirect.com/science/article/pii/S096706450000151X.

Beaulieu, C. et al. (2013). “Factors challenging our ability to detect long-term trends in ocean chlorophyll”. In: Biogeosciences 10.4, pp. 2711–2724. ISSN:1726-4189. DOI:10.5194/bg-10-2711-2013.

Beaulieu, Claudie et al. (2012). “Identification and characterization of abrupt changes in the land uptake of carbon”. In: Global Biogeochemical Cycles 26.1. ISSN: 0886-6236. DOI:10.1029/2010GB004024. URL: https://doi.org/10.1029/2010GB004024.

Behrenfeld, J. Michael et al. (2002). “Photoacclimation and nutrient-based model of light saturated photosynthesis for quantifying oceanic primary production”. In: Marine Ecology Progress Series 228, pp. 103–117. URL: http://www.int-res.com/abstracts/meps/v228/p103-117/.

Behrenfeld, M. J. et al. (2006). “Climate-driven trends in contemporary ocean productivity”. In: Nature 444.7120, pp. 752–5. ISSN: 1476-4687 (Electronic) 0028-0836 (Linking). DOI: 10.1038/nature05317. URL: https://www.ncbi.nlm.nih.gov/pubmed/17151666.

Behrenfeld, Michael J. et al. (2005). “Carbon-based ocean productivity and phytoplankton physiology from space”. In: Global Biogeochemical Cycles 19.1. ISSN: 08866236. DOI: 10. 1029/2004gb002299.

Behrenfeld, Michael J. et al. (2016). “Revaluating ocean warming impacts on global phytoplankton”. In: Nature Clim. Change 6.3, pp. 323–330. ISSN: 1758-678X. DOI: 10.1038/nclimate2838http://www.nature.com/nclimate/journal/v6/n3/abs/nclimate2838.html

Berrisford, P et al. (2011). The ERA-Interim archive Version 2.0. Report.

Bonjean, Fabrice and Gary S. E. Lagerloef (2002). “Diagnostic Model and Analysis of the Surface Currents in the Tropical Pacific Ocean”. In: Journal of Physical Oceanography 32.10, pp. 2938–

2954. ISSN: 0022-3670. DOI: 10.1175/1520-0485(2002)032<2938:DMAAOT> 2.0.CO;2. URL: https://doi.org/10.1175/1520- 0485(2002)032<2938:DMAAOT>2.0.CO;2.

Bopp, L. et al. (2005). “Response of diatoms distribution to global warming and potential implications: A global model study”. In: Geophysical Research Letters 32.19, ISSN: 1944-8007. DOI: 10.1029/2005GL023653. URL: http://dx.doi.org/10.1029/2005GL023653.

Bopp, Laurent et al. (2001). “Potential impact of climate change on marine export production”. In: Global Biogeochemical Cycles 15.1, pp. 81–99. ISSN: 0886-6236. DOI: 10.1029/ 1999GB001256. URL: https://doi.org/10.1029/1999GB001256.

Boss, E. and M. Behrenfeld (2010). “In situ evaluation of the initiation of the North Atlantic phytoplankton bloom”. In: Geophysical Research Letters 37.18, n/a–n/a. ISSN: 00948276. DOI: 10.1029/2010gl044174.

Boyce, D. G., M. R. Lewis, and B. Worm (2010). “Global phytoplankton decline over the past century”. In: Nature 466.7306, pp. 591–6. ISSN: 1476-4687 (Electronic) 0028-0836 (Linking). DOI: 10.1038/nature09268. URL: https://www.ncbi.nlm.nih.gov/pubmed/20671703.

Boyd, P.W. et al. (1996). “In vitro iron enrichment experiments in the NE subarctic Pacific”. In: Marine Ecology Progress Series 136, pp. 179–193. URL: https://www.intres.com/abstracts/meps/v136/p179-193/.

Boyd, Philip W. and Scott C. Doney (2002). “Modelling regional responses by marinepelagic ecosystems to global climate change”. In: Geophysical Research Letters 29.16, pp. 53–1–53–4. ISSN: 1944-8007. DOI: 10.1029/2001GL014130. URL: http://dx.doi.org/10.1029/2001GL014130.

Boyd, Philip W. et al. (2013). “Marine Phytoplankton Temperature versus Growth Responses from Polar to Tropical Waters – Outcome of a Scientific Community-Wide Study”. In: PLoSONE 8.5, e63091. ISSN: 1932-6203. DOI: 10.1371/journal.pone.0063091. URL: http://www.ncbi.nlm.nih.gov/pmc/articles/PMC3660375/.

Boyd, Philip W. et al. (2014). “Biological ramifications of climate-change-mediated oceanic multi-stressors”. In: Nature Climate Change 5, p. 71. DOI: 10.1038/nclimate2441https://www.nature.com/articles/nclimate2441 #

Boyer Montégut, Clément de et al. (2004). “Mixed layer depth over the global ocean: An examination of profile data and a profile-based climatology”. In: Journal of Geophysical Research: Oceans 109.C12, n/a–n/a. ISSN: 2156-2202. DOI: 10.1029/2004JC002378. URL: http://dx.doi.org/10.1029/2004JC002378.

Bracher, A. et al. (2009). “Quantitative observation of cyanobacteria and diatoms from space using PhytoDOAS on SCIAMACHY data”. In: Biogeosciences 6.5, pp. 751–764. ISSN: 17264189. DOI: 10.5194/bg-6-751-2009. URL: https://www.biogeosciences.net/6/751/2009/.

Bracher, Astrid et al. (2017). “Obtaining Phytoplankton Diversity from Ocean Color: A Scientific Roadmap for Future Development”. In: Frontiers in Marine Science 4, p. 55. ISSN: 2296-7745. URL: http://journal.frontiersin.org/article/10.3389/fmars.2017.00055.

Brewin, Robert J. W. et al. (2010). “A three-component model of phytoplankton size class for the Atlantic Ocean”. In: Ecological Modelling 221.11, pp. 1472–1483. ISSN: 0304-3800. DOI: https://doi.org/10.1016/j.ecolmodel.2010.02.014. URL: http://www.sciencedirect.com/science/article/pii/S0304380010001092.

Brewin, Robert J.W. et al. (2011). “An intercomparison of bio-optical techniques for detecting dominant phytoplankton size class from satellite remote sensing”. In: Remote Sensing of

Environment 115.2, pp. 325–339. ISSN: 0034-4257. DOI: https://doi.org/10.1016/j.rse.2010.09.004. URL: http://www.sciencedirect.com/science/article/pii/S0034425710002774.

Bricaud, A., A. M. Ciotti, and B. Gentili (2012). “Spatial-temporal variations in phytoplankton size and colored detrital matter absorption at global and regional scales, as derived from twelve years of SeaWiFS data (1998–2009)”. In: Global Biogeochemical Cycles 26.1. ISSN: 0886-6236. DOI: 10.1029/2010GB003952. URL: https://doi.org/10.1029/2010GB003952.

Bricaud, Annick et al. (2010). “Light absorption properties and absorption budget of Southeast Pacific waters”. In: Journal of Geophysical Research: Oceans 115.C8. ISSN: 0148-0227. DOI: 10.1029/2009JC005517.URL:https://doi.org/10.1029/2009JC005517.

Brody, Sarah R. and M. Susan Lozier (2014). “Changes in dominant mixing length scales as a driver of subpolar phytoplankton bloom initiation in the North Atlantic”. In: Geophysical

Research Letters 41.9, pp. 3197–3203. ISSN: 00948276. DOI: 10.1002/2014gl059707.– (2015). “Characterizing upper-ocean mixing and its effect on the spring phytoplankton bloom within situdata”. In: ICES Journal of Marine Science: Journal du Conseil 72.6, pp. 1961–1970. ISSN: 1054-3139 1095-9289. DOI: 10.1093/icesjms/fsv006.

Buesseler, Ken O. and Philip W. Boyd (2009). “Shedding light on processes that control particle export and flux attenuation in the twilight zone of the open ocean”. In: Limnology and Oceanography 54.4, pp. 1210–1232. ISSN: 0024-3590. DOI: 10.4319/lo.2009.54.4.1210. URL: https://doi.org/10.4319/lo.2009.54.4.1210.

Cabré, A. et al. (2015). “Oxygen minimum zones in the tropical Pacific across CMIP5 models: mean state differences and climate change trends”. In: Biogeosciences Discussions 12.8, pp. 6525–6587. ISSN: 1810-6285. DOI: 10.5194/bgd-12-6525-2015.

Cabré, Anna, Irina Marinov, and Shirley Leung (2015). “Consistent global responses of marine ecosystems to future climate change across the IPCC AR5 earth system models”. In: Climate Dynamics 45.5, pp. 1253–1280. ISSN: 1432-0894. DOI: 10.1007/s00382-014-2374-3. URL: http://dx.doi.org/10.1007/s00382-014-2374-3.

Cabré, Anna et al. (2016). “Phenology of Size-Partitioned Phytoplankton Carbon-Biomass from Ocean Color Remote Sensing and CMIP5 Models”. In: Frontiers in Marine Science 3.39. ISSN: 2296-7745. DOI: 10.3389/fmars.2016.00039. URL: http://journal.frontiersin.org/article/10.3389/fmars.2016.00039.

Campbell, Janet et al. (2002). “Comparison of algorithms for estimating ocean primary production from surface chlorophyll, temperature, and irradiance”. In: Global Biogeochemical Cycles 16.3, pp. 9–1–9–15. ISSN: 0886-6236. DOI: 10 . 1029 / 2001GB001444. URL: https://doi.org/10.1029/2001GB001444.

Capotondi, Antonietta and Prashant D. Sardeshmukh (2017). “Is El Niño really changing?” In: Geophysical Research Letters 44.16, pp. 8548–8556. ISSN: 0094-8276. DOI: 10.1002/ 2017GL074515. URL: https://doi.org/10.1002/2017GL074515.

Capotondi, Antonietta et al. (2012). “Enhanced upper ocean stratification with climate change in the CMIP3 models”. In: Journal of Geophysical Research: Oceans 117.C4. ISSN: 0148-0227. DOI: 10.1029/2011JC007409. URL: https://doi.org/10.1029/2011JC007409.

Capotondi, Antonietta et al. (2014). “Understanding ENSO Diversity”. In: Bulletin of the American Meteorological Society 96.6, pp. 921–938. ISSN: 0003-0007. DOI: 10.1175/BAMSD-13-00117.1. URL: https://doi.org/10.1175/BAMS-D-13-00117.1.

Carr, Mary-Elena et al. (2006). “A comparison of global estimates of marine primary production from ocean color”. In: Deep Sea Research Part II: Topical Studies in Oceanography. 53.5-7, pp. 741–770. ISSN: 09670645. DOI: 10.1016/j.dsr2.2006.01.028.

Carter, B. R. et al. (2016). “When can ocean acidification impacts be detected from decadal alkalinity measurements?” In: Global Biogeochemical Cycles 30.4, pp. 595–612. ISSN: 0886-6236. DOI: 10.1002/2015GB005308. URL: https://doi.org/10.1002/2015GB005308.

Carton, James A., Gennady Chepurin, and Xianhe Cao (2000). “A Simple Ocean Data Assimilation Analysis of the Global Upper Ocean 1950–95. Part II: Results”. In: Journal of Physical Oceanography 30.2, pp. 311–326. ISSN: 0022-3670. DOI: 10.1175/1520-0485(2000)030<0311:ASODAA> 2.0.CO;2. URL: http://dx.doi.org/10.1175/1520-0485(2000)030<0311:ASODAA>2.0.CO;2.

Carton, James A. and Benjamin S. Giese (2008). “A Reanalysis of Ocean Climate Using Simple Ocean Data Assimilation (SODA)”. In: Monthly Weather Review 136.8, pp. 2999–3017. ISSN: 0027-0644 1520-0493. DOI: 10.1175/2007mwr1978.1.

Chavez, F. P. et al. (1999). “Biological and Chemical Response of the Equatorial Pacific Ocean to the 1997-98 El Niño”. In: Science 286.5447, p. 2126. URL: http://science. sciencemag.org/content/286/5447/2126.abstract.

Chavez, F. P. et al. (2002). “Biological and chemical consequences of the 1997–1998 El Niño in central California waters”. In: Progress in Oceanography 54.1, pp. 205–232. ISSN: 0079- 6611. DOI: https://doi.org/10.1016/S0079-6611(02)00050-2. URL: http://www.sciencedirect.com/science/article/pii/S0079661102000502.

Chavez, Francisco P., Peter G. Strutton, and Michael J. McPhaden (1998). “Biological physical coupling in the Central Equatorial Pacific during the onset of the 1997–98 El Niño”. In: Geophysical Research Letters 25.19, pp. 3543–3546. ISSN: 1944-8007. DOI: 10.1029/98GL02729. URL: http://dx.doi.org/10.1029/98GL02729.

Chavez, Francisco P. et al. (2003). “From Anchovies to Sardines and Back: Multidecadal Change in the Pacific Ocean”. In: Science 299.5604, p. 217. URL: http://science. sciencemag.org/content/299/5604/217.abstract.

Chenillat, F. et al. (2012). “North Pacific Gyre Oscillation modulates seasonal timing and ecosystem functioning in the California Current upwelling system”. In: Geophysical Research Letters 39.1. ISSN: 0094-8276. DOI: 10.1029/2011GL049966. URL: https://doi.org/10.1029/2011GL049966.

Chisholm, SallieW. (1992). “Phytoplankton Size”. In: Primary Productivity and Biogeochemical Cycles in the Sea. Ed. by Paul G. Falkowski, Avril D. Woodhead, and Katherine Vivirito. Boston, MA: Springer US, pp. 213–237. ISBN: 978-1-4899-0762-2. DOI: 10.1007/978-1-4899-0762-2_12. URL: https://doi.org/10.1007/978-1-4899-0762-2_12.

Chiswell, Stephen M. et al. (2013). “Climatology of surface chlorophyll-a, autumn-winter and spring blooms in the southwest Pacific Ocean”. In: Journal of Geophysical Research: Oceans 118.2, pp. 1003–1018. ISSN: 21699275. DOI: 10.1002/jgrc.20088.

Christian, J. R. et al. (2001). “Biogeochemical modelling of the tropical Pacific Ocean. I: Seasonal and interannual variability”. In: Deep Sea Research Part II: Topical Studies in Oceanography 49.1–3, pp. 509–543. ISSN: 0967-0645. DOI: http://doi.org/10.1016/S0967-0645(01)00110-2. URL: http://www.sciencedirect.com/science/article/pii/S0967064501001102.

Ciotti, Aurea M. and Annick Bricaud (2006). “Retrievals of a size parameter for phytoplankton and spectral light absorption by colored detrital matter from water-leaving radiances at SeaWiFS channels in a continental shelf region off Brazil”. In: Limnology and Oceanography: Methods 4.7, pp. 237–253. ISSN: 1541-5856. DOI: 10.4319/lom.2006.4.237. URL: https://doi.org/10.4319/lom.2006.4.237.

Cole, Harriet et al. (2012). “Mind the gap: The impact of missing data on the calculation of phytoplankton phenology metrics”. In: Journal of Geophysical Research: Oceans 117.C8. ISSN: 01480227. DOI: 10.1029/2012jc008249.

Corno, Guido et al. (2007). “Impact of climate forcing on ecosystem processes in the North Pacific Subtropical Gyre”. In: Journal of Geophysical Research 112.C4. ISSN: 0148-0227. DOI: 10.1029/2006jc003730.

Dandonneau, Yves et al. (2004). “Seasonal and interannual variability of ocean color and composition of phytoplankton communities in the North Atlantic, equatorial Pacific and South Pacific”. In: Deep Sea Research Part II: Topical Studies in Oceanography 51.1-3, pp. 303–318. ISSN: 09670645. DOI: 10.1016/j.dsr2.2003.07.018.

Dave, Apurva C. and M. Susan Lozier (2010). “Local stratification control of marine productivity in the subtropical North Pacific”. In: Journal of Geophysical Research: Oceans 115.C12, n/a–n/a. ISSN: 2156-2202. DOI: 10.1029/2010JC006507. URL: http://dx.doi.org/10.1029/2010JC006507.

Dave, Apurva C. and M. Susan Lozier (2013). “Examining the global record of interannual variability in stratification and marine productivity in the low-latitude and mid-latitude ocean”. In: Journal of Geophysical Research: Oceans 118.6, pp. 3114–3127. ISSN: 21699275. DOI: 10.1002/jgrc.20224.

Devred, E. et al. (2006). “A two-component model of phytoplankton absorption in the openocean: Theory and applications”. In: Journal of Geophysical Research: Oceans 111.C3. ISSN: 0148-0227. DOI: 10.1029/2005JC002880. URL: https://doi.org/10.1029/2005JC002880.

Di Lorenzo, E. et al. (2008). “North Pacific Gyre Oscillation links ocean climate and ecosystem change”. In: Geophysical Research Letters 35.8. ISSN: 0094-8276. DOI: 10 . 1029 /2007gl032838.

Di Lorenzo, E. et al. (2010). “Central Pacific El Niño and decadal climate change in the North Pacific Ocean”. In: Nature Geoscience 3.11, pp. 762–765. ISSN: 1752-0894 1752-0908. DOI: 10.1038/ngeo984.

Diffenbaugh, Noah S. and Martin Scherer (2011). “Observational and model evidence of global emergence of permanent, unprecedented heat in the 20th and 21st centuries”.In: Climatic Change 107.3, pp. 615–624. ISSN: 1573-1480. DOI: 10.1007/s10584-011-0112-y. URL: https://doi.org/10.1007/s10584-011-0112-y.

Doney, S. C. et al. (2009). “Ocean acidification: the other CO2 problem”. In: Ann Rev Mar Sci 1, pp. 169–92. ISSN: 1941-1405 (Print) 1941-0611 (Linking). DOI: 10.1146/annurev.marine.010908.163834. URL: https://www.ncbi.nlm.nih.gov/pubmed/21141034.

Dufois, François et al. (2016). “Anticyclonic eddies are more productive than cyclonic eddies in subtropical gyres because of winter mixing”. In: Science Advances 2.5. URL: http://advances.sciencemag.org/content/2/5/e1600282.abstract.

Dunne, John P. et al. (2005). “Empirical and mechanistic models for the particle export ratio”. In: Global Biogeochemical Cycles 19.4. ISSN: 0886-6236. DOI: 10.1029/2004GB002390. URL: https://doi.org/10.1029/2004GB002390.

Dunne, John P. et al. (2012). “GFDL’s ESM2 Global Coupled Climate–Carbon Earth System Models. Part II: Carbon System Formulation and Baseline Simulation Characteristics”. In: Journal of Climate 26.7, pp. 2247–2267. ISSN: 0894-8755. DOI: 10.1175/JCLI-D-12- 00150.1. URL: https://doi.org/10.1175/JCLI-D-12-00150.1.

DuRand, Michele D., Robert J. Olson, and SallieW. Chisholm (2001). “Phytoplankton population dynamics at the Bermuda Atlantic Time-series station in the Sargasso Sea”. In: Deep Sea Research Part II: Topical Studies in Oceanography 48.8, pp. 1983–2003. ISSN: 0967-0645. DOI: https://doi.org/10.1016/S0967-0645(00)00166-1. URL: http://www.sciencedirect.com/science/article/pii/S0967064500001661.

Dutkiewicz, S. et al. (2015). “Capturing optically important constituents and properties in a marine biogeochemical and ecosystem model”. In: Biogeosciences 12.14, pp. 4447–4481. ISSN: 1726-4189. DOI: 10.5194/bg- 12- 4447- 2015. URL: https://www.biogeosciences.net/12/4447/2015/.

Dutkiewicz, Stephanie et al. (2001). “Interannual variability of phytoplankton abundances in the North Atlantic”. In: Deep Sea Research Part II: Topical Studies in Oceanography 48.10, pp. 2323–2344. ISSN: 0967-0645. DOI: http://doi.org/10.1016/S0967-0645(00)00178- 8. URL: http://www.sciencedirect.com/science/article/pii/S0967064500001788.

Edwards, Kyle F. et al. (2012). “Allometric scaling and taxonomic variation in nutrient utilization traits and maximum growth rate of phytoplankton”. In: Limnology and Oceanography 57.2, pp. 554–566. ISSN: 0024-3590. DOI: 10.4319/lo.2012.57.2.0554. URL: https://doi.org/10.4319/lo.2012.57.2.0554.

Eppley, Richard W. and Bruce J. Peterson (1979). “Particulate organic matter flux and planktonic new production in the deep ocean”. In: Nature 282.5740, pp. 677–680. URL: http://dx.doi.org/10.1038/282677a0.

Evans, Geoffrey T. and John S. Parslow (1985). “A Model of Annual Plankton Cycles”. In: Biological Oceanography 3.3, pp. 327–347. ISSN: 0196-5581. DOI: 10.1080/01965581. 1985.10749478. URL: https://www.tandfonline.com/doi/abs/10.1080/01965581.1985.10749478.

Feng, Juan and Jianping Li (2011). “Influence of El Niño Modoki on spring rainfall over south China”. In: Journal of Geophysical Research: Atmospheres 116.D13. ISSN: 0148-0227. DOI:10.1029/2010JD015160. URL: https://doi.org/10.1029/2010JD015160.

Ferrari, Raffaele, Sophia T. Merrifield, and John R. Taylor (2015). “Shutdown of convection triggers increase of surface chlorophyll”. In: Journal of Marine Systems 147, pp. 116–122. ISSN: 09247963. DOI: 10.1016/j.jmarsys.2014.02.009.

Field, Christopher B. et al. (1998). “Primary Production of the Biosphere: Integrating Terrestrial and Oceanic Components”. In: Science 281.5374, pp. 237–240. ISSN: 0036-8075. DOI: 10.1126/science.281.5374.237.eprint:http://science.sciencemag.org/content/281/5374/237.full.pdf . URL: http://science.sciencemag.org/content/281/5374/237.

Finkel, V. Zoe, J. Irwin Andrew, and Schofield Oscar (2004). “Resource limitation alters the 3/4 size scaling of metabolic rates in phytoplankton”. In: Marine Ecology Progress Series 273, pp. 269–279. URL: http://www.int- res.com/abstracts/meps/v273/p269-279/.

Finkel, Zoe Vanessa (2001). “Light absorption and size scaling of light-limited metabolism in marine diatoms”. In: Limnology and Oceanography 46.1, pp. 86–94. ISSN: 1939-5590. DOI: 10.4319/lo.2001.46.1.0086. URL: http://dx.doi.org/10.4319/lo.2001.46.1.0086.

Freeman, Natalie M. and Nicole S. Lovenduski (2015). “Decreased calcification in the Southern Ocean over the satellite record”. In: Geophysical Research Letters 42.6, pp. 1834–1840. ISSN: 1944-8007. DOI: 10.1002/2014GL062769. URL: http://dx.doi.org/10.1002/2014GL062769.

Friedrichs, Marjorie A. M. et al. (2007). “Assessment of skill and portability in regional marine biogeochemical models: Role of multiple planktonic groups”. In: Journal of Geophysical Research 112.C8. ISSN: 0148-0227. DOI: 10.1029/2006jc003852.

Gierach, Michelle M. et al. (2012). “Biological response to the 1997-98 and 2009-10 El Niño events in the equatorial Pacific Ocean”. In: Geophysical Research Letters 39.10. ISSN: 00948276. DOI: 10.1029/2012gl051103.

Gnanadesikan, Anand and Whit G. Anderson (2009). “OceanWater Clarity and the Ocean General Circulation in a Coupled Climate Model”. In: Journal of Physical Oceanography 39.2, pp. 314–332. ISSN: 0022-3670. DOI: 10.1175/2008JPO3935.1. URL: https://doi.org/10.1175/2008JPO3935.1.

Gordon, R. Michael, Kenneth H. Coale, and Kenneth S. Johnson (1997). “Iron distributions in the equatorial Pacific: Implications for new production”. In: Limnology and Oceanography 42.3, pp. 419–431. ISSN: 1939-5590. DOI: 10.4319/lo.1997.42.3.0419. URL: http://dx.doi.org/10.4319/lo.1997.42.3.0419.

Graff, Jason R., Allen J. Milligan, and Michael J. Behrenfeld (2012). “The measurement of phytoplankton biomass using flow-cytometric sorting and elemental analysis of carbon”. In: Limnology and Oceanography: Methods 10.11, pp. 910–920. ISSN: 1541-5856. DOI: 10.4319/lom.2012.10.910. URL: https://doi.org/10.4319/lom.2012.10.910.

Gregg, W. W. and C. S. Rousseaux (2014). “Decadal trends in global pelagic ocean chlorophyll: A new assessment integrating multiple satellites, in situ data, and models”. In: J Geophys Res Oceans 119.9, pp. 5921–5933. ISSN: 2169-9275 (Print) 2169-9275 (Linking).DOI: 10.1002/2014JC010158. URL: https://www.ncbi.nlm.nih.gov/pubmed/26213675.

Gregg, Watson W. (2005a). “Recent trends in global ocean chlorophyll”. In: Geophysical Research Letters 32.3. ISSN: 0094-8276. DOI: 10.1029/2004gl021808.

Gregg, Watson W. (2005b). “Recent trends in global ocean chlorophyll”. In: Geophysical Research Letters 32.3. ISSN: 0094-8276. DOI: 10.1029/2004gl021808.

Gregg, Watson W. and Cécile S. Rousseaux (2016). “Directional and Spectral Irradiance in Ocean Models: Effects on Simulated Global Phytoplankton, Nutrients, and Primary Production”. In: Frontiers in Marine Science 3, p. 240. ISSN: 2296-7745. URL: https://www.frontiersin.org/article/10.3389/fmars.2016.00240.

Gregg, WatsonW., Cécile S. Rousseaux, and Bryan A. Franz (2017). “Global trends in ocean

phytoplankton: a new assessment using revised ocean colour data”. In: Remote Sensing Letters 8.12, pp. 1102–1111. ISSN: 2150-704X. DOI: 10.1080/2150704X.2017.1354263. URL: https://doi.org/10.1080/2150704X.2017.1354263.

Gregg, Watson W. et al. (2003). “Ocean primary production and climate: Global decadal changes”. In: Geophysical Research Letters 30.15. ISSN: 00948276. DOI: 10.1029/2003gl016889.

Hare, Steven R. and Nathan J. Mantua (2000). “Empirical evidence for North Pacific regime shifts in 1977 and 1989”. In: Progress in Oceanography 47.2, pp. 103–145. ISSN: 0079-6611. DOI: https://doi.org/10.1016/S0079-6611(00)00033-1.URL: http://www.sciencedirect.com/science/article/pii/S0079661100000331.

Harrison, P. J. (2006). “SERIES (subarctic ecosystem response to iron enrichment study): A Canadian–Japanese contribution to our understanding of the iron–ocean–climate connection”. In: Deep Sea Research Part II: Topical Studies in Oceanography 53.20-22, pp. 2006–2011. ISSN: 09670645. DOI: 10.1016/j.dsr2.2006.08.001.

Harrison, P. J. et al. (1999). “Comparison of factors controlling phytoplankton productivity in the NE and NW subarctic Pacific gyres”. In: Progress in Oceanography 43.2-4, pp. 205–234. ISSN: 00796611. DOI: 10.1016/s0079-6611(99)00015-4.

Harrison, Paul J. (2002). “Station Papa Time Series: Insights into Ecosystem Dynamics”. In: Journal of Oceanography 58.2, pp. 259–264. ISSN: 1573-868X. DOI: 10.1023/A: 1015857624562. URL: https://doi.org/10.1023/A:1015857624562.

Harrison, Paul J. et al. (2004). “Nutrient and Plankton Dynamics in the NE and NW Gyres of the Subarctic Pacific Ocean”. In: Journal of Oceanography 60.1, pp. 93–117. ISSN: 1573-868X. DOI: 10.1023/B:JOCE.0000038321.57391.2a. URL: https://doi.org/10.1023/B:JOCE.0000038321.57391.2a.

Hashioka, T. et al. (2013). “Phytoplankton competition during the spring bloom in four plankton functional type models”. In: Biogeosciences 10.11, pp. 6833–6850. ISSN: 1726-4189. DOI: 10.5194/bg-10-6833-2013. URL: https://www.biogeosciences.net/10/6833/2013/.

Hawkins, E. and R. Sutton (2012). “Time of emergence of climate signals”. In: Geophysical Research Letters 39.1. ISSN: 0094-8276. DOI: 10.1029/2011GL050087. URL: https://doi.org/10.1029/2011GL050087.

Henson, S. A. et al. (2010). “Detection of anthropogenic climate change in satellite records of ocean chlorophyll and productivity”. In: Biogeosciences 7.2, pp. 621–640. ISSN: 1726-4189. DOI: 10.5194/bg-7-621-2010. URL: http://www.biogeosciences.net/7/621/2010/.

Henson, Stephanie A., Claudie Beaulieu, and Richard Lampitt (2016). “Observing climate change trends in ocean biogeochemistry: when and where”. In: Global Change Biology 22.4, pp. 1561–1571. ISSN: 1354-1013. DOI: 10.1111/gcb.13152. URL: https://doi.org/10.1111/gcb.13152.

Henson, Stephanie A., John P. Dunne, and Jorge L. Sarmiento (2009). “Decadal variability in North Atlantic phytoplankton blooms”. In: Journal of Geophysical Research 114.C4. ISSN:0148-0227. DOI: 10.1029/2008jc005139.

Henson, Stephanie A. et al. (2009). “Decadal variability in biogeochemical models: Comparison with a 50-year ocean colour dataset”. In: Geophysical Research Letters 36.21. ISSN: 0094-8276. DOI: 10.1029/2009gl040874.

Henson, Stephanie A. et al. (2017). “Rapid emergence of climate change in environmental drivers of marine ecosystems”. In: Nature Communications 8, p.14682. DOI: 10.1038/ncomms14682https://www.nature.com/articles/ncomms14682 #supplementary-information. URL: http://dx.doi.org/10.1038/ncomms14682.

Hinder, Stephanie L. et al. (2012). “Changes in marine dinoflagellate and diatom abundance under climate change”. In: Nature Clim. Change 2.4, pp. 271–275. ISSN: 1758-678X. DOI: http : / / www.nature.com/nclimate/journal/v2/n4/abs/nclimate1388.html#supplementary- information. URL: http://dx.doi.org/10.1038/nclimate1388.

Hirata, T. et al. (2011). “Synoptic relationships between surface Chlorophyll-a and diagnostic pigments specific to phytoplankton functional types”. In: Biogeosciences 8.2, pp. 311–327. ISSN: 1726-4189. DOI: 10.5194/bg-8-311-2011. URL: http://www.biogeosciences.net/8/311/2011/.

Hirata, Takafumi, Nick Hardman-Mountford, and Robert J. W. Brewin (2012). “Comparing satellite-based phytoplankton classification methods”. In: Eos, Transactions American Geophysical Union 93.6, pp. 59–60. ISSN: 2324-9250. DOI: 10.1029/2012EO060008. URL: http://dx.doi.org/10.1029/2012EO060008.

Iglesias-Rodriguez, M. Debora et al. (2008). “Phytoplankton Calcification in a High COlt;subgt;2lt;/subgt; World”. In: Science 320.5874, p. 336. URL: http://science. sciencemag.org/content/320/5874/336.abstract.

Ilyina, Tatiana et al. (2013). “Global ocean biogeochemistry model HAMOCC: Model architecture and performance as component of the MPI-Earth system model in different

CMIP5 experimental realizations”. In: Journal of Advances in Modeling Earth Systems 5.2, pp. 287–315. ISSN: 1942-2466. DOI: 10.1029/2012MS000178. URL: https://doi.org/10.1029/2012MS000178.

Irwin, Andrew J. and Matthew J. Oliver (2009). “Are ocean deserts getting larger?” In: Geophysical Research Letters 36.18. ISSN: 0094-8276. DOI: 10.1029/2009gl039883.

Jerlov, N. G. (1953). “Influence of Suspended and Dissolved Matter on the Transparency of Sea Water”. In: Tellus 5.1, pp. 59–65. ISSN: 0040-2826. DOI: 10.1111/j.2153-3490.1953.tb01036.x. URL: https://doi.org/10.1111/j.2153- 3490.1953.tb01036.x.

Jin, X. et al. (2006). “Diagnosing the contribution of phytoplankton functional groups to the production and export of particulate organic carbon, CaCO3, and opal from global nutrient and alkalinity distributions”. In: Global Biogeochemical Cycles 20.2. ISSN: 0886-6236. DOI: 10.1029/2005GB002532. URL: https://doi.org/10.1029/2005GB002532.

Johnson, Gregory C. et al. (2002). “Direct measurements of upper ocean currents and water properties across the tropical Pacific during the 1990s”. In: Progress in Oceanography 52.1, pp. 31–61. ISSN: 0079-6611. DOI: https://doi.org/10.1016/S0079-6611(02)00021- 6. URL: http://www.sciencedirect.com/science/article/pii/S0079661102000216.

Kahru, M. et al. (2010). “Global correlations between winds and ocean chlorophyll”. In: Journal of Geophysical Research 115.C12. ISSN: 0148-0227. DOI: 10.1029/2010jc006500.

Kao, Hsun-Ying and Jin-Yi Yu (2009). “Contrasting Eastern-Pacific and Central-Pacific Types of ENSO”. In: Journal of Climate 22.3, pp. 615–632. ISSN: 0894-8755 1520-0442. DOI:10.1175/2008jcli2309.1.

Karl, D. M., R. R. Bidigare, and R. M. Letelier (2001). “Long-term changes in plankton community structure and productivity in the North Pacific Subtropical Gyre: The domain shift hypothesis”. In: Deep Sea Research Part II: Topical Studies in Oceanography 48.8, pp. 1449–1470. ISSN: 0967-0645. DOI: https://doi.org/10.1016/S0967-0645(00) 00149 - 1. URL: http://www.sciencedirect.com/science/article/pii/S0967064500001491.

Kearney, K. A., C. Stock, and J. L. Sarmiento (2013). “Amplification and attenuation of increased primary production in a marine food web”. In: Marine Ecology Progress Series 491, pp. 1–14. ISSN: 0171-8630 1616-1599. DOI: 10.3354/meps10484.

Kearney, Kelly A., Desiree Tommasi, and Charles Stock (2015). “Simulated ecosystem response to volcanic iron fertilization in the subarctic Pacific Ocean”. In: Fisheries Oceanography 24.5, pp. 395–413. ISSN: 10546006. DOI: 10.1111/fog.12118.

Kim, G. E., M. A. Pradal, and A. Gnanadesikan (2015). “Quantifying the biological impact of surface ocean light attenuation by colored detrital matter in an ESM using a new optical parameterization”. In: Biogeosciences 12.16, pp. 5119–5132. ISSN: 1726-4189. DOI:10.5194/bg-12-5119-2015. URL: https://www.biogeosciences.net/12/5119/2015/.

Kim, Seon Tae and Jin-Yi Yu (2012). “The two types of ENSO in CMIP5 models”. In: Geophysical Research Letters 39.11, n/a–n/a. ISSN: 00948276. DOI: 10.1029/2012gl052006.

Kostadinov, T. S., D. A. Siegel, and S. Maritorena (2009). “Retrieval of the particle size distribution from satellite ocean color observations”. In: Journal of Geophysical Research 114.C9. ISSN: 0148-0227. DOI: 10.1029/2009jc005303.

– (2010). “Global variability of phytoplankton functional types from space: assessment via the particle size distribution”. In: Biogeosciences 7.10, pp. 3239–3257. ISSN: 1726-4189. DOI: 10.5194/bg-7-3239-2010.

Kostadinov, T. S. et al. (2016). “Carbon-based phytoplankton size classes retrieved via ocean color estimates of the particle size distribution”. In: Ocean Sci. 12.2, pp. 561–575. ISSN: 1812-0792. DOI: 10.5194/os- 12- 561- 2016. URL: http://www.oceansci.net/12/561/2016/.

Kostadinov, Tihomir S. et al. (2017). “Inter-comparison of phytoplankton functional type phenology metrics derived from ocean color algorithms and Earth System Models”. In: Remote Sensing of Environment 190, pp. 162–177. ISSN: 0034-4257. DOI: http://doi.org/10.1016/j.rse.2016.11.014. URL: http://www.sciencedirect.com/science/article/pii/S003442571630459X.

Krumhardt, Kristen M. et al. (2016). “Apparent increase in coccolithophore abundance in the subtropical North Atlantic from 1990 to 2014”. In: Biogeosciences 13.4, pp. 1163–1177. ISSN: 1726-4189. DOI: 10.5194/bg-13-1163-2016.

Kruskopf, Mikaela and Kevin J. Flynn (2005). “Chlorophyll content and fluorescence responses cannot be used to gauge reliably phytoplankton biomass, nutrient status or growth rate”. In: New Phytologist 169.3, pp. 525–536. ISSN: 0028-646X. DOI: 10.1111/j.1469-8137.2005.01601.x. URL: https://doi.org/10.1111/j.1469-8137.2005.01601.x.

Kug, Jong-Seong, Fei-Fei Jin, and Soon-Il An (2009). “Two Types of El Niño Events: Cold Tongue El Niño andWarm Pool El Niño”. In: Journal of Climate 22.6, pp. 1499–1515. ISSN: 0894-8755 1520-0442. DOI: 10.1175/2008jcli2624.1.

Kvale, K. F. and K. J. Meissner (2017). “Primary production sensitivity to phytoplankton light attenuation parameter increases with transient forcing”. In: Biogeosciences 14.20, pp. 4767–4780. ISSN: 1726-4189. DOI: 10.5194/bg- 14- 4767- 2017. URL: https://www.biogeosciences.net/14/4767/2017/.

Laufkötter, C., M. Vogt, and N. Gruber (2013). “Long-term trends in ocean plankton production and particle export between 1960–2006”. In: Biogeosciences 10.11, pp. 7373–7393. ISSN: 1726-4189. DOI: 10.5194/bg-10-7373-2013. URL: http://www.biogeosciences.net/10/7373/2013/.

Laws, Edward A. and T. T. Bannister (1980). “Nutrient- and light-limited growth of Thalassiosira fluviatilis in continuous culture, with implications for phytoplankton growth in the ocean1”. In: Limnology and Oceanography 25.3, pp. 457–473. ISSN: 1939-5590. DOI: 10.4319/lo.1980.25.3.0457. URL: http://dx.doi.org/10.4319/lo.1980.25.3.0457.

Laës, A. et al. (2003). “Deep dissolved iron profiles in the eastern North Atlantic in relation to water masses”. In: Geophysical Research Letters 30.17. ISSN: 0094-8276. DOI: 10.1029/2003GL017902. URL: https://doi.org/10.1029/2003GL017902.

Lehahn, Yoav et al. (2017). “Dispersion/dilution enhances phytoplankton blooms in lownutrient waters”. In: Nature Communications 8, p. 14868. ISSN: 2041-1723. DOI: 10.1038/ncomms14868. URL: http ://www.ncbi.nlm.nih.gov/pmc/articles/PMC5380962/.

Levitus, S. et al. (2009). “Global ocean heat content 1955–2008 in light of recently revealed instrumentation problems”. In: Geophysical Research Letters 36.7. ISSN: 0094-8276. DOI: 10.1029/2008GL037155. URL: https://doi.org/10.1029/2008GL037155.

Levitus, Sydney et al. (2000). “Warming of the World Ocean”. In: Science 287.5461, p. 2225. URL: http://science.sciencemag.org/content/287/5461/2225.abstract.

Litchman, E., C. A. Klausmeier, and K. Yoshiyama (2009). “Contrasting size evolution in marine and freshwater diatoms”. In: Proc Natl Acad Sci U S A 106.8, pp. 2665–70. ISSN:1091-6490 (Electronic) 0027-8424 (Linking). DOI: 10.1073/pnas.0810891106. URL: https://www.ncbi.nlm.nih.gov/pubmed/19202058.

Litchman, Elena and Christopher A. Klausmeier (2008). “Trait-Based Community Ecology of Phytoplankton”. In: Annual Review of Ecology, Evolution, and Systematics 39.1, pp. 615–639. ISSN: 1543-592X 1545-2069. DOI: 10.1146/annurev.ecolsys.39.110707.173549.

Litchman, Elena et al. (2015). “Global biogeochemical impacts of phytoplankton: a traitbased perspective”. In: Journal of Ecology 103.6, pp. 1384–1396. ISSN: 1365-2745. DOI: 10.1111/1365-2745.12438. URL: http://dx.doi.org/10.1111/1365-2745.12438.

Loisel, H. et al. (2011). “Characterization of the bio-optical anomaly and diurnal variability of particulate matter, as seen from scattering and backscattering coefficients, in ultra-oligotrophic eddies of the Mediterranean Sea”. In: Biogeosciences 8.11, pp. 3295–3317. ISSN: 1726-4189. DOI: 10.5194/bg-8-3295-2011. URL: https://www.biogeosciences.net/8/3295/2011/.

Lomas, M. W. et al. (2010). “Increased ocean carbon export in the Sargasso Sea linked to climate variability is countered by its enhanced mesopelagic attenuation”. In: Biogeosciences 7.1, pp. 57-70. ISSN: 1726-4189. DOI: 10.5194/bg-7-57-2010. URL: http://www.biogeosciences.net/7/57/2010/.

Lozier, M. Susan et al. (2011). “On the relationship between stratification and primary productivity in the North Atlantic”. In: Geophysical Research Letters 38.18, n/a–n/a. ISSN: 00948276. DOI: 10.1029/2011gl049414.

Lundry, Michael R. et al. (2003). “Iron and grazing constraints on primary production in the central equatorial Pacific: An EqPac synthesis”. In: Limnology and Oceanography 42.3, pp. 405–418. ISSN: 0024-3590. DOI: 10.4319/lo.1997.42.3.0405. URL: https://doi.org/10.4319/lo.1997.42.3.0405.

Lyu, Kewei et al. (2014). “Time of emergence for regional sea-level change”. In: Nature Climate Change 4, p. 1006. DOI: 10.1038/nclimate2397https://www.nature.

com/articles/nclimate2397#supplementary-information. URL: http://dx.doi.org/10.1038/nclimate2397.

Mackinson, B. L. et al. (2015). “Estimates of micro-, nano-, and picoplankton contributions to particle export in the northeast Pacific”. In: Biogeosciences 12.11, pp. 3429–3446. ISSN: 1726-4189. DOI: 10.5194/bg- 12- 3429- 2015. URL: https://www.biogeosciences.net/12/3429/2015/.

Mahadevan, Amala et al. (2012). “Eddy-Driven Stratification Initiates North Atlantic Spring Phytoplankton Blooms”. In: Science 337.6090, p. 54. URL: http://science.sciencemag.org/content/337/6090/54.abstract.

Mahlstein, Irina, Gabriele Hegerl, and Susan Solomon (2012). “Emerging local warming signals in observational data”. In: Geophysical Research Letters 39.21. ISSN: 0094-8276. DOI: 10.1029/2012GL053952. URL: https://doi.org/10.1029/2012GL053952.

Maldonado, Maria T. et al. (1999). “Co-limitation of phytoplankton growth by light and Fe during winter in the NE subarctic Pacific Ocean”. In: Deep Sea Research Part II: Topical Studies in Oceanography 46.11, pp. 2475–2485. ISSN: 0967-0645. DOI: https://doi.org/10.1016/S0967-0645(99)00072-7. URL: http://www.sciencedirect.com/science/article/pii/S0967064599000727.

Mantua, Nathan J. and Steven R. Hare (2002). “The Pacific Decadal Oscillation”. In: Journal of Oceanography 58.1, pp. 35–44. ISSN: 1573-868X. DOI: 10.1023/A:1015820616384. URL: https://doi.org/10.1023/A:1015820616384.

Mantua, Nathan J. et al. (1997). “A Pacific Interdecadal Climate Oscillation with Impacts on Salmon Production*”. In: Bulletin of the American Meteorological Society 78.6, pp. 1069–1080. ISSN: 0003-0007. DOI: 10.1175/1520- 0477(1997)078<1069:APICOW> 2.0.CO;2. URL: https://doi.org/10.1175/1520- 0477(1997)078<1069:APICOW>2.0.CO;2.

Maranon, E. (2015). “Cell size as a key determinant of phytoplankton metabolism and community structure”. In: Ann Rev Mar Sci 7, pp. 241–64. ISSN: 1941-0611 (Electronic) 1941-0611 (Linking). DOI: 10.1146/annurev-marine-010814-015955. URL: https://www.ncbi.nlm.nih.gov/pubmed/25062405.

Maranon, E. et al. (2014). “Resource supply overrides temperature as a controlling factor of marine phytoplankton growth”. In: PLoS One 9.6, e99312. ISSN: 1932-6203 (Electronic)

1932-6203 (Linking). DOI: 10.1371/journal.pone.0099312. URL: https://www.ncbi.nlm.nih.gov/pubmed/24921945.

Marchetti, Adrian et al. (2006). “Iron requirements of the pennate diatom Pseudo-nitzschia: Comparison of oceanic (high-nitrate, low-chlorophyll waters) and coastal species”. In: Limnology and Oceanography 51.5, pp. 2092–2101. ISSN: 0024-3590. DOI: 10.4319/lo.2006.51.5.2092. URL: https://doi.org/10.4319/lo.2006.51.5.2092.

Marinov, Irina et al. (2013). “North-South asymmetry in the modeled phytoplankton community response to climate change over the 21st century”. In: Global Biogeochemical Cycles 27.4, pp. 1274–1290. ISSN: 1944-9224. DOI: 10.1002/2013GB004599. URL: http://dx.doi.org/10.1002/2013GB004599.

Martin, J. H. et al. (1994). “Testing the iron hypothesis in ecosystems of the equatorial Pacific Ocean”. In: Nature 371, p. 123. DOI: 10.1038/371123a0. URL: http://dx.doi.org/10.1038/371123a0.

Martin, John H. (1990). “Glacial-interglacial CO2 change: The Iron Hypothesis”. In: Paleoceanography 5.1, pp. 1–13. ISSN: 1944-9186. DOI: 10.1029/PA005i001p00001. URL: http://dx.doi.org/10.1029/PA005i001p00001.

Martin, John H. and Steve E. Fitzwater (1988). “Iron deficiency limits phytoplankton growth in the north-east Pacific subarctic”. In: Nature 331, p. 341. DOI: 10.1038 /331341a0. URL: http://dx.doi.org/10.1038/331341a0.

Martinez, Elodie, Keitapu Maamaatuaiahutapu, and Vincent Taillandier (2009). “Floating marine debris surface drift: Convergence and accumulation toward the South Pacific subtropical gyre”. In: Marine Pollution Bulletin 58.9, pp. 1347–1355. ISSN: 0025-326X. DOI: https://doi.org/10.1016/j.marpolbul.2009.04.022. URL: http://www.sciencedirect.com/science/article/pii/S0025326X09001787.

Martinez, Elodie et al. (2009). “Climate-Driven Basin-Scale Decadal Oscillations of Oceanic Phytoplankton”. In: Science 326.5957, p. 1253. URL: http://science.sciencemag.org/content/326/5957/1253.abstract.

Mawji, Edward et al. (2015). “The GEOTRACES Intermediate Data Product 2014”. In: Marine Chemistry 177, pp. 1–8. ISSN: 0304-4203. DOI: https://doi.org/10.1016/j.marchem.2015.04.005. URL: http://www.sciencedirect.com/science/article/pii/S0304420315000997.

McClain, Charles R., Sergio R. Signorini, and James R. Christian (2004). “Subtropical gyre variability observed by ocean-color satellites”. In: Deep Sea Research Part II: Topical Studies in Oceanography 51.1-3, pp. 281–301. ISSN: 09670645. DOI: 10.1016/j.dsr2.2003.08.002.

McKinley, Galen A. et al. (2016). “Timescales for detection of trends in the ocean carbon sink”. In: Nature 530, p. 469. DOI: 10.1038/nature16958. URL: http://dx.doi.org/10.1038/nature16958.

McPhaden, M. J., T. Lee, and D. McClurg (2011). “El Niño and its relationship to changing background conditions in the tropical Pacific Ocean”. In: Geophysical Research Letters 38.15. ISSN: 00948276. DOI: 10.1029/2011gl048275.

McPhaden, Michael J. et al. (1998). “The Tropical Ocean-Global Atmosphere observing system: A decade of progress”. In: Journal of Geophysical Research: Oceans 103.C7, pp. 14169–14240. ISSN: 0148-0227. DOI: 10.1029/97JC02906. URL: https://doi.org/10.1029/97JC02906.

Menden-Deuer, Susanne and Evelyn J. Lessard (2000). “Carbon to volume relationships for dinoflagellates, diatoms, and other protist plankton”. In: Limnology and Oceanography 45.3, pp. 569–579. ISSN: 1939-5590. DOI: 10.4319/lo.2000.45.3.0569. URL: http://dx.doi.org/10.4319/lo.2000.45.3.0569.

Messié, Monique and Francisco P. Chavez (2012). “A global analysis of ENSO synchrony: The oceans’ biological response to physical forcing”. In: Journal of Geophysical Research: Oceans 117.C9, n/a–n/a. ISSN: 01480227. DOI: 10.1029/2012jc007938.

– (2013). “Physical-biological synchrony in the global ocean associated with recent variability in the central and western equatorial Pacific”. In: Journal of Geophysical Research: Oceans 118.8, pp. 3782–3794. ISSN: 21699275. DOI: 10.1002/jgrc.20278.

Messié, Monique and Marie-Hélène Radenac (2006). “Seasonal variability of the surface chlorophyll in the western tropical Pacific from SeaWiFS data”. In: Deep Sea Research Part I: Oceanographic Research Papers 53.10, pp. 1581–1600. ISSN: 09670637. DOI: 10.1016/j. dsr.2006.06.007.

Mobley, Curtis D., Lydia K. Sundman, and Emmanuel Boss (2002). “Phase function effects on oceanic light fields”. In: Applied Optics 41.6, pp. 1035–1050. DOI: 10.1364/AO.41.001035. URL: http://ao.osa.org/abstract.cfm?URI=ao-41-6-1035.

Montes-Hugo, Martin et al. (2009). “Recent Changes in Phytoplankton Communities Associated with Rapid Regional Climate Change Along the Western Antarctic Peninsula”. In: Science 323.5920, p. 1470. URL: http://science.sciencemag.org/content/323/5920/1470.abstract.

Moore, J. Keith, Scott C. Doney, and Keith Lindsay (2004). “Upper ocean ecosystem dynamics and iron cycling in a global three-dimensional model”. In: Global Biogeochemical Cycles 18.4. ISSN: 0886-6236. DOI: 10.1029/2004GB002220. URL: https://doi.org/10.1029/2004GB002220.

Moore, J. Keith et al. (2006). “Nitrogen fixation amplifies the ocean biogeochemical response to decadal timescale variations in mineral dust deposition”. In: Tellus B 58.5, pp. 560–572. ISSN: 0280-6509. DOI: 10.1111/j.1600-0889.2006.00209.x. URL:https://doi.org/10.1111/j.1600-0889.2006.00209.x.

Mora, Camilo et al. (2013). “The projected timing of climate departure from recent variability”. In: Nature 502, p. 183. DOI: 10.1038/nature12540. URL: http://dx.doi.org/10.1038/nature12540.

Mouw, Colleen B. and James A. Yoder (2010). “Optical determination of phytoplankton size composition from global SeaWiFS imagery”. In: Journal of Geophysical Research: Oceans 115.C12, n/a–n/a. ISSN: 2156-2202. DOI: 10.1029/2010JC006337. URL: http://dx.doi.org/10.1029/2010JC006337.

Mouw, Colleen B. et al. (2017). “A Consumer’s Guide to Satellite Remote Sensing of Multiple Phytoplankton Groups in the Global Ocean”. In: Frontiers in Marine Science 4, p. 41. ISSN: 2296-7745. URL: https://www.frontiersin.org/article/10.3389/fmars.2017.00041.

Muggli, Deborah L. and Paul J. Harrison (1996). “EDTA suppresses the growth of oceanic phytoplankton from the Northeast Subarctic Pacific”. In: Journal of Experimental Marine Biology and Ecology 205.1, pp. 221–227. ISSN: 0022-0981. DOI: https://doi.org/10.1016/S0022-0981(96)02611- 1. URL: http://www.sciencedirect.com/science/article/pii/S0022098196026111.

Nelson, David M. et al. (1995). “Production and dissolution of biogenic silica in the ocean: Revised global estimates, comparison with regional data and relationship to biogenic sedimentation”. In: Global Biogeochemical Cycles 9.3, pp. 359–372. ISSN: 0886-6236. DOI: 10.1029/95GB01070. URL: https://doi.org/10.1029/95GB01070.

Nelson, Norman B. and David A. Siegel (2013). “The Global Distribution and Dynamics of Chromophoric Dissolved Organic Matter”. In: Annual Review of Marine Science 5.1, pp. 447–476. ISSN: 1941-1405. DOI: 10.1146/annurev-marine-120710-100751.URL: https://doi.org/10.1146/annurev-marine-120710-100751.

Niiler, Pearn P., Nikolai A. Maximenko, and James C. McWilliams (2003). “Dynamically balanced absolute sea level of the global ocean derived from near-surface velocity observations”. In: Geophysical Research Letters 30.22. ISSN: 0094-8276. DOI: 10.1029/2003GL018628. URL: https://doi.org/10.1029/2003GL018628.

Nishioka, Jun and Hajime Obata (2017). “Dissolved iron distribution in the western and central subarctic Pacific: HNLC water formation and biogeochemical processes”. In: Limnology and Oceanography 62.5, pp. 2004–2022. ISSN: 0024-3590. DOI: 10.1002/lno .10548. URL: https://doi.org/10.1002/lno.10548.

Oschlies, Andreas (2001). “Model-derived estimates of new production: New results point towards lower values”. In: Deep Sea Research Part II: Topical Studies in Oceanography 48.10, pp. 2173–2197. ISSN: 0967-0645. DOI: https://doi.org/10.1016/S0967-0645(00) 00184-3. URL: http://www.sciencedirect.com/science/article/pii/S0967064500001843.

Paasche, E. (1998). “Roles of nitrogen and phosphorus in coccolith formation in Emiliania huxleyi (Prymnesiophyceae)”. In: European Journal of Phycology 33.1, pp. 33–42. ISSN: 0967-0262. DOI: 10.1080/09670269810001736513. URL: http://dx.doi.org/10.1080/09670269810001736513.

Palmer, J. R. and I. J. Totterdell (2001). “Production and export in a global ocean ecosystem model”. In: Deep Sea Research Part I: Oceanographic Research Papers 48.5, pp. 1169–1198. ISSN: 0967-0637. DOI: https://doi.org/10.1016/S0967-0637(00)00080-7. URL: http://www.sciencedirect.com/science/article/pii/S0967063700000807.

Palter, Jaime B., M. Susan Lozier, and Richard T. Barber (2005). “The effect of advection on the nutrient reservoir in the North Atlantic subtropical gyre”. In: Nature 437, p. 687. DOI: 10 . 1038 / nature03969https://www.nature.com/articles/nature03969#supplementary-information. URL: http://dx.doi.org/10.1038/nature03969.

Park, Jong-Yeon et al. (2011). “Variability of chlorophyll associated with El Niño–Southern Oscillation and its possible biological feedback in the equatorial Pacific”. In: Journal of Geophysical Research: Oceans 116.C10. ISSN: 2156-2202. DOI: 10 . 1029 / 2011JC007056. URL: http://dx.doi.org/10.1029/2011JC007056.

Parslow, John Stanley (1981). “Phytoplankton-zooplankton interactions : data analysis and modelling (with particular reference to Ocean Station P (50N, 145W) and controlled ecosystem experiments)”. Text. URL: https://open.library.ubc.ca/collections/831/items/1.0080145.

Plant, Joshua N. et al. (2016). “Net community production at Ocean Station Papa observed with nitrate and oxygen sensors on profiling floats”. In: Global Biogeochemical Cycles 30.6, pp. 859–879. ISSN: 0886-6236. DOI: 10.1002/2015GB005349. URL: https://doi. org/10.1002/2015GB005349.

Polovina, J. J. et al. (2011). “Projected expansion of the subtropical biome and contraction of the temperate and equatorial upwelling biomes in the North Pacific under global warming”. In: ICES Journal of Marine Science 68.6, pp. 986–995. ISSN: 1054-3139 1095-9289. DOI: 10.1093/icesjms/fsq198.

Polovina, Jeffrey J., Evan A. Howell, and Melanie Abecassis (2008). “Ocean’s least productive waters are expanding”. In: Geophysical Research Letters 35.3. ISSN: 0094-8276. DOI: 10.1029/2007gl031745.

Polovina, Jeffrey J. and Phoebe A. Woodworth (2012). “Declines in phytoplankton cell size in the subtropical oceans estimated from satellite remotely-sensed temperature and chlorophyll, 1998 2007”. In: Deep Sea Research Part II: Topical Studies in Oceanography 77-80, pp. 82–88. ISSN: 09670645. DOI: 10.1016/j.dsr2.2012.04.006.

Quéré, Corinne Le et al. (2005). “Ecosystem dynamics based on plankton functional types for global ocean biogeochemistry models”. In: Global Change Biology 11.11, pp. 2016–2040. ISSN: 1365-2486. DOI: 10.1111/j.1365- 2486.2005.1004.x. URL: http://dx.doi.org/10.1111/j.1365-2486.2005.1004.x.

Racault, M. F. et al. (2017a). “Phenological Responses to ENSO in the Global Oceans”. In: Surveys in Geophysics 38.1, pp. 277–293. ISSN: 1573-0956. DOI: 10.1007/s10712-016-9391-1. URL: https://doi.org/10.1007/s10712-016-9391-1.

Racault, Marie-Fanny et al. (2014). “Plankton indicators and ocean observing systems: support to the marine ecosystem state assessment”. In: Journal of Plankton Research 36.3, pp. 621–629. ISSN: 0142-7873. DOI: 10.1093/plankt/fbu016. URL: http://dx.doi.org/10.1093/plankt/fbu016.

Racault, Marie-Fanny et al. (2017b). “Impact of El Niño Variability on Oceanic Phytoplankton”. In: Frontiers in Marine Science 4, p. 133. ISSN: 2296-7745. URL: https://www. frontiersin.org/article/10.3389/fmars.2017.00133.

Radenac, M. H. et al. (2001). “Modeled and observed impacts of the 1997–1998 El Niño on nitrate and new production in the equatorial Pacific”. In: Journal of Geophysical Research: Oceans 106.C11, pp. 26879–26898. ISSN: 2156-2202. DOI: 10.1029/2000JC000546. URL: http://dx.doi.org/10.1029/2000JC000546.

Radenac, Marie-Hélène et al. (2012). “Sea surface chlorophyll signature in the tropical Pacific during eastern and central Pacific ENSO events”. In: Journal of Geophysical Research: Oceans 117.C4. ISSN: 01480227. DOI: 10.1029/2011jc007841.

Ren, Hong-Li and Fei-Fei Jin (2011). “Niño indices for two types of ENSO”. In: Geophysical Research Letters 38.4, n/a–n/a. ISSN: 1944-8007. DOI: 10.1029/2010GL046031. URL: http://dx.doi.org/10.1029/2010GL046031.

Riahi, Keywan et al. (2011). “RCP 8.5—A scenario of comparatively high greenhouse gas emissions”. In: Climatic Change 109.1, p. 33. ISSN: 1573-1480. DOI: 10.1007/s10584-011-0149-y. URL: https://doi.org/10.1007/s10584-011-0149-y.

Rivero-Calle, S. et al. (2015). “Multidecadal increase in North Atlantic coccolithophores and the potential role of rising CO(2)”. In: Science 350.6267, pp. 1533–7. ISSN: 1095-9203 (Electronic) 0036-8075 (Linking). DOI: 10.1126/science.aaa8026. URL: https://www.ncbi.nlm.nih.gov/pubmed/26612836.

Roche, Julie La et al. (1996). “Flavodoxin as an in situ marker for iron stress in phytoplankton”. In: Nature 382, p. 802. DOI: 10.1038/382802a0. URL: http://dx.doi.org/10.1038/382802a0.

Rodgers, K. B., J. Lin, and T. L. Frölicher (2015). “Emergence of multiple ocean ecosystem drivers in a large ensemble suite with an Earth system model”. In: Biogeosciences 12.11, pp. 3301–3320. ISSN: 1726-4189. DOI: 10.5194/bg-12-3301-2015. URL: https://www.biogeosciences.net/12/3301/2015/.

Rodríguez, F. et al. (2006). “Photoacclimation in phytoplankton: implications for biomass estimates, pigment functionality and chemotaxonomy”. In: Marine Biology 148.5, pp. 963–971. ISSN: 1432-1793. DOI: 10.1007/s00227- 005- 0138- 7. URL: http://dx.doi.org/10.1007/s00227-005-0138-7.

Roy, Shovonlal, Trevor Platt, and Shubha Sathyendranath (2011). “Modelling the timeevolution of phytoplankton size spectra from satellite remote sensing”. In: ICES Journal of Marine Science 68.4, pp. 719–728. DOI: 10.1093/icesjms/fsq176. eprint: /oup/backfile/content_public/journal/icesjms/68/4/10.1093/icesjms/fsq176/2/fsq176.pdf. URL: http://dx.doi.org/10.1093/icesjms/fsq176.

Roy, Shovonlal et al. (2013). “The global distribution of phytoplankton size spectrum and size classes from their light-absorption spectra derived from satellite data”. In: Remote Sensing of Environment 139, pp. 185–197. ISSN: 00344257. DOI: 10.1016/j.rse.2013.08.004.

Ryan, John P. et al. (2002). “Unusual large-scale phytoplankton blooms in the equatorial Pacific”. In: Progress in Oceanography 55.3, pp. 263–285. ISSN: 0079-6611. DOI:

https://doi.org/10.1016/S0079-6611(02)00137-4. URL: http://www.sciencedirect.com/science/article/pii/S0079661102001374.

Ryan, John P. et al. (2006). “Western Pacific modulation of large phytoplankton blooms in the central and eastern equatorial Pacific”. In: Journal of Geophysical Research: Biogeosciences 111.G2. ISSN: 2156-2202. DOI: 10.1029/2005JG000084. URL: http://dx.doi.org/10.1029/2005JG000084.

Sarthou, Géraldine et al. (2005). “Growth physiology and fate of diatoms in the ocean: a review”. In: Journal of Sea Research 53.1, pp. 25–42. ISSN: 1385-1101. DOI: https://doi.org/10.1016/j.seares.2004.01.007. URL: http://www.sciencedirect.com/science/article/pii/S1385110104000644.

Saulquin, Bertrand et al. (2013). “Detection of linear trends in multisensor time series in the presence of autocorrelated noise: Application to the chlorophyll-a SeaWiFS and MERIS data sets and extrapolation to the incoming Sentinel 3-OLCI mission”. In: Journal of Geophysical Research: Oceans 118.8, pp. 3752–3763. ISSN: 2169-9275. DOI: 10.1002/jgrc.20264. URL: https://doi.org/10.1002/jgrc.20264.

Schluter, Lothar et al. (2014). “Adaptation of a globally important coccolithophore to ocean warming and acidification”. In: Nature Clim. Change 4.11, pp. 1024–1030. ISSN: 1758-678X. DOI: 10.1038/nclimate2379http://www.nature.com/nclimate/journal/v4/n11/abs/nclimate2379.html #supplementary-information. URL: http://dx.doi.org/10.1038/nclimate2379.

Schneider, Niklas and Bruce D. Cornuelle (2005). “The Forcing of the Pacific Decadal Oscillation”. In: Journal of Climate 18.21, pp. 4355–4373. ISSN: 0894-8755. DOI: 10.1175/ JCLI3527.1. URL: https://doi.org/10.1175/JCLI3527.1.

Seager, Richard and Ragu Murtugudde (1997). “Ocean Dynamics, Thermocline Adjustment, and Regulation of Tropical SST”. In: Journal of Climate 10.3, pp. 521–534. ISSN: 0894-8755. DOI: 10.1175/1520-0442(1997)010<0521:ODTAAR>2.0.CO;2. URL: http://dx.doi.org/10.1175/1520-0442(1997)010<0521:ODTAAR>2.0.CO;2.

Siegel, D. A. et al. (2013). “Regional to global assessments of phytoplankton dynamics from the SeaWiFS mission”. In: Remote Sensing of Environment 135, pp. 77–91. ISSN: 00344257. DOI: 10.1016/j.rse.2013.03.025.

Siegel, David A. et al. (2016). “Prediction of the Export and Fate of Global Ocean Net Primary Production: The EXPORTS Science Plan”. In: Frontiers in Marine Science 3, p. 22. ISSN: 2296-7745. URL: https://www.frontiersin.org/article/10.3389/fmars.2016.00022.

Signorini, Sergio R., Bryan A. Franz, and Charles R. McClain (2015). “Chlorophyll variability in the oligotrophic gyres: mechanisms, seasonality and trends”. In: Frontiers in Marine Science 2. ISSN: 2296-7745. DOI: 10.3389/fmars.2015.00001.

Signorini, Sergio R. and Charles R. McClain (2012). “Subtropical gyre variability as seen from satellites”. In: Remote Sensing Letters 3.6, pp. 471–479. ISSN: 2150-704X 2150-7058. DOI: 10.1080/01431161.2011.625053.

Singh, Awnesh, Thierry Delcroix, and Sophie Cravatte (2011). “Contrasting the flavors of El Niño-Southern Oscillation using sea surface salinity observations”. In: Journal of Geophysical Research 116.C6. ISSN: 0148-0227. DOI: 10.1029/2010jc006862.

Steinberg, Deborah K. et al. (2001). “Overview of the US JGOFS Bermuda Atlantic Timeseries Study (BATS): a decade-scale look at ocean biology and biogeochemistry”. In: Deep Sea

Research Part II: Topical Studies in Oceanography 48.8, pp. 1405–1447. ISSN: 0967-0645. DOI: https://doi.org/10.1016/S0967-0645(00)00148-X. URL: http://www.sciencedirect.com/science/article/pii/S096706450000148X.

Stevenson, Samantha et al. (2010). “ENSO Model Validation Using Wavelet Probability Analysis”. In: Journal of Climate 23.20, pp. 5540–5547. ISSN: 0894-8755. DOI: 10.1175/ 2010JCLI3609.1. URL: https://doi.org/10.1175/2010JCLI3609.1.

Stock, C. A., J. P. Dunne, and J. G. John (2014). “Drivers of trophic amplification of ocean productivity trends in a changing climate”. In: Biogeosciences 11.24, pp. 7125–7135. ISSN: 1726-4189. DOI: 10.5194/bg- 11- 7125- 2014. URL: https://www.biogeosciences.net/11/7125/2014/.

Stone, L. et al. (1999). “Mass Coral Reef Bleaching: A Recent Outcome of Increased El Niño Activity?” In: Ecology Letters 2.5, pp. 325–330. ISSN: 1461-0248. DOI: 10.1046/j.1461-0248.1999.00092.x. URL: http://dx.doi.org/10.1046/j.1461-0248.1999.00092.x.

Stramski, D. et al. (2008). “Relationships between the surface concentration of particulate organic carbon and optical properties in the eastern South Pacific and eastern Atlantic relationship to changes in subarctic primary productivity”. In: Deep Sea Research Part II: Topical Studies in Oceanography 46.11, pp. 2735–2760. ISSN: 0967-0645. DOI: https://doi.org/10.1016/S0967-0645(99) 00082 - X. URL: http://www.sciencedirect.com/science/article/pii/S096706459900082X.

Wong, Chi Shing et al. (2002). “Seasonal and Interannual Variability in the Distribution of Surface Nutrients and Dissolved Inorganic Carbon in the Northern North Pacific: Influence of El Niño”. In: Journal of Oceanography 58.2, pp. 227–243. ISSN: 1573-868X. DOI: 10. 1023/A:1015897323653. URL: https://doi.org/10.1023/A:1015897323653.

Yeh, S. W. et al. (2009). “El Nino in a changing climate”. In: Nature 461.7263, pp. 511–4. ISSN: 1476-4687 (Electronic) 0028-0836 (Linking). DOI: 10.1038/nature08316. URL: https://www.ncbi.nlm.nih.gov/pubmed/19779449.

Yentsch, Charles S. and David A. Phinney (1989). “A bridge between ocean optics and microbial ecology”. In: Limnology and Oceanography 34.8, pp. 1694–1705. ISSN: 0024-3590. DOI: 10.4319/lo.1989.34.8.1694. URL: https://doi.org/10.4319/lo.1989.34.8.1694.

Yu, Jin-Yi and Seon Tae Kim (2010). “Identification of Central-Pacific and Eastern-Pacific types of ENSO in CMIP3 models”. In: Geophysical Research Letters 37.15. ISSN: 0094- 8276. DOI: 10.1029/2010GL044082. URL: https://doi.org/10.1029/2010GL044082.

Zahariev, Konstantin, James R. Christian, and Kenneth L. Denman (2008). “Preindustrial, historical, and fertilization simulations using a global ocean carbon model with new parameterizations of iron limitation, calcification, and N2 fixation”. In: Progress in Oceanography 77.1, pp. 56–82. ISSN: 0079-6611. DOI: https://doi.org/10.1016/j.pocean.2008.01.007. URL: http://www.sciencedirect.com/science/article/pii/S0079661108000104.

Zhang, Min et al. (2017). “Shifting Trends in Bimodal Phytoplankton Blooms in the North Pacific and North Atlantic Oceans from Space With the Holo-Hilbert Spectral Analysis”. In: IEEE Journal of Selected Topics in Applied Earth Observations and Remote Sensing 10.1, pp. 57–64. ISSN: 1939-1404 2151-1535. DOI: 10.1109/jstars.2016.2625813.Oceans”. In: Biogeosciences 5.1, pp. 171–201. DOI: 10.5194/bg-5-171-2008. URL: https://www.biogeosciences.net/5/171/2008/.

Stramski, Dariusz and Dale A. Kiefer (1991). “Light scattering by microorganisms in the open ocean”. In: Progress in Oceanography 28.4, pp. 343–383. ISSN: 0079-6611. DOI: http://dx.doi.org/10.1016/0079-6611(91)90032-H. URL: http://www.sciencedirect.com/science/article/pii/007966119190032H.

Strutton, Peter G. and Francisco P. Chavez (2000). “Primary productivity in the equatorial Pacific during the 1997–1998 El Niño”. In: Journal of Geophysical Research: Oceans 105.C11, pp. 26089–26101. ISSN: 2156-2202. DOI: 10.1029/1999JC000056. URL: http://dx.doi.org/10.1029/1999JC000056.

Sverdrup, H. U. (1953). “On Conditions for the Vernal Blooming of Phytoplankton”. In: ICES Journal of Marine Science 18.3, pp. 287–295. ISSN: 1054-3139. DOI: 10.1093/icesjms/18.3.287. URL: http://dx.doi.org/10.1093/icesjms/18.3.287.

Sydeman, William J. et al. (2013). “Increasing variance in North Pacific climate relates to unprecedented ecosystem variability off California”. In: Global Change Biology 19.6, pp. 1662–1675. ISSN: 1354-1013. DOI: 10.1111/gcb.12165. URL: https://doi.org/ 10.1111/gcb.12165.

Szeto, M. et al. (2011). “Are the world’s oceans optically different?” In: Journal of Geophysical Research: Oceans 116.C7. ISSN: 0148-0227. DOI: 10.1029/2011JC007230. URL: https://doi.org/10.1029/2011JC007230.

Tagliabue, A. et al. (2012). “A global compilation of dissolved iron measurements: focus on distributions and processes in the Southern Ocean”. In: Biogeosciences 9.6, pp. 2333–2349. ISSN: 1726-4189. DOI: 10.5194/bg-9-2333-2012. URL: https://www.biogeosciences.net/9/2333/2012/.

Tagliabue, Alessandro (2014). “More to hydrothermal iron input than meets the eye”. In: Proceedings of the National Academy of Sciences 111.47, p. 16641. URL: http://www.pnas.org/content/111/47/16641.abstract.

Takahashi, Taro et al. (2009). “Climatological mean and decadal change in surface ocean pCO2, and net sea–air CO2 flux over the global oceans”. In: Deep Sea Research Part II: Topical Studies in Oceanography 56.8, pp. 554–577. ISSN: 0967-0645. DOI: https://doi.org/10.1016/j.dsr2.2008.12.009. URL: http://www.sciencedirect.com/science/article/pii/S0967064508004311.

Taylor, John R. and Raffaele Ferrari (2011). “Shutdown of turbulent convection as a new criterion for the onset of spring phytoplankton blooms”. In: Limnology and Oceanography 56.6, pp. 2293–2307. ISSN: 00243590. DOI: 10.4319/lo.2011.56.6.2293.

Timothy, D. A. et al. (2013). “Climatology of sediment flux and composition in the subarctic Northeast Pacific Ocean with biogeochemical implications”. In: Progress in Oceanography 116, pp. 95–129. ISSN: 00796611. DOI: 10.1016/j.pocean.2013.06.017.

Trenberth, Kevin E. and David P. Stepaniak (2001). “Indices of El Niño Evolution”. In: Journal of Climate 14.8, pp. 1697–1701. ISSN: 0894-8755. DOI: 10.1175/1520-0442(2001)014<1697: LIOENO>2.0.CO;2. URL: https://doi.org/10.1175/1520-0442(2001)014<1697:LIOENO>2.0.CO;2.

Turk, D. et al. (2011). “Implications of changing El Niño patterns for biological dynamics in the equatorial Pacific Ocean”. In: Geophysical Research Letters 38.23, n/a–n/a. ISSN:00948276. DOI: 10.1029/2011gl049674.

Turk, Daniela et al. (2001). “Remotely Sensed Biological Production in the Equatorial Pacific”. In: Science 293.5529, p. 471. URL: http://science.sciencemag.org/content/293/5529/471.abstract.

Uitz, Julia et al. (2006). “Vertical distribution of phytoplankton communities in open ocean: An assessment based on surface chlorophyll”. In: Journal of Geophysical Research 111.C8. ISSN: 0148-0227. DOI: 10.1029/2005jc003207.

Vantrepotte, V. and F. Mélin (2011). “Inter-annual variations in the SeaWiFS global chlorophyll a concentration (1997–2007)”. In: Deep Sea Research Part I: Oceanographic Research Papers 58.4, pp. 429–441. ISSN: 09670637. DOI: 10.1016/j.dsr.2011.02.003.

Volpe, G. et al. (2007). “The colour of the Mediterranean Sea: Global versus regional biooptical algorithms evaluation and implication for satellite chlorophyll estimates”. In: Remote Sensing of Environment 107.4, pp. 625–638. ISSN: 0034-4257. DOI: https://doi.org/10.1016/j.rse.2006.10.017. URL: http://www.sciencedirect.com/science/article/pii/S0034425706004081.

Volpe, Gianluca et al. (2012). “Seasonal to interannual phytoplankton response to physical processes in the Mediterranean Sea from satellite observations”. In: Remote Sensing of Environment 117, pp. 223–235. ISSN: 0034-4257. DOI: https://doi.org/10.1016/j.rse.2011.09.020. URL: http://www.sciencedirect.com/science/article/pii/S0034425711003476.

Wang, Xiujun et al. (2005). “Ecosystem dynamics and export production in the central and eastern equatorial Pacific: A modeling study of impact of ENSO”. In: Geophysical Research Letters 32.2, n/a–n/a. ISSN: 1944-8007. DOI: 10.1029/2004GL021538. URL: http://dx.doi.org/10.1029/2004GL021538.

Weatherhead, Elizabeth C. et al. (1998). “Factors affecting the detection of trends: Statistical considerations and applications to environmental data”. In: Journal of Geophysical Research: Atmospheres 103.D14, pp. 17149–17161. ISSN: 0148-0227. DOI: 10.1029/98JD00995. URL: https://doi.org/10.1029/98JD00995.

Weber, Thomas S. and Curtis Deutsch (2010). “Ocean nutrient ratios governed by plankton biogeography”. In: Nature 467, p. 550. DOI: 10.1038/nature09403https://www.nature.com/articles/nature09403 #supplementary - information. URL: http://dx.doi.org/10.1038/nature09403.

Wernand, M. R., H. J. van der Woerd, and W. W. Gieskes (2013). “Trends in ocean colour and chlorophyll concentration from 1889 to 2000, worldwide”. In: PLoS One 8.6, e63766. ISSN: 1932-6203 (Electronic) 1932-6203 (Linking). DOI: 10.1371/journal.pone.0063766. URL: https://www.ncbi.nlm.nih.gov/pubmed/23776435.

Westberry, Toby K. et al. (2016). “Annual cycles of phytoplankton biomass in the subarctic Atlantic and Pacific Ocean”. In: Global Biogeochemical Cycles 30.2, pp. 175–190. ISSN:1944-9224. DOI: 10.1002/2015GB005276. URL: http://dx.doi.org/10.1002/2015GB005276.

Whitney, F. A., C. S.Wong, and P.W. Boyd (1998). “Interannual variability in nitrate supply to surface waters of the Northeast Pacific Ocean”. In: Marine Ecology Progress Series 170, pp. 15–23. URL: https://www.int-res.com/abstracts/meps/v170/p15-23/.

Wilson, Cara and David Adamec (2001). “Correlations between surface chlorophyll and sea surface height in the tropical Pacific during the 1997-1999 El Niño-Southern Oscillation event”. In: Journal of Geophysical Research: Oceans 106.C12, pp. 31175–31188. ISSN: 01480227. DOI: 10.1029/2000jc000724.

Wong, C. S. et al. (1999). “Seasonal and interannual variability in particle fluxes of carbon, nitrogen and silicon from time series of sediment traps at Ocean Station P, 1982–1993: relationship to changes in subarctic primary productivity”. In: Deep Sea Research Part II: Topical Studies in Oceanography 46.11, pp. 2735–2760. ISSN: 0967-0645. DOI: https://doi.org/10.1016/S0967-0645(99)00082-X. URL:http://www.sciencedirect.com/science/article/pii/S096706459900082X.

Wong, Chi Shing et al. (2002). “Seasonal and Interannual Variability in the Distribution of Surface Nutrients and Dissolved Inorganic Carbon in the Northern North Pacific: Influence of El Niño”. In: Journal of Oceanography 58.2, pp. 227–243. ISSN: 1573-868X. DOI: 10.1023/A:1015897323653. URL: https://doi.org/10.1023/A:1015897323653.

Yeh, S. W. et al. (2009). “El Nino in a changing climate”. In: Nature 461.7263, pp. 511–4. ISSN: 1476-4687 (Electronic) 0028-0836 (Linking). DOI: 10.1038/nature08316. URL:https://www.ncbi.nlm.nih.gov/pubmed/19779449.

Yentsch, Charles S. and David A. Phinney (1989). “A bridge between ocean optics and microbial ecology”. In: Limnology and Oceanography 34.8, pp. 1694–1705. ISSN: 0024-3590. DOI: 10.4319/lo.1989.34.8.1694. URL: https://doi.org/10.4319/lo.1989.34.8.1694.

Yu, Jin-Yi and Seon Tae Kim (2010). “Identification of Central-Pacific and Eastern-Pacific types of ENSO in CMIP3 models”. In: Geophysical Research Letters 37.15. ISSN: 0094-8276. DOI: 10.1029/2010GL044082. URL: https://doi.org/10.1029/2010GL044082.

Zahariev, Konstantin, James R. Christian, and Kenneth L. Denman (2008). “Preindustrial, historical, and fertilization simulations using a global ocean carbon model with new parameterizations of iron limitation, calcification, and N2 fixation”. In: Progress in Oceanography 77.1, pp. 56–82. ISSN: 0079-6611. DOI: https://doi.org/10.1016/j.pocean.2008.01.007. URL: http://www.sciencedirect.com/science/article/pii/S0079661108000104.

Zhang, Min et al. (2017). “Shifting Trends in Bimodal Phytoplankton Blooms in the North Pacific and North Atlantic Oceans From SpaceWith the Holo-Hilbert Spectral Analysis”. In: IEEE Journal of Selected Topics in Applied Earth Observations and Remote Sensing 10.1, pp. 57–64. ISSN: 1939-1404 2151-1535. DOI: 10.1109/jstars.2016.2625813.

Zhang, Wenjun et al. (2011). “Contrasting Impacts of Two-Type El Nino over the Western North Pacific during Boreal Autumn”. In: Journal of the Meteorological Society of Japan. Ser. II 89.5, pp. 563–569. DOI: 10.2151/jmsj.2011-510.

Zhang, Yuan, John M. Wallace, and David S. Battisti (1997). “ENSO-like Interdecadal Variability: 1900–93”. In: Journal of Climate 10.5, pp. 1004–1020. ISSN: 0894-8755. DOI: 10.1175/1520-0442(1997)010<1004:ELIV>2.0.CO;2. URL: https://doi.org/10.1175/15200442(1997)010<1004:ELIV>2.0.CO;2.

INDEX

absorption-based, *4*, *5*, *31*
abundance-based, *4*, *31*
active mixing length scale, *x*, *xi*, *xii*, *3*, *6*, *33*, *34*, *36*, *47*, *50*, *56*, *73*, *90*, *92*
agglomerative hierarchical clustering, *v*, *20*
AHC. *See* agglomerative hierarchical clustering
atmospheric forcing, *14*, *74*
backscattering-based algorithms, *4*
biological pump, *vi*, *1*, *3*, *30*
buoyancy frequency, *64*
Carbon Model Intercomparison Project, *v*
carbondioxide, *7*
Central Pacific El Niño, *16*
CESM1. *See* CMIP5 or Earth System Models
Chl/C. *See* photoacclimation
Chl-a. *See* chlorophyll-a
chlorophyll-a, *v*, *1*, *2*, *27*, *29*, *30*, *53*, *54*, *90*, *100*, *105*, *117*
climatology. *See* seasonal cycle
CMIP5. *See* Carbon Model Intercomparison Project
CO_2. *See* carbondioxide
coccolithophores, *1*, *2*, *7*, *116*
CPEN. *See* Central Pacific El Niño
DCM. *See* Deep Chlorophyll Maximum
Deep Chlorophyll Maximum, *8*
diatoms, *1*, *2*, *3*, *30*, *32*, *34*, *35*, *39*, *40*, *43*, *49*, *90*, *95*, *96*, *97*, *102*, *107*, *111*, *113*, *117*
diffuse attenuation coefficient for downwelling irradiance at 490 nm, *2*, *4*, *33*, *62*
Earth systems climate models, *6*
Eastern Pacific El Niño, *16*
Ekman length scale, *50*, *64*
El Niño, *xii*, *6*, *5*, *15*, *16*, *17*, *19*, *21*, *22*, *23*, *56*, *63*, *81*, *84*, *87*, *100*, *103*, *104*, *105*, *106*, *107*, *110*, *113*, *115*, *116*, *118*, *119*, *120*, *121*
El Niño Modoki. *See* Central Pacific El Niño
El Niño Southern Oscillation, *6*, *5*, *15*, *16*, *63*
empirical orthogonal functional analysis, *v*
ENSO. *See* El Niño Southern Oscillation
EOF. *See* empirical orthogonal functional analysis
EPEN. *See Eastern Pacific El Niño*
Equatorial Undercurrent, *56*
Error bars, *74*, *78*, *79*
EUC. *See* Equatorial Undercurrent
Fe. *See* Iron
generalized least square, *4*, *64*, *66*
GLS. *See* generalized least square
grazing, *7*, *10*, *30*, *34*, *35*, *36*, *37*, *41*, *42*, *43*, *45*, *56*, *57*, *95*, *111*
high nutrient-low chlorophyll, *30*
HNLC. *See* high nutrient-low chlorophyll
Holling type, *43*
Holling type III, *43*
interannual, *v*, *3*, *7*, *3*, *5*, *6*, *9*, *10*, *15*, *18*, *30*, *31*, *55*, *56*, *63*, *105*, *120*, *121*
Iron, *29*, *34*, *37*, *42*, *44*, *50*, *51*, *95*, *97*, *107*, *111*, *112*, *113*
isothermal depth, *17*, *27*
$K_d(490)$. *See* diffuse attenuation coefficient for downwelling irradiance at 490 nm

L_OZ. *See* Ozmidov length scale
La Niña, *5*, *9*, *10*, *16*, *20*, *81*
L_{EK}. *See* Ekman length scale
L_{MIX}. *See* Active mixing length Scale
L_{OB}. *See* Obukhov length
MEI. *See* Multivariate El Niño Index
microphytoplankton, *x*
Microphytoplankton, *9*
mixed layer depth, *2*, *7*, *3*, *29*, *50*, *51*, *53*, *94*
MLD. *See* mixed layer depth
Monte-Carlo, *4*
Multivariate El Niño Index, *17*
N^2. *See* buoyancy frequency
nanophytoplankton, *x*, *9*, *55*
NAO. *See* North Atlantic Oscillation
NATL. *See* North Atlantic Gyre
North Atlantic Gyre, *5*, *74*
North Atlantic Oscillation, *6*
North Pacific gyre, *6*, *67*
North Pacific Gyre Oscillation, *6*, *104*, *105*
NPAC. *See* North Pacific gyre
NPGO. *See* North Pacific Gyre Oscillation
nutricline, *5*, *20*, *21*
Obukhov length, *64*
Ocean Color Index, *9*, *33*, *62*, *88*
OCI. *See* Ocean Color Index
OLS. *See* ordinary least square
one-sigma error. *See* Error bars
ordinary least square, *64*, *66*
Ozmidov length scale, *64*
PAR. *See* photosynthetically available radiation
particle size distribution (PSD), *4*, *3*, *17*, *38*, *62*
particulate inorganic carbon, *4*, *62*
PFTs. *See* Phytoplankton Functional Types
phosphate, *1*, *4*
photoacclimation, *2*, *7*, *10*, *3*, *8*, *10*, *22*, *30*, *33*, *38*, *42*, *49*, *50*, *51*, *55*, *63*
photosynthesis, *v*, *1*, *2*, *3*, *7*, *21*, *30*, *36*, *58*, *101*
photosynthetically available radiation, *2*, *4*, *33*, *62*
Phytoplankton, *v*, *vi*, *1*, *2*, *3*, *4*, *8*, *16*, *27*, *30*, *40*, *43*, *50*, *51*, *55*, *95*, *102*, *103*, *104*, *106*, *107*, *108*, *109*, *111*, *112*, *113*, *114*, *115*, *116*, *118*, *119*, *121*
phytoplankton functional types (PFTs), *1*, *30*
PIC. *See* particulate inorganic carbon
picophytoplankton, *x*, *9*, *34*
primary production, *1*, *2*, *3*, *10*, *16*, *34*, *35*, *36*, *37*, *45*, *53*, *54*, *55*, *95*, *101*, *103*, *104*, *108*, *110*, *111*
pycnocline, *3*, *6*, *7*
radiance-based, *4*, *31*
regression, *xii*, *4*, *19*, *64*, *66*, *69*, *70*, *79*, *84*, *86*
remineralization, *1*, *3*, *44*, *55*, *58*
SATL. *See* South Atlantic gyre
sea surface temperature, *x*, *xii*, *7*, *3*, *16*, *17*, *29*, *33*, *47*, *63*, *90*, *94*
seasonal cycle, *8*, *4*, *7*, *29*, *31*, *35*, *37*, *38*, *40*, *41*, *42*, *45*, *56*, *58*, *64*, *66*
Sea-Viewing Wide Field-of-View Sensor, *v*, *3*
SeaWiFS. *See* Sea-Viewing Wide Field-of-View Sensor

South Atlantic gyre, *7*, *67*
South Pacific gyre, *6*, *67*
Southern Hemispheres, *9*
SPAC. *See* South Pacific gyre
$spCO_2$. *See* surface partial pressure of carbondioxide
SST. *See* sea surface temperature
stratification, *3*, *5*, *6*, *9*, *10*, *21*, *36*, *38*, *55*, *64*, *104*, *105*, *111*
subpolar gyre, *44*
subtropical gyres, *vii*, *ix*, *xi*, *xii*, *3*, *2*, *4*, *5*, *6*, *8*, *9*, *10*, *18*, *23*, *36*, *55*, *56*, *63*, *64*, *71*, *73*, *78*, *79*, *81*, *83*, *106*
surface partial pressure of carbondioxide, *7*
thermocline, *5*, *20*, *21*, *22*, *44*, *64*
trade winds, *5*
tropical Pacific, *v*, *x*, *4*, *5*, *10*, *13*, *16*, *17*, *21*, *23*, *55*, *56*, *63*, *67*, *81*, *103*, *105*, *109*, *113*, *116*, *121*
uncertainty, *4*, *46*, *64*, *66*, *79*
upwelling, *1*, *10*, *18*, *21*, *22*, *23*, *30*, *44*, *56*, *104*, *115*
$Z_{20°C}$. *See* isothermal depth
zoo. *See* zooplankton
zooplankton, *xii*, *1*, *7*, *34*, *35*, *38*, *39*, *41*, *42*, *43*, *44*, *45*, *46*, *53*, *54*, *57*, *89*, *93*, *95*, *96*, *97*, *115*